MODELLING DEGRADATION OF BIODEGRADABLE POLYMERS AND THEIR MECHANICAL PROPERTIES

Thesis submitted for the degree of
Doctor of Philosophy
At the University of Leicester

by

Andrew Colin Gleadall (MEng)
Department of Engineering
University of Leicester

April 2015

ABSTRACT

THESIS:

Modelling degradation of biodegradable polymers and their mechanical properties

AUTHOR:

Andrew Colin Gleadall

Bioresorbable polymers are used for a wide range of medical applications inside the human body including fixation screws and plates for broken bones, sutures and scaffolds for tissue regeneration. Over a period of months or years, these devices degrade by hydrolysis of the ester bonds; they become fully absorbed into the body, thus removing the need for repeat surgery. The degradation pathway of these devices, including the loss of mechanical properties, is of great importance. However, the complexity of the degradation process, and the number of factors involved, means that degradation trends are not fully understood. Also, for many of the commonly used biodegradable polymers, no theoretical understanding exists for changes to mechanical properties during degradation. The devices are therefore currently designed to be over-supportive, which may inhibit the healing process due to the stress shielding effect. A general mathematical framework has been developed through several PhD projects at Leicester to model the degradation of bioresorbable polymers. This PhD thesis consists of three parts. The first part reviews the existing understanding of bioresorbable polymer degradation. In the second part, the previous models are simplified and improved. These new models are then used to reveal an in-depth understanding of the underlying mechanisms of the degradation process. The third part of this thesis focuses on understanding the change in Young's modulus of degrading polymers. In order to do so, a novel atomistic finite element method is developed, which can simulate the mechanical response of a representative unit of a biodegradable polymer. The method is used to study the mechanical behaviour of polymer chains once chain scissions are introduced. The study leads to a concept for effective cavities for polymer chain scission, called the Effective Cavity Theory, which can be used to predict the change in Young's modulus of a degrading polymer.

Acknowledgements

I am eternally grateful to my supervisor, Jingzhe Pan, for all his help throughout my PhD. He gave me the freedom to explore any direction of research I desired whilst at the same time keeping my focus on areas of scientific interest. He has the vision and empathy to be able to make everything seem perfectly fine with just a few words of encouragement. And without exception, he offered his time and support whenever it was needed. He has inspired me to hopefully one day offer similar support to PhD students of my own.

I'm thankful to my co-supervisor Helen Atkinson and industrial supervisor Marc-Anton Kruft for their broad guidance. And to Minna Kellomäki, David Curcó, Xinpu Chen and Lifeng Ding for their contributions towards several areas of my work.

Also, those people who made my conference visits both entertaining and inspiring including: Mikko Huttunen, Ville Ellä, Niina Ahola, Kaarlo Paakinaho, Dirk Grijpma, Michiel van Alst and Carolien Geurts.

I am grateful to the EPSRC and the University of Leicester for my PhD studentship.

Finally, I'm thankful to my friends and family for all their support. In particular, I'd like to thank: my wonderful wife Rachel who supported me, encouraged me and gives me great happiness; and my mum, dad, sister and brother, who showed persistent enthusiasm about my PhD but also helped me enjoy so many things alongside my PhD.

Contents

List of publications and conference presentations

Journal Publications

1. Andrew Gleadall, Jingzhe Pan and Helen Atkinson. (2012). A simplified theory of crystallisation induced by polymer chain scissions for biodegradable polyesters. Polymer Degradation and Stability 97(9): 1616-1620.
2. Andrew Gleadall and Jingzhe Pan. (2013). Computer Simulation of Polymer Chain Scission in Biodegradable Polymers. Journal of Biotechnology & Biomaterials 3:154
3. Andrew Gleadall, Jingzhe Pan, Marc-Anton Kruft and Minna Kellomäki. (2014). Degradation mechanisms of bioresorbable polyesters. Part 1. Effects of random scission, end scission and autocatalysis. Acta Biomaterialia 10(5): 2223-2232.
4. Andrew Gleadall, Jingzhe Pan, Marc-Anton Kruft and Minna Kellomäki. (2014). Degradation mechanisms of bioresorbable polyesters. Part 2. Effects of initial molecular weight and residual monomer. Acta Biomaterialia 10(5): 2233-2240.
5. Andrew Gleadall, Jingzhe Pan, Lifeng Ding, Marc-Anton Kruft and David Curcó. An atomic finite element model for biodegradable polymers. Part 1. Formulation of the finite elements. Submitted for publication.
6. Andrew Gleadall, Jingzhe Pan and Marc-Anton Kruft. An atomic finite element model for biodegradable polymers. Part 2. A model for change in Young's modulus due to polymer chain scission. Submitted for publication.

Book Chapter

Andrew Gleadall. (2015). Mechanical properties of biodegradable polymers. In: Jingzhe Pan, Modelling degradation of bioresorbable polymeric medical devices. Woodhead Publishing.

Conference presentations

1. A Simplified Model to Predict Molecular Weight and Crystallisation of Bioresorbable Polymers during Hydrolysis. Poster presentation at the European Biomaterials Conference 2011, Dublin, Ireland.
2. A Critical Survey of Degradation Data for Mechanical Properties of Bioresorbable Polymers. Poster presentation at the European Biomaterials Conference 2011, Dublin, Ireland.
3. Mechanical properties of degrading polymers – a critical review of the literature. Oral presentation in workshop, Loughborough University 2011, UK.
4. A Molecular Model for Young's Modulus Degradation in Biodegradable Polymers. Poster presentation at the World Biomaterials Congress 2012, Chengdu, China.
5. Modelling the Degradation of Mechanical Properties of Bioresorbable Polymers. Poster presentation at the Festival of Postgraduate Research 2012, University of Leicester, UK.
6. Computer model for the effect of residual monomer on biodegradable polyesters. Poster presentation at the European Biomaterials Conference 2013, Madrid, Spain.

List of symbols

Symbol	Model parameter description	Units
Symbols used in Chapters 1 to 3 and in the mathematical degradation model in Chapters 4, 5 and 10		
α	oligomer production rate parameter	no units
β	oligomer production rate parameter	no units
C_e	concentration of ester bonds in amorphous chains	mol m^{-3}
C_{e0}	initial concentration of ester bonds in all phases	mol m^{-3}
E	Young's modulus	GPa
k_1	generic noncatalytic scission reaction rate constant	day^{-1}
k_2	generic autocatalytic scission reaction rate constant	$[mol^{-1}m^3]^{0.5}day^{-1}$
m	average degree of polymerisation of oligomers	no units
M_0	molar mass	g mol^{-1}
M_n	number averaged molecular weight	g mol^{-1}
M_w	weight averaged molecular weight	g mol^{-1}
$N_{chains0}$	original concentration of chains	mol m^{-3}
R_s	total scissions concentration	mol m^{-3}
R_{ol}	oligomer concentration (produced)	mol m^{-3}
T_g	glass transition temperature	°C
ω	inverse molar volume of crystalline phase	mol m^{-3}
X_c	degree of crystallinity	volume fraction
X_{ext}	extended degree of crystallinity	volume fraction
X_{max}	maximum degree of crystallinity	volume fraction
p_x	crystal nucleation probability	no units
V_c	crystallite volume	m^3
η_A	Avogadro's constant	mol^{-1}
Additional symbols in the model developed in Chapters 6 and 7		
C_{acid}	concentration of carboxylic acid end groups	mol m^{-3}
C_{end}	concentration of long chain ends	mol m^{-3}
C_{ol}	oligomer concentration (after diffusion)	mol m^{-3}
C_m	monomer concentration (after diffusion)	mol m^{-3}
D_0	diffusion coefficient (amorphous phase)	m^2 day^{-1}
D_{pore}	diffusion coefficient (pores)	m^2 day^{-1}
k_{e1}	noncatalytic end scission reaction rate constant	day^{-1}
k_{r1}	noncatalytic random scission reaction rate constant	day^{-1}
k_{e2}	autocatalytic end scission reaction rate constant	$[mol^{-1}m^3]^{0.5}day^{-1}$
k_{r2}	autocatalytic random scission reaction rate constant	$[mol^{-1}m^3]^{0.5}day^{-1}$
n	dissociation power of the acid end group	no units
N_{chain}	current concentration of chains	mol m^{-3}
R_{es}	concentration of end scissions	mol m^{-3}
R_{rs}	concentration of random scissions	mol m^{-3}
R_m	monomers per unit volume	mol m^{-3}
Additional symbols in the Effective Cavity Theory developed in Chapter 9		
E_p	overall polymer Young's modulus	GPa
E_∞	Young's modulus of amorphous polymer with no effective cavities	GPa
$\overline{E}$	normalised Young's modulus	no units

ρ_p	density of the polymer	g m^{-3}
V_{ec}	molar volume of an effective cavity	m mol^{-3}
X_{ec}	volume fraction of effective cavities	no units
Symbols used in the atomic simulation model in Chapters 8 and 9		
σ_{ii}	Lennard-Jones radius for atoms i	nm
θ	bond-angle	rad
θ_0	equilibrium bond angle	rad
Φ	bond-dihedral angle	rad
Φ_0	bond-dihedral phase shift	rad
C_n	Ryckaert-Bellemans coefficients	kJ mol^{-1}
d_{el}	AFEM element change in length or angle	nm or rad
ε_{ii}	Lennard-Jones well-depth parameter for atom i	kJ mol^{-1}
ε_0	electric constant	F m^{-1}
F	externally applied force	N
k_a	bond-angle force constant	kJ mol^{-1} rad^{-2}
k_b	bond-stretch force constant	kJ mol^{-1} nm^{-2}
k_d	periodic dihedral force constant	kJ mol^{-1}
k_{el}	AFEM element force constant	kJ mol^{-1} nm^{-2} or kJ mol^{-1} rad^{-2}
k_{d_FEM}	bond-dihedral force constant adapted for AFEM	kJ mol^{-1} rad^{-2}
k_{nb_FEM}	nonbond force constant adapted for AFEM	kJ mol^{-1} nm^{-2}
n_Φ	bond-dihedral multiplicity	no units
q_i	electric charges for atom i	elementary charge
r_{ij}	atomic separation	nm
r_0	equilibrium atomic separation	nm
u	displacement where F is applied	nm
u_{cell}	periodic cell elongation	nm
u_i	single atom Cartesian displacement	nm
V_a	bond-angle potential energy	kJ mol^{-1}
V_b	bond-stretch potential energy	kJ mol^{-1}
$V_{Coulomb}$	Coulomb interaction potential energy	kJ mol^{-1}
V_d	bond-dihedral potential energy	kJ mol^{-1}
$V_{d(periodic)}$	periodic dihedral potential energy	kJ mol^{-1}
$V_{d(Ryckaert-Bellemans)}$	Ryckaert-Bellemans dihedral potential energy	kJ mol^{-1}
$V_{Lennard-Jones}$	Lennard-Jones potential energy	kJ mol^{-1}
V_{nb}	nonbond potential energy	kJ mol^{-1}
V_{MD}	total interatomic potential energy	kJ mol^{-1}
V_{MD_FEM}	total interatomic potential energy adapted for AFEM	kJ mol^{-1}
V_{el}	AFEM element strain energy	kJ mol^{-1}

List of abbreviations

DSC	differential scanning calorimetry
GPC	gel permeation chromatography
PBS	phosphate buffer solution
PLA	poly lactic acid
PLLA	poly L-lactic acid
PLGA	poly lactic-co-glycolic acid copolymer
PDLA	poly D-lactic acid
PDLLA	poly DL-lactic-co-L-lactic acid copolymer
PCL	poly caprolactone
PDI	polydispersity index
MD	molecular dynamics
FEA	finite element analysis
FEM	finite element method
AFEM	atomic finite element method
IV	inherent viscosity

Part 1: Background information and literature review

Chapter 1: Introduction

This chapter gives some details about bioresorbable polymers, including their uses, degradation mechanisms and microstructure. Theoretical models for degradation are discussed. Mechanical properties are discussed in depth in the critical review of mechanical properties of biodegradable polymers in Chapter 2. More detailed information, specific to the work presented in individual chapters, is given in the respective introductions of those chapters. The overall structure of this thesis and knowledge gaps that it addresses are summarised in Chapter 3.

1.1 Typical bioresorbable polymers and their uses

Bioresorbable polyesters such as poly(lactide), poly(glycolide) and poly(caprolactone) are used in many medical applications including fixation devices for broken bones, sutures, drug delivery and scaffolds for tissue regeneration. Fig. 1.1 shows two bioresorbable plates that are used to support a spine and an ankle joint. The degradation of bioresorbable polymers is often characterised by the reduction of molecular weight, mass, stiffness or strength over time and a large number of experiments have been conducted to understand the degradation [1-31]. The biodegradable polymers must degrade slowly enough to perform their intended purpose, but not degrade so slowly that the device remains in the body for unnecessarily long time periods after healing.

Biodegradable polymer fixation devices offer advantages over metal devices because they become fully absorbed into the body over a period of weeks, months or years, depending on the type of polymer being used; this avoids the need for repeat surgery to remove the device after it has performed its function. It is not ideal to leave metallic devices in the body permanently because there is an increased risk of infection associated with foreign objects inside the human body. In addition, since biodegradable polymer stiffness reduces over time, there is a gradual reduction in mechanical support for the healing bones. This may facilitate a quicker or more complete recovery because bones may grow stronger when they are subject to mechanical loading [32, 33]. Biodegradable fixation devices are currently used in healthcare (surgeons have a choice of whether to use metallic or polymeric devices) but there is scope for more wide-spread use. The benefit of biodegradable polymer devices being absorbed into the body is offset by the fact that in some cases biodegradable polymer implants can

lead to inflammation, most likely due to an acidic environment resulting from degradation products [34-38]. Also, the degradation rates of biodegradable polymers are not fully understood and surgeons do not desire an implant to remain in the body longer than necessary. The widespread use of biodegradable polymer implants could increase if their degradation was more predictable. This could ultimately lead to a better experience and better recovery for patients due to the benefits mentioned above and also because biodegradable polymers may potentially be tailored to degrade at a patient-specific rate so that the optimal level of support is given throughout the duration of the healing process.

Bioresorbable polymers are also used as scaffolds for tissue engineering. In these applications, tissue can be grown outside the body on a porous scaffold, the shape of which dictates the shape of the tissue that is grown. As the tissue grows, the biodegradable scaffold degrades, and hence ultimately, there are no remnants of the original scaffold. This field is relatively premature at present but is subject to a huge amount of research. Tissue growth can also be supported inside the human body, for example to grow bone over a screw hole or to grow cartilage on a replacement nose scaffold for facial reconstruction. Tissue regeneration may be one of the most important scientific developments over the next decades and centuries. Throughout this period, stepwise developments will be of great individual importance. Currently, tissue engineering is becoming more widespread for the growth of basic tissues such as bone, skin and cartilage. Even simple tissue can offer huge benefits to patients for applications such as burns recovery or facial reconstruction to treat birth defects or physically deforming accidents. Tissue engineering of simple tissues is a relatively mature field in an academic context. The more widespread use of tissue engineering for simple tissue will occur as clinical use generates greater confidence in the surgical field. More complex tissues such as organ tissues are the focus of current state of the art academic research. This involves primarily a biological focus but research into the structure and degradation of biodegradable polymers is also of critical importance. As complex tissues become more achievable, patients will benefit from the replacement of diseased organs, or functional body parts such as blood vessels and nerves, without the need for transplantation. Benefits over transplants are that there is no need to wait for a donor, there may be a reduced chance of organ rejection, and tissue may be tailored to the specific patient's requirements. In the longer-term, fully complex organs such as hearts and lungs may be replaced in patients. This is particularly valuable for patients who are otherwise healthy except for a single diseased organ, in particular

children with organ defects from birth. These developments can only be realised if the biodegradable polymer scaffolds degrade in the correct manner to facilitate the complicated cell-growth requirements. Presently, a key step for tissue engineering with regards to the biodegradable polymer scaffold is to further the understanding of biodegradable polymer degradation.

Another application of bioresorbable polymers is drug delivery. This is an extremely broad field. Two examples of state of the art drug delivery may be the timed and targeted release of drugs to promote cell growth at a healing site or to destroy cells that are cancerous. To further the capabilities of achieving the correct release profile of drugs, the degradation profile of the biodegradable polymer must be further understood through work such as that conducted in this thesis.

The degradation process of biodegradable polymers is complicated because a large number of factors affect degradation. The interaction between all of these factors is not fully understood. One of the most important characteristics of biodegradable polymers is the degradation profile for mechanical properties. The optimal degradation pathway for mechanical properties of fixation devices is to lose mechanical properties gradually as the bone strength increases. The gradual transfer of stress from the fixation device to the bone can aid healing because bones become weaker when they are not subject to stress. Overall mechanical properties are the result of several underlying properties of the polymer including polymer chain structure, water absorption, molecular weight and crystallinity. Since the factors that affected mechanical properties are in turn affected by degradation, the current understanding of how mechanical properties degrade is limited. There are no theoretical models for the degradation of biodegradable polymers that are used below their glass transition temperature, including poly(lactide) and poly(glycolide). A detailed discussion of polymer mechanical properties and their degradation mechanisms is included in the next chapter of this thesis.

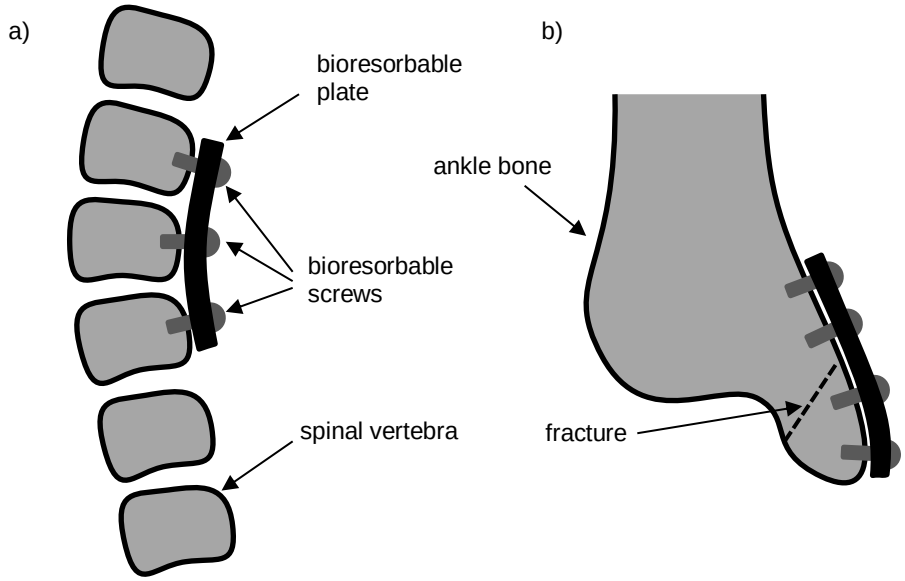

Fig. 1.1 Example medical fixation devices used to support (a) a healing spine and (b) an ankle bone.

1.2 Degradation of bioresorbable polymers by hydrolysis

A polymer consists of long chains, which are made up of several hundred or thousand polymer repeat units, also referred to as monomers. Poly(lactide) is an aliphatic polyester, which is of particular interest in the medical field because it has relatively high stiffness and typically degrades over a period of years. The polymer repeat unit of poly(lactide) consists of 3 carbon atoms, 4 hydrogen atoms and 2 oxygen atoms. An ester bond between adjacent polymer repeat units bonds an oxygen atom of one repeat unit to a carbon atom of the next. During degradation by hydrolysis, water molecules diffuse into the amorphous regions of the polymer and hydrolyse the ester bonds. The hydrolysis reaction is slow compared to the intake of water molecules and water can be assumed to be abundant [39]. Hence, degradation typically occurs throughout the bulk of the polymer rather than from the surface inwards. The result of a scission is that two new chain ends are formed; one has an alcohol end group while the other has a carboxylic acid end group. As the number of carboxylic acid chain ends increases, the acidity of the polymer increases overall and this can lead to the catalysis of further hydrolysis due to the increase in acidity [1, 15, 40-42].

Molecular weight is used to characterise the average number of polymer repeat units in each polymer chain. As a result of a chain scission, the molecular weight of a polymer chain decreases because the chain is divided into two smaller chains. Mathematical

models for chain scission in biodegradable polymers can be used to predict the rate of reduction of molecular weight and compared to experimental data. In order to measure molecular weight experimentally, gel permeation chromatography (GPC) is often used. In GPC the time taken for polymer chains to pass through a column of porous beads, which is affected by their molecular weight, is measured. The fraction of the polymer within chains of a given molecular weight range can be calculated to find the distribution of molecular weights. However, it may not be possible to differentiate between low molecular weight chains, which are beyond the scope of GPC. As a result, it may be most appropriate for theoretical calculations of molecular weight to exclude chains below a certain length. It may also be the case that water-soluble chains can diffuse out of the polymer [43], and hence they would be excluded from GPC analysis. Two common measurements are number average molecular weight and weight average molecular weight. For number average molecular weight, the total mass of all polymer chains is divided by the total number of chains in order to give the numerical average length of each individual polymer chain. Weight average molecular weight however allows for the fact that, when selecting a polymer repeat unit at random from the whole polymer, it is probabilistically more likely that a repeat unit contained in any given long polymer chain is selected rather than one in any given short chain.

The position along polymer chains at which scissions occur is of interest because chain scissions near the end of polymer chains lead to water-soluble oligomers, which may catalyse the hydrolysis reaction. Also, a scission at the end of a polymer chain may have different effects on mechanical properties than a scission towards the centre of a polymer chain. Two theories are generally considered in the literature: random scission and end scission. In random scission, it is assumed that each ester bond in the polymer has an equal chance of chain cleavage whereas end scission assumes that only ester bonds at the end of polymer chains are cleaved, resulting in a monomer for every end scission. The final bond of a polymer chain may be more susceptible to hydrolysis because of its proximity to the acidic chain end, which may catalyse the hydrolysis reaction [44, 45]. Given that a typical polymer chain may consist of several thousand bonds, a large number of end scissions may be required per chain in order for the reduction in chain length to be comparable to a single random scission. It has been suggested that both random scission and end scission hydrolysis mechanisms may occur concurrently [46] and mathematical models have been able to fit experimental data with assumptions of random scission [27, 28, 47], end scission [48] or a combination of both [26].

Experimental evidence for which hydrolysis mechanisms are dominant is conflicting due to the number of factors that affect degradation and inconsistency between experiments. Shih [46] suggested that end scission is dominant with approximately 10 times the rate of random scission. However for a high molecular weight sample, a single random scission has a greater impact on molecular weight than 1000 end scissions, and thus their experiment actually indicates that random scission may control the molecular weight reduction. The experiment by Schliecker et al. [13] supports the theory of noncatalytic hydrolysis because it was found that the addition of oligomers does not accelerate degradation. However, several experimental publications support the theory of autocatalysis [14, 15, 18, 22, 23, 27, 41, 42]. Antheunis et al. [27] found that polymers in which the chain possessed carboxylic acid chain end groups degraded at a faster rate than polymers in which the acid chain ends were capped. Therefore in the mathematical models of Pan and his co-workers [48-50] the hydrolysis reaction is modelled for both noncatalytic and autocatalytic degradation. In their model, the autocatalytic hydrolysis reaction is assumed to be catalysed by the acidic environment generated by carboxylic acid chain ends of water-soluble oligomers and monomers. This reflects a theory that long chain ends contribute less to autocatalysis than shorter chains because they have lower mobility and may not initially possess carboxylic acid end groups. Water-soluble oligomers and monomers may diffuse out of the polymer near the surface of a polymer. This results in a lower concentration of carboxylic acid chain ends than in the centre of the polymer and therefore a slower rate of hydrolysis near the surface. It has been widely observed that degradation occurs faster at the core of large samples compared to the surface [14, 15, 22, 27, 41, 42], which supports this theory. However, heterogeneous degradation does not occur in all experiments. It is not expected to occur in thin film samples since the rate of diffusion, of oligomers and monomers, relative to overall sample size is greater than in large samples, and does not allow for a significant build-up of oligomers and monomers in the core of the film.

1.3 Polymer crystallinity

In amorphous polymers, the polymer chains have a random configuration and are entangled within each other, similar to cooked spaghetti. Given the freedom to occupy the most stable atomic positions, the chains align next to one another, similar to uncooked spaghetti. Such alignment is referred to as crystallisation. The chains align as close as possible until an overlap of the atoms' electron fields results in large repulsive forces. A single collection of aligned polymer chains is referred to as a

crystallite. It is not possible, except under extreme conditions, for a polymer to be 100% crystalline because a polymer chain may be entangled with several other polymer chains and therefore unable to straighten out into a single crystal. The ends of polymer chains are also likely to be unable to fit directly into a crystallite because the atomic configuration and energy state is different to that of regular polymer repeat units in the middle of a long polymer chain. The close packing of polymer chains in a crystallite, compared to the amorphous phase, results in an increased overall interatomic attraction between the chains, and therefore the crystallites have a more stable atomic configuration and a higher value of stiffness than regions of amorphous polymer chains.

Crystalline polymer structures have been observed experimentally for over 50 years. The review of Oppenlander in 1968 [51] discussed many theories for crystal structure with a particular focus on how the polymer chains organise into crystal and amorphous phases. Fig. 1.2 is reproduced from the study of Oppenlander and shows schematics of how chains may be organised in a crystallite. In Fig. 1.2 (a) the chains fold back into the crystallite immediately, while in (b) the chains may leave and re-enter at a crystal over a greater distance. In Fig. 1.2 (c), the combination of amorphous and crystalline phases is shown, where a single polymer chain may be distributed over several crystallites and amorphous regions. A more recent study by Zong et al. in 1999 [52] considered the crystal structure in poly(glycolide) and poly(lactide) homopolymers and co-polymers during degradation. The crystal structures were analysed using small-angle X-ray scattering to identify the size of the crystal lamellae and amorphous regions. It was found that chain scissions, during polymer degradation, enables new crystallites to develop in the amorphous phase between crystal lamellae. This is due to the scissions providing the polymer chains with extra mobility and therefore more freedom to adopt the most stable configuration. There is a gradual and significant increase in the degree of crystallinity during degradation, which is seen regularly in experimental degradation studies. The atomic structure of crystalline poly(lactide) has been studied extensively by a combination of theoretical simulations and experimental analysis [53-56]. Three different atomic configurations of crystalline poly(lactide) have been identified, referred to as α-, β- and γ- forms, which occur under different processing conditions. Semi-crystalline polymers often exhibit a spherulitic microstructure in which there is large-scale orientation of the crystal lamellae and inter-lamellae amorphous regions. The crystallites are arranged relative to each other in a large overall structure such as a spiral for example. Typically, a spherulite is spherical and several orders of magnitude larger than the individual crystallites.

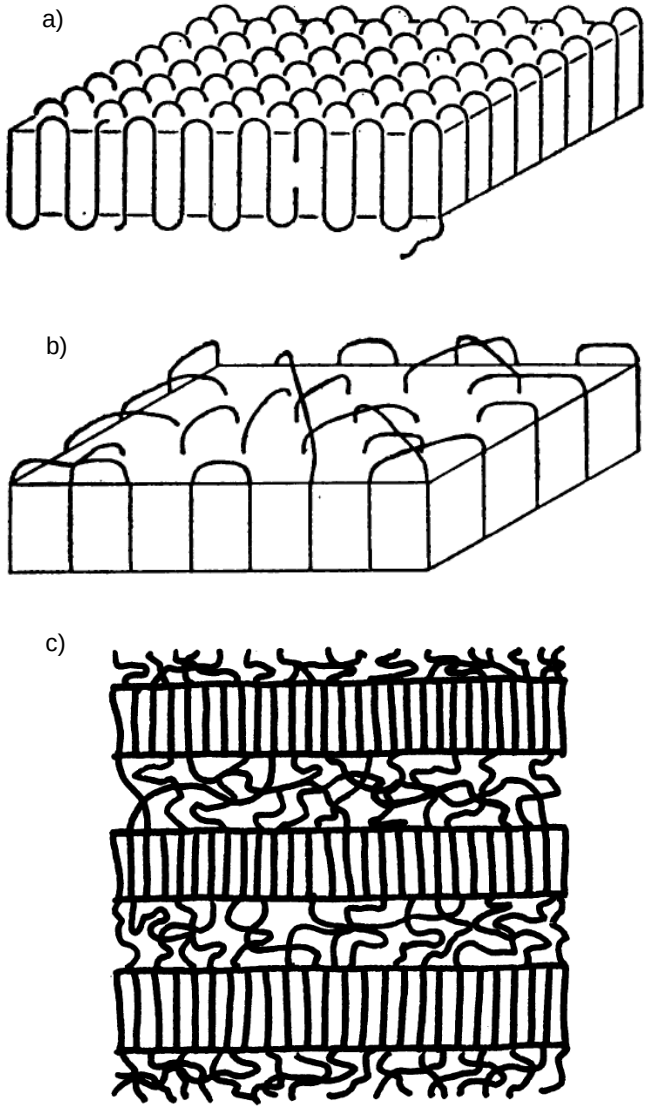

Fig. 1.2 reproduced from the publication of Oppenlander [51] with permission via the Copyright Clearance Centre.

It is very important to be able to predict how crystallinity changes during the degradation process because crystallinity affects both the mechanical properties and the degradation rate of biodegradable polymer devices [5, 57, 58]. The effect of crystallinity on mechanical properties is discussed in detail in the critical review of mechanical properties in the next chapter of this thesis. The degradation rate is affected because water molecules are unable to penetrate the crystalline regions, due to the close packing of the aligned polymer chains, and therefore crystalline regions are generally considered to resist hydrolysis. Oligomers and monomers may also be

excluded from the crystalline fraction. As the crystalline fraction of a polymer increases, the amorphous volume fraction reduces and so too therefore does the volume in which oligomers and monomers are contained. This can lead to an increased concentration of acidic chain ends in the amorphous region, which accelerates the rate of chain scission as discussed in Section 1.2 above.

1.4 Existing models for the degradation of bioresorbable polymers

Mathematical models for chain scission in biodegradable polymer have evolved over several decades. In 1981 and 1987, Pitt and his co-workers [30, 59] developed models for autocatalytic and noncatalytic hydrolysis individually. The autocatalytic model considered the hydrolysis reaction to be linearly related to the concentration of carboxylic acid chain end groups. In 1998 and 2007, Siparsky et al. [40] and Lyu et al. [1] modified the autocatalytic model to be linearly related to the concentration of H+ acid catalyst, rather than chain end concentration, based on the equilibrium condition for acid disassociation. The group at the University of Leicester then combined both noncatalytic and autocatalytic hydrolysis models into a single model in the study by Wang et al. [50] in 2008. Many experimental data sets can be fitted by a model that combines both hydrolysis mechanisms, but not by each mechanism individually. The study of Wang et al. [50] included diffusion of the water-soluble small chains out of the polymer device, which leads to a reduction in the concentration of acid catalyst and reduces the rate of chain scission. Model parameters were non-dimensionalised and degradation maps were produced, which clearly indicate under what conditions the degradation of molecular weight is controlled by noncatalytic hydrolysis, autocatalytic hydrolysis or oligomer diffusion. Batycky et al. [26] and Antheunis et al. [27] developed noncatalytic and autocatalytic models, respectively, in 1997 and 2009, which could simulate full molecular weight distributions. In 2009 and 2010, Han and Pan [48, 49] extended the model of Wang et al. [50] to include increases in polymer crystallinity during degradation. In addition to considering both noncatalytic and autocatalytic hydrolysis mechanisms and the diffusion of water-soluble short chains out of the polymer for mass loss, the model of Han and Pan [48, 49] also considered both random and end scission mechanisms and the effect of temperature on degradation. Han and Pan [60] further extended the model in 2011 to allow for individual polymer chains to be modelled in order to simulate the full molecular weight distribution. In 2010, Wang et al. [61] developed a theory for the degradation of Young's modulus in bioresorbable polymers used above their glass transition temperature. This theory was incorporated into their earlier model [50]. In 2011, Ding et al. [62] also studied the effect

of chain scission on Young's modulus. This was an atomistic study rather than a mathematical one, and hence they did not develop a mathematical model for Young's modulus degradation. The studies of Wang et al. [61] and Ding et al. [62] are discussed in detail in the next chapter of this thesis.

Chapter 2: Critical review of mechanical properties of biodegradable polymers

This chapter presents a critical review of the experimental data available in the literature for the degradation of mechanical properties. The methods of measurement are discussed, along with the major factors that influence mechanical properties and the effect of hydrolysis during degradation. A general relationship is found between molecular weight and Young's modulus for poly(lactide). Existing theoretical models for the degradation of mechanical properties are also discussed. A large part of this chapter is to be published as a book chapter [63].

2.1 Polymers and polymer properties considered in this thesis

The mathematical models for degradation in this thesis are generic so can be used to model many polymers including poly(lactide)s, poly(glycolide)s, poly(caprolactone)s, and polymer blends or copolymers. Typical values of the glass transition temperature (T_g) for poly(lactide), poly(glycolide) and poly(caprolactone) are in the region of 60°C, 40°C and -60°C, respectively. Poly(lactide) is the most common polymer used in experimental publications and therefore features most frequently when using the models to fit experimental data. The atomic simulations also focus on poly(lactide) due to its popularity in clinical applications and the associated interest in mechanical properties.

The molecular structure for poly(lactide) is given in Fig. 2.1, in which n indicates the number of repeat unit in the polymer chain. Poly(L-lactide) (PLLA) and poly(D-lactide) (PDLA) are mirror images of each other and are identical except for the fact that the CH_3 and H side-groups swap sides. A copolymer of these polymer units includes a combination of both units in each individual chain and is written as poly(L-lactide-co-D-lactide). A polymer blend of these polymers includes a mixture of L-lactide and D-lactide polymer chains, although each individual polymer chain contains only one type of polymer repeat unit: L-lactide or D-lactide. The terminology used for such a polymer blend is poly(L-lactide/D-lactide). During chain scission, a water molecular attacks the site of the carbonyl group, as shown in the figure, in order to split a single polymer chain into two chains.

For polymers, mechanical properties are strongly dependent on the strain rate. In addition, polymers do may not display a linear relationship between stress and strain and therefore Young's modulus is not necessarily the most comprehensive measure of mechanical properties since it may introduce some ambiguity. However, for typical experimental publications that study biodegradable polymers, Young's modulus is reported since the relationship between stress and strain is approximately linear for small strains. The effect of strain rate is typically not investigated since the focus of the experimental publications is on degradation and they are not targeted at technical engineers who are interested in dynamic polymer properties. In this thesis Young's modulus is considered, following on from the experimental publications on which the work in this thesis is based. When referring to plastic deformation in this chapter, it is considered to occur when the polymer chains undergo non-reversible reconfiguration in response to an applied force.

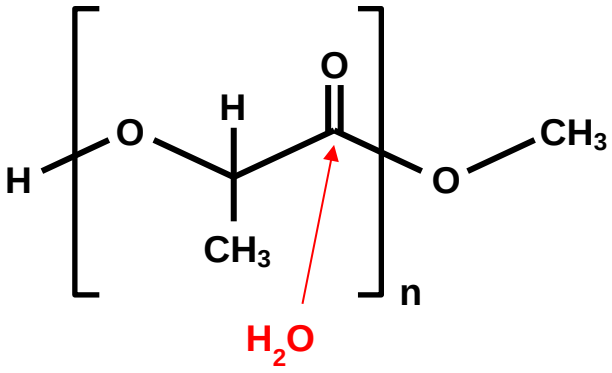

Fig. 2.1 Molecular structure of poly(lactide).

2.2 Fundamentals of mechanical properties in polymers

Due to the complexity of the molecular structure of polymers compared to other materials, the understanding of mechanical properties with respect to molecular interaction is currently quite limited. One of the most important factors in polymer mechanical properties is the glass transition temperature, which is quite well understood. Polymers deform via different mechanisms at temperatures above and below their T_g. The polymer chains are effectively frozen in position for "glassy" polymers below T_g and only small strains (typically <5%) can be accommodated elastically, during which the distance between polymer chains slightly increases or decreases. For "rubbery" polymers above T_g however, the chains can slide over one

another and elongation is accommodated by chains straightening out in the direction of strain.

2.2.1 Elastic deformation of polymers

For a glassy polymer, elastic deformation is accommodated by small displacements between polymer chains as shown in Fig. 2.2. The average distance between adjacent polymer chains is likely to slightly increase in the direction of an applied tensile strain. This separation is expected to be aided by small deformations of the polymer chains too. It is not expected that the distance of main-chain covalent bonds changes because these bonds are much stronger than the weak interactions between chains. However, the polymer chains may be able to bend or twist to a small degree in order to assist deformation between polymer chains. The elastic deformation of glassy polymers is not well understood, and thus simple, generally-accepted theories for Young's modulus in terms of molecular interaction do not exist.

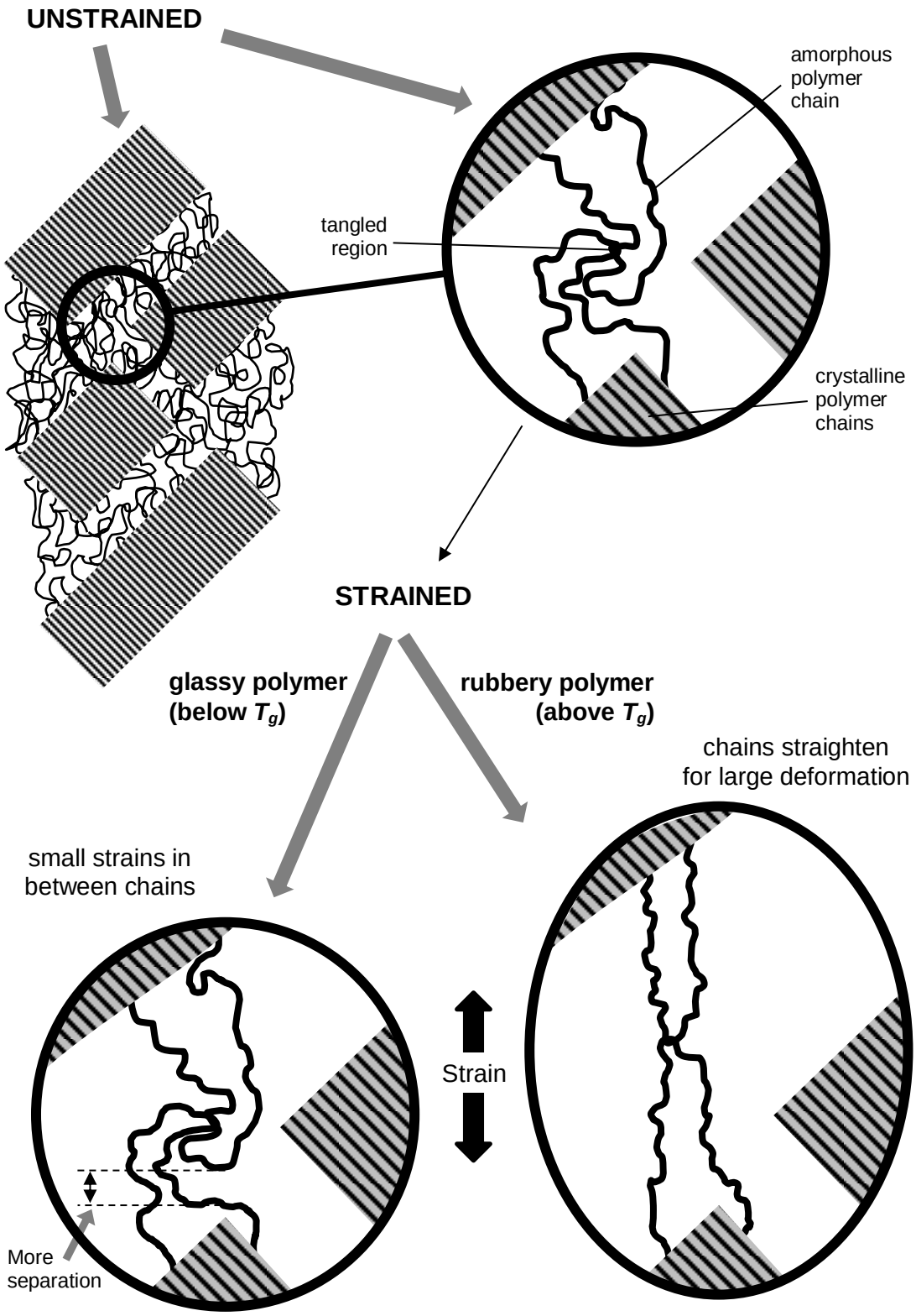

Fig. 2.2 Elastic deformation occurs in the amorphous phase of polymers. Mechanisms for glassy deformation (small strains) and rubbery deformation (large strains) are shown.

Another mechanism for elastic deformation is for polymer chains to straighten out and orient in the direction of applied strain. This is also shown in Fig. 2.2 and can facilitate large elastic deformation (>500%) but it is only possible in polymers that are above their glass transition temperature. Below T_g, the polymer chains are not able to slide over one another in order to straighten out. For this type of deformation to still be considered elastic in nature, the polymer chains must return to the original position after stress is removed. For rubbery elasticity, the polymer chains return to the original position due to entropy. In order to consider entropy, the deformation of polymers is often discussed in terms of Helmholtz free energy, *F*, which is given in Eq. 2.1 as

$$F = E - TS \tag{2.1}$$

in which the internal energy, *E*, is the kinetic and potential energy of all atoms and atomic interactions, *S* is the entropy of the system, and *T* is temperature. During the deformation of glassy polymers, free energy is dominated by the potential energy change that results from variation in the distance between atoms. This can be simply physically interpreted by considering strain to be resisted by bond elongation/compression. The entropy term can be considered as negligible for a polymer below T_g since elastic deformation is limited to small strains: significant entropy changes only result from large strains as demonstrated by rubbery polymers. In rubber elasticity the polymer chains slide over one another and rearrange with relative ease to adopt a considerably different configuration (strained) without significant changes to the internal energy. The entropy of the system does change however, and thus it is variation of entropy as the polymer is strained that dominates the free energy change. Entropy theory cannot be described with such an intuitive interpretation as internal energy. It is related to the total possible configurations of chains in a polymer. Consider a polymer chain whose ends are quite close to each other. The middle section of the polymer chains can occupy a large number of different configurations without the polymer ends having to change position, as shown in Fig. 2.3. This means entropy is high: the structure is not highly ordered. When the overall polymer is elongated however, the distance between the chain ends (end-to-end distance) increases. For a longer end-to-end distance the polymer chain cannot exist in as many different configurations as demonstrated in Fig. 2.4. Entropy decreases, free energy increases, and therefore work must be applied to the system. In statistical mechanics, entropy can be defined according to Eq. 2.2 as

$$S = k_b \ln \Omega \qquad 2.2$$

in which k_b is Boltzmann's constant and Ω is the number of possible configurations for the polymer chains. When a polymer is elongated, the chains adopt a more aligned configuration on average than they would naturally be in. And when the applied force is removed, random thermal motion means that the chains naturally return to the original un-aligned positions in a structure with minimum potential energy. Because the chains are inclined to return to their original unstrained configuration they exert a retractive force. The sum contribution of all the polymer chains' retractive forces is equal and opposite to the external force that must be applied in order to keep the polymer in a strained state. The stiffness of the polymer is simply the rate at which this retractive force changes with elongation. The entropy change as a result of strain can be calculated in order to predict Young's modulus [64]. Wang et al. [61] discuss entropy change in relation to the molecular weight of a degrading polymer and present a modified theory.

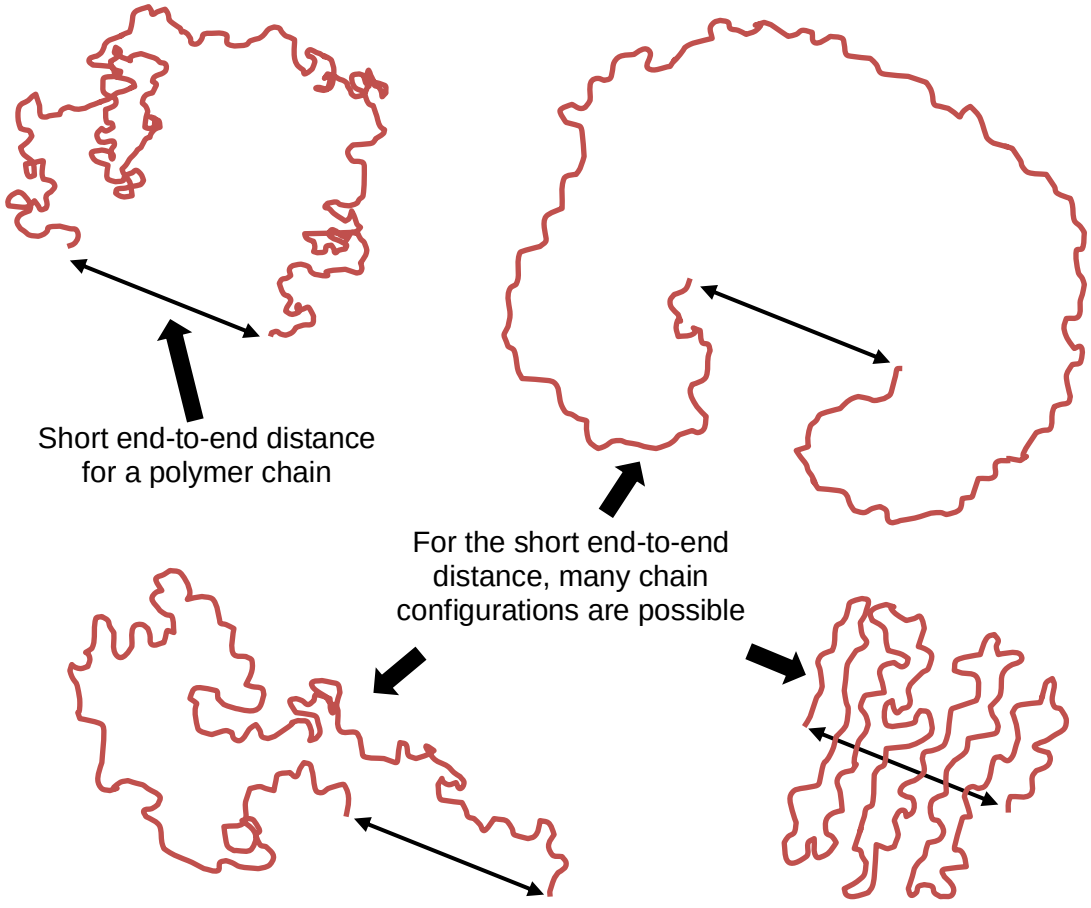

Fig. 2.3 A long polymer chain can take many different configurations if it has a short end-to-end distance. The entropy of the system is therefore high.

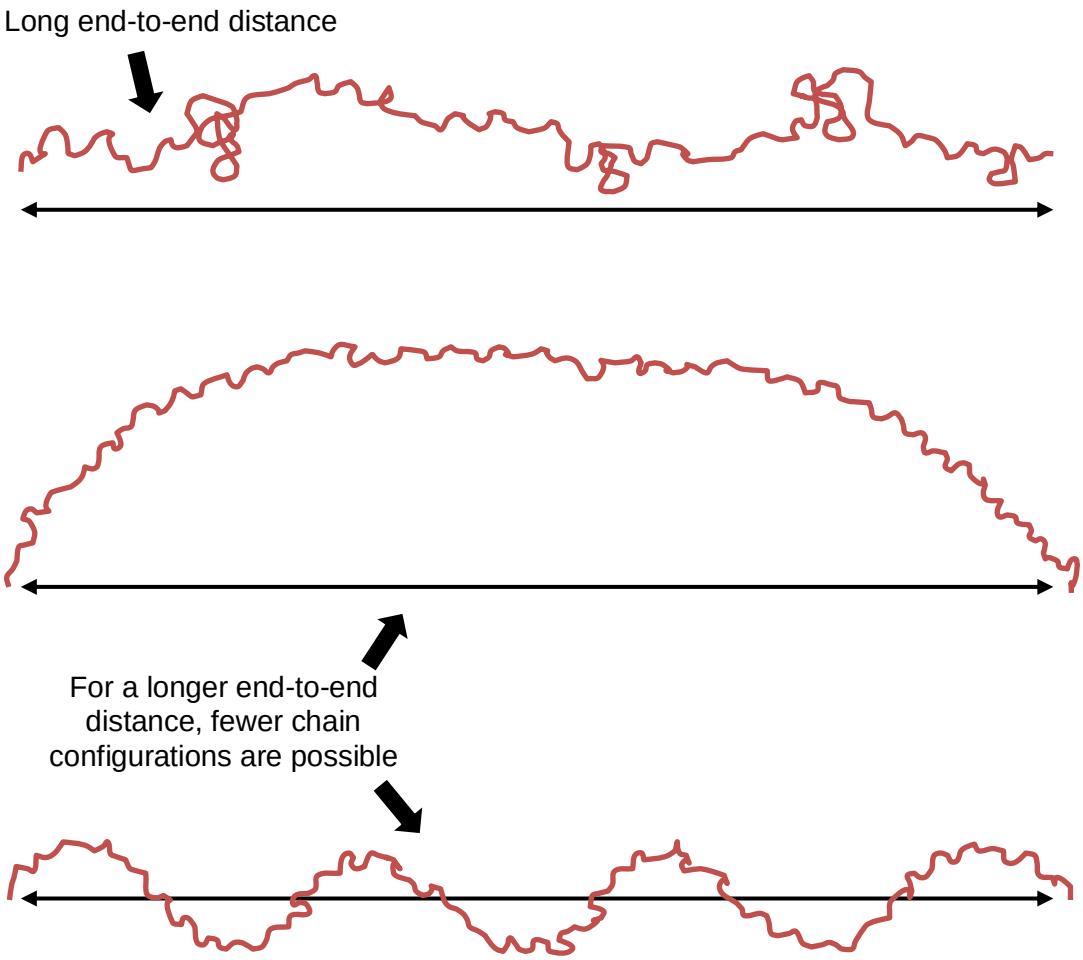

Fig. 2.4 A long polymer chain can take fewer configurations if it has a longer end-to-end distance as a result of applied strain. Entropy is lower than for a short end-to-end distance.

2.2.2 Plastic deformation of polymers

In rubbery polymers, high strains of several hundred percent are often possible without plastic deformation. Yielding occurs when the polymer chains do not return to their original positions of minimum energy. A new minimum energy configuration may result from polymer chains being broken, if crosslinks break or reposition, or if chain entanglements untangle. During plastic deformation, necking may occur and the polymer chains become highly aligned with each other. As a result, the stiffness typically increases at high strains because further deformation requires the physical stretching or breaking of bonds as opposed to the straightening-out of chains. For glassy polymers, the polymer chains do not straighten out, and hence yielding occurs at lower strains (typically <5%). For elastic deformation of glassy polymers, the strain is accommodated by changes in the inter-molecular distance between polymer chains but

when the applied stress exceeds the limit of elasticity, plastic deformation occurs as a result of polymer segments shifting relative to one another. Fig. 2.5 shows how three segments of polymer can shift relative to one another without any deformation occurring within each segment. Once the segments have been forced into new positions, they do not return to the original position upon removal of the force; the chains are frozen in the new position unless further plastic deformation occurs.

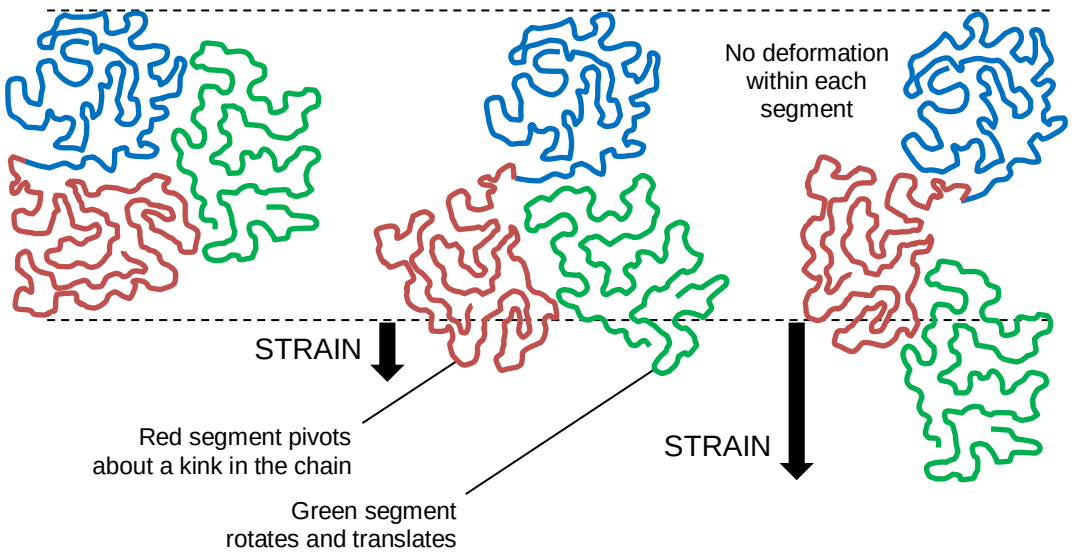

Fig. 2.5 Segmental motion during plastic deformation of a glassy amorphous polymer.

For semi-crystalline polymers, it is different again; the amorphous phases can deform in the manners described above depending on whether the polymer is above or below the glass transition temperature, but the crystallites also deform plastically. Fig. 2.6 shows how initially, the crystallites shear in the direction of stress to align the chains in that direction. Upon further straining, the crystallites fragment into smaller crystallites, which allows the amorphous phase to deform more freely.

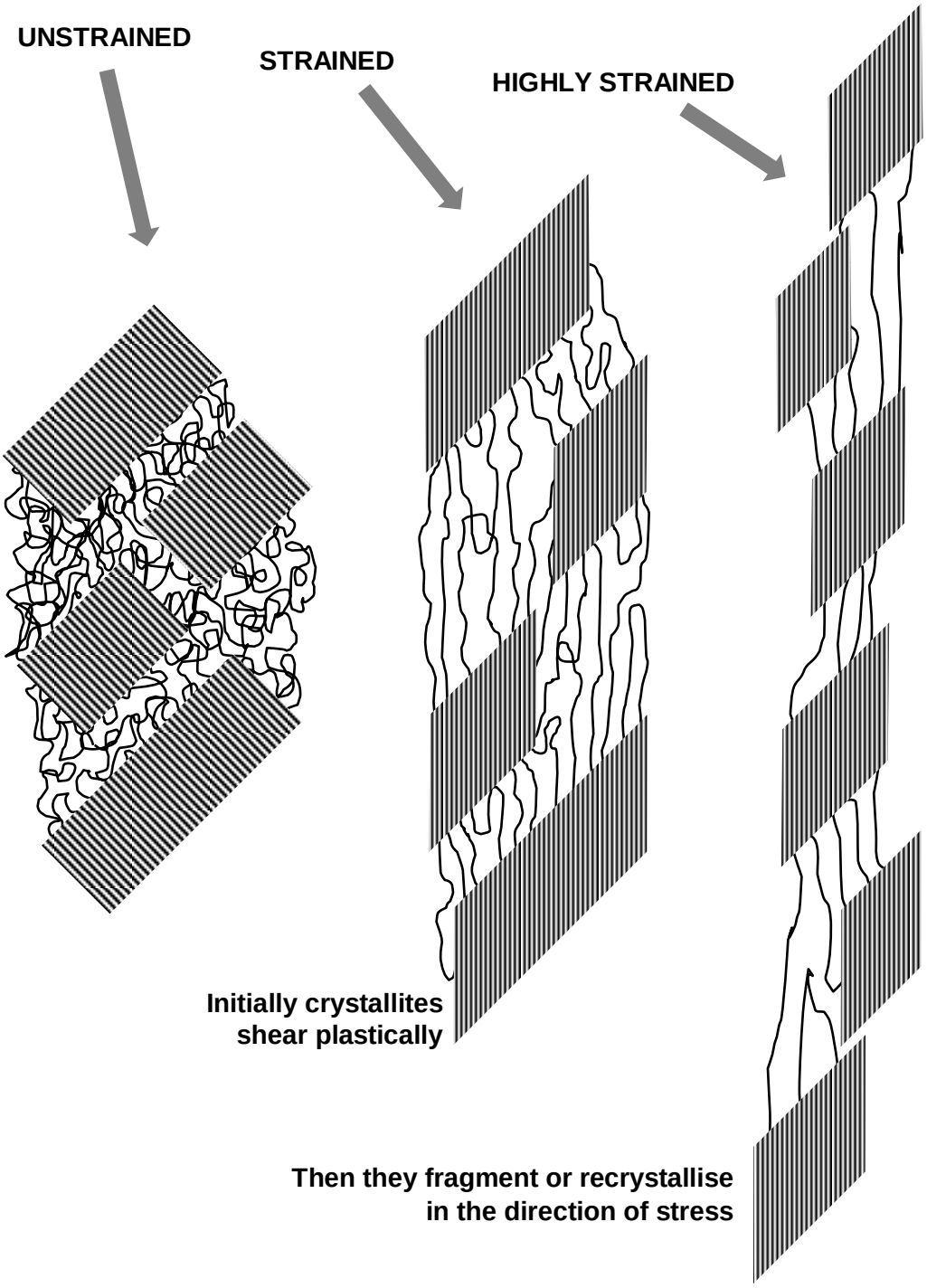

Fig. 2.6. Plastic deformation of crystallites in a semi-crystalline polymer.

2.2.3 Strength of polymers

Strength is more complicated than stiffness because it concerns polymers in the highly plastically strained state and is ultimately dictated by a small concentration of microscale features in the polymer. In glassy polymers, which display brittle behaviour,

the strength may be dictated by the single weakest point in a polymer, which initiates a crack during plastic deformation. Such weaknesses in a glassy polymer may result from features such as the local chain configuration, material imperfections (voids and impurities) or surface imperfections. Increases in crystallinity may result in an increased overall strength due to the crystalline fraction having high strength. Alternatively, they may have the opposite affect and reduce overall strength as a result of extra constraints on the amorphous phase. Rubbery polymers may only break at very high strains and the strength is affected by a small concentration of factors such as the frequency and distribution of crosslinks or entanglements. Crystallites may act as extra entanglements to increase strength.

2.3 Methods of measurement for mechanical properties

There are a wide range of techniques that may be used to determine mechanical properties. A well trusted method is tensile testing, in which the two ends of a tensile sample are clamped in a tensile testing machine and pulled apart as shown in Fig. 2.7. While the sample is being stretched, the forces that the machine must apply are measured. The greater the required forces, the higher the stiffness of the sample. The Young's modulus is determined by relating stress in the sample to strain. The strength of a sample is determined from the maximum force applied at any time during a test in which the specimen is broken into two halves. Other mechanical properties may also be determined. Elongation-at-break is frequently published in experimental publications related to biodegradable polymers, and is calculated as the final length (immediately before breaking) of the sample test section divided by the initial length.

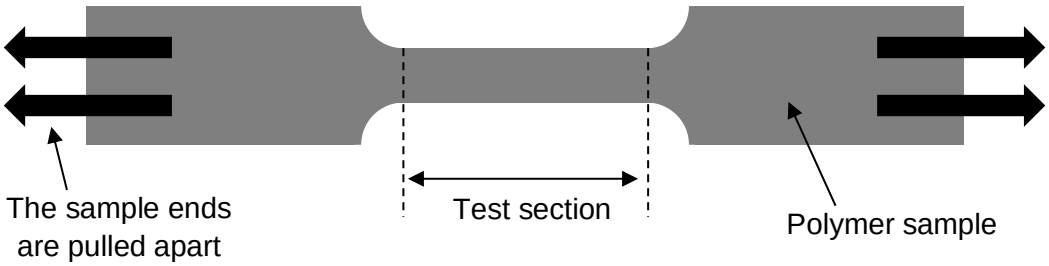

Fig. 2.7 Example of a polymer specimen used in a tensile testing machine in order to analyse mechanical properties.

In addition to tensile testing, there are many other common techniques for testing mechanical properties such as compression, bending and shear tests. They are all similar in that they measure the force required for deformation or failure. In bending tests, a sample is bent, which causes the top and bottom of the sample to be subject to opposite forces of either compression or tension. In shear tests the force required to break to sample in shear can be used to determine the shear strength. As opposed to compression or tensile tests, in which two halves of a polymer may be considered to be pulled apart or crushed together, in shear tests the two halves slide over one another similar to cutting a deck of cards. A polymer reacts to the different types of deformation in different manners. For example, a polymer chain can fold up when subject to compression without stretching the strong covalent bonds in the polymer chains whereas under tension the covalent bonds must be stretched. It may be the case that the elastic moduli calculated through tensile, compressive and bending tests degrade in different manners.

In addition to the different testing techniques, the testing setup is also important. Temperature and strain rate have a large impact on the measurements. Nakafuku and Takehisa [65] conducted mechanical property tests at various temperatures for 80 μm amorphous films of poly(L-lactide) and poly(DL-lactide-co-glycolide) 50:50, which had glass transition temperatures of 57.7°C and 30.0°C respectively. The results are shown in Fig. 2.8. There is over an order of magnitude increase in Young's modulus as the polymers transition from a rubbery state to a glass state. Interestingly, there is also a significant increase in Young's modulus as the testing temperature of the poly(L-lactide) sample decreases from 20°C to 10°C even though both temperatures are well below T_g and there is little change in Young's modulus for temperature changes from 35°C to 20°C. These results highlight the complexity of mechanical properties in polymers.

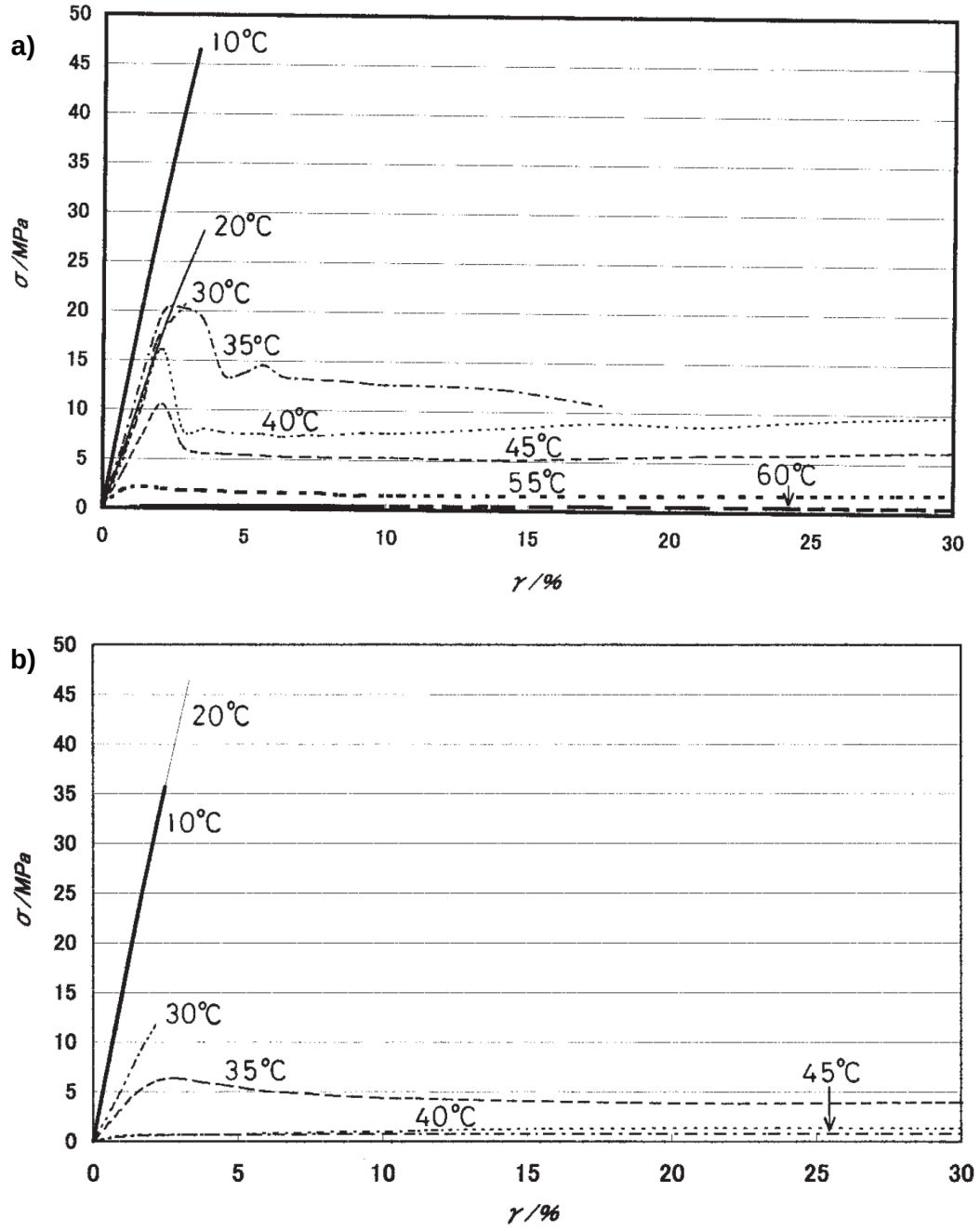

Fig. 2.8 Applied stress (MPa) versus applied strain (%) at various temperatures for 80 µm amorphous films of a) poly(L-lactide), T_g = 57.7°C, and b) poly(DL-lactide-co-glycolide) 50:50, T_g = 30.0°C, reproduced from the publication of Nakafuku and Takehisa [65] with permission via the Copyright Clearance Centre.

Since biodegradable polymers are degraded in a hydrolysis solution, which is absorbed by the polymer, the water molecules plasticise the polymer chains and can affect all of the mechanical properties. In most experimental publications, the testing of mechanical properties is completed using dry samples, which have been dried to ensure the results are comparable to initial tests of samples before they were introduced to the hydrolysis solution.

Due to the number of factors that affect the mechanical properties and the fact that many of these factors are not well understood, there are often large error margins on experimental data measurements. Even before degradation begins there are many factors during polymerisation and processing than can lead to large error margins >50%, particularly for elongation-at-break [5, 66, 67].

2.4 Factors that influence the mechanical properties of bioresorbable polymers before degradation

The mechanical properties that are most often measured during biodegradable polymer degradation experiments are stiffness, strength and elongation-at-break. These mechanical properties are influenced by a large number of factors, the most important of which may be molecular weight. The longer the polymer chains, the more likely they are to be more entangled. For strength, the polymer chains must either untangle from each other or physically break in order to allow a polymer sample to separate into two parts. Therefore the more tangled a polymer, the more chains that must be broken in order for the overall polymer sample to break. Elongation-at-break increases when polymer chains are able to unravel to a greater degree without breaking, and therefore more entanglements may reduce the value of elongation-at-break. Stiffness increases with molecular weight although as a result of the complexity of molecular interactions and the lack of comprehensive understanding, there are no widely accepted theories that relate Young's modulus to molecular weight. Crystallinity affects the mechanical properties because chains that are aligned side-by-side in a crystalline region are strongly bonded to each other. As a result, they become resistant to deformation and stiffness is likely to increase significantly compared to that of the amorphous polymer phase. Strength also generally increases because the crystallites act as extra entanglements or may be considered as high-strength particles. In a similar manner to crystallinity, amorphous polymer chains may become oriented during processes such as fibre drawing or extrusion. Oriented amorphous polymer chains are aligned to a lesser degree than crystalline regions but are more closely packed than unoriented amorphous chains. The bonding between the chains is therefore stronger. As a result, both strength and stiffness increase versus a fully unoriented amorphous polymer. Other factors that affect mechanical properties before degradation are polymer type/composition and processing techniques/conditions. The focus of this thesis is on the degradation of Young's modulus for polymers in a glassy state, which is not well understood at present.

2.5 The degradation of mechanical properties

Not all of the factors discussed in the previous section vary during degradation. The rest of this chapter considers the degradation of mechanical properties and the factors that affect it. The experimental data plots in Fig. 2.9 are reproduced from the publication of Tsuji [2], which studies the degradation of amorphous poly(lactide) films in phosphate buffer solution (pH7.4) at 37°C. The polymer types L-lactide, D-lactide, and a blend of both L- and D-lactide are considered, which are described in the first section of this chapter. The evolution of Young's modulus and tensile strength can be seen to be quite erratic in nature; the properties reduce and increase in value during different periods of degradation and can demonstrate a sudden drop to zero.

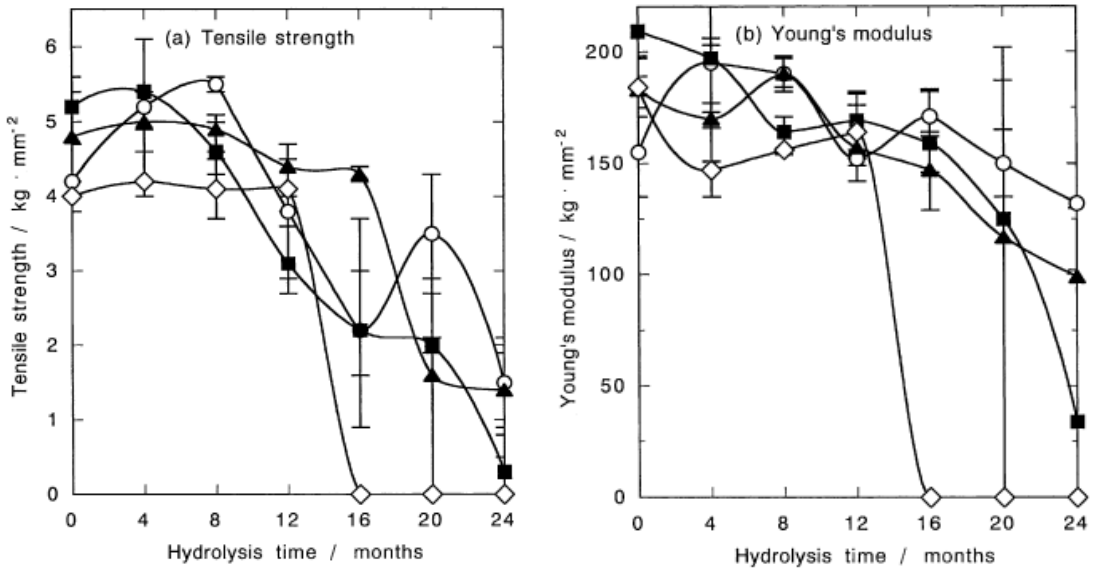

Fig. 2.9 Experimental data figures reproduced from the publication of Tsuji [2] with permission via the Copyright Clearance Centre. Tensile strength (left) and Young's modulus (right) versus degradation time for various polymer compositions: poly(L-lactide) filled triangles, poly(D-lactide) filled squares, copolymer poly(DL-lactide) open diamonds, and blend polymer poly(L/D-lactide) open circles.

The relatively sudden changes in mechanical properties during degradation are a result of the high number of factors that affect them. Since the data presented in Fig. 2.9 are from a single publication many of the potential factors are kept constant for all of the samples but the degradation trends are irregular and error margins are large. The standard polymer processing conditions, degradation conditions and measuring techniques vary between institutions, which adds uncertainty when comparing data in the literature. In many publications [2, 6, 8-11, 67-71], the value of Young's modulus holds or increases initially during degradation experiments, whereas in some [5, 7, 17], Young's modulus reduction occurs from the outset. These trends can be linked to

molecular weight degradation and changes in crystallinity as discussed in the next sections.

2.5.1 The effect of molecular weight degradation on Young's modulus and strength

Fig. 2.10 shows the experimental data of Tsuji [9] for the Young's modulus and strength of semi-crystalline poly(lactide) films that were degraded in a phosphate buffer solution (pH7.4) at 37°C for 30 months. The polymers used in the films were poly(D-lactide), poly(L-lactide) and a 1:1 blend of poly(D-lactide) and poly(L-lactide). The figure shows that the blended polymer retained mechanical properties for two years of degradation, whereas the non-blended polymers displayed a reduction in strength almost linearly from the start of hydrolysis and an initial delay of less than one year before the Young's modulus reduced.

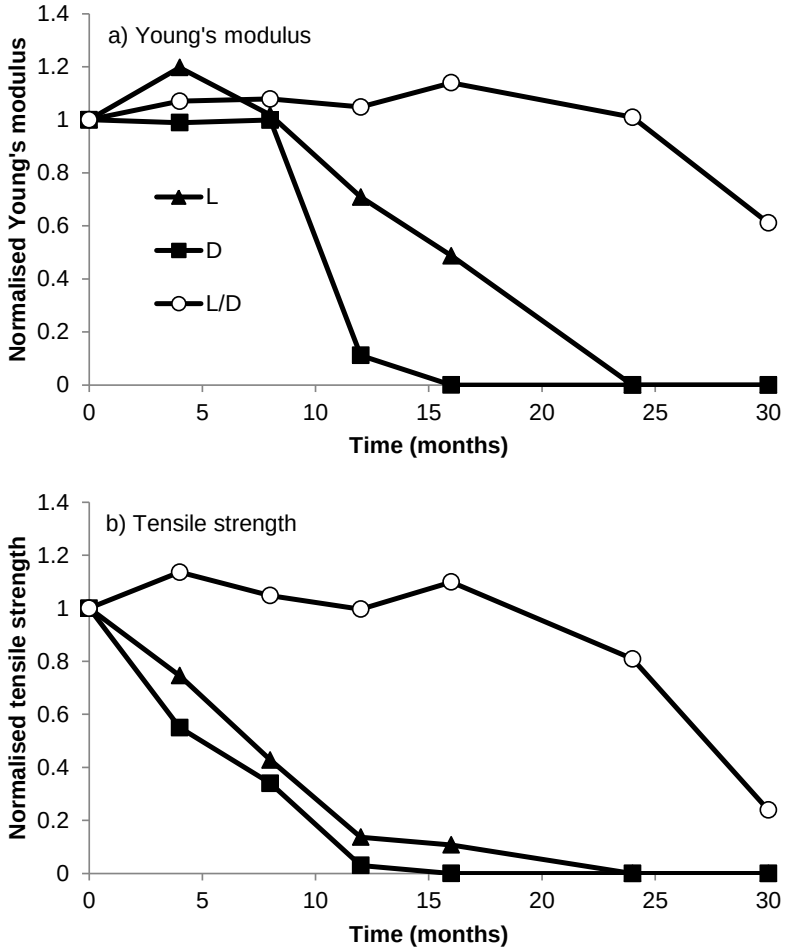

Fig. 2.10 Experimental data of Tsuji [9] for the reduction of Young's modulus (top) and tensile strength (bottom). There is a significant difference between the degradation of mechanical properties for different polymer types: L-lactide (filled triangle); D-lactide (filled square); and the polymer blend (hollow circle).

The trends for the degradation of mechanical properties bear quite a resemblance to the degradation of molecular weight, which is shown in Fig. 2.11. This suggests that mechanical properties are largely dependent on molecular weight degradation. Reduction of molecular weight is generally considered to be the most important factor for long-term mechanical properties during degradation. Strength may reduce as a result of shorter polymer chains being less entangled or more able to untangle during plastic deformation. The film samples in the study [9] were tested below their glass transition temperature.

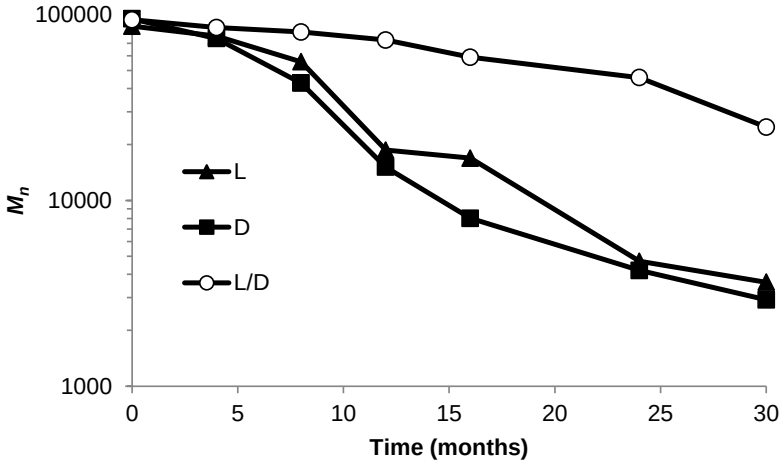

Fig. 2.11 Experimental data of Tsuji [9] for the reduction number averaged molecular weight. As with mechanical properties, the rate of degradation is reduced for the blended polymer film (hollow circle) as opposed to the homopolymer films L-lactide (filled triangle) and D-lactide (filled square).

2.5.2 A direct relationship between the degradation of Young's modulus and the degradation of molecular weight

Since molecular weight has a great impact on Young's modulus, the direct relationship between the Young's modulus and molecular weight is of interest. Mathematical models have been developed to simulate polymer chain scission and therefore the evolution of molecular weight during degradation [27, 28, 48-50, 60]. By relating mechanical properties to molecular weight, the models could also be used to simulate the degradation of mechanical properties. It is often found experimentally that the degradation of Young's modulus occurs after molecular weight reduction as shown in Fig. 2.12 [2, 5, 8-10, 68, 69].

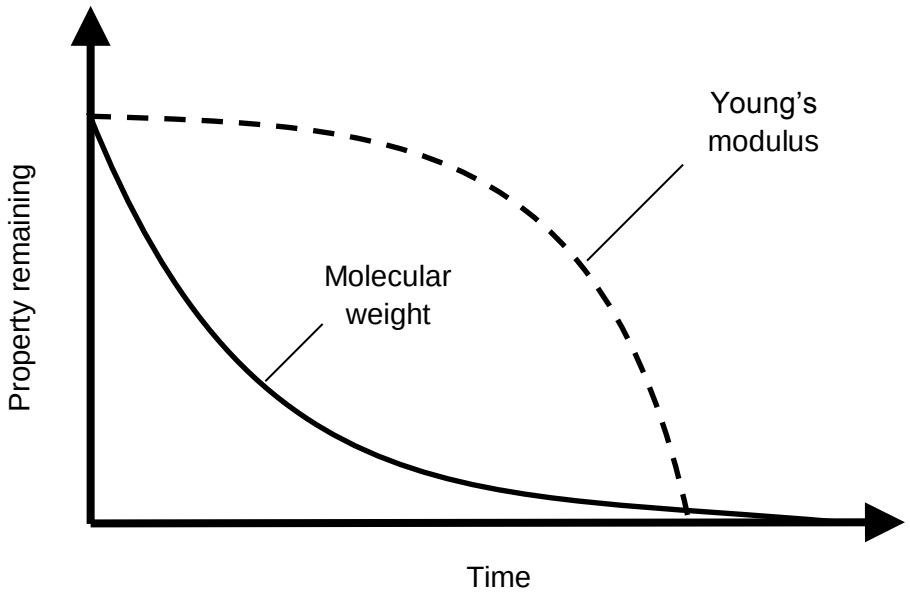

Fig. 2.12 Molecular weight reduction often precedes the reduction of Young's modulus.

In order to determine a relationship between the Young's modulus and molecular weight, it is useful to consider a plot of the properties against one another. Fig. 2.13 shows such a plot for the experimental data shown in Fig. 2.10 and Fig. 2.11. Due to the loss of Young's modulus being delayed behind the loss of molecular weight, the relationship is nonlinear. Molecular weight reduces by over 50% before Young's modulus begins to drop quite suddenly. The dashed line in the Fig. 2.13 highlights the typical trend that may be identified from the data to relate normalised Young's modulus to normalised molecular weight.

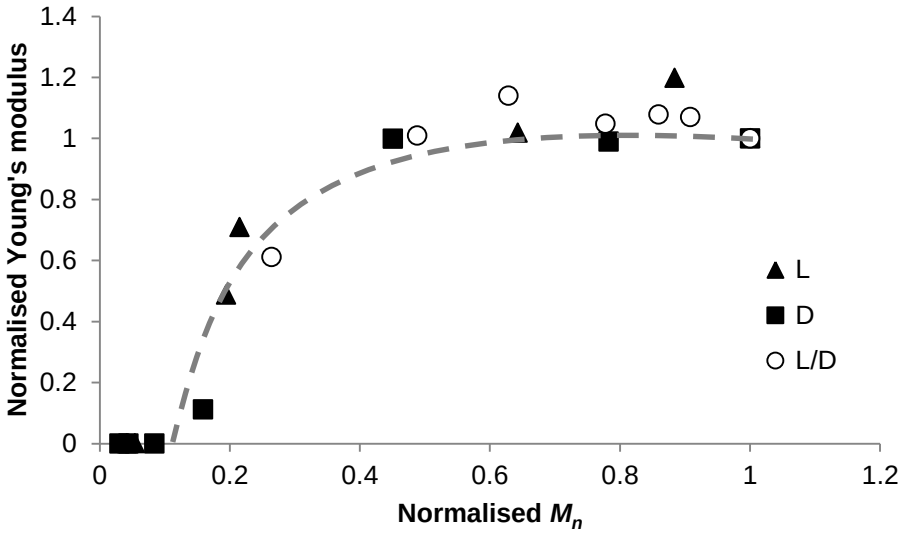

Fig. 2.13 A plot of Young's modulus versus molecular weight can be used to identify a relationship between the two properties. The experimental data of Tsuji [9] (discrete symbols) are the same as used in Fig. 2.10 and Fig. 2.11.

The relationship between molecular weight and Young's modulus varies considerably between experimental data sets in the literature. The experimental data of Duek et al. [58] for Young's modulus versus molecular weight is shown in Fig. 2.14. Initially amorphous and crystalline poly(L-lactide) pins were degraded in phosphate buffer solution (pH7.4) at 37°C for 6 months. Several of the values used for molecular weight in the figure are linearly interpolated (with relation to time) between measurements because molecular weight was analysed less frequently than Young's modulus and after different times of degradation. The initially amorphous sample shows a considerable initial delay in the reduction of Young's modulus compared to molecular weight whereas the initially crystalline sample shows little delay. The effect of crystallinity on mechanical properties degradation is considered in the next section of this review. The dashed black and grey curves show typical trends that may be identified from the data for the initially amorphous and crystalline samples respectively. The variation between these samples highlights how a simple relationship between Young's modulus and molecular weight is difficult to identify by considering individual samples in detail.

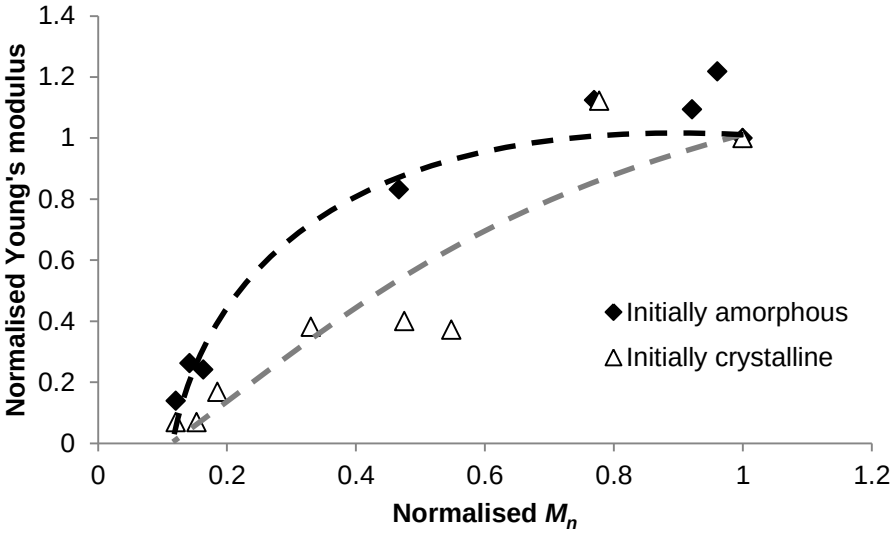

Fig. 2.14 A plot of Young's modulus versus molecular weight for experimental data of Duek et al. [58] for initially crystalline and initially amorphous samples during degradation.

In order to find a simple general relationship between Young's modulus and molecular weight, 21 experimental data sets for the degradation of poly(L- or D-lactide) are analysed together [2, 5-7, 9-11, 17, 66, 72]. The experimental data utilise a broad range of experimental circumstances: initial crystallinity varies from amorphous to

highly crystalline; initial molecular weight varies by over an order of magnitude; and several other factors vary including processing conditions, degradation temperature, sample size and mechanical property measurement techniques/conditions. An overall plot of all the experimental data sets is shown in Fig. 2.15. For one experimental study [17] weight averaged molecular weight data was supplied therefore the number average molecular weight was calculated using a simple assumption of polydispersity = M_w / M_n = 2.0, which was most frequent initial value measured in that study. As can be seen in the figure, almost all of the samples demonstrate a delay of Young's modulus reduction behind molecular weight reduction as discussed in relation to Fig. 2.13 and Fig. 2.14. A single curve of best fit cannot fit the data well.

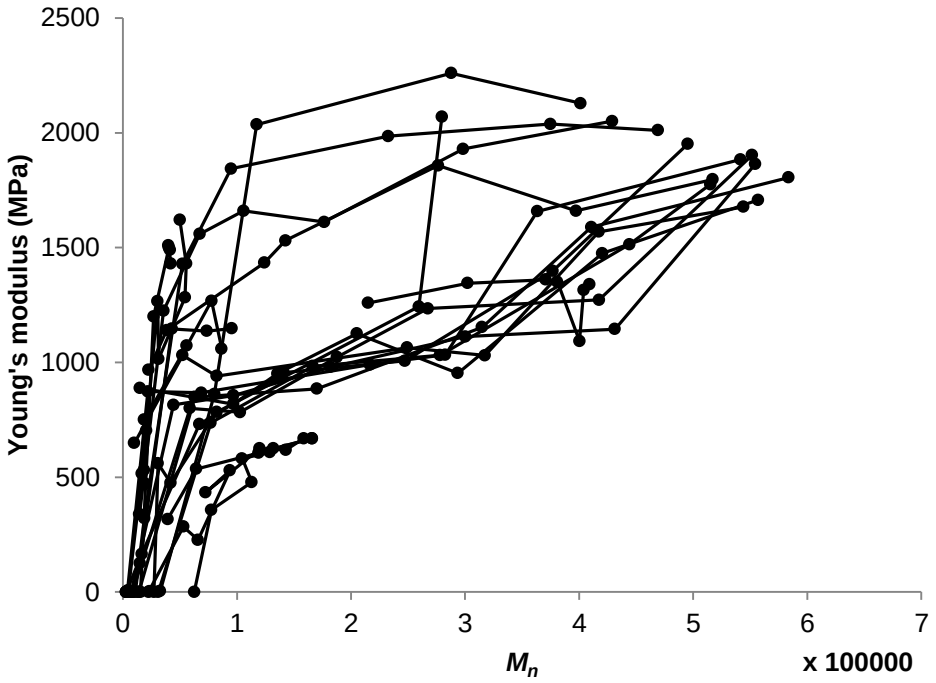

Fig. 2.15 A plot of Young's modulus versus molecular weight for 21 degradation experiments of poly(lactide) [2, 5-7, 9-11, 17, 66, 72]. Each set of data points linked by lines represents a single experimental setup.

Fig. 2.16 shows an alternative presentation of the data with molecular weight on a logarithmic scale. By considering log(M_n), it can be seen that experimental data typically demonstrate a similar gradient for a linear relationship between Young's modulus degradation and the reduction of log(M_n). This is highlighted by the master curves (dashed lines), which are arbitrarily offset to either side of the experimental data. For any given set of experimental data, the master curve can be shifted along the log(M_n) axis until it passes through the point of measured initial M_n and initial Young's modulus. The gradient of the master curves in the figure are 1400MPa, which indicates

that each time molecular weight reduces by a factor of 10, Young's modulus may reduce by 1400MPa. From an alternative viewpoint, for each 500MPa reduction in Young's modulus the molecular weight must reduce by ≈56%. This linear relationship between Young's modulus and log(M_n) can be used to predict the rate of Young's modulus degradation if M_n degradation is measured or modelled. Young's modulus can be calculated during degradation as

$$E = E_0 + k_m \log \frac{M_n}{M_{n0}} \qquad 2.3$$

in which E (GPa) and E_0 (GPa) are the instantaneous and original values of Young's modulus respectively, k_m (GPa) is the degradation rate constant for Young's modulus, and M_n (g mol^{-1}) and M_{n0} (g mol^{-1}) are the instantaneous and original values of number averaged molecular weight respectively. The value of k_m is 1400 GPa according to the dashed lines in Fig. 2.16. It should be noted that the relationship identified here is a very general relationship, which was established from experimental data with a broad range of initial properties and experimental circumstances. The master curve relating Young's modulus degradation to molecular weight degradation incorporates the uncertainties associated with these factors, including crystallinity, which is known to considerably affect Young's modulus. Eq. 2.3 can be used to simply estimate the Young's modulus of a poly(lactide) sample at any time during degradation if molecular weight is measured along with the initial value of Young's modulus. The model is not based on theoretical understanding so should be used with caution. However, no other models exist for Young's modulus degradation and Eq. 2.3 can be used for estimation purposes. Atomistic finite element simulations are conducted in this thesis in order to explain and help analyse these findings.

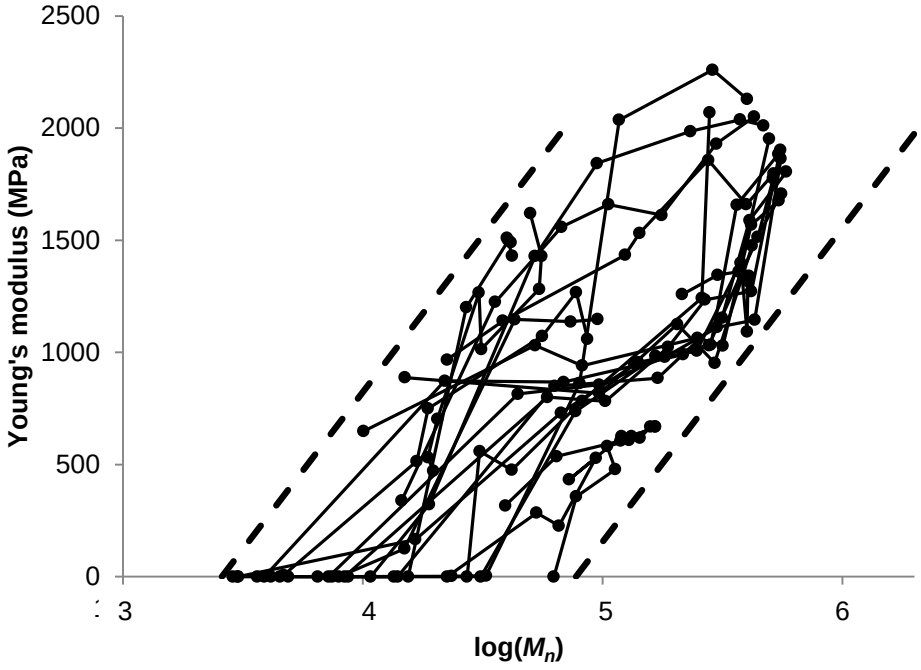

Fig. 2.16 Alternative presentation of the data in Fig. 2.15 with a logarithmic scale for molecular weight. The dashed lines represent a possible interpretation of the data that the Young's modulus of poly(lactide) samples during degradation is linearly related to log(M_n). The gradients of the dashed lines are 1400 MPa per order of magnitude reduction in M_n.

2.5.3 The effect of increasing crystallinity during degradation on Young's modulus and strength

Crystallinity can increase the values of Young's modulus and strength for polymers. Fig. 2.17 shows the effect of crystallinity on Young's modulus (top in figure) and strength (bottom) according to poly(L-lactide) experiments conducted by Tsuji and Ikada [57] for three different manufacturing techniques, referred to as film A, B and C in the figure.

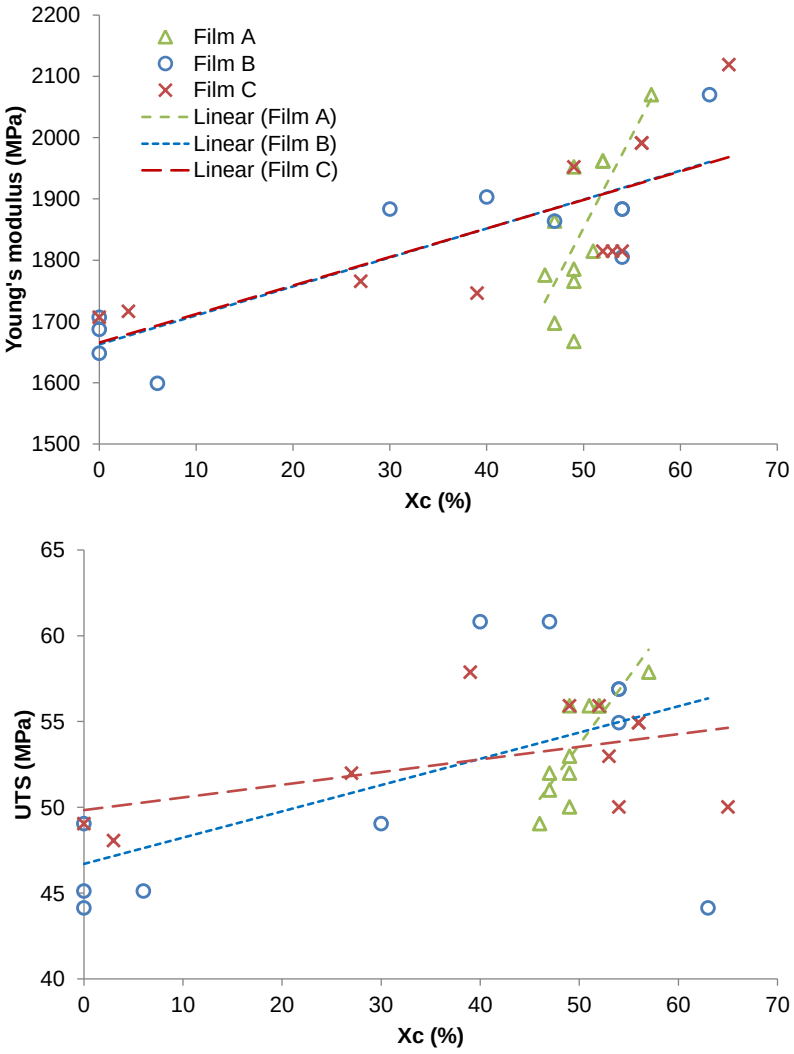

Fig. 2.17 Experimental data by Tsuji and Ikada [57] for poly(L-lactide) films shows that increasing crystallinity results in an increase in polymer stiffness (top) and strength (bottom).

Crystallinity increases as a result of chain scission, and thus the Young's modulus and strength may be expected to increase during degradation. This effect is offset by the fact that as crystallinity increases, molecular weight reduces, which in turn reduces the values of Young's modulus and strength. Nevertheless, increases in Young's modulus or strength are often found to occur at some point during degradation experiments [2, 5, 9-12, 17, 58, 67-72]. The experimental data of Duek et al. [58] shown in Fig. 2.18 demonstrates how Young's modulus (top) and strength (bottom) can increase during degradation. These experiments were also discussed in relation to molecular weight in the previous section.

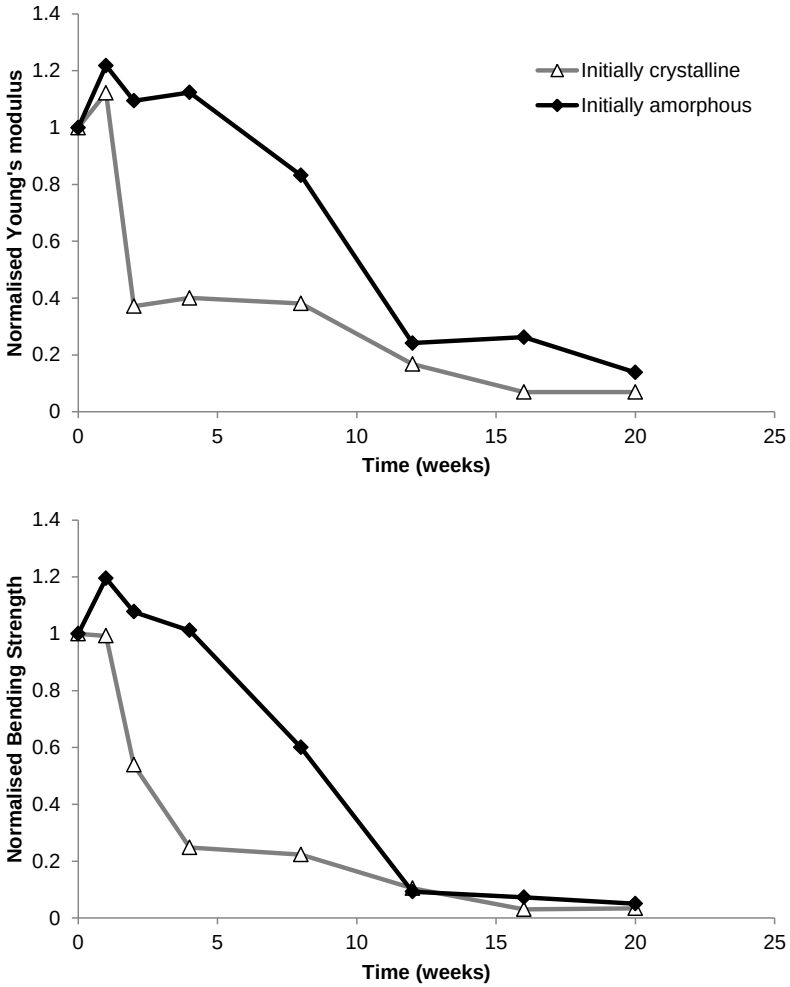

Fig. 2.18 Experimental data of Duek et al. [58] for poly(L-lactide) pins show an increase in stiffness (top) and strength (bottom) during the early stages of degradation.

The molecular weight and crystallinity data for the same study are given in Fig. 2.19. It can be seen in the top of Fig. 2.19 that molecular weight drops at a greater rate for the crystalline samples than the amorphous samples. This can explain why the mechanical properties reduce more quickly for the crystalline sample. However, consider the data at a time of two weeks; the amorphous and crystalline samples demonstrate an increase in Young's modulus of 10-25% even though there is a reduction in molecular weight of up to 50%. This can be explained by the increase in crystallinity of 10-50% over the first few weeks as shown in the bottom of Fig. 2.19. Also, consider both samples after 12 weeks of degradation. The crystallinity of the initially amorphous sample has increased by ≈50% whereas the initially crystalline sample has only increased by 10-20%. As a result, the amorphous sample retains a higher value of normalised Young's modulus even though it demonstrates a slightly greater reduction of molecular weight.

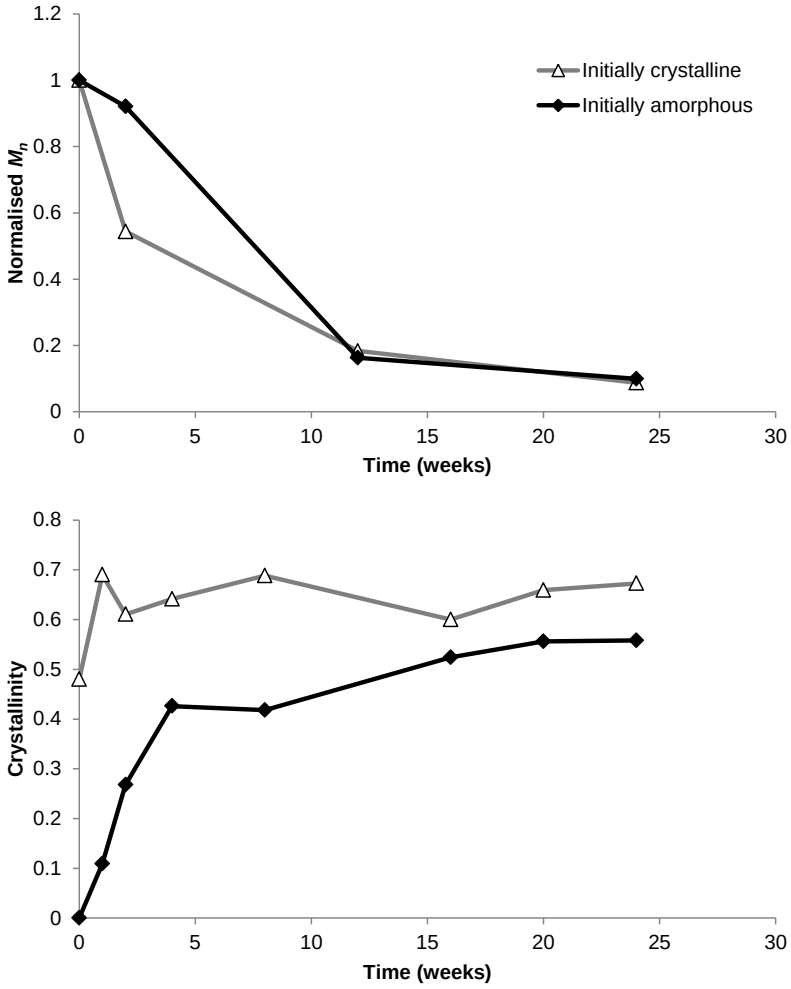

Fig. 2.19 Experimental data of Duek et al. [58] for the molecular weight (top) and crystallinity (bottom) in poly(L-lactide) pins.

The experimental data of Saha and Tsuji [69] is reproduced in Fig. 2.20 for crystallinity, molecular weight, Young's modulus and strength. In the study, a sample which undergoes hydrolysis is compared to a sample which is stored at the same temperature but in the absence of water, and therefore does not undergo polymer chain scission. In the early stages of degradation, the mechanical properties are most affected by crystallinity, which increases rapidly at the start of degradation. Therefore the polymer becomes stiffer and stronger even if molecular weight is reducing. During the later stages of degradation however, the reduction of molecular weight becomes the dominating factor and both Young's modulus and tensile strength properties reduce to zero for the degrading sample. In the sample that doesn't degrade, crystallinity is the major factor affecting the mechanical properties throughout the experiment, and thus the stiffness and strength increase without subsequent reductions. The data clearly

supports the above discussion in regards to Fig. 2.18 and Fig. 2.19 that strength and stiffness are increased by crystallinity and reduced by molecular weight.

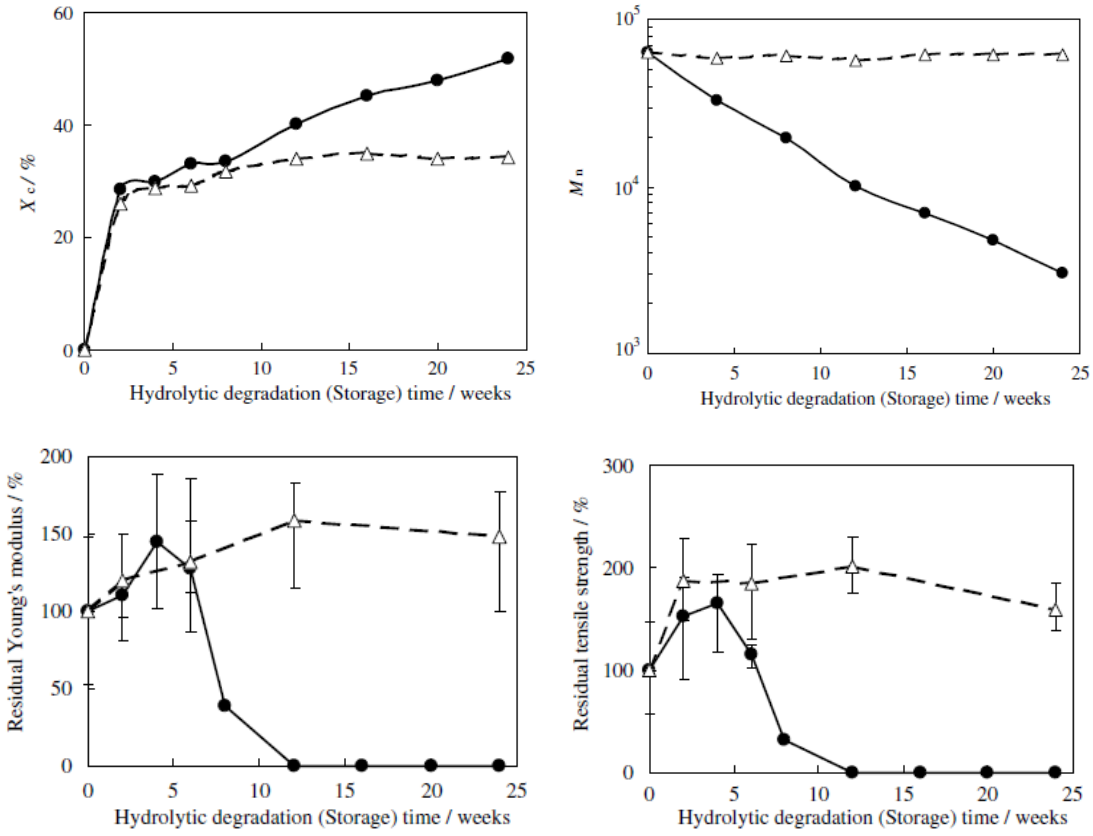

Fig. 2.20 Experimental data figures reproduced from the publication of Saha and Tsuji [69] with permission via the Copyright Clearance Centre. The plots show various properties of Poly(L-lactide) films during degradation: crystallinity (top left); molecular weight (top right); Young's modulus (bottom left); and strength (bottom right). Samples were either stored in the absence of water (hollow triangles) or degraded via hydrolysis (black circles).

In some experimental studies, Young's modulus increases in the early stages of degradation even if crystallinity does not [2, 67, 71, 73]. Tsuji and Suzuyoshi [67, 71, 73] attributed this increase to the "stabilized chain packing in the amorphous region in the presence of water molecules" with regards to their amorphous samples. This is similar to crystallinity increasing during annealing of the polymer; although the amorphous chains are not able to pack into a crystal form, they may reorient into a more close-packed structure than the initial structure. If samples are stored at temperatures below 37°C before degradation, the reorientation of chains is assisted, when degradation is initiated at 37°C, by the increased movability of chains at the higher temperature in addition to the plasticising effects of water molecules. This understanding is particularly appropriate for initially amorphous samples that are

quenched from the melt since quenching prevents the chains from relaxing into the most stable configuration.

When modelling the degradation of mechanical properties, it is clearly important to consider both molecular weight and crystallinity. In this thesis, a model is presented which considers both effects.

2.5.4 The degradation of elongation-at-break property

Reductions in molecular weight due to chain scission during degradation generally reduce the maximum elongation sustained by the polymer before it breaks (elongation-at-break). The variation of elongation-at-break with degradation time is often more erratic than for strength and Young's modulus. The data presented in Fig. 2.21 is reproduced from the study of Tsuji [9], which was discussed in relation to Fig. 2.10 and Fig. 2.11. It demonstrates how elongation-at-break values can reduce and increase dramatically and how the error margins can be large. Such large error margins may indicate that the value of elongation-at-break is not dependent on overall macroscale polymer structure since variability in the polymer would then be expected to average out and reduce error margins. It may be the case that the elongation-at-break value is dependent on the material properties in the single weakest section of the polymer sample. This is analogous to the unpredictable strength in ceramics, which is dependent on the largest flaw size.

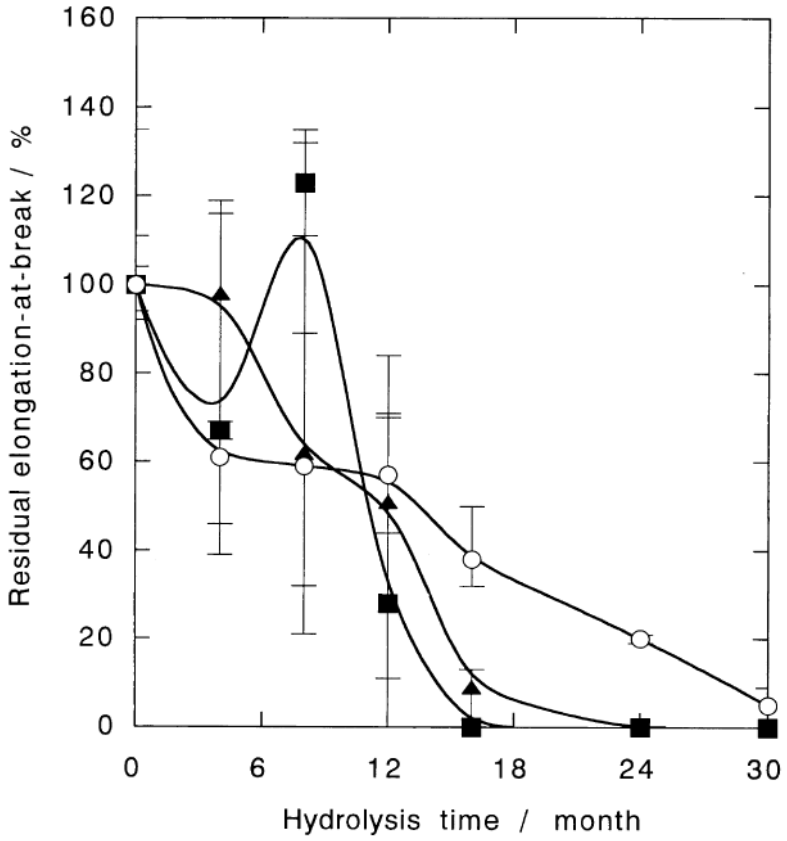

Fig. 2.21 Experimental data figure reproduced from the publication of Tsuji [9] with permission via the Copyright Clearance Centre for elongation-at-break versus time. The data is quite erratic and has high error margins. Three polymers are studied: L-lactide (filled triangle); D-lactide (filled square); and a 1:1 blend of L- and D-lactide (hollow circle).

Elongation to break may be expected to decrease as molecular weight reduces because shorter chains can untangle more easily, and hence two halves of a polymer sample may be pulled apart at a lower elongation percentage. Conversely if chain scission results in the glass transition temperature of a polymer reducing, the deformation mechanism for the polymer may change from a glassy to rubbery deformation, in which case elongation-at-break would significantly increase. Similarly, if chain scission reduces the chain entanglement, it is possible that elongation-at-break values could increase due to the polymer chains being more able to unravel rather than break during deformation. As mechanical properties reduce towards zero however, the polymer approaches a state where it falls apart under its own weight, and thus elongation-at-break also approaches zero. The effect of chain scission is a complicated interplay between these effects, and likely many others, but in general for long term degradation the value of elongation-at-break reduces as molecular weight reduces. This can be seen in the data presented in Fig. 2.11 and Fig. 2.21 because the

molecular weight reduces to a greater extent for the homopolymers than the polymer blend, as does long-term elongation-at-break.

In addition to changes that result from molecular weight, increases in crystallinity (as a result of chain scission) also affect elongation-at-break during degradation. In contrast to Young's modulus and strength, increasing crystallinity reduces the value of elongation-at-break because the stiff crystal particles cannot elongate like amorphous polymer chains and they may constrain the chains in a similar manner to chain entanglements. The study of Tsuji and Ikada [57], which was discussed above in relation to Fig. 2.17, also considered elongation-at-break. The effect of crystallinity on elongation-at-break was studied for 3 different manufacturing processes. The experimental data is shown in Fig. 2.22 and clearly demonstrates that elongation-at-break reduces as crystallinity increases. However, the relationship is quite noisy and strongly dependent on the manufacturing process used.

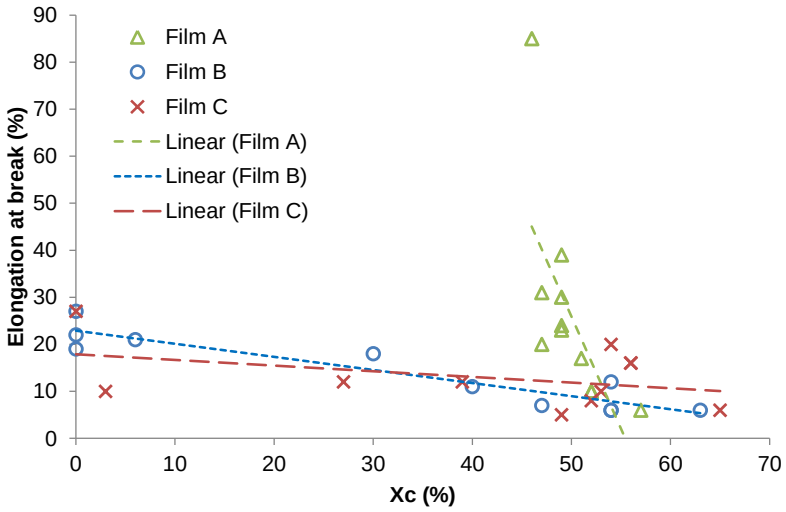

Fig. 2.22 Experimental data by Tsuji and Ikada [57] for poly(L-lactide) films shows that increasing crystallinity results in a decrease in elongation-at-break.

The effects of both molecular weight reduction and crystallinity on elongation-at-break can be seen in the experiments of Saha and Tsuji [69]. The experimental data for elongation-at-break is reproduced in Fig. 2.23. Molecular weight and crystallinity data are presented in Fig. 2.20. Initially amorphous samples were studied both with (solid line in the figure) and without (dashed line) hydrolytic degradation. Both samples show a sudden increase in crystallinity in the first 2 weeks and as a result elongation-at-break reduces sharply in that timeframe. The value of elongation-at-break for the sample which undergoes hydrolysis, and therefore experiences a reduction in molecular weight, continues to reduce and equals zero after 8 weeks of degradation,

by which time Young's modulus is approximately 40% of the original value. In contrast, the sample which sees no reduction in molecular weight demonstrates a relatively constant elongation-at-break value for several weeks after the initial crystallinity-induced drop.

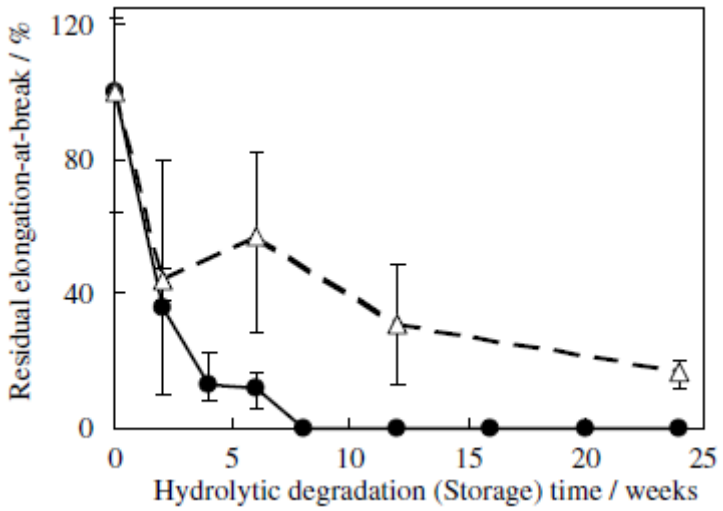

Fig. 2.23 Experimental data figure reproduced from the publication of Saha and Tsuji [69] with permission via the Copyright Clearance Centre for elongation-at-break of poly(L-lactide) films. Samples were either stored in the absence of water (hollow triangles) or degraded via hydrolysis (black circles).

Although crystallinity has a considerable effect on elongation-at-break, it is reductions in molecular weight that ultimately reduce the value to zero. Several experimental publications [2, 5, 9, 10, 12, 17, 58, 69] show that the samples for which molecular weight reduces most rapidly also demonstrate an earlier total loss of the elongation-at-break value. Although in many cases [2, 5, 9, 12] the samples which degrade most rapidly in terms of molecular weight do not necessarily demonstrate the greatest reduction in normalised elongation-at-break during the early stages of degradation. One important factor is that the initial values of elongation and break can vary greatly between samples. Samples that are initially amorphous generally have a high initial value of elongation-at-break, which reduces significantly in the early stages of degradation as the samples crystallise. However, these initially amorphous samples may ultimately retain non-zero values of elongation-at-break for longer because the molecular weight of initially crystalline samples tends to reduce more rapidly. This theory that less crystalline samples experience greater reduction in elongation-at-break early (due to higher initial values) but ultimately retain non-zero values longer (due to slower reduction of M_n) is the most likely situation in the experiments of Tsuji [9] and of

Tsuji et al. [5]. Other experimental studies [2, 12] demonstrate significant reduction of high initial elongation-at-break values during the early stages of degradation for amorphous polymers that do not crystallise during degradation. Initially amorphous samples are generally quenched during processing to prevent crystallization. Therefore it may be the case that when water enters the polymer during the early stages of degradation, the amorphous polymer chains are plasticised and reorient into a more tangled or more oriented configuration, which does not allow high elongation-at-break.

2.5.5 Other factors that affect the degradation of mechanical properties

Since the reduction of molecular weight has a major effect on mechanical properties, any factors that affect the rate of molecular weight degradation in turn affect mechanical properties. In some cases, the effects may be counter-intuitive. A particular example is with regards to the structural design of biodegradable polymers fixation devices. It has been found that the molecular weight of large polymer samples degrade more rapidly than small samples [22]. Therefore increasing the initial strength and stiffness of a fixation device through an increase in physical size may ultimately lead to a weaker device if degradation occurs more rapidly. Factors that may affect the degradation of molecular weight include:

- Temperature, type, pH, replacement frequency and characteristics of the degradation medium, including the solution:polymer volume ratio;
- The initial molecular weight, polydispersity and residual monomer content of the polymer samples;
- Polymer micro/nano-structure including crystallinity, orientation of amorphous chains and spherulite size;
- Physical sample size and shape;
- Homopolymer, copolymer or polymer-blend composition including any added composite particles or drug loading;
- Polymer processing conditions and techniques including polymerisation, heat treatment, shape forming and sterilisation;
- And polymer glass transition temperature.

There are some other factors that can directly affect the degradation of mechanical properties. The initial values of mechanical properties affect the rates of their degradation as discussed in Section 2.5.4 for samples with high initial values of elongation-at-break. The rate of degradation may be affected for both normalised and

absolute property values. The micro/nano-structure is mentioned in the bullet points above because it may affect the rate of chain scission. In addition to that effect, the micro/nano-structure is likely to affect the impact that each chain scission has on mechanical properties. For example, in a drawn fibre many of the polymer chains are aligned in the fibre direction and chain scission in a fibre-oriented chain will have a different effect on mechanical properties than chain scission in a non-oriented chain. Therefore, for a given scission rate, the reduction of mechanical properties with time may depend on the chain configuration in the polymer. Mass loss may be proposed to affect mechanical properties if it results in a porous structure. However, in numerous experimental publications [2, 5-7, 9, 10, 12, 17, 68, 69] mass loss occurs after mechanical properties have significantly reduced, or completely lost, and hence it is not expected to be an important factor for mechanical properties. The glass transition temperature (T_g) could play a significant role in the degradation of mechanical properties for polymers whose glass transition temperature is in the region of the testing temperature. During hydrolytic degradation, T_g often decreases [2, 5-7, 17, 58] as a result of chain scission allowing the polymer chains to move relative to one another more easily. Alternatively, T_g may also increase, particularly in the early stages of degradation, due to an increase in crystallinity [5, 6, 17, 66, 68]. If T_g lowers to the extent that the polymer transitions from a glassy state (testing temperature below T_g) to a rubbery state (above T_g), the stiffness would dramatically reduce. This is a separate mechanism for the degradation of Young's modulus to chain scissions in a polymer which remains in a glassy state. Whether a polymer loses stiffness due to a weakening of the glassy polymer or due to a lowering of the glass transition temperature may not always be clear, particularly given that the glass transition temperature sometimes becomes poorly defined towards the later stages of degradation [9, 10]. Since polymers may contain a mixture of amorphous, aligned or crystalline polymer chains, it may be the case that some regions of the polymer are below T_g and other regions (which would facilitate the overall deformation) are above T_g.

2.6 Modelling changes in mechanical properties of degrading polymers

The master curve which relates Young's modulus to molecular weight in Fig. 2.16 is simply a fitting to experimental data; the identified relationship is not a theoretical understanding of how the two material properties are related. This section reviews some models which simulate the degradation of mechanical properties based on a molecular understanding. Two models for polymer strength are considered briefly along with more in depth analysis of two models for Young's modulus. Flory [74] proposed that fracture strength, σ_f, could be related to initial strength, σ_∞, according to Eq. 2.4 as:

$$\sigma_f = \sigma_\infty - \frac{B}{M_n} \qquad 2.4$$

in which *B* is a constant. Similarly, Deng et al. [75] found that a fitting to their experimental data for strength retention could be described by Eq. 2.5 as:

$$BSR = a + b \ln MW \qquad 2.5$$

in which *BSR* is breaking strength retention, *a* and *b* are constants to be determined from the data fitting, and *MW* is number or weight average molecular weight.

Currently, there is no mathematical model for the degradation of Young's modulus in polymers below their glass transition temperature. Many medical fixation devices are manufactured from biodegradable polymers below their glass transition temperature, and hence further understanding of their mechanical properties degradation is required. In this thesis, atomic simulations of a glassy biodegradable polymer lead to a simple mathematical model for Young's modulus. The author of this thesis is aware of two studies which relate Young's modulus to the degradation of molecular weight in bioresorbable polymers based on a theoretical understanding of how mechanical properties change during degradation: the first study is conducted by Wang et al. [61] and considers the entropy spring model for rubbery amorphous polymers; the second, by Ding et al. [62], is a molecular dynamics study of chain scission in a semicrystalline polymer both above and below T_g. These studies are briefly reviewed here along with an overview of atomic simulation techniques.

2.6.1 An entropy spring model for the degradation of Young's modulus by Wang et al. [61]

Wang et al. [61] developed a model for Young's modulus degradation based on theoretical entropy change during deformation. For polymers above their glass transition temperature, Young's modulus is controlled by the entropy change during degradation as discussed at the start of this chapter. Since the polymer chains straighten out during deformation, there are fewer possible configurations for the polymer chains to occupy, which causes the entropy change. This is shown schematically in Fig. 2.24 a), which shows a polymer chain (black line) in a matrix of other amorphous polymer chains (grey area) before and after strain is applied. From entropy theory [74], the Young's modulus, *E*, of a polymer can be related to the number of polymer chains per unit volume, *N*, according to

$$E = 3Nk_bT \tag{2.6}$$

in which k_b is Boltzmann's constant and *T* is the absolute testing temperature. The relationship proposed in Eq. 2.6 appears to indicate that Young's modulus should increase during degradation because as chain scissions occur, the number of chains per unit volume, *N*, increases. However, Wang et al. [61] argued that 1) a fundamental assumption when deriving Eq. 2.6 from entropy theory is that the end-to-end distance is much smaller than the extended chain length of a polymer chain, and 2) the end-to-end length should follow a Gaussian distribution, which is not valid for random scission. Rather than include random scission directly into entropy theory, which is a complicated task, Wang et al. [61] suggested an intuitive modification to Eq. 2.6. Since the individual polymer chains are highly constrained by the surrounding polymer chains, an isolated chain scission may have little effect on the overall chain configuration before and after deformation. This can be seen in Fig. 2.24, by comparison of situations a) and b) with zero and one scissions respectively. Wang et al. [61] proposed that since the change in entropy, as a result of the applied strain, is similar for both situations, isolated chain scissions can be considered to have no effect on the entropy increase during deformation and therefore the value of *N* should not increase as a result of chain scission. They referred to this argument as the "no-rise rule." To account for the effect of chain scission, Wang et al. [61] suggested that once a polymer chain is cleaved to the extent that it is divided into very short chains, it no longer contributes to the overall entropy of the polymer. Fig. 2.24 c) shows the justification for this theory schematically because the individual chain fragments do not need to straighten out

during overall polymer deformation, therefore the total entropy of all the small chains (that once made up the long chain) can be assumed not to change during deformation. Wang et al. [61] implemented this theory by utilising a molecular weight threshold, M_{th}. When a polymer chain undergoes chain cleavage to the extent that its molecular weight reduces below M_{th}, the chain is removed from the entropy calculation and therefore the value of N in Eq. 2.6 reduces by 1.

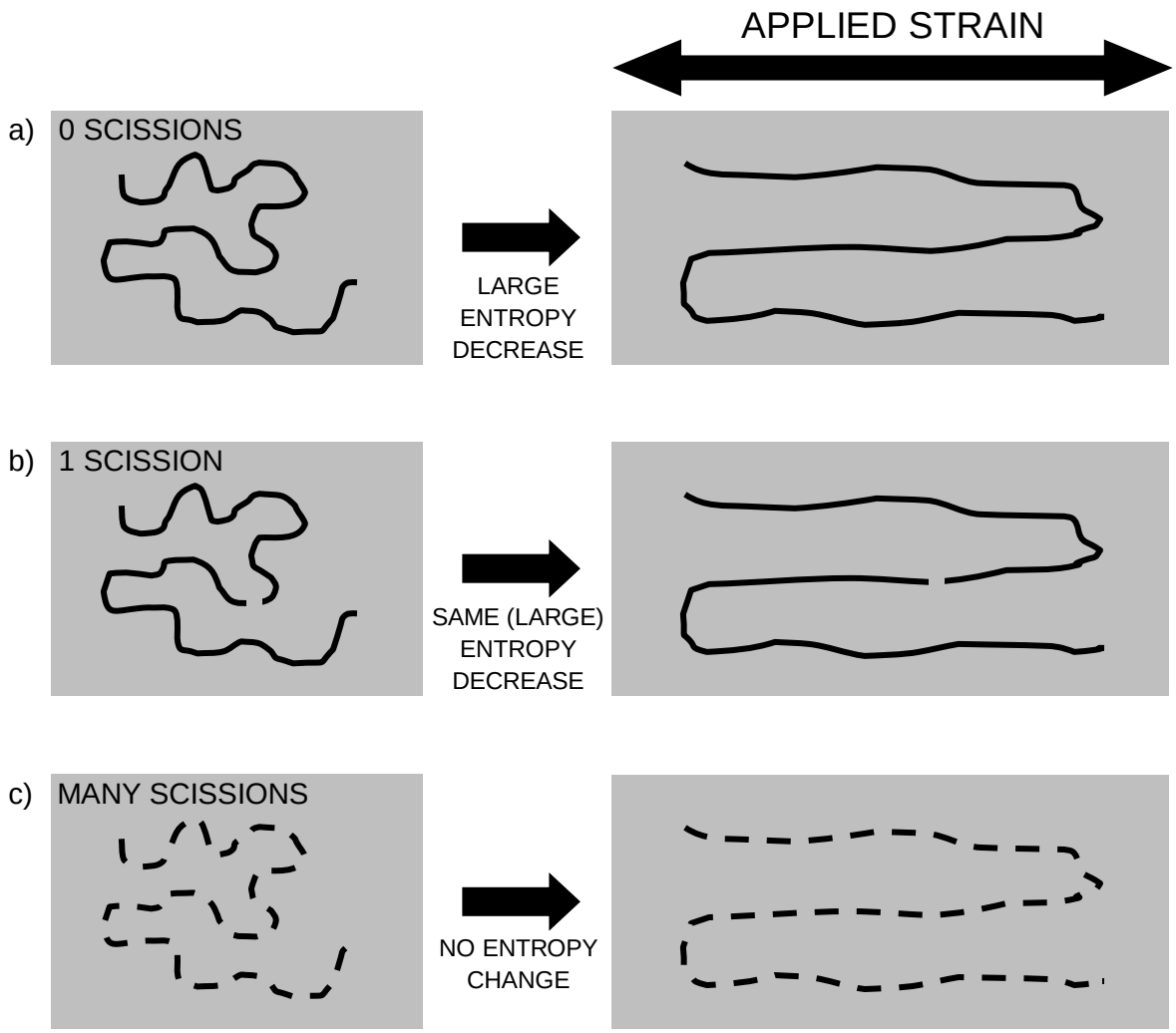

Fig. 2.24 The theory presented by Wang et al. [61] considers how a polymer chain (black line) embedded in a matrix of other amorphous polymer chains (grey box) straightens out during elongation of the overall polymer. A chain is shown with a) 0 scissions, b) 1 scission and c) many scissions. There is little effect of a single scission on entropy change during deformation, whereas many scissions can result in entropy no longer reducing during deformation.

Wang et al. [61] used their concepts of the “no-rise rule” and a molecular weight threshold to relate Young’s modulus to average molecular weight. They ran computer simulations of chain scissions in a discrete number of polymer chains. In the simulations, polymer chains were created numerically with random chain lengths according to an initial molecular weight distribution. Chain scissions were then numerically simulated with consideration given to both random scission and end scission theories. Based on a set value of M_{th}, the value of N was calculated after each chain scission. The new value of N allowed a normalised value of Young’s modulus to be calculated, according to Eq. 2.6, and therefore directly related to average molecular weight, which was also calculated.

Wang et al. [61] compared the model prediction to the experimental data of Tsuji [2] for Young’s modulus and average molecular weight. In Tsuji’s experiments [2], thin films of poly(L-lactide) and poly(D-lactide) were degraded in phosphate buffer solution (pH7.4) at 37°C. Fig. 2.25 shows the experimental gel permeation chromatography (GPC) curves at 4 different times during degradation. A molecular weight threshold of M_{th} = 9.36 x 10^4 g mol^{-1} was determined, which is indicated in the figure by the shaded region. The portions of the experimental molecular weight distributions that lie within the shaded region were assumed to be too short to contribute to the entropy change during deformation. The value of N was calculated by integrating over the area to the right of the shaded region. Computer simulations were then completed to find the relationship between normalised Young’s modulus and normalised average molecular weight, according to Eq. 2.6 utilising the “no-rise rule” and M_{th} = 9.36 x 10^4 g mol^{-1}. The relationship is shown (solid line) in Fig. 2.26 along with experimental measurements of Tsuji [2]. There is clearly a very good fitting between the model and the experimental data.

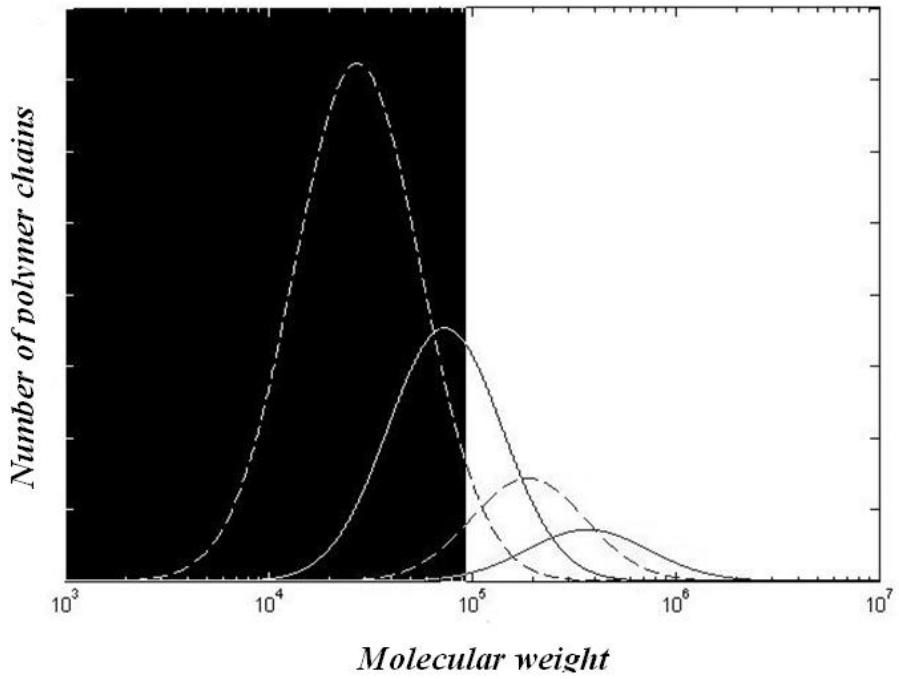

Fig. 2.25 Figure reproduced with permission from the publisher Elsevier and the author Wang [61] via the Copyright Clearance Centre. Experimental GPC curves for molecular weight distributions of poly(D-lactide) [2] are shown at various times during degradation: 0, 8, 16 and 24 months from right to left. The shaded region indicates polymer chains that are below a molecular weight threshold of M_{th} = 9.36 x 10^4 g mol^{-1}.

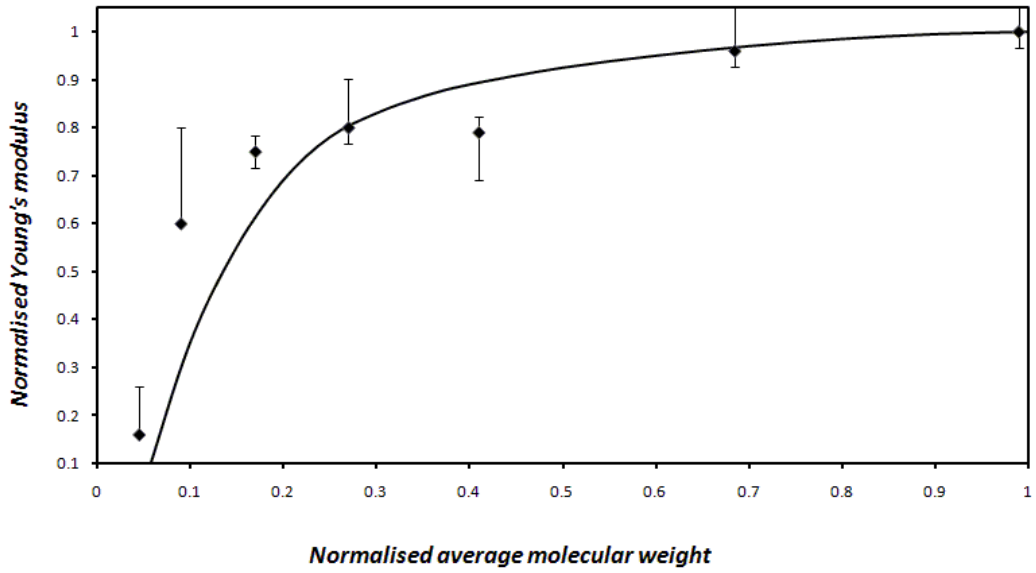

Fig. 2.26 Figure reproduced with permission from the publisher Elsevier and the author Wang [61] via the Copyright Clearance Centre. Experimental data for normalised Young's modulus versus normalised average molecular weight for poly(D-lactide) [2] (discrete data points) are compared to the model prediction assuming a molecular weight threshold of M_{th} = 9.36 x 10^4 g mol^{-1}.

Simple mathematical models exists which can simulate the degradation of average molecular weight in biodegradable polymers [27, 28, 48-50, 60]. Wang et al. [61] combined such a model with their entropy spring model to predict the degradation of Young's modulus of a biodegradable rod using finite element analysis (FEA). Fig. 2.27 shows the results for normalised molecular weight in the rod during degradation. The rod degraded more quickly in the middle because an advanced mathematical model [48, 50] was used, that can consider the diffusion of short polymer chains, which accelerate the rate of chain cleavage, out of the rod near the surface. Wang et al. [61] completed simulations for several rod sizes, and related the predicted average molecular weight degradation to Young's modulus degradation. The results for Young's modulus versus degradation time are shown in Fig. 2.28. The three different curves with non-dimensional diffusion coefficients $\overline{D}$ = 10 : 0.1 : 0.0001 correspond to three different normalised rod diameters of 1 : 10 : 100 respectively. The largest rod lost mechanical properties earliest because the short polymer chains had a further distance to diffuse before leaving the rod. The model of Wang et al. [61] can be used to predict the degradation of several biodegradable device designs, in order to identify which design offers the optimal mechanical properties during the degradation process.

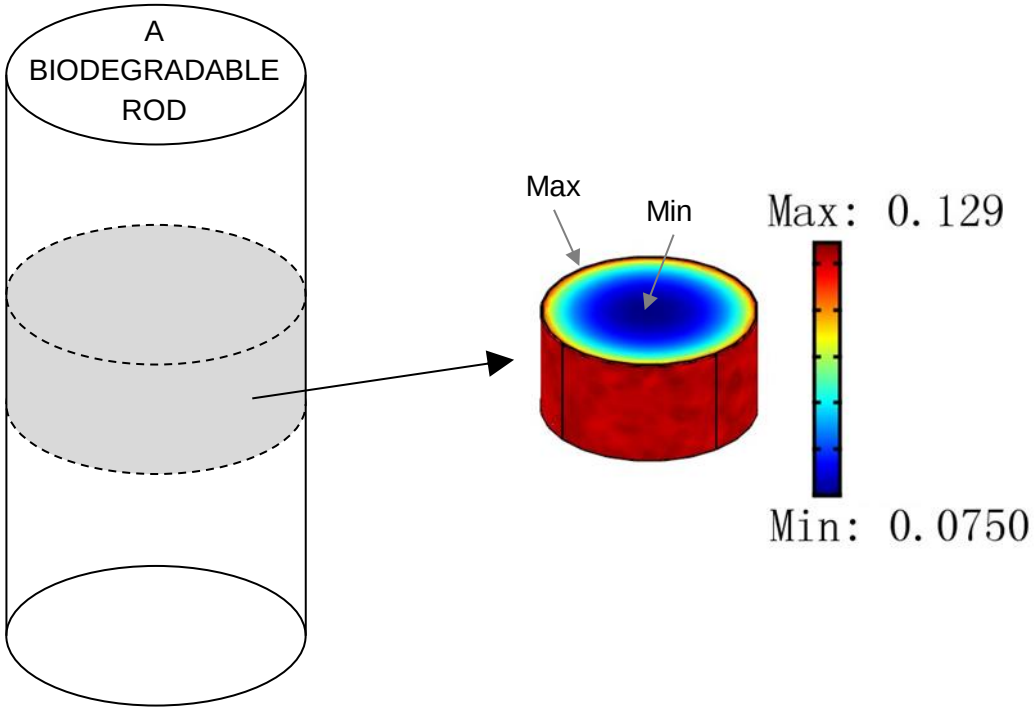

Fig. 2.27 Figure adapted from the original publication with permission from the publisher Elsevier and the author Wang [61] via the Copyright Clearance Centre. A mathematical model for degradation of molecular weight was implemented in a FEA simulation for a section of a biodegradable rod. The colour indicates normalised molecular weight part-way through degradation. The molecular weight degraded more rapidly in the centre of the rod than at the surface.

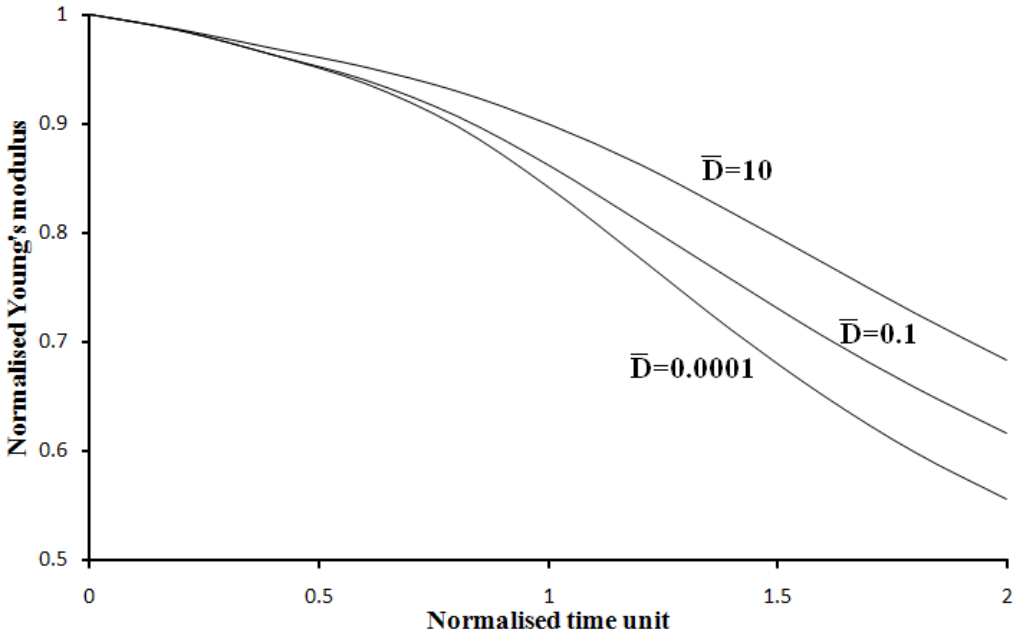

Fig. 2.28 Figure reproduced with permission from the publisher Elsevier and the author Wang [61] via the Copyright Clearance Centre. The degradation of normalised Young's modulus versus time was modelled for a biodegradable rod using FEA. The non-dimensional diffusion coefficient $\overline{D}$ was varied to represent different rod diameters.

2.6.2 Atomic computer simulations for polymers

Computer simulations can be used to model the positions of atoms in a polymer material and the interactions between atoms. Molecular dynamics (MD) is a commonly used simulation technique, in which the atoms' positions are updated in time-based simulations. In MD simulations, the energy states of electrons in molecules according to quantum mechanics are represented as functions of the atoms' nuclei coordinates alone. Since the atomic structure is represented by a single coordinate per atom, the structures are often graphically presented as a collection of 3D spheres: one per atom. In some cases, united-atom models are used, in which a group of atoms may be represented by a single coordinate in order to reduce the number of computations. The forces that atoms apply to one another as a result of their chemical bonds and other nonbonded interactions are used to find the acceleration of atoms. Discrete time steps are used to calculate the variation of atoms' speed and positions, based on those accelerations.

In MD simulations, an overall force can be applied to a polymer and the simulated atomic response can indicate the large scale deformation that is expected to result from the force. Such simulations can be used to model the value of Young's modulus for the overall material. A critical aspect of MD simulations is how the interactions

between atoms are modelled. This information is described in a force field. The force field is effectively a list of equations, which describe the forces that atoms exert on each other based on their position relative to one another. The equations are founded on fundamental theories of atomic potential energy. For example, one equation in the force field may describe the force exerted by an oxygen atom on a carbon atom, to which it is covalently bonded, depending on the distance between the atoms.

The forces that are described in the force field are based on atomic theories including: the attraction between atoms that are covalently bonded; the Coulomb attraction between atoms that have positive and negative charges; the Pauli repulsion, which occurs when the electron fields of two atoms overlap; and long range van der Waals attraction between atoms. Force fields vary by application because in the analysis of a regularly repeating structure, such as diamond, the simulations may consider just a few atoms, which are assumed to repeat periodically, and therefore represent a large volume of material. Hence, the computational demands are much lower than for more complex molecular structures such as polymers. A force field for diamond may represent the interatomic potentials with a higher degree of complexity such as 1) the potential energy for interatomic separation may take the exponential Morse potential instead of a simple harmonic potential, or 2) the interaction between atoms over a greater distance may be considered.

MD simulations are computationally intense, and therefore cannot consider time periods greater than a few picoseconds or a large number of atoms. Whereas MD simulations consider time to elapse, static simulations such as molecular statics and finite element analysis (FEA) may not consider time and therefore offer significant computational benefits. In molecular statics, the atoms have no velocity. Instead, the atomic coordinates are iterated by methods including random iteration, iteration according to a probability distribution, or iteration along the steepest gradient of potential energy. The atoms' coordinates are iterated in order to minimise the overall interatomic potential energy of the structure. Although molecular statics simulations require less computational power than molecular dynamics, large atomic structures such as high molecular weight amorphous polymers may still be unfeasible due to the high number of iterations required.

Liu et al. [76, 77] developed an atomic-scale finite element method (AFEM), in which the molecular dynamics force field is represented by finite elements. Their method

offered reductions in computational demands versus the conjugate gradient method in molecular mechanics. For nonlinear potential energy functions, an iterative procedure was required in order to minimise the total potential energy in a structure. In finite element method (FEM) simulations, the interatomic potential energy functions are considered in a single set of linear equations. These equations can be solved simultaneously in order to model displacements in a single computation step. Wang et al. [78, 79] also developed atomistic finite elements to represent the interaction between atoms through finite element analysis. The elements they developed represent the polymer as a chain of elastic rods connected to each other by elastic joints, which facilitate angular potential energy terms to be considered. As a result of both angular and Cartesian coordinates being used, there were six degrees of freedom for each atom. An iterative procedure was used in the simulations.

Ab initio simulations, which are based on quantum mechanics, are an alternative to molecular dynamics, which consider the sub-atomic scale and include electron orbits. Ab initio simulations are more computationally demanding than MD simulations. Due to high computational demands, ab initio simulations are only suitable for a small number of atoms. Several studies have conducted atomic simulations for biodegradable polymers [55, 56, 80-86]. The author of this thesis is only aware of three studies that consider the mechanical properties of poly(lactide) or poly(glycolide) [82-84]. These studies all consider the crystalline polymer phase because amorphous polymer phase simulations require a large number of atoms. There is only one study, by Ding et al. [62], that considers the effect of chain scission on the mechanical properties of amorphous biodegradable polymers, which is discussed in the next section.
, chain scissions were applied to a polyethylene atomic structure through molecular dynamics (MD) simulations. It was not possible for Ding et al. [62] to use more complex molecular structure, such as poly(lactide), due to the high computational requirements of MD simulations.

2.6.3 A molecular dynamics study of Young's modulus during degradation of bioresorbable polymers by Ding et al. [62]

Ding et al. [62] studied polymer chain scission with MD in order to understand the atomic effects of polymer chain scission with a particular focus on changes to Young's modulus. In the MD simulations, atoms are linked to each other by covalent bonds along with nonbonded interactions such as Lennard-Jones potentials. Fig. 2.29 shows one of the semicrystalline polymer structures that Ding et al. [62] produced in order to

simulate the degradation of bioresorbable polymers. The structure shown in the figure is a periodic unit cell. In the simulations it was considered to repeat in all directions to infinity. Each bead represents one polymer unit. Crystalline phases exist at either end and an amorphous phase is sandwiched in between them; this interlamellar amorphous phase represents the polymer chains that are trapped between crystal lamellae in a semicrystalline polymer. A polyethylene atomic structure was simulated because it was not possible to use more complex molecular structure, such as poly(lactide), due to the high computational requirements of MD simulations

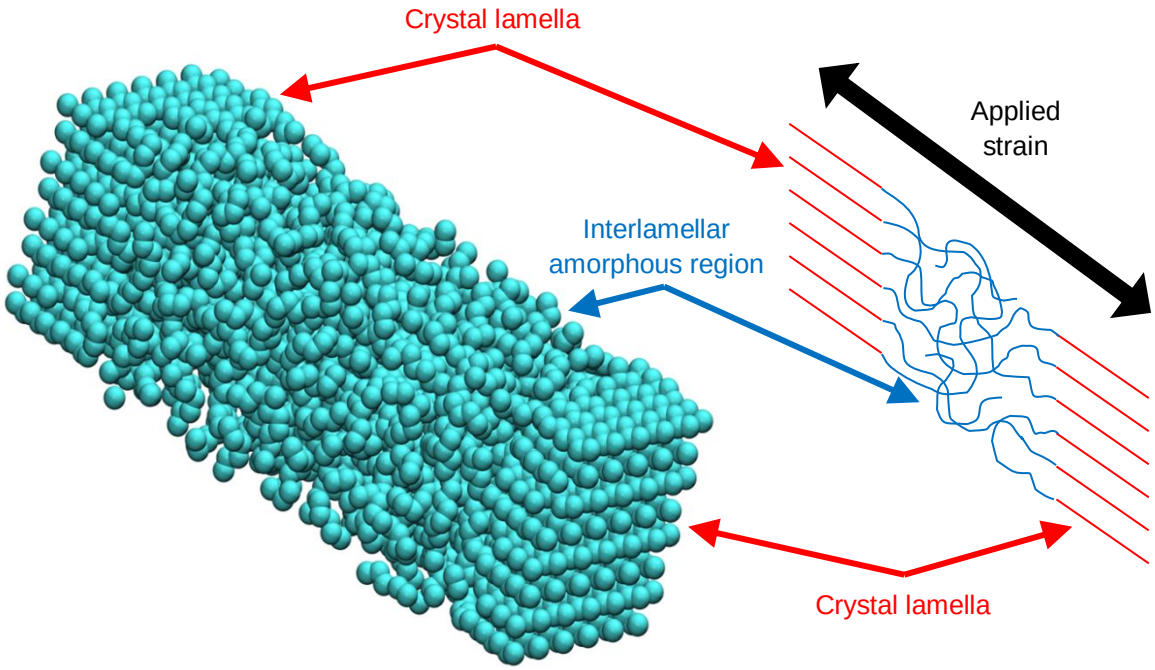

Fig. 2.29 The polymer structure used in MD simulations by Ding et al. [62] consisted of an amorphous phase in between two crystalline phases, which represent crystal lamellae. To calculate Young's modulus, the distance between crystal lamellae was elongated.

Chain cleavage was only simulated in the amorphous phase because the crystalline phase is known to resist hydrolysis. To calculate Young's modulus, Ding et al. [62] carried out the following procedure:

- Fix one crystal lamella and allow the structure to relax.
- Slowly move the other crystal lamella away from the fixed one whilst allowing the atoms to rearrange into a relaxed configuration during elongation.
- Sum up all the forces acting on a crystal lamella and divide by the cross sectional area to find stress.

- Repeat this process over a range of strains up to 0.5% and then use linear regression to relate stress to strain and therefore derive the value of Young's modulus.

Temperature is considered in MD simulations based on the kinetic energy of the structure. At higher temperatures, atoms vibrate with more energy and therefore a structure can be expected to expand. In the simulations of Ding et al. [62] this expansion was quantified by the distance between the crystal lamellae (interlamellar spacing). Simulations were conducted at 10 different temperatures almost ranging from absolute zero to the polymer melting point. The values of interlamellar spacing and Young's modulus at the different temperatures are shown in Fig. 2.30. The units in the figure are taken directly from the publication of Ding et al [62]. Above a temperature of 8 (in the MD units used in the figure) Young's modulus began to increase as temperature increased. This clearly suggested that mechanical properties at temperatures above 8 were being controlled by the entropy change during degradation rather than changes in interatomic potential energy, as discussed at the start of this chapter. The gradient of the slope of interlamellar spacing versus temperature becomes steeper at a temperature of 8, which also suggests the glass transition temperature was ≈8.

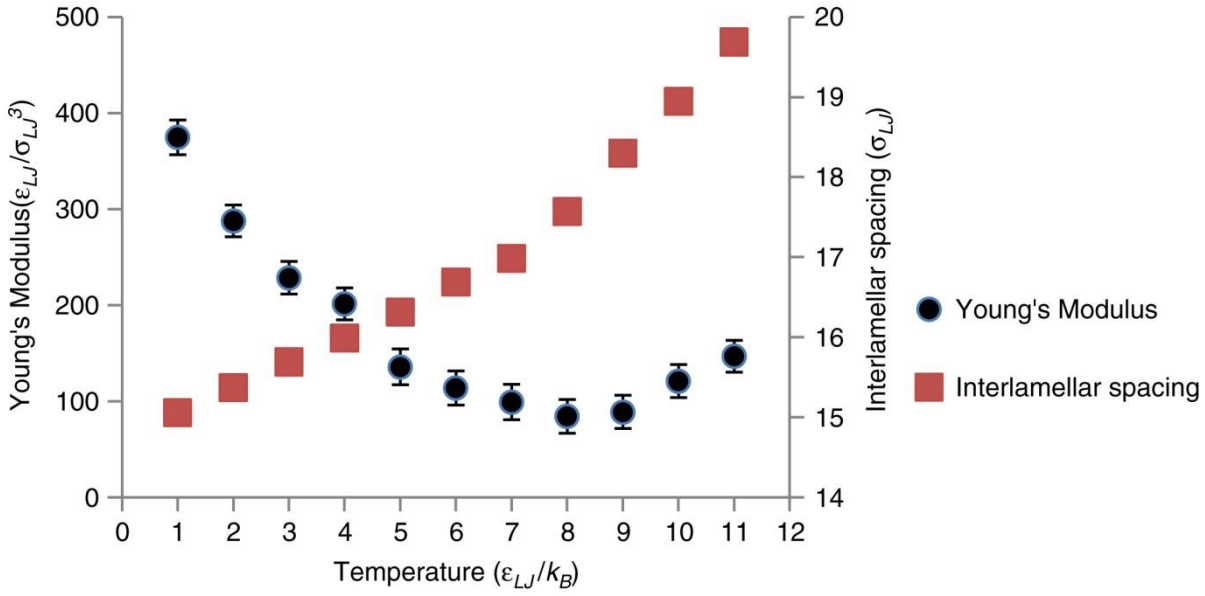

Fig. 2.30 Figure reproduced with permission from the publisher Elsevier and the author Ding [62] via the Copyright Clearance Centre. The Young's modulus and distance between crystal lamellae were calculated at various temperatures. The units were based on MD parameters.

Fig. 2.31 shows the results of the studies of Ding et al. [62] for the effect of chain scissions on Young's modulus both above and below the glass transition temperature. There was a considerable delay while chain scissions were applied before Young's modulus reduced for the simulations above T_g, whereas below T_g this delay may not have existed. The theory of Wang et al. [61] for Young's modulus degradation above T_g, discussed in the previous section of this chapter, can explain the delay in Young's modulus versus chain scission. In that theory it was argued that scissions may have little effect on the entropy change during deformation until a polymer chain has been subjected to a significant number of scissions. For simulations both above and below T_g, the results in Fig. 2.31 indicate that the average molecular weight of the structure reduced before the value of Young's modulus did, which agrees with the review of experimental data in Fig. 2.15.

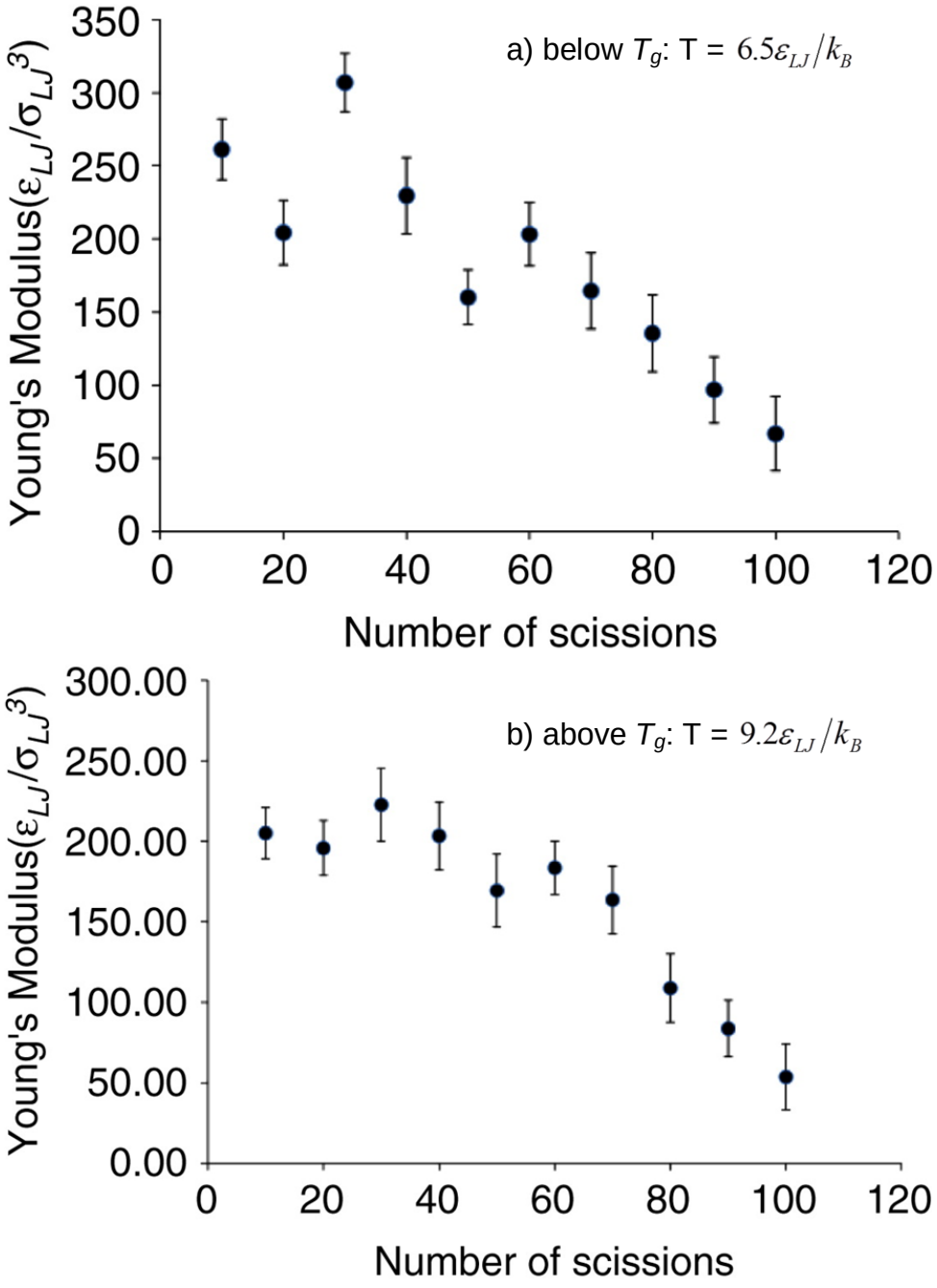

Fig. 2.31 Figure reproduced with permission from the publisher Elsevier and the author Ding [61] via the Copyright Clearance Centre. Young's modulus was calculated for several numbers of chain scissions at temperatures of a) 6.5 and b) 9.2, which were below and above T_g respectively. The units were based on MD parameters.

2.7 Conclusions

A literature review was carried out for both experimental and theoretical studies for the degradation of bioresorbable polymer mechanical properties. The effects of the degradation of molecular weight and crystallinity were analysed in terms of changes to polymer strength, Young's modulus and elongation-at-break values. The experimental data for Young's modulus versus molecular weight of poly(lactide) was compared in order to identify a simple model to relate the two factors. It was found that a linear relationship exists between Young's modulus degradation and the reduction of $\log(M_n)$. This relationship was found for polymer degradation studies over a wide range of conditions and experimental setups. It can be used to estimate Young's modulus degradation for polymer degradation studies in which mechanical properties are not measured. Existing models for the degradation of mechanical properties were discussed in detail.

Chapter 3: Aims, objectives and methodology

This chapter gives details about the overall aims, objectives and methodology of the thesis. The overall structure of this thesis and knowledge gaps that it addresses are summarised.

3.1 Aims

The overall aim of this thesis is to further the understanding of biodegradable polymers in order to encourage further work in the field which will ultimately lead to the more wide-spread use of biodegradable polymers in medical applications and therefore enable new opportunities to improve healthcare. There is a vast range of medical applications and potential benefits from the use of biodegradable polymers. Presently, biodegradable polymers are being used in fixation devices to support broken bones during healing. Some of the benefits that may be realised by the use of biodegradable polymers are:

- No need for repeat surgery to remove the device after healing.
- A gradual reduction in the mechanical support provided by a biodegradable fixation device can enable a gradual transition of load from the device to the healing bone, which may encourage bone growth.
- Scope for bone growth to replace the biodegradable polymer and therefore avoid permanent screw holes which may be painful, susceptible to infection and reduce the mechanical strength of the bones.

These benefits are currently realised but many surgeons opt not to use biodegradable polymers due to the fact that they are not fully understood and there can therefore be some unwanted side effects such as local inflammation or device degradation over too long a time period. Many more important benefits will be realised in the longer term including tissue engineering of organs outside the human body and targeted drug delivery.

It is not possible for this thesis to complete the understanding of biodegradable polymers because there are a large number of factors that are not currently understood in detail, even for studies in controlled environments outside the human body. Rather this thesis will make steps in the direction of more complete understanding and focus

on some of the most important factors that affect degradation. There are currently no mechanical property degradation models for glassy polymers including poly(lactide), the most popular biodegradable polymer for fixation devices. This thesis will take the first step in such models through atomic-scale analysis and the development of a simple mathematical model for Young's modulus degradation. Future work must continue to further the understanding of degradation in order to encourage the wide-spread and confident use of biodegradable polymers by surgeons.

Furthering the understanding of biodegradable polymer degradation can also benefit many fields alongside biodegradation. The models developed in this thesis can simply be translated to consider areas such as UV degradation, polymer chain growth, glass degradation and biological materials such as collagen.

3.2 Gaps in the current knowledge

Current models for the degradation of bioresorbable polymers that consider the increases of crystallinity during degradation are complicated due to the use of integrational terms. This may inhibit their widespread use, particularly by researchers or polymer device designers from a non-modelling background. Simpler models, which are more accessible for non-experts, do not exist for crystallinity. Also, models that consider polymer chain scission of individual polymer chains are often very detailed and therefore not likely to be used or fully understood by non-experts. Experiments have suggested that the small sections of amorphous polymer phase that lie in between the crystallites in a spherulite, may have considerably different degradation profiles to large volumes of amorphous polymer outside of spherulite. However, no models of biodegradable polymer degradation have been used to quantify these theories. Fundamental hydrolysis mechanisms, including noncatalytic hydrolysis, autocatalytic hydrolysis, random scission and end scission, have all been found to occur in experimental degradation studies for biodegradable polymers such as poly(lactide). It is not known which hydrolysis mechanisms have the greatest impact, nor which occur most frequently, in biodegradable polymer degradation experiments. The precise effects that underlying hydrolysis mechanisms have on the degradation trends for molecular weight reduction and weight loss are complicated and have not been studied in detail. As a result, there is not a simple way to analyse experimental results in order to identify which hydrolysis mechanisms were likely to have been prominent. Residual monomer left in the polymer after processing has a significant effect on degradation [18, 23, 87, 88]. This topic is receiving an increasing amount of

attention in the literature. There is currently no mathematical model which incorporates the effect of residual monomer. Also, initial molecular weight has been analysed in several experimental studies [8, 29-31, 88, 89] but the effect it has on the degradation of molecular weight and mass loss is inconsistent. The effect has not been considered by theoretical models for degradation.

The degradation of mechanical properties, including Young's modulus and strength, is not well understood. Mechanical properties degrade in an erratic manner, which varies considerably between experimental degradation studies. As a result, a general model for mechanical properties degradation has never been identified. There are no studies in the literature that conduct atomic simulations of chain scission in biodegradable polymer atomic structures. This is because existing simulation techniques have too high computational demands. Along with a lack of understanding of overall mechanical properties degradation, theories for the effect of polymer chain scission on mechanical properties at the atomic scale do not currently exist for polymers below their glass transition temperature. As a result there are no mathematical models for the degradation of mechanical properties versus time for bioresorbable polymers below their glass transition temperature, including the popular poly(lactide) and poly(glycolide) polymers.

3.3 Objectives

The objectives of this thesis are to:

- Simplify the existing models for biodegradable polymer degradation to enable their more widespread use.
- Further the understanding of how the following factors affect degradation:
    - Autocatalysis
    - Random and end scission
    - Initial molecular weight
    - Residual monomer
- Improve the understanding of how and why Young's modulus reduces during degradation
- Extend the existing mathematical degradation models to include the degradation of Young's modulus for glassy polymers.

3.4 Methodology

In order to simplify the existing degradation model, the equations for crystal growth are adapted for a new theory and fitted to the same experimental data as the original model to ensure a similar capability to model experimental trends. In order to fit experimental data, the adjustable parameters are manually adjusted to minimise the root-mean-square error. During the fitting, each parameter in the model is varied through the full range of their extreme values in order to understand their effect on the fitting. This helps to avoid a local minima because the quantitative minimisation of the root-mean-square error is supported by the qualitative analysis of the shape of the degradation curve by the human eye. Potential changes to its shape, which may be achieved through variation of the model parameters, can be identified through human intuition but evaluated quantitative through minimisation of the root-mean-square error.

In order to understand the effect of degradation by chain scission on Young's modulus of a polymer, atomic-scale simulations are conducted on an atomic model of amorphous polymer to which chain scissions are applied. Atomic structures for amorphous poly(lactide) contain a large number of atoms and therefore existing simulation techniques, including molecular dynamics and molecular statics, would require too great computation demands to analyse Young's modulus. A new simulation technique is developed in this thesis that translates the equations for interatomic potential energy directly from molecular dynamics to static linear finite element analysis. The reduction in computation demands of the new method enable amorphous poly(lactide) to be analysed. The interatomic potential equations are adapted in order to be suitable for linear analysis. A new computer program is written in this thesis to perform the finite element analysis and analyse the results. Chain scissions are applied to the model in order to analyse their effect on Young's modulus. The new understanding gained through this analysis is used to extend the mathematical degradation model to also consider Young's modulus degradation.

3.5 Work conducted in this thesis

This thesis consists of three parts. In the first part, background theory is discussed and the existing literature is reviewed. In the second part, previous mathematical models for bioresorbable polymer degradation are simplified and adapted in order to be used to further the current understanding of polymer degradation. In part three, the change of Young's modulus during polymer degradation is analysed and a mathematical model for Young's modulus degradation is presented.

Thesis part one:

Chapter 1 discusses the existing theory and models for bioresorbable polymers degradation. In **Chapter 2**, a review of experimental studies for the degradation of mechanical properties is conducted in order to determine an overall trend for the degradation of Young's modulus. In **Chapter 3**, the aims, objectives and methodology are presented.

Thesis part two:

In **Chapter 4**, a simple model for chain scissions in individual polymer chains is presented. The effects of the individual hydrolysis mechanisms, end scission and random scission, are investigated. The work in Chapters 5 – 7 of this thesis is founded on the existing mathematical degradation models of Pan and his co-workers [48-50]. The existing mathematical models for simultaneous degradation of molecular weight and increases in crystallinity are complicated. Therefore, a new simplified mathematical model is developed in **Chapter 5**. The small sections of amorphous polymer phase that lie in between the crystallites in a spherulite may have considerable different properties to a large volume of amorphous polymer outside of a spherulite, including the susceptibility to hydrolysis. Therefore, also in Chapter 5, the model is extended in order to further the current understanding of the spherulitic microstructure. The degradation of bioresorbable polymers is complicated due to the number of factors involved, which are not fully understood. To further the understanding, a new model is developed in **Chapters 6 and 7**, which can analyse the effect of the most important factors for degradation including:

- The effects of chain scissions occurring randomly throughout the polymer or predominantly at the ends of the polymer chains;
- The effects of autocatalytic degradation and noncatalytic degradation;
- The effect of initial molecular weight;
- And the effect of residual monomer, which catalyses the autocatalytic hydrolysis reaction.

Many researchers or polymer device designers do not want to conduct detailed mathematical modelling in order to interpret experimental data results. In order to make the benefits of model analysis more accessible to them, a simple qualitative method to interpret experimental data, based on parametric studies with the mathematical model, is presented in **Chapter 6**. This allows trends in degradation to be related to the

underlying hydrolysis mechanisms by simple visual inspection of experimental data plots. A large number of experimental data publications are reviewed using the qualitative analysis scheme in order to determine which hydrolysis mechanisms are most frequent. The effects of initial molecular weight and residual monomer have been studied in several experimental publications [8, 18, 23, 29-31, 87-89]. Neither factor is fully understood, nor have they been investigated by a theoretical degradation model. In **Chapter 7**, both factors are investigated using the mathematical model developed in Chapter 6.

Thesis part three:

In **Chapter 8** of this thesis, a new atomic finite element analysis technique is developed, in which nonlinear interatomic potential energy functions are translated into linear functions. This allows static linear analysis simulations to be conducted, which offer a significant reduction in computational demands over the simulation techniques that have previously been used to analyse biodegradable polymers. The simulation technique can use existing MD coordinate input files and force fields. Linear elastic finite elements are derived to represent all atomic interactions included in the molecular dynamics force field PLAFF2 [85], which was developed specifically for poly(lactide). The low computational demands of the new simulation method allow for numerous simulations of large amorphous poly(lactide) structures, in which chain scissions are applied to represent hydrolytic degradation. In **Chapter 9**, these simulations are conducted to further the understanding of the effects of chain scission, during hydrolytic biodegradation, on mechanical properties. The atomic simulations model the overall reduction of Young's modulus in a polymer due to chain scission. Also, the local atomic-scale effect of chain scission on Young's modulus is analysed in order to further the existing understanding of the effects of chain scission on mechanical properties degradation. This new theoretical understanding is then used to develop a model for Young's modulus degradation in biodegradable polymers in **Chapter 10**. This model is combined with the simplified mathematical model developed in Chapter 5 to give a complete overall degradation model for simultaneous molecular weight, crystallinity and Young's modulus. **Chapter 11** discusses the overall achievements of this thesis and **Chapter 12** presents conclusions and recommended future work.

Part 2: Simplification, modification and application of previous models for polymer degradation

In part 2 of this thesis, models for the degradation of molecular weight and for changes to crystallinity are presented. The existing mathematical degradation models of Pan and his co-workers [48-50] are simplified in order to be easier to implement. They are also extended to enable the detailed analysis of important factors that affect degradation including random / end scission, autocatalytic / noncatalytic hydrolysis, initial molecular weight and residual monomer content. These models enable the degradation of biodegradable polymers to be modelled and further understood, which is necessary for biodegradable polymer fixation devices to be optimised for specific applications or specific patients. In the future this may lead to faster or more complete patient recovery.

Chapter 4: Computer Simulation of Polymer Chain Scission in Biodegradable Polymers

In this chapter, a simple simulation tool for chain scission in biodegradable polymers is presented. It is used to simulate a finite number of chains and apply chain scissions to these chains to represent degradation. Such a model is useful to further the understanding of how biodegradable polymers degrade. Ultimately this and future work will lead to more appropriate polymers being used for fixation devices, which support the healing process of broken bones. These polymers are tailored to degrade at the optimal rate for the specific patient. The effects of random scission and end scission on degradation are considered in terms of number average molecular weight, weight average molecular weight and the production of small water-soluble chains. The simulation tool, which is Excel-based, is available as supplementary information with this thesis. This chapter has been published in the Journal of Biotechnology & Biomaterials [90].

4.1 Introduction

In experimental studies in the literature, the values of number average and weight average molecular weight are often used to measure the degradation of bioresorbable polymers. As discussed in Chapter 1, Gel Permeation Chromatography (GPC) is used to measure molecular weight, but chains below a threshold length may to too small to be identified by GPC. Hence, those small chains should also be excluded from the calculation of molecular weight. Many mathematical models in the literature can only calculate number average molecular weight because the overall polymer is considered rather than individual chains. In this chapter, a more computationally demanding model is developed which considers all polymer chains individually. Similar models have been developed before, including one from the group at the University of Leicester [60], but the necessary complexity of the models may prevent researchers and polymer device designers who have little modelling experience from using the models. To reduce complexity and computational demands, the simulations in this chapter are simplified to focus on random and end scission. The model does not consider diffusion, crystallinity, or time-based reaction rates. Also, to make the model more accessible to non-experts, Excel 2010 is used to develop the simulation tool, which can model chain scission of individual polymer chains. Excel contains functionality to include user-written programs

in the Visual Basic programming language. The information about the polymer chains is stored in the cells of an Excel spreadsheet in the simulation tool. Graphs are plotted based on this information. The numerical simulations of chain scission are conducted using arrays in the Visual Basic environment within Excel, which enables great computational benefits over continuously interacting with the cells of the spreadsheet for each simulated chain scission. In the simulation tool, the lengths of all polymer chains are known by the model. In order to replicate GPC measurements, polymer chains below a threshold length may be excluded from the calculation of molecular weight in the simulation tool. The simulation tool is demonstrated through four case studies, which analyse the effect of random scission and end scission on molecular weight degradation and the production rate of water-soluble small chains. The molecular weight distribution of poly(D-lactide) during degradation is compared to experimental GPC measurements.

4.2 Details of the computer simulation scheme

A simulation tool is developed in the form of a Microsoft Excel 2010 spreadsheet, which is available upon request from the author. A list of initial polymer chain lengths are manually entered into a column of the Excel spreadsheet. Each row contains a number, which represents the length of an individual polymer chain. Macros use the visual basic programming language within Excel to simulate end scission and random scission of polymer chains.

The random scission scheme contains the following steps:

1. Randomly select a bond from the total number available.
2. Determine which chain contains the selected bond.
3. Determine the length of the two chains that are produced when the original chain is cleaved at the selected bond.
4. Replace the number that represents the original chain length with a number that represents one of the new chains' lengths.
5. Add a number that represents the length of the other new chain to the list of chains.

The end scission scheme is as follows:

1. Randomly select a chain from the total number of chains containing at least 1 bond.
2. Reduce the number that represents the original chain length by 1.

3. Add a new chain to the bottom of the list of chains with a length of 1.

The combined random scission and end scission scheme is as follows:

1. Randomly select whether to perform a random scission or end scission. The probability of selecting each scission type is weighted proportionally to the fraction of forthcoming scissions that are of that type.
2. Run the end scission or random scission scheme.
3. Update the number of scissions and repeat steps 1 to 2 until all scissions are performed.

The simulation tool sets a limit of 10000 chains in order to ensure fast performance, although this number can be increased with simple modifications. The same set of initial chain lengths can be used for multiple simulations in order to determine the average effect of random or end scissions. The number averaged molecular weight, M_n (g mol^{-1}), weight averaged molecular weight, M_w (g mol^{-1}), and polydispersity index, PDI, of the polymer chains are calculated by the simulation tool according to Eqs. 4.1 and 4.2. M_n is calculated as the total weight of all chains divided by the number of chains according to

$$M_n = \frac{N_{total} M_0}{n_t} \tag{4.1}$$

where N_{total} is the sum of polymer units in all chains, M_0 is the molar mass (g mol^{-1}) and n_t is the total number of chains. M_w is the sum for all chains of molar mass multiplied by chain length, N_i, and the probability of a polymer unit lying in that chain, N_i/N_{total}, as given by

$$M_w = \sum_{i=1}^{i=n_t} \frac{N_i^2}{N_{total}} M_0 \ . \tag{4.2}$$

The molecular weights are also calculated excluding water-soluble chains because they may be too small to be measured by GPC or may diffuse from the polymer. The maximum length of water-soluble chains is manually chosen. N_{total} becomes the total number of polymer units of water-insoluble chains, n_t becomes the number of water-insoluble chains, and the summation in Eq. 4.2 considers only water-insoluble chains. The threshold length, below which the polymer chains become too small for GPC to

measure, can be varied. If the small chains are considered to be water-soluble, the sum of all of the small water-soluble chains can give an indication of the possible mass loss, which may result from the diffusion of these water-soluble chains out of the polymer. The simulation tool plots graphs of molecular weight distribution and chain-length distribution as demonstrated in case study 1. The fraction of the total polymer units that are contained within chains of a given length-range is plotted on the molecular weight distribution graph. The ranges are chosen to have equal widths on a log scale, 10 divisions per order of magnitude. The number of chains within a given length-range is plotted on the chain length distribution graph, which is useful for analysis of low molecular weight chains. All calculations are visible in the simulation tool spreadsheet.

4.3 Case studies

4.3.1 Case study 1: initial test of molecular weight distribution

The simulation tool is used to produce a typical random poly(lactide) polymer of M_w=522000 g mol^{-1}, M_n=256000 g mol^{-1} and PDI=M_w/M_n=2.02 by performing 9999 random scissions on a single chain of 35.5x10^6 ester units with M_0 = 72 g mol^{-1}. The molecular weight distribution is shown in Fig. 4.1 (a) and the chain length distribution is shown in Fig. 4.1 (b). The peak of each curve is approximately 513000 and 257000 g mol^{-1}, which is in good agreement with the calculated values of M_w = 515000 and M_n = 256000 g mol^{-1}. Due to the random nature of the simulation, the results vary each time they are calculated but PDI is always ≈2.

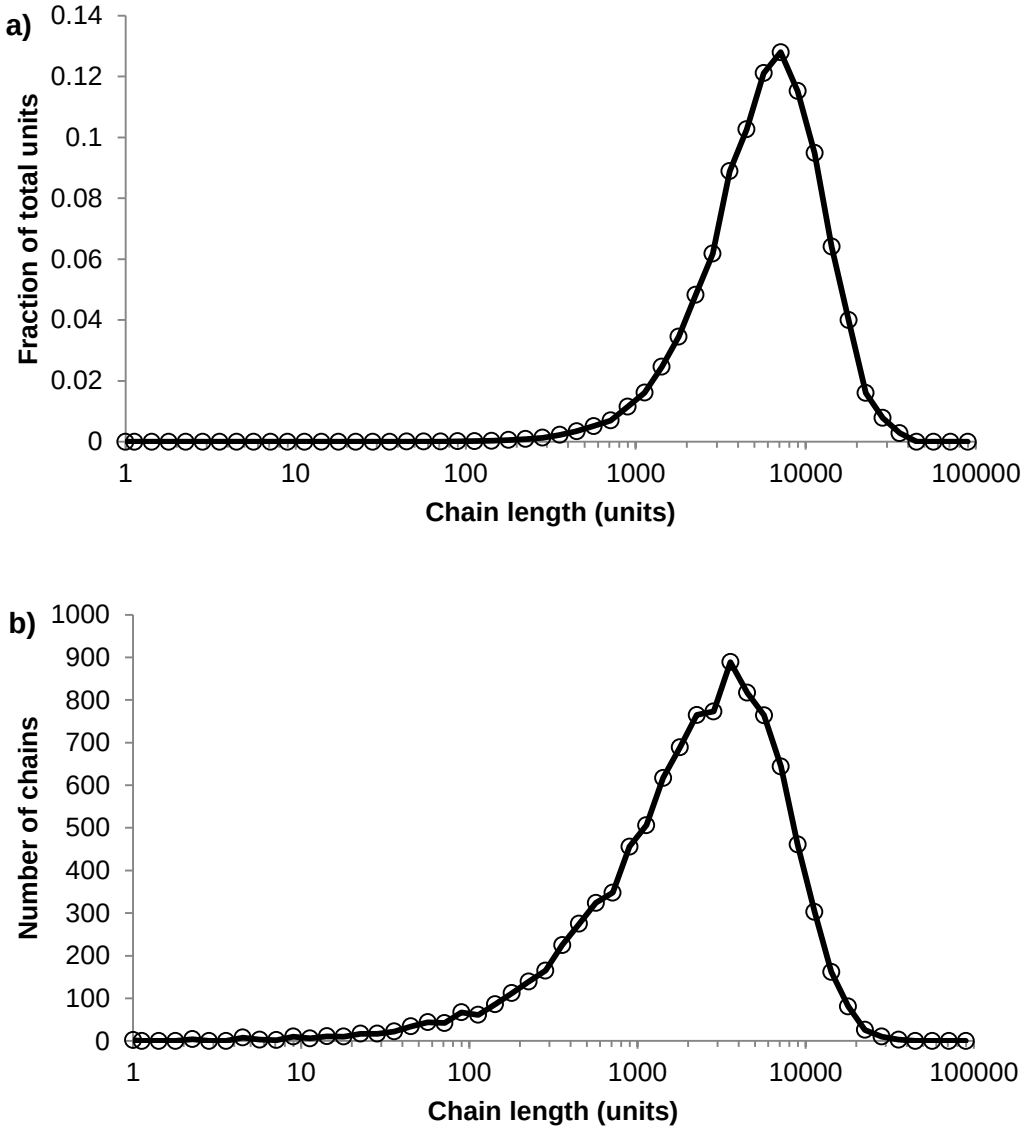

Fig. 4.1 Molecular weight distribution (a) and chain length distribution (b) for the random polymer chain distribution generated in case study 1.

4.3.2 Case study 2: the effect of random and end scission

The effect of end scission and random scission on the reduction of average molecular weight is tested for three polymers with molecular weights M_n ≈ 40000, 120000 and 360000 g mol^{-1} and PDI ≈ 2. The different polymers are simulated by performing 99 random scissions on initial chains of 55556, 166667 or 500000 units. Chains containing less than 12 units are considered to be water-soluble [44] and are not included in the calculation of molecular weight. The results for M_n reduction and M_w reduction are given in Table 4.1 and Table 4.2 respectively. Each value is the average of 250 simulations. The average initial average molecular weights are slightly higher than the nominal values due to some of the initial 99 scissions leading to water-soluble chains.

The visual basic macro that is used to produce the results is included in the simulation tool. It can be seen that end scissions do not reduce average molecular weight and can in fact cause it to increase due to low molecular weight chains being shortened below the solubility limit, as shown in Fig. 4.2. In contrast, even a small number of random scissions cause a reduction in M_n and M_w. It has been reported that end scission may occur 100 times more frequently than random scission in poly(lactide) [46], in which case the results here indicate the degradation of average molecular weight is due to random scission as opposed to end scission. It should be noted that for a very narrow molecular weight distribution, the effect of end scission is that M_n reduces at the same rate as the monomer weight fraction increases in the polymer. If the water-soluble chains are included in the calculations for average molecular weight, the results are generally unaffected for M_w; for M_n degradation due to random scission the results are also unaffected, whereas end scission simulation results for M_n become identical to random scission.

Polymer initial M_n (g mol^{-1})	Reduction in M_n due to:					
	50 end scissions	500 end scissions	5000 end scissions	5 random scissions	50 random scissions	500 random scissions
40506	0%	0%	0%	5%	33%	82%
120509	0%	0%	0%	5%	33%	83%
360483	0%	0%	0%	5%	33%	83%

Table 4.1 Reduction in M_n due to end scission and random scission in case study 2

Polymer initial M_w (g mol^{-1})	Reduction in M_w due to:					
	50 end scissions	500 end scissions	5000 end scissions	5 random scissions	50 random scissions	500 random scissions
78905	0%	0%	1%	4%	33%	83%
237943	0%	-1%	-1%	5%	33%	83%
714741	-1%	0%	0%	5%	33%	83%

Table 4.2 Reduction in M_w due to end scission and random scission in case study 2. A negative number indicates an increase in M_w.

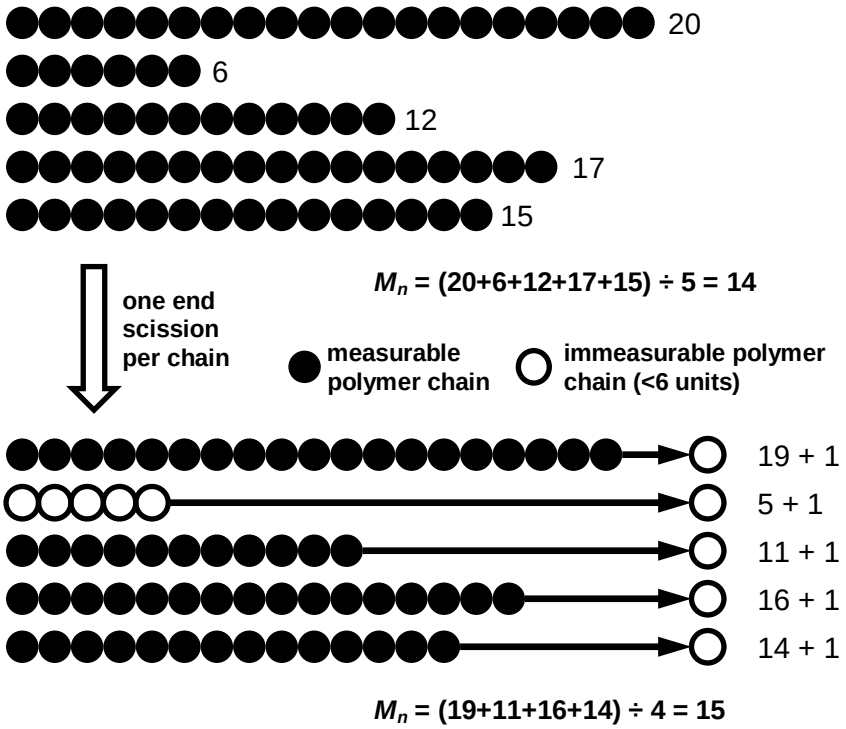

Fig. 4.2 Demonstration of end scission on five polymer chains without causing a reduction in average molecular weight. Initial chain lengths are 6, 12, 15, 17 and 20 polymer units. Molecular weight reduces due to the reduction in length of longer chains but increases as short chains become too small to be detected by GPC. In this example chains of less than 6 units are considered too short to be measured by GPC.

4.3.3 Case study 3: prediction of the water-soluble fraction of degrading polymers

The simulation tool is able to calculate the fraction of the polymer that is water-soluble, which is equivalent to maximum possible mass loss due to the diffusion of water-soluble chains. The simulation tool is used 1) to determine the rate at which the fraction of waters-soluble chains increases, and 2) to identify at what molecular weight the water-soluble chains account for 5% of total polymer mass (5 wt.%) in a degrading polymer. Simulations are run for random scission and end scission of a random initial polymer chain distribution, which is generated by 99 random scissions of an initial chain containing 150000 units. The reported maximum length of water-soluble chains varies in the literature [1, 43, 44, 91, 92], and hence this study considers values of 7, 11 or 15 polymer units. The average initial values of molecular weight are $M_n \approx 109000$ and $M_w \approx 214000$ g mol^{-1}. For end scission, there is virtually no change in molecular weight when the polymer is degraded to the extent that water-soluble chains account for 5% of total mass. This is due to the phenomenon previously explained in Fig. 4.2. Mass loss is therefore possible without any apparent degradation of M_n if end scission

occurs. For random scission however, Fig. 4.3 shows that in order to achieve 5 wt.% water-soluble chains, the average molecular weight reduces to approximately 2100, 3100 or 4200 g mol^{-1} for M_n, and 3200, 4800 or 6500 g mol^{-1} for M_w, when the solubility limit is considered to be 8, 12 or 16 units respectively. The relationship between the solubility limit and the average molecular weight at which 5 wt.% of water-soluble chains are achieved is linear for random scission as can be seen in Fig. 4.3. Each data point is the average of 100 simulations.

The simulations were also run for a polymer of monodisperse distribution, which consisted of 100 chains each containing 1500 units. For random scission, the results are almost identical to those for an initial random distribution because average molecular weight reduces to such an extent that the initial distribution has little or no effect. The magnitude of initial M_n and M_w also has negligible effect for random scission. For end scission, a monodisperse initial distribution results in a molecular weight reduction of 5% in order to generate 5 wt.% soluble chains.

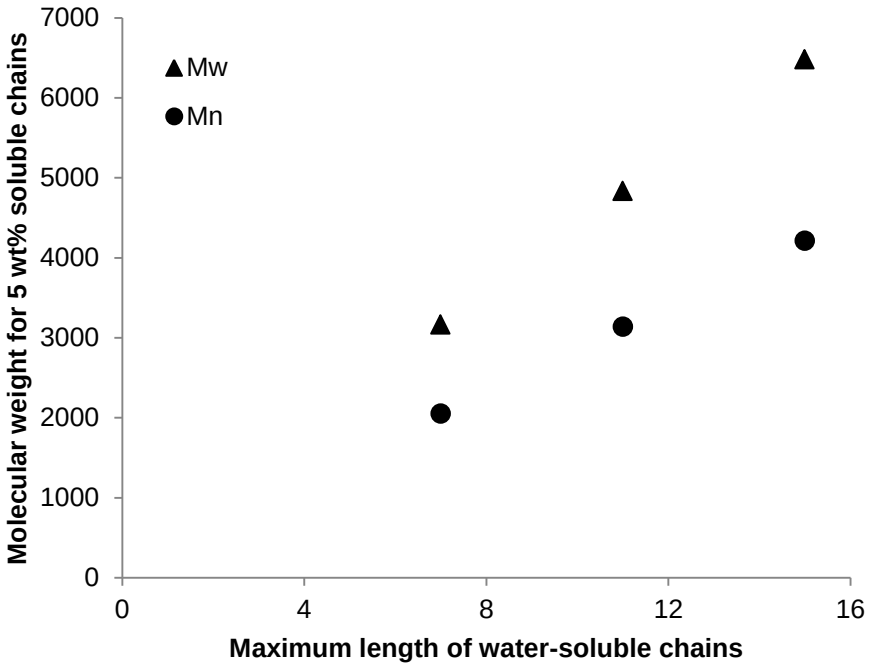

Fig. 4.3 Molecular weight of polymers after degradation by random scission to generate 5 wt.% water-soluble chains in case study 3. The maximum length of water-soluble chains is set to 7, 11 or 15 units.

The rates of production of water-soluble chains for random scission and end scission are shown in Fig. 4.4. The same random initial polymer chain distribution is used as before (150000 polymer units in 100 random chains) and the curves are the average of 100 simulations. For end scission, the soluble fraction increases linearly and is not

sensitive to the solubility limit because monomers are always considered to be soluble. The effect of reducing chains beneath the solubility limit is negligible compared to the production of monomers. In contrast, random scission is sensitive to the solubility limit and the rate of production of water-soluble chains accelerates as the number of random scissions increases. In degradation experiments, there is often an initial delay followed by a sudden onset of mass loss. This may be due to soluble chains being unable to diffuse out of the polymer until the polymer is significantly degraded. Alternatively, for the relationships between soluble weight fraction and chain scission found in Fig. 4.4, a delay then sudden mass loss may be achieved if autocatalytic degradation causes the rate of chain scission to increase significantly during degradation. For noncatalytic hydrolysis, where the rate of chain scission may be constant, the production of the water soluble polymer chains does not increase suddenly during degradation and therefore sudden mass loss is consistent with autocatalytic hydrolysis.

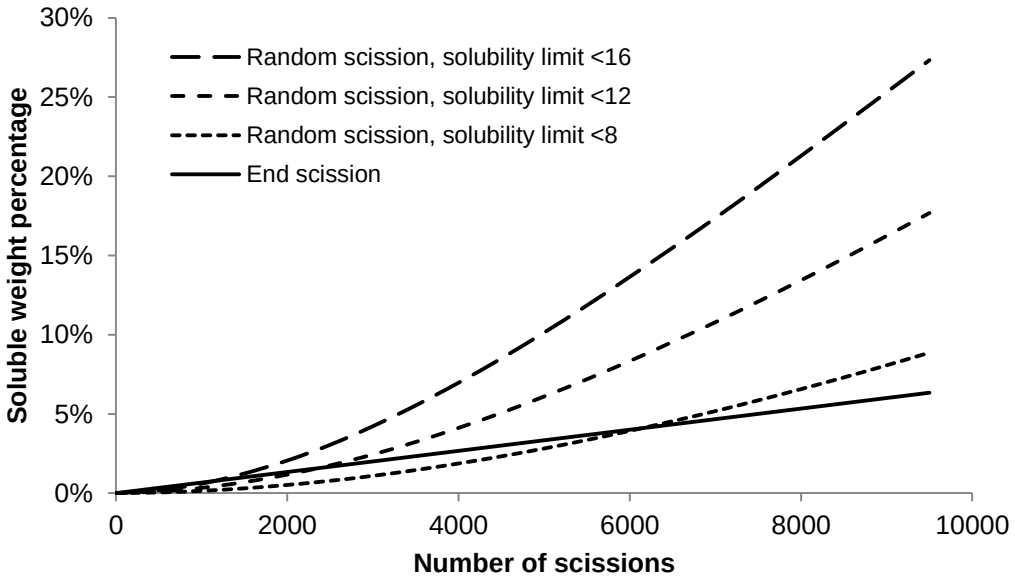

Fig. 4.4 Production of water-soluble weight percentage versus number of scissions for random scission and end scission. Three different solubility limits are considered for random scission: <16 units (long dash); <12 units (medium dash); <8 units (short dash).

4.3.4 Case study 4: comparison of molecular weight distribution to experimental data

The simulation tool can be used to model the changes to molecular weight distribution for a polymer during degradation. Tsuji [2] measured the molecular weight distribution of poly(D-lactide) films during hydrolysis in phosphate buffer solution (pH 7.4) at 37°C. Measurements were taken after 0, 8, 16 and 24 months in the degradation solution. The initial molecular weight distribution used in the simulation tool was derived from the experimental data at time = 0. It consisted of 425 polymer chains. The best fitting of simulated molecular weight distributions to the experimental data was achieved by performing 800, 1750 and 5300 random scissions in the time periods 0-8, 8-16 and 16-24 months respectively. The increase in scission rate supports the theory of autocatalysis [40]. The simulated and experimental distributions are shown in Fig. 4.5. Each curve is the average of 200 simulations. The molecular weight distributions generated by the simulation tool are similar to the distributions measured by GPC, which suggests that molecular weight degradation is due to random scission. After 24 months, the simulated and experimental curves begin to diverge because the polydispersity of the samples increases, which cannot be accounted for by random scission. Although an increase in polydispersity could be achieved by a simple combination of random scission and end scission, the resulting molecular weight distribution includes a sharp peak at a molecular weight of 72 g mol^{-1}; therefore the fitting between simulated and experimental curves is not improved, and in any case, it is likely that the monomers are too small to be detected by GPC. In order to achieve a better fitting to the 24 month experimental data, a wider distribution of chains is required than can be achieved by random and/or end scission. The distribution cannot be achieved by noncatalytic or autocatalytic hydrolysis. It is necessary to generate a greater fraction of long and short chains versus average-length chains. This may be possible if chain scission occurs either (i) preferentially towards the end of chains, but not only in the final bond, or (ii) preferentially in shorter chains.

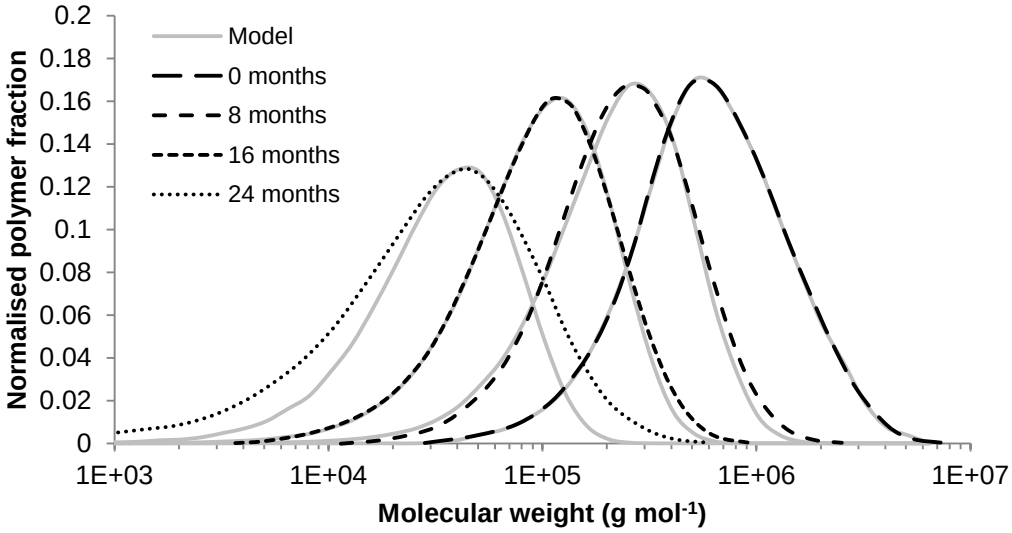

Fig. 4.5 Molecular weight distribution of experimental data [2] (black lines) and the model (grey lines) after degradation of poly(D-lactide) for various times: 0 months (long dash); 8 months (medium dash); 16 months (short dash); and 24 months (dotted).

4.4 Conclusions

A simulation tool was developed, which can be used to simulate end scission and random scission for a manually entered distribution of initial polymer chains. Case studies demonstrated the use of the simulation tool. It is possible to generate a random initial distribution of chain lengths with PDI ≈ 2. The case studies also generated interesting findings about the effect of random scission and end scission. Random scission has over 1000 times more impact than end scission on the reduction of M_n and M_w. However, for 5 wt.% mass loss to be attributed to the diffusion of water-soluble small chains, produced as a result of random scission, M_n must reduce to <5000 g mol^{-1}. This value of M_n reduces as the assumed solubility limit of small chains reduces. In contrast, end scission may produce 5 wt.% soluble chains with no reduction of M_n. The fraction of water-soluble small chains increases linearly with the number of end scissions but increases acceleratedly with random scissions. Simulated distributions of molecular weight, due to random scission, achieve a good fitting to experimental molecular weight distributions during hydrolysis of poly(D-lactide) for up to 18 months of degradation. The simulation tool is freely available upon request from the author and can be simply modified if desired.

4.5 Supplementary information

The simulation tool is available upon request from the author. A preview of the spreadsheet is shown in Fig. 4.6. The user must enable the macros when prompted upon first opening the spreadsheet. The macros that are used to simulate random scission, end scission, and produce the results for case studies 2-3 can be analysed and edited freely.

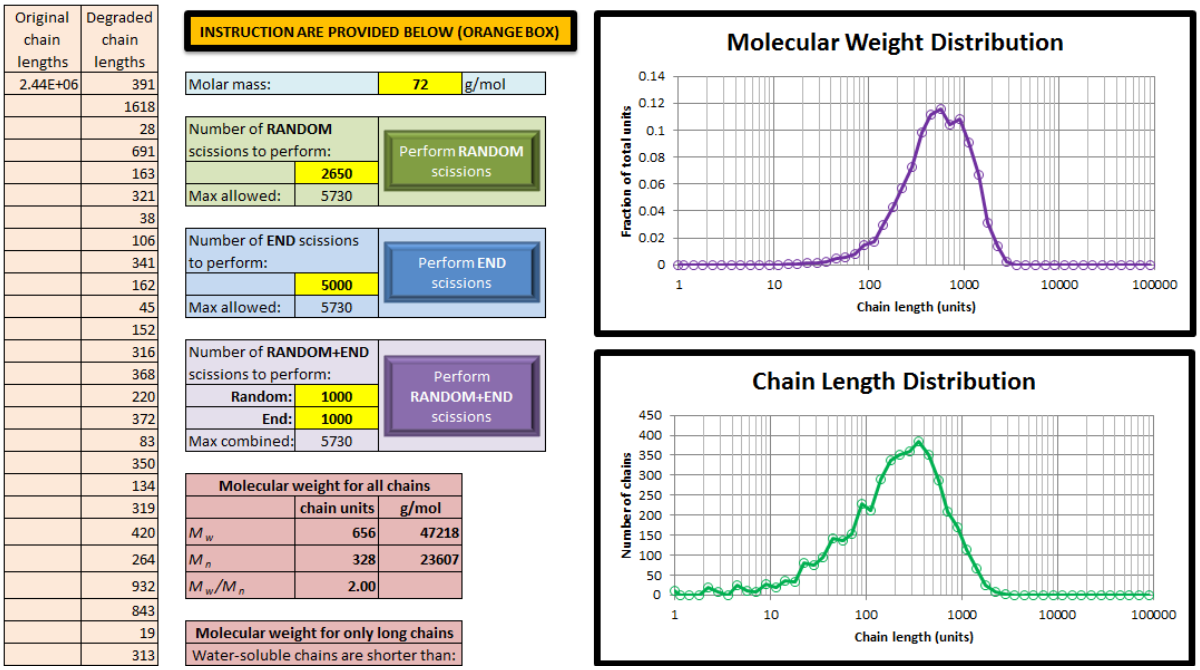

Fig. 4.6 The simulation tool that is available from the author upon request.

Chapter 5: A simplified theory of crystallisation induced by polymer chain scissions

The mathematical model that was previously developed in the group at Leicester [48, 49], to model molecular weight and crystallinity during degradation, involved integrational terms and is relatively complicated for non-experts to use. The majority of work in this thesis aims to extend the previous models to include mechanical properties. Therefore it is useful to simplify the model where possible. In this chapter, the model is simplified and demonstrated to be able to achieve an equally good fit to experimental data. The model is also extended to include consideration of the different polymer phases that exist as a result of the spherulite microstructure in poly(lactides). This chapter has been published in Polymer Degradation and Stability [47].

5.1 Introduction

Bioresorbable polymers have been the subject of extensive experimental testing, giving details on average molecular weight, crystallinity and mechanical properties as functions of time. A clear degradation pathway has been established [2, 5-10, 17, 58, 69]. The chain scissions provide the polymer chains with extra mobility so that they crystallise, leading to a gradual and significant increase in the degree of crystallinity. It is very important to be able to predict how crystallinity changes during the degradation process because crystallinity affects both the degradation rate and mechanical properties of the devices [5, 57, 58]. Pan and his co-workers summarised the existing experimental observations and understanding into a set of mathematical models for polymer degradation [48-50]. In particular, they developed a theory for chain-scission induced crystallisation [48, 49] by extending the classical Avrami theory [93-95]. Their theory considers time-depended nucleation and growth of crystallites due to chain scission. Therefore it involves both differential and integrational equations, which are difficult to implement. The objective of this chapter is to show that the theory can be greatly simplified if the crystals are considered to nucleate and grow instantly to a finite size. This reflects an assumption that crystal growth occurs at a significantly faster rate than chain scission. The integration equation is eliminated and the number of material parameters in the theory is reduced. Furthermore it is shown that the spherulite structure widely observed in semicrystalline bioresorbable polymers can be taken into

account in the theory. This is achieved by considering polymer phases inside and outside spherulites to have different properties.

5.2 A simplified theory for crystallisation induced by polymer chain scission

In the model developed by Han and Pan [48, 49], the rate of polymer chain scission due to hydrolysis reaction is given by

$$\frac{dR_s}{dt} = k_1 C_e + k_2 C_e \left(\frac{R_{ol}}{1 - X_c} \right)^{0.5} \tag{5.1}$$

in which R_s (mol m^{-3}) is the molar number of scissions per unit volume, k_1 (day^{-1}) and k_2 ([mol^{-1}m^3]$^{0.5}$day^{-1}) are the reaction constants for the noncatalytic and autocatalytic hydrolysis reactions respectively, C_e (mol m^{-3}) is the molar concentration of ester bonds in the amorphous polyester chains, and X_c is the degree of crystallinity (volume fraction). Water is assumed to be abundant hence its concentration does not appear in the rate equation. The polymer chains have a distribution in length. In order to make the model traceable, Wang and Pan [50] made a key simplification in their original model – the polymers chains are divided into two groups: long polymer chains that are water insoluble and cannot diffuse, and short chains, referred to as oligomers, that are water-soluble and can diffuse. In the degradation model, this distinction is important because the oligomers can diffuse away to reduce the local acidity and reduce the degradation rate. On the other hand the actual distribution of the chain length does not have a major effect on the degradation rate. If a chain scission occurs near either end of the chain, then an oligomer is produced. The molar number of ester bonds in oligomers per unit volume, R_{ol} (mol m^{-3}), is calculated based on the concentration of scissions according to the following empirical relation [12,13]:

$$\frac{R_{ol}}{C_{e0}} = \alpha \left(\frac{R_s}{C_{e0}} \right)^{\beta} \tag{5.2}$$

in which α and β are empirical parameters (no units) and C_{e0} (mol m^{-3}) is the initial concentration of ester bonds in the overall polymer. The values of α and β can be adjusted to reflect the probability of scissions creating oligomers, thereby allowing the model to be suitable for degradation ranging from end scission to random scission. For

crystallisation, Han and Pan [48, 49] assume that each chain scission has a probability of nucleating a crystal, which gradually grows to a maximum size. Because crystals are nucleated at different times of the degradation process, the current degree of crystallinity is history dependent, and thus an integrational equation over time is required. In fact the individual crystals are all nano-sized [52] and the time taken to form these crystals are much shorter than the typical time taken by the hydrolysis reaction. In the current chapter, it is assumed that each chain scission has a probability, p_x (no units), of nucleating a crystal, which immediately grows to a finite volume of V_c (m^3). The extended degree of crystallinity, X_{ext} (volume fraction), which assumes the crystals do not impinge on each other, is then given by

$$X_{ext} = p_x \eta_A R_s V_c \tag{5.3}$$

in which η_A is Avogadro's constant (mol^{-1}). Following the Avrami theory [93-95], it is assumed that the actual and extended degrees of crystallinity are related by

$$\frac{dX_c}{dX_{ext}} = X_{\max} - X_c \tag{5.4}$$

in which the maximum degree of crystallinity, X_{max} (volume fraction), has been introduced as a model parameter. Finally following Han and Pan [48, 49] the consumption of amorphous polymer chains by the oligomer production and crystallisation leads to

$$\frac{dC_e}{dt} = -\frac{dR_{ol}}{dt} - \frac{\omega dX_c}{dt} \tag{5.5}$$

in which ω is the inverse molar volume (mol m^{-3}) of the crystalline phase. The number-averaged molecular weight (g mol^{-1}) is given by

$$M_n = \frac{(C_e + \omega X_c) M_0}{N_{chains0} + (R_s - (R_{ol}/m))} \tag{5.6}$$

in which $N_{chains0}$ (mol m^{-3}) is the initial molar concentration of the polymer chains, M_0 (g mol^{-1}) is the molar mass of a lactic acid unit and m (no units) is the average number of

repeating units of the oligomers. The term on the top of Eq. 5.6 is the total weight of the crystalline and amorphous phases in the calculation unit excluding oligomers due to the assumption that oligomers are too small to be measured experimentally. The term on the bottom is the total number of polymer chains excluding oligomers, in which $(R_s - (R_{ol}/m))$ is the number of new chains produced by chain scission excluding oligomers. Eqs. 5.1 to 5.6 completely define the simplified model for simultaneous degradation and crystallisation of polyesters. Here the oligomer diffusion is ignored in order for us to focus on the new elements of the crystallisation theory. The diffusion equation used by Pan and co-workers [48-50] can be readily added to the above equations to accommodate oligomer diffusion.

The original model by Han and Pan [48, 49] is described in Eq. 5.7 to 5.9. The changing rate of molar concentration of nucleation sites, N (mol m^{-3}), is calculated as

$$dN = -\xi N dt - \frac{N}{1-X_c} dX_c + p_x dR_s \qquad 5.7$$

The extended degree of crystallinity is given by

$$X_{ext} = \int_0^t \alpha_0 r_{\max}^3 \left(1 - e^{\frac{G}{r_{\max}}(t-\tau)}\right)^3 \xi N(\tau) \eta_A d\tau \qquad 5.8$$

in which crystal growth is integrated from the time since their nucleation, τ (day), to the current time t (day). The model parameters ξ (day^{-1}), λ (no units), α_0 (no units), r_{max} (m) and G (m day^{-1}) have been removed in the simplified theory. The actual and extended degrees of crystallinity are related by

$$\frac{dX_c}{dX_{ext}} = \left[\left(1 - \frac{R_{ol}}{C_{e0}}\right) - X_c\right]^{\lambda} \qquad 5.9$$

A minor correction is made in Eq. 5.9 to that used by Han and Pan to ensure mass conservation.

5.3 Validation of the theory using data obtained by Weir et al. [6, 7]

Weir et al. [6, 7] carried out a set of degradation experiments for poly(L-lactide) (PLLA) in phosphate buffer solution (PBS) with pH 7.4 at three temperatures: 37°C, 50°C and 70°C. Compression-moulded samples of 0.8mm in thickness were used. Measurements of average molecular weights, mass loss, crystallinity, and thermal and mechanical properties were taken at various follow-up times during degradation. Weir et al. [6, 7] found that their molecular weight data can be fitted to a hydrolysis model using a single activation energy despite testing at temperatures on both sides of the glass transition temperature. This was later confirmed by Han et al. [49] who fitted their model to the molecular weight and crystallinity data. Following Han et al. [49], the work in this thesis assumes the parameters given in Eq. 5.10 to be temperature dependent according to Arrhenius relation:

$$k_1 = k_{10}e^{-\frac{E_{k_1}}{RT}} \quad k_2 = k_{20}e^{-\frac{E_{k_2}}{RT}} \quad G = G_0 e^{-\frac{E_G}{RT}} \quad \xi = \xi_0 e^{-\frac{E_\xi}{RT}} \quad X_{\max} = X_{\max 0} e^{-\frac{E_{X\max}}{RT}} \tag{5.10}$$

in which k_{10} (day^{-1}), k_{20} ([mol^{-1}m^3]$^{0.5}$day^{-1}), G_0 (m day^{-1}), ξ_0 (day^{-1}) and X_{max0} (no units) are pre-exponential constants, E_{k1}, E_{k2}, E_G, E_ξ and E_{Xmax} (all kJ mol^{-1}) are the corresponding activation energies, R (kJ K^{-1}mol^{-1}) is the gas constant and T (K) is the absolute temperature.

In order to quantitatively indicate how well a model can fit the experimental data, a root mean square error is used in the following discussion, which is defined in Eq. 5.11 as

$$\mathrm{RMSE} = \sqrt{\frac{\sum (x_i - y_i)^2}{n_d}} \tag{5.11}$$

where x_i are the calculated values from the model, y_i are the measured values and n_d is the number of data points.

Fig. 5.1 shows the best fit between the models and the experimental data obtained by Weir et al. [6, 7]. The solid lines represent the simplified theory, the dashed lines represent the original theory and the discrete symbols represent the experimental data. It can be observed from Fig. 5.1 that the simplified theory works with similar accuracy to that of the original one. For the degree of crystallinity, *RMSE* = 0.0425 for both theories. For the normalised molecular weight, *RMSE* = 0.0678 and 0.0688 for the original and simplified theories respectively. The initial conditions for the numerical

calculations are $X_c = X_{c0}$; $C_e = C_{e0}\left(1 - X_{c0}\right)$; and X_{ext}, R_s, R_{ol}, t, N = 0. The model parameters used in the fitting are provided in Table 5.1. X_{c0}, $N_{chains0}$, C_{e0} and M_0 are all initial properties of the polymer before degradation, which are taken from Weir et al. [6, 7]. The inverse molar volume of the crystalline phase, ω, is taken as the same as that of the amorphous phase. V_c is the volume of a polymer crystal, which was estimated from the literature [52]; for simplicity, V_c is taken to equal $\alpha_0 * r_{max}^3$ from the original model. The values of $\alpha = 28$ and $\beta = 2$ represent a probability of scissions producing oligomers when the polymer degradation is assumed to occur by random scission [49]. m is the average degree of polymerisation of the oligomers, which is taken as 4 since it is generally believed that short chains with less than 8 degree of polymerisation become water-soluble and mobile [96]. The best fit is achieved by setting the activation energies such that noncatalytic degradation is more dominant at high temperatures and autocatalytic degradation is more dominant at low temperatures. This is supported by existing experimental data [14, 41], in which hollow specimens resulted from degradation at 37°C but not at 60°C. The zero activation energy for G and very large value of G_0 in the original theory reflect that crystals grow very fast growth, which reassures the validity of the simplified model.

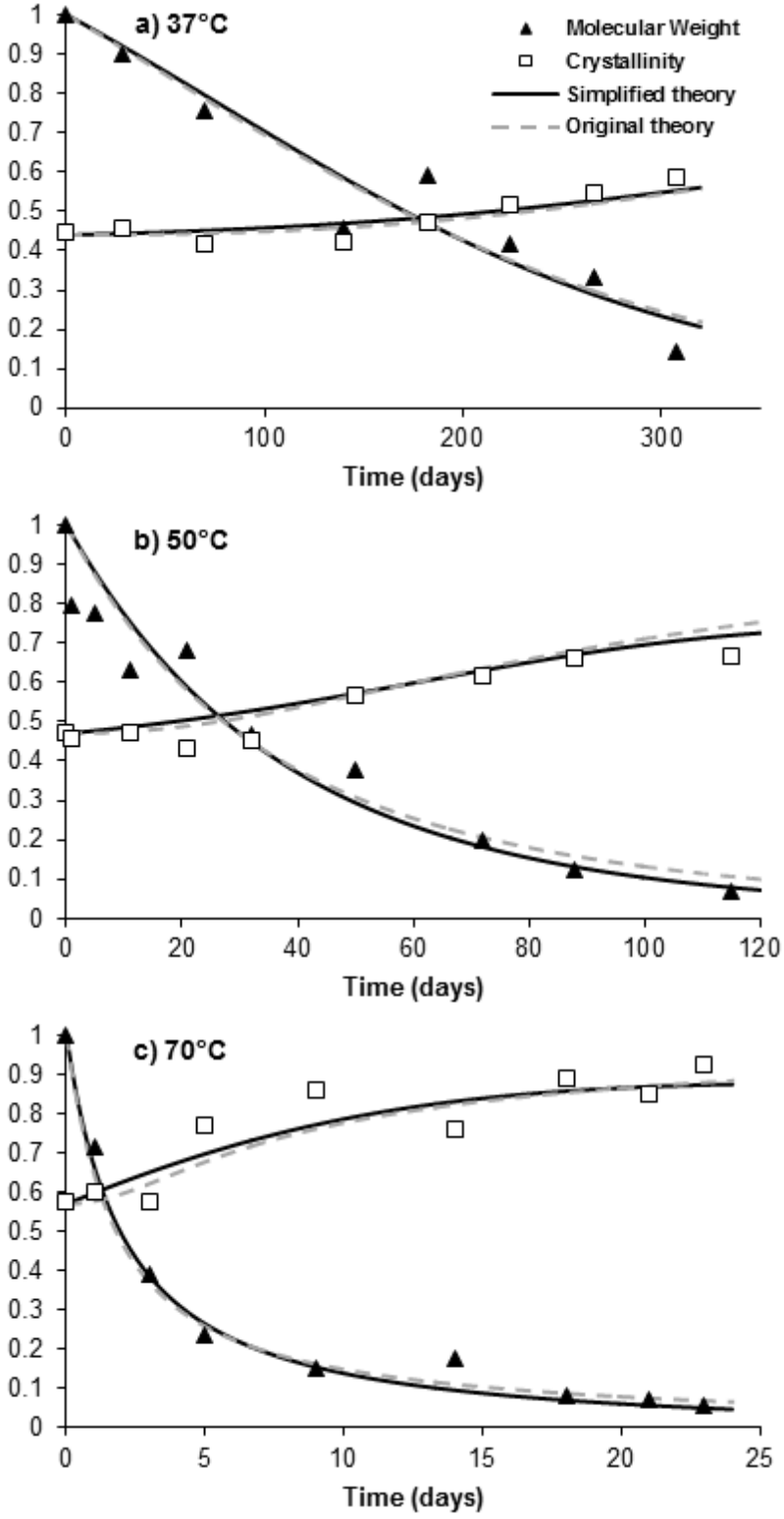

Fig. 5.1 Normalised number-average molecular weight and crystallinity as a function of hydrolysis time. Experimental data points [6, 7] (discrete symbols) are plotted for three temperatures: a)37°C, b)50°C and c)70°C. Simplified and original models are shown as solid and dashed lines respectively.

Parameters that did not vary between the models:								
T (°C)	X_{c0}	$N_{chains0}$ (mol m^{-3})	C_{e0} (mol m^{-3})	M_0 (g mol^{-1})	ω (mol m^{-3})	α	β	m
37	0.448	7.85	17300	72	$=C_{e0}$	28	2	4
50	0.470	7.50						
70	0.575	7.50						

Parameters that varied between the models:			
		Original model	Simplified model
λ		3	---
α_0		4π/3	---
r_{max}	(nm)	10	---
p_x		1	0.01
E_G	(kJ mol^{-1})	0	---
E_ξ	(kJ mol^{-1})	130	---
E_{k1}	(kJ mol^{-1})	145	145
E_{k2}	(kJ mol^{-1})	65	75
E_{Xmax}	(kJ mol^{-1})	---	7.5
G_0	(m day^{-1})	1.0×10^{100}	---
ξ_0	(day^{-1})	1.1×10^{18}	---
k_{10}	(day^{-1})	6.5×10^{18}	6.0×10^{18}
k_{20}	($[mol^{-1}m^3]^{0.5}day^{-1}$)	1.3×10^{6}	7.0×10^{7}
X_{max0}		---	12.2
V_c	(nm^3)	---	4.19×10^{3}

Table 5.1 Model parameters that are used to fit the experimental data. Values are the same for the simplified and original model unless otherwise stated

5.4 The effect of spherulite structures

When amorphous PLLA is annealed, crystallinity gradually increases producing a typical spherulite microstructure. The spherulites contain crystal lamellae, which are connected to each other by amorphous regions [52], hereon referred to as inter-lamellae amorphous regions. If the annealing process is ended before spherulites have grown to engulf the entire volume of the polymer then in addition to the inter-lamellae amorphous phase inside spherulites, there is a fully amorphous phase outside spherulites [5, 57] as shown schematically in Fig. 5.2. The two different amorphous phases are likely to vary in many ways due to, for example, the constraints put on the inter-lamellae amorphous phase by the nearby crystal lamellae. Tsuji et al. [5]

suggested that the inter-lamellae amorphous regions may have an increased density of terminal carboxyl and hydroxyl groups, which are excluded from the crystalline region during crystallisation (annealing). This indicates that the free amorphous regions and the inter-lamellae amorphous regions may degrade at different rates. To account for this difference, the simplified theory is applied to the volume occupied by the spherulites and the amorphous phase outside the spherulites separately using two different sets of parameters.

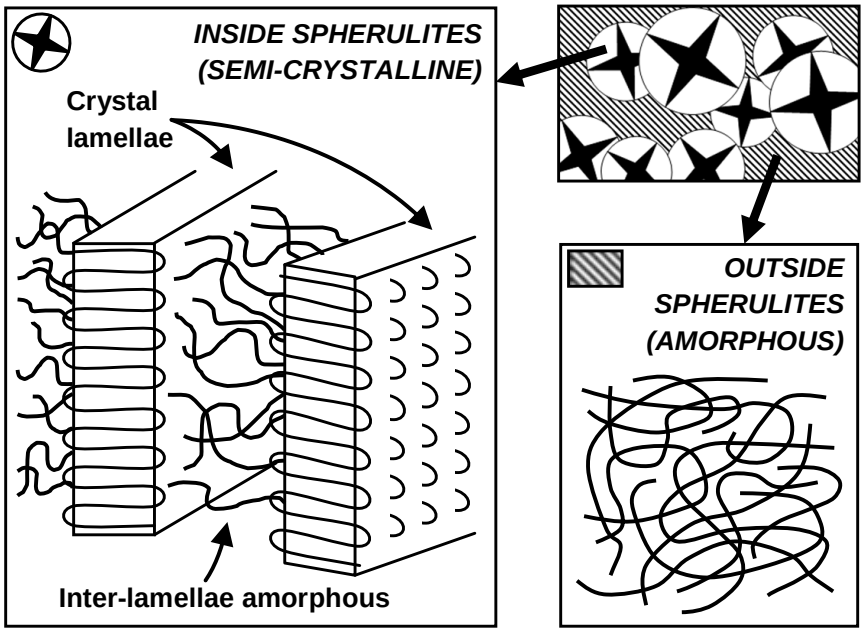

Fig. 5.2 Top right: spherulites and fully amorphous phases in a polymer. Left, within spherulite: close-packed chains in crystal lamellae and connecting amorphous phase. Bottom right, outside spherulite: fully amorphous chain entanglement

Using "*/in*" and "*/out*" subscript suffixes to indicate the phases inside and outside the spherulites, respectively, and f_s (no units) to represent the volume fraction of the spherulites, the overall polymer values of crystallinity, chain scission concentration, oligomer concentration and molecular weight are given in Eqs. 5.12 to 5.15 as

$$X_c = X_{c/in} f_s + X_{c/out} \left(1-f_s\right) \tag{5.12}$$

$$R_s = R_{s/in} f_s + R_{s/out} \left(1-f_s\right) \tag{5.13}$$

$$R_{ol} = R_{ol/in} f_s + R_{ol/out}(1\text{-}f_s) \quad 5.14$$

and

$$M_n = \frac{[f_s(C_{e/in}+\omega.X_{c/in})+(1\text{-}f_s)(C_{e/out}+\omega.X_{c/out})]M_0}{N_{chains0}+(R_s-(R_{ol}/m))} \quad 5.15$$

Variables without "*/in*" or "*/out*" suffixes represent average values for the whole polymer. Tsuji et al. [5] tested the degradation behaviour of PLLA samples of different initial degrees of crystallinity. PLLA films, 25–50μm thick, were hydrolysed in PBS, pH 7.4, at 37°C for 36 months. Five sets of films were tested with initial degrees of crystallinity of 0.00, 0.02, 0.30, 0.45 and 0.54; they are identified as PLLA0, PLLA15, PLLA30, PLLA45 and PLLA60 respectively to reflect annealing times of 0, 15, 30, 45 and 60 minutes at 140°C. A distinctive spherulite structure was observed in their semi-crystalline PLLA samples. Tsuji et al. [5] fitted their molecular weight data to a simple model for autocatalytic hydrolysis without taking into account its interaction with crystallisation. Different values of the reaction constant, *k*, had to be used for different periods of the degradation, which indicates that the model is not able to fit the data or that *k* is dependent on crystallinity.

Fig. 5.3 shows the fitting between the simplified theory and the experimental data for molecular weight and degree of crystallinity. The overall RMSE is 0.0424 and 0.0370 for the normalised molecular weight and degree of crystallinity respectively. In the fitting the autocatalytic hydrolysis rate, k_2, was the only parameter that was set at different values for the amorphous volumes inside and outside the spherulites. The best fit was obtained by setting k_2 inside the spherulites to be six times faster than that in the free amorphous regions, which suggests that the amorphous chains entrapped by the spherulites degrade in a more autocatalytic manner than those outside the spherulites. This is consistent with the finding by Tsuji et al. [5] that the higher the initial degree of crystallinity, the faster their PLLA samples degraded. Table 5.2 provides all the parameters used in the fitting. It was found that when PLLA is annealed at 140°C for sufficient time to allow spherulites to consume the entire volume, the crystallinity is approximately 0.55 [17, 57], which was taken as the initial crystallinity inside the spherulites ($X_{c0/in}$). A same crystal limit, X_{max}, was used for polymer volumes inside and outside the spherulites. Setting $\alpha = 28$ and $\beta = 2$ implies oligomers are produced at the rate representing random scission [49]. The values of $N_{chains0}$ and f_s are derived

from the measurement by Tsuji et al. [5]. The following initial conditions were used for the numerical calculation: $X_{c/in} = X_{c0/in}$; $X_{c/out} = X_{c0/out}$; $C_{e0/in} = C_{e0/out} = C_{e0}$; $C_{e/out} = C_{e0/out}$; $C_{e/in} = C_{e0/in}\left(1 - X_{c0/in}\right)$; and $X_{ext/in}$, $X_{ext/out}$, $R_{s/in}$, $R_{s/out}$, $R_{ol/in}$, $R_{ol/out}$ = 0. In the fitting k_1, $k_{2/in}$, $k_{2/out}$, p_x *and* X_{max} are the parameters that were adjusted. It can be observed from Fig. 5.3 that the simplified theory is able to fit the experimental data for all five different films using a same set of parameters except for the autocatalytic hydrolysis constants $k_{2/in}$ and $k_{2/out}$.

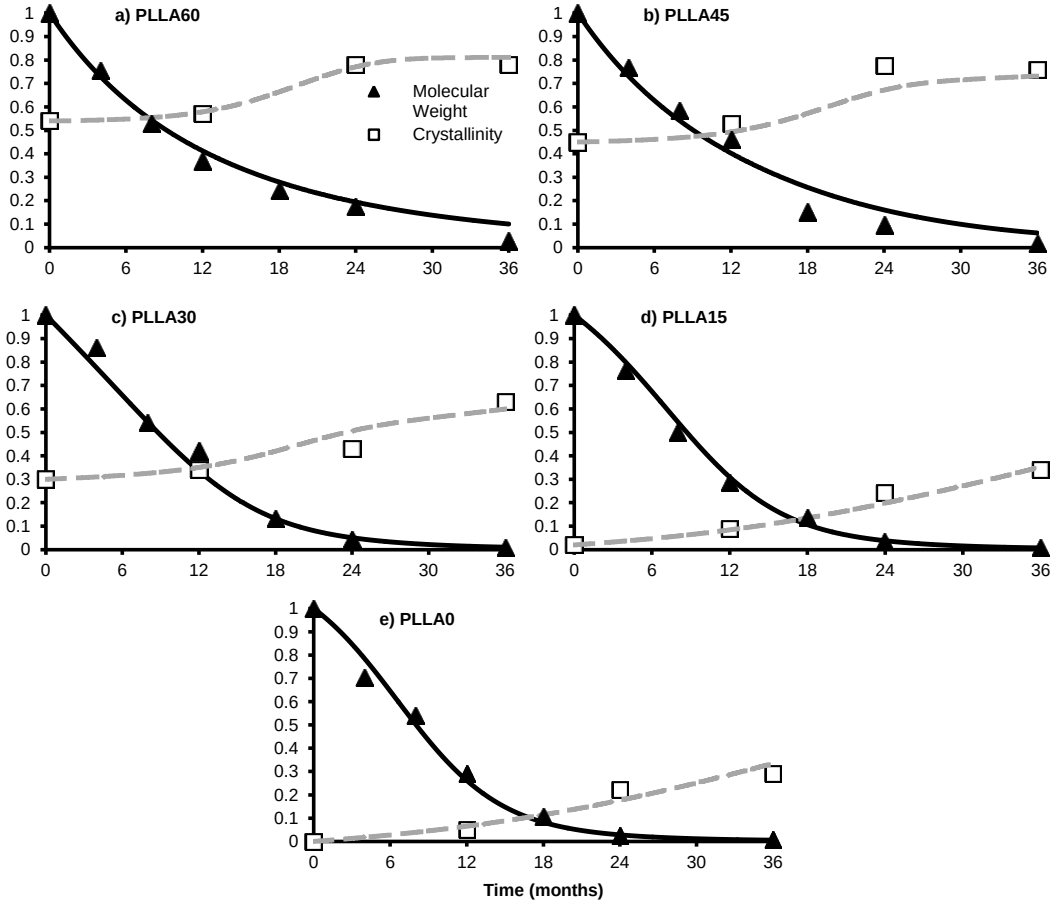

Fig. 5.3 Normalised number-average molecular weight (solid lines) and crystallinity (dashed lines) as a function of time for PLLA with different initial degrees of crystallinity of (a) X_c = 0.54, (b) X_c = 0.45, (c) X_c = 0.30, (d) X_c = 0.02, (e) X_c = 0.00. The discrete symbols are experimental data obtained by Tsuji et al. [5] while lines represent the fitting using the simplified model.

Test ID	$N_{chains0}$ (mol m^{-3})	$k_{2.in}$ ($[mol^{-1}m^3]^{0.5}day^{-1}$)	p_x	M_0 (g mol^{-1})	m	f_S	$X_{c0.in}$	$X_{c0.out}$
PLLA0	2.31	53×10^{-5}	0.01	72	4	0	0.55	0
PLLA2	2.29					0.36		
PLLA30	2.42					0.55		
PLLA45	2.49					0.82		
PLLA54	2.13					0.98		
C_{e0} (mol m^{-3})	ω (mol m^{-3})	$k_{2.out}$ ($[mol^{-1}m^3]^{0.5}day^{-1}$)	k_1 (day^{-1})	α	β	X_{max}	V_c (nm^3)	
17300	$=C_{e0.TOTAL}$	9.0×10^{-5}	1.1×10^{-5}	28	2	0.82	4.19×10^3	

Table 5.2 Model parameters that are used to fit the experimental data

5.5 Conclusions

It was found that, when modelling chain cleavage induced crystallisation in biodegradable poly(lactides), it can be assumed that the crystal growth occurs much faster than the hydrolysis reaction. The fitting of the model to experimental data indicated that, in semi-crystalline poly(lactides), the amorphous polymer chains entrapped by the spherulites degrade much faster than the free amorphous polymer chains outside the spherulites. Based on the above understanding, the simplified model proposed in this paper is able to fit experimental data of both molecular weight and crystallinity to a good accuracy.

Chapter 6: The effects of random scission, end scission and autocatalysis on degradation mechanisms of bioresorbable polyesters

In this chapter, the model presented in Chapter 5 is extended in order to analyse the effect of individual hydrolysis mechanisms. Parametric analysis is conducted to identify the key degradation trends associated with the various hydrolysis mechanisms. Although the model is more complicated, the analysis leads to a simple qualitative scheme, which non-experts are able to use to analyse degradation experimental results without conducting any mathematical modelling. A large number of experimental data sets from the literature are reviewed in order to identify the prevalent hydrolysis mechanisms. This chapter has been published in Acta Biomaterialia [97].

6.1 Introduction

The model that is presented in Chapter 5, based on previous work of Pan and his co-workers [47-50], allows for degradation rate of bioresorbable polymers, due to chain scission, to be modelled. It is demonstrated that the model is able to fit a wide range of experimental data for changes in molecular weight, mass and crystallinity as functions of degradation time. In this chapter, a more detailed model is presented, which can be used to relate degradation behaviour to the underlying hydrolysis mechanisms. The mathematical model is used in order to understand how the different hydrolysis mechanisms affect the degradation behaviour while the model in Chapter 5 is more suitable for device design because it contain fewer parameters, which may be difficult to measure experimentally.

The hydrolysis mechanisms being considered include random scission, end scission, noncatalytic hydrolysis and autocatalytic hydrolysis, which are described in the introduction chapter of this thesis. Briefly, in noncatalytic degradation, the ester bonds are cleaved in the presence of water whereas for autocatalytic degradation the hydrolysis reaction is catalysed by the carboxylic acid chain ends of water-soluble oligomers and monomers [1]. In random scission it is assumed that each ester bond in the polymer has an equal chance of chain cleavage whereas end scission assumes that only ester bonds at the end of polymer chains are cleaved.

It has been suggested that a linear relationship between $(1/M_n)$ and time indicates noncatalytic hydrolysis [91] and a linear relationship between $(1/M_n)^{0.5}$ and time indicates autocatalytic hydrolysis [1, 40]. However, there is considerable experimental data in the literature which demonstrates a delay before the reduction of molecular weight [10, 22-29], and therefore does not fit either trend. The experiments of Antheunis et al. [27] demonstrate a delay trend when initial polymer chains do not possess carboxylic acid end groups but no delay when they do. The model here considers hydrolysis to only be catalysed by the acid chain ends of water-soluble oligomers and monomers, not the chain ends of long chains, which may be unable to catalyse hydrolysis due to lack of mobility or may initially not possess carboxylic acid end groups. It is not fully understood which hydrolysis mechanisms are generally most prevalent in degradation experiments. In this chapter, an analysis scheme is presented which can quickly identify the hydrolysis mechanisms that are likely to be dominant based on experimental data for molecular weight and/or mass loss. The trends of molecular weight degradation and mass loss predicted by the mathematical model for various combinations of noncatalytic/autocatalytic hydrolysis and random/end scission are analysed and translated into the simple analysis scheme. Case studies demonstrate the use of the scheme and a large set of experimental data from the literature is evaluated to identify the dominant hydrolysis mechanisms. The particular focus of the work presented here is predominantly on poly(lactide) and poly(glycolide) polymers in order to draw unambiguous conclusions regarding their degradation. The effects of initial molecular weight and residual monomer, in relation to the hydrolysis mechanism, are the subject of the next chapter.

6.2 The mathematical model

The phenomenological model presented in Chapter 5 is modified to separate the different hydrolysis mechanisms including noncatalytic random scission, autocatalytic random scission, noncatalytic end scission and autocatalytic end scission. The polymer is assumed to consist of amorphous polymer chains, oligomers, monomers and a crystalline phase. It is assumed that the crystalline phase, characterised by the degree of crystallinity X_c (no units) strongly resists hydrolysis such that only the amorphous polymer chains suffer from hydrolysis chain scission. The rate of chain scission is determined by the concentrations of the reactants and catalyst. For random scission, the reactant is the ester bonds in amorphous chains, which are characterised by the concentration C_e (mol m^{-3}). For end scission the reactant is the amorphous chain ends characterised by C_{end} (mol m^{-3}). It is assumed that water is always abundant [39] and

its concentration does not affect the hydrolysis rate. The hydrolysis reaction can be catalysed by H^+ disassociated from the carboxylic acid end groups. Using C_{acid} (mol m^{-3}) to represent the concentration of the carboxylic end groups, the concentration of H^+ can be calculated as $C_{H^+} = \left(K_a C_{acid}\right)^n$ [49] where K_a is the acid disassociation constant and n (no units) is usually taken to be 0.5 as suggested by Siparsky et al. [40]. The term R_{rs} (mol m^{-3}) and R_{es} (mol m^{-3}) are used to represent the molar concentrations for random and end scissions respectively. Following Han et al. [49] the rate of random scission is given by

$$\frac{dR_{rs}}{dt} = k_{r1}C_e + k_{r2}C_e\left(\frac{C_{acid}}{1-X_c}\right)^n \qquad 6.1$$

and the rate of end scission is given by

$$\frac{dR_{es}}{dt} = k_{e1}C_{end} + k_{e2}C_{end}\left(\frac{C_{acid}}{1-X_c}\right)^n . \qquad 6.2$$

Here k_{r1} and k_{e1} (day^{-1}) are the noncatalytic reaction constants and k_{r2} and k_{e2} ([mol^{-1}m^3]$^{0.5}$day^{-1}) are the autocatalytic reaction constants where subscripts r and e indicate random and end scission respectively. The acid disassociation constant K_a has been merged into k_{r2} and k_{e2}. The single rate equation for chain scission proposed by Han et al. [49] has been split into two equations so that the random and end scissions can be evaluated separately. The total scission concentration R_s (mol m^{-3}) is then given by

$$R_s = R_{rs} + R_{es} . \qquad 6.3$$

In end scission, a monomer is produced by each scission and the production of monomers per unit volume R_m (mol m^{-3}) is simply given by

$$R_m = R_{es} . \qquad 6.4$$

In random scission, an oligomer may be produced by chance if an ester bond near a chain end is cleaved. Following the statistical analysis by Flory [74] the production of

ester units of oligomers per unit volume, R_{ol} (mol m^{-3}), can be related to the concentration of random scissions R_{rs} through

$$\frac{R_{ol}}{C_{e0}} = \alpha\left(\frac{R_{rs}}{C_{e0}}\right)^{\beta} \tag{6.5}$$

in which C_{e0} (mol m^{-3}) is the concentration of ester bonds in all phases at time t = 0. The values α = 28 (no units) and β = 2 (no units) apply if the oligomers are defined as short chains of less than 8 units [91] as assumed in this work.

Assuming Fick's law of diffusion, the oligomer and monomer concentrations, C_{ol} and C_m (mol m^{-3}), are governed by

$$\frac{dC_a}{dt} = \frac{dR_a}{dt} + \underset{x_i}{div}\left(D\,\underset{x_i}{grad}\left(C_a\right)\right) \tag{6.6}$$

in which the nomenclature of vector analysis is used and the subscript a is either m to represent monomer diffusion or ol to represent oligomer diffusion. The terms R_{ol} and R_m represent the concentrations of oligomers and monomers which have been produced due to chain scission, whereas C_{ol} and C_m (mol m^{-3}) represent the current concentrations due to both production and diffusion. A finite difference scheme is implemented for the spatial discretisation of the second term on the right hand side in Eq. 6.6. The diffusion coefficient D (m^2 day^{-1}) depends on the porosity and crystallinity of the polymer. It is calculated based on the diffusion coefficient of the polymer D_0 (m^2 day^{-1}) and of pores D_{pore} (m^2 day^{-1}), as discussed in the work of Han and Pan [48]. The diffusion coefficient can be set to zero to facilitate parametric analysis or if experimental data is not available for mass loss.

Pan and co-workers [48-50] further assumed that only the oligomers and monomers can catalyse the hydrolysis reaction because the carboxylic end groups of the long chains could be initially capped and the chains are not mobile. C_{acid} in Eqs. 6.1 and 6.2 can then be calculated as

$$C_{acid} = C_m + \left(C_{ol}/m\right) \tag{6.7}$$

in which m (no units) is the average degree of polymerisation of the oligomers. In this study, m is set to be 4 because oligomers are assumed to have less than 8 units of degree of polymerisation. The molar concentration of polymer chains N_{chain} (mol m^{-3}) is given by

$$N_{chain} = N_{chain0} + \left(R_{rs} - \left(R_{ol}/m\right)\right) \tag{6.8}$$

in which N_{chain0} (mol m^{-3}) is the initial molar concentration of chains and $C_{end} = 2N_{chain}$ in Eq. 6.2.

According to Avrami [93-95], the degree of crystallinity X_c can be calculated through the extended degree of crystallinity X_{ext} (no units) by

$$\frac{dX_c}{dX_{ext}} = X_{\max} - X_c \tag{6.9}$$

in which X_{max} (no units) has been introduced to set a limit for the maximum degree of crystallinity. In Chapter 5 it was shown that the extended degree of crystallinity can be related to the concentration of chain scission R_s using

$$X_{ext} = p_x \eta_A R_s V_c \tag{6.10}$$

in which p_x (no units) is the probability of crystallisation of a cleaved chain, η_A is Avogadro's constant (mol^{-1}), V_c (m^3) is the volume of a single polymer crystallite. During biodegradation amorphous polymer chains are consumed by oligomer production, monomer production and crystallisation, which leads to

$$C_e = C_{e0} - \left(R_{ol} + R_m + \omega X_c\right) \tag{6.11}$$

where ω (no units) is the inverse molar volume of the crystalline phase. The number-averaged molecular weight, M_n (g mol^{-1}), can be calculated as

$$M_n = \frac{\left(C_e + \omega X_c\right) M_0}{N_{chain}} \tag{6.12}$$

in which M_0 (g mol^{-1}) is the molar mass of each polymer repeat unit. In the molecular weight calculation, oligomers and monomers are excluded because they are too small to be detected by typical measuring techniques such as gel permeation chromatography. Each random scission increases the chain number by one but has a probability to produce R_{ol} / m number of oligomers. For end scission, N_{chain} remains constant and M_n reduces due to the reduction of amorphous ester units C_e. In contrast, for random scission, the main factor for M_n reduction is the increase in the number of chains.

Eqs. 6.1 to 6.12 are numerically integrated using the direct Euler scheme giving the molecular weight, degree of crystallinity, and concentrations of oligomers and monomers as functions of degradation time. Although there are a large number of parameters in the model, only the kinetic parameters change from polymer to polymer for the type of polyesters studied and hence are the focus of the parametric study. The kinetic parameters include k_{r1}, k_{r2}, k_{e1} and k_{e2}, which are determined by the rate of molecular weight reduction, X_{max} and p_x, which are determined by the rate of crystallisation and D_0 and D_{pore}, which are determined by the mass loss. Other parameters in the model cannot be arbitrarily varied. For example, the acid disassociation exponent n is usually taken as 0.5, which is determined by the charge balance of the acid disassociation reaction. The average number of ester units, m, of the short chains is determined by the widely accepted assumption that at this level the short chains becomes water-soluble. The values for of α and β for random scission are then directly calculated from m according to Flory's theory [49]. p_x and V_c for crystallisation always appear as a single parameter in the model and are only kept separate to preserve their physical meanings. C_{e0} and ω are set as the same value of 17300 mol/m^3 representing an assumption that the densities of poly lactic acid amorphous and crystalline phases are both 1250 kg/m^3. The parameters that have the greatest effect on the degradation are k_{r1}, k_{r2}, k_{e1}, k_{e2} and n. They affect the rate of chain scission, which in turn affects molecular weight, crystallinity and mass loss. Increasing the reaction rates increases the rate of chain scission for each hydrolysis mechanism. The values of X_{max}, p_x and V_c control crystallinity and do not significantly affect other aspects of degradation. The values of m, D_0 and D_{pore} affect the size and diffusion of small chains and therefore affect mass loss and the rate of autocatalytic hydrolysis.

6.3 Degradation trends by different hydrolysis mechanisms

The change in molecular weight and accumulation of oligomers and monomers as functions of time are computed using the mathematical model for different combinations of random or end scission with autocatalytic or noncatalytic hydrolysis. For simplicity, the simulations in this section focus on amorphous polymer and use a typical set of data for poly(lactide) of M_0 = 72 g mol^{-1}, N_{chain0} = 4.35 mol m^{-3} and C_{e0} = 17300 mol m^{-3}, which represents an initial molecular weight of M_n = 286,000 g mol^{-1}. When presenting the data, the molecular weight is normalised by its initial value and the degradation time is normalised by a characteristic time t_c, which is the time taken for the molecular weight to reduce to 10% of its initial value. Consequently, the absolute values of the reaction constants do not have an effect on the presented results and only their relative values are important. It is worthwhile to point out that the degradation rate of a polymer is not necessarily related to whether the hydrolysis is noncatalytic or autocatalytic. The rate of degradation in the figures in this section simply reflects the chosen method of scaling on the time axis and should not be related to any particular hydrolysis reaction under discussion. In each case study in this section the ratio between the two reaction rate constants is varied from zero to infinity while other parameters do not change. The oligomers and monomers are water-soluble and may diffuse out of a device. The diffusion of these water-soluble chains is not considered in this section because its effect on degradation was fully studied by Wang et al. [50]. The accumulation of oligomers and monomers together is referred to as small chains and used as an indication for potential mass loss. This reflects an assumption that mass loss is due to the bulk diffusion of water-soluble small chains as opposed to other mechanisms such as surface erosion or loss of residual monomer. It has been recognised that there can be a significant amount of residual monomers after polymer processing. The effect of residual monomers on degradation is the topic of the next chapter. In the current chapter, the initial concentration of the short chains is set as zero (10^{-10} C_{e0} or 10^{-8} wt.% for numerical reasons). This allows the parametric studies to focus on the transition from autocatalytic to noncatalytic hydrolysis. To demonstrate that the general conclusions are not affected by residual monomers, a case study with a significant amount of residual monomers is also included.

6.3.1 Random scission and the effect of autocatalytic strength

Fig. 6.1 shows the transition from noncatalytic to autocatalytic hydrolysis assuming only random scission occurs (by setting k_{e1}=k_{e2}=0 in the model). The ratio of k_{r2}/k_{r1}, which reflects the relative strength of autocatalysis to non-autocatalysis, is set at 0, 5, 20, 100, 500 and infinity. It can be observed from the figure that a strong autocatalytic hydrolysis is characterised by a delay in the reduction of the molecular weight while a weak autocatalytic hydrolysis is characterised by an initially sharp reduction in the molecular weight. This is because for a strong autocatalytic hydrolysis, the rate of chain scission accelerates greatly as small chains build up while noncatalytic chain scission does not accelerate during degradation. The pure noncatalytic random scission curve (A) is the only curve which gives a linear line on a plot of ($1/M_n$) versus time. A high residual monomer content can shift the curves towards the appearance of the noncatalytic curve (A), which is discussed in detail in the next chapter of this thesis. Therefore the characteristic shape of curve shown by case F is a sufficient condition to indicate autocatalysis, but not necessary.

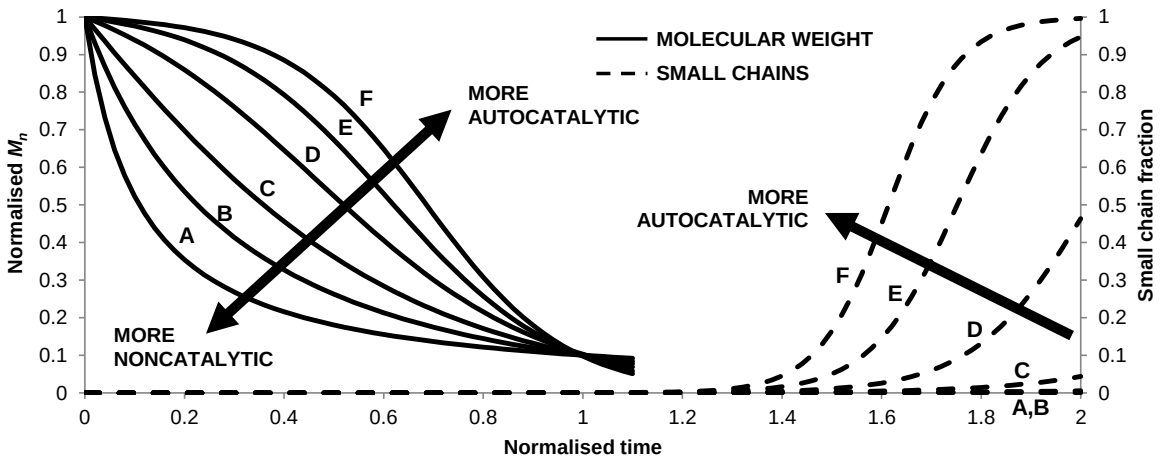

Fig. 6.1 Random scission simulations with variable degrees of autocatalysis. Normalised M_n (solid lines) and the sum weight fraction of oligomers plus monomers (dashed lines) are shown versus normalised time. The autocatalytic:noncatalytic rate ratios (k_{r2}/k_{r1}) are 0 (A), 5 (B), 20 (C), 100 (D), 500 (E) and infinity (F).

Another important observation from the figure is that the accumulation of oligomers and monomers as a percentage of total ester units is insignificant until the molecular weight reaches a very small value. The short chains do however affect the degradation rate. The number of carboxylic end groups of these small water-soluble chains are sufficient enough to significantly alter the behaviour in the molecular weight reduction. However any measurable mass loss would not be expected before the polymer breaks apart if its

degradation occurs entirely by random scission. This is because random scission is very inefficient at producing oligomers but quite efficient at reducing the molecular weight. Autocatalytic hydrolysis is associated with relatively early oligomer production (measurable at normalised time ≈ 1.5) while very few oligomers are produced in noncatalytic hydrolysis (negligible even at normalised time = 10). This simply reflects the fact that molecular weight reduces at a greater rate in the latter stages of degradation for autocatalytic hydrolysis. For random scission, the small chain fraction depends mainly on the absolute value of molecular weight. For a purely random scission model setup (k_{e1}=k_{e2}=0), oligomers account for 1% of the total polymer when M_n has reduced to approximately 5000 g mol^{-1}. A simple Monte Carlo random chain scission simulation also gives similar results.

6.3.2 End scission and the effect of autocatalytic strength

Fig. 6.2 shows the transition from noncatalytic to autocatalytic degradation assuming only end scission occurs (k_{r1}=k_{r2}=0). The ratio of k_{e2}/k_{e1} is set as 0, 0.02 and infinity. Similar to random scission, strong autocatalytic hydrolysis is characterised by an initial delay in the molecular weight reduction. However no sharp initial reduction in molecular weight can be observed in any of the cases. This is because each end scission has the same effect on molecular weight throughout degradation whereas the effect of each random scission reduces as the number of chains increases, which is discussed in detail in the next chapter of this thesis. In strong contrast to random scission, the accumulation of oligomers and monomers occurs very early. This means significant mass loss could be expected if the degradation is controlled by end scission. It can also be observed that stronger autocatalytic hydrolysis delays the production of small chains. Both the reduction in molecular weight and production of short chains are delayed in strong autocatalytic hydrolysis due to lack of the catalyst (short chains) at the start of degradation. Noncatalytic hydrolysis does not require the short chains as a catalyst, and hence does not demonstrate a delay.

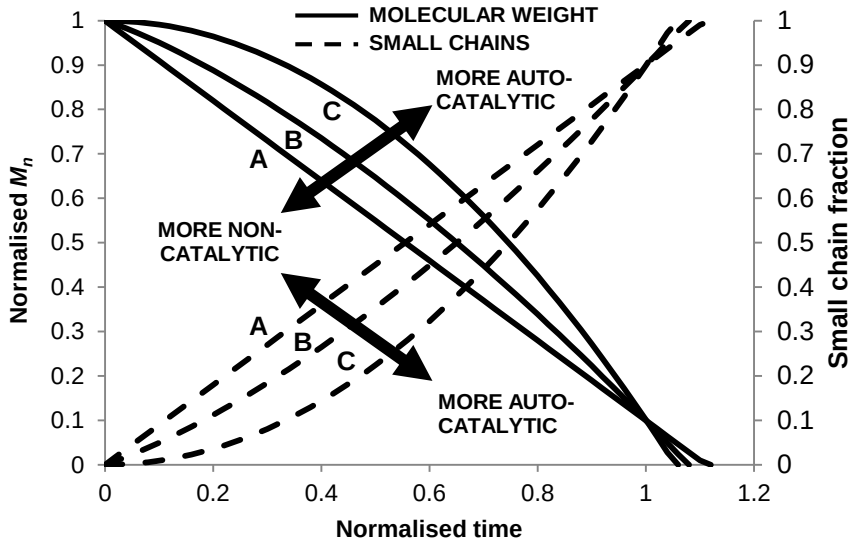

Fig. 6.2 End scission simulations with variable degrees of autocatalysis. Normalised M_n (solid lines) and the sum weight fraction of oligomers plus monomers (dashed lines) are shown versus normalised time. The autocatalytic:noncatalytic rate ratios (k_{e2}/k_{e1}) are 0 (A), 0.02 (B) and infinity (C).

6.3.3 Autocatalytic hydrolysis and the transition from random to end scission

Fig. 6.3 shows the transition from random to end scission assuming autocatalytic hydrolysis (k_{r1}=k_{e1}=0). The ratio of k_{e2}/k_{r2}, which reflects relative strength of end scission to random scission, is set as 10^2, 10^3, 10^4, $5x10^5$ and infinity. The case for pure random scission is already shown in Fig. 6.1 and omitted here for clarity. It can be observed from Fig. 6.3 that random scission is characterised by a deceleration (the concave section on the curve) in the reduction rate of molecular weight at some stage of the degradation, which can also be clearly observed in Fig. 6.1. No such deceleration can be observed for the end scission cases (Fig. 6.2 and Fig. 6.3). It is also interesting to focus on cases *A, B* and *C* in Fig. 6.3. A difference of two orders of magnitude in the ratio of k_{e2}/k_{r2} has very little effect on the molecular weight behaviour but greatly affects the production of oligomers and monomers and hence potential mass loss. This once again highlights that the effect of the underlying hydrolysis mechanisms may be significant on one aspect of the degradation behaviour but undetectable on a different aspect. The type of buffer solution used in degradation experiments, along with the frequency of its replacement and volume relative to the polymer sample, is an important factor in degradation. The pH of the solution for example is known to strongly affect the rate of degradation. In this current study it is assumed that the buffer solution is replaced frequently enough that there is no pH change caused by the monomer release from the samples. It is likely that the individual

hydrolysis mechanisms are affected in different ways by the polymer solution, and thus the trends identified in this study may be useful in identifying the effect of the solution. The fraction of acidic chain ends present in oligomers as opposed to monomers is negligible even for low levels of end scission. An interesting observation is therefore that the rate of autocatalytic random scission is most likely determined by monomers, and thus although molecular weight reduction is due to random scissions, the rate of reduction is controlled by end scissions.

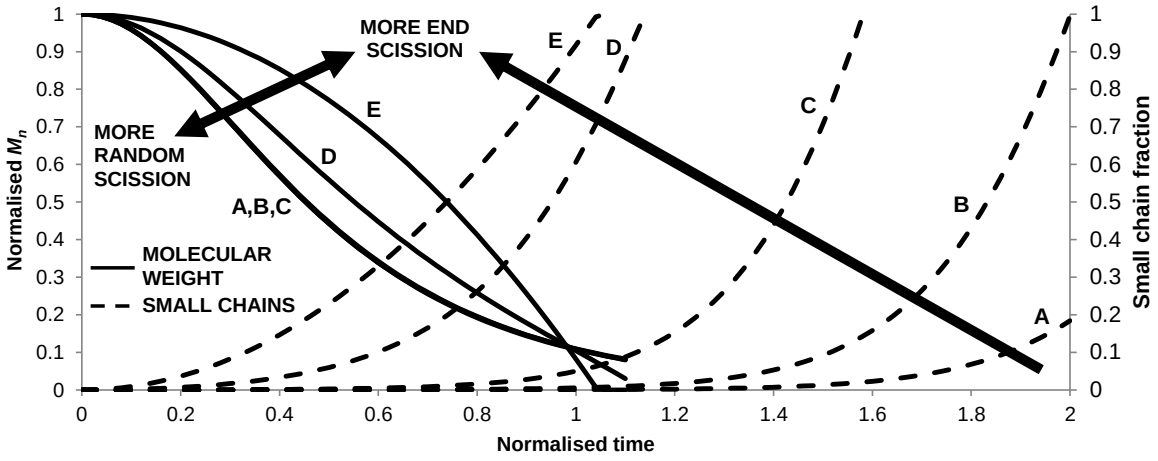

Fig. 6.3 Autocatalytic hydrolysis simulations with variable ratios of end scission to random scission reaction rates. Normalised M_n (solid lines) and the sum weight fraction of oligomers plus monomers (dashed lines) are shown versus normalised time. The end:random scission rate ratios (k_{e2}/k_{r2}) are 10^2 (A), 10^3 (B), 10^4 (C), $5x10^5$ (D) and infinity (E).

6.3.4 Noncatalytic hydrolysis and the transition from random to end scission

Fig. 6.4 shows the transition from random to end scission assuming noncatalytic hydrolysis ($k_{r2}=k_{e2}=0$). The ratio of k_{e1}/k_{r1}, which reflects the relative strength of end scission to random scission, is set as 0, $1x10^4$, $5x10^4$, $1x10^5$, $5x10^5$ and infinity. A threshold for the end scission rate can also be observed from cases A and B for the molecular weight behaviour but not for the accumulation of the small chains. Examining the small chain accumulation as a function of time and comparing Fig. 6.3 and Fig. 6.4, it can be observed that autocatalytic hydrolysis is characterised by a delay in the accumulation of the small chains hence a delay in mass loss while noncatalytic hydrolysis is characterised by almost linear increase in the amount of oligomers and monomers.

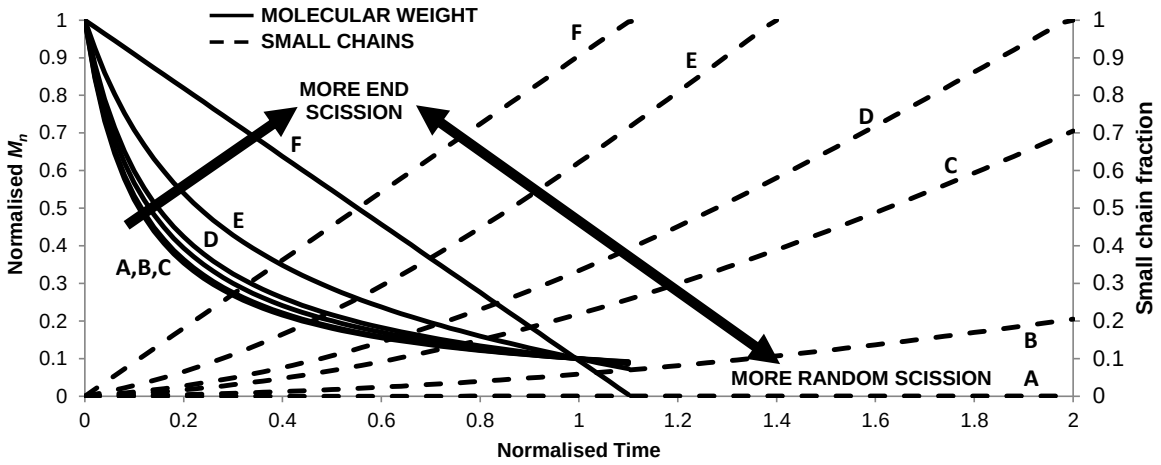

Fig. 6.4 Noncatalytic hydrolysis simulations with variable ratios of end scission to random scission reaction rates. Normalised M_n (solid lines) and sum weight fraction of oligomers plus monomers (dashed lines) are shown versus normalised time. The end:random scission rate ratios (k_{e1}/k_{r1}) are 0 (A), $1x10^4$ (B), $5x10^4$ (C), $1x10^5$ (D), $5x10^5$ (E) and infinity (F).

6.4 A qualitative scheme to identify dominant hydrolysis mechanisms and case studies

When analysing experimental data, a set of values for parameters in the mathematical model can be found that provide the best fit between the model prediction and the data. This set of parameters can then be used to identify the underlying hydrolysis mechanism. For example, a large ratio of k_{e2}/k_{r2} would indicate end scission dominates. However the analysis presented in Section 6.3 provides a quick and qualitative analysis to identify the dominant hydrolysis mechanism. In this section both approaches are used to analyse two sets of experimental data obtained from the literature. This serves two purposes: (a) validation of the mathematical model and (b) a demonstration of the analysis scheme. The two case studies were chosen because they require different combinations of hydrolysis mechanisms to achieve the best fitting. Hence they suitably exemplify how to use the qualitative analysis scheme. The level of fitting accuracy shown in this section is representative for the capacity of the model to fit all the experimental data that are available in the literature.

The analysis in Section 6.3 can be briefly summarised as

i. A deceleration (concave section) on the molecular weight - time curve indicates random scission. Lack of the deceleration indicates end scission.
ii. A nonlinear relationship between ($1/M_n$) and time indicates autocatalytic random scission. This condition is sufficient but not necessary. An initial delay in the reduction of the molecular weight indicates a greater contribution from autocatalytic hydrolysis.
iii. Significant mass loss while $M_n > 5000$ g mol^{-1} indicates end scission.
iv. A linear increase in mass loss with time indicates noncatalytic end scission.

Because mass loss also requires the small chains to diffuse out of the specimen, a lack of mass loss does not necessarily indicate that end scissions do not occur. Similarly, a delay in mass loss does not prove autocatalysis. Points (i)-(iv) can be used as a simple and quick scheme to identify the underlying hydrolysis mechanisms. Fig. 6.5 shows schematically the typical regimes of the molecular weight behaviour. Only curve A would be linear on a plot of ($1/M_n$) versus time. It is important to note that although curves A and B may initially appear quite similar in appearance, they differ greatly and cannot fit the same experimental data.

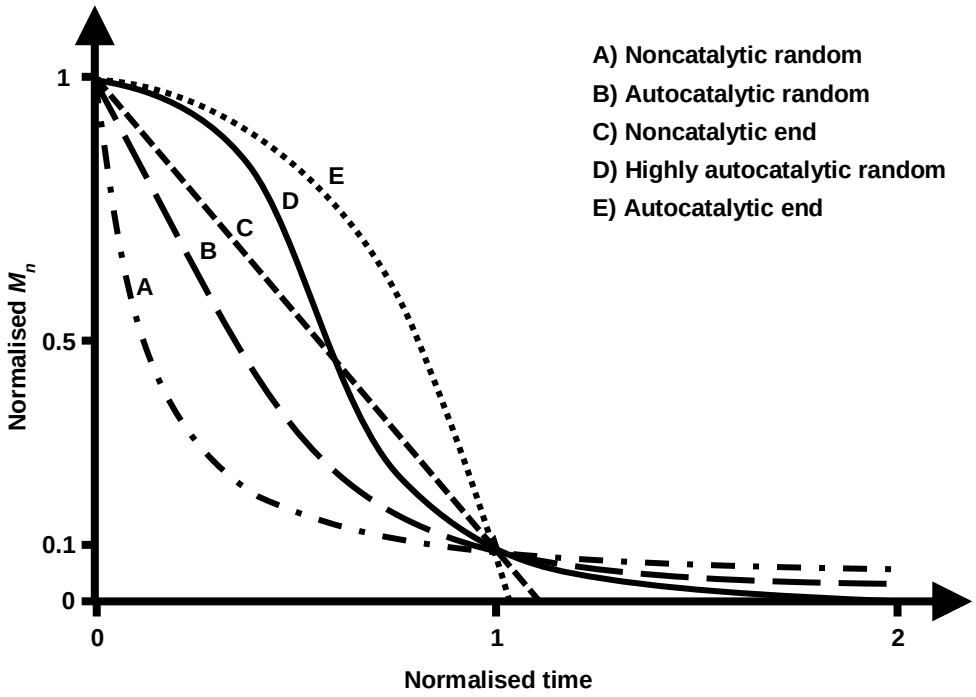

Fig. 6.5 Typical curves for normalised M_n versus normalised time for various theories of hydrolysis: (A) noncatalytic random scission, (B) autocatalytic random scission, (C) noncatalytic end scission, (D) highly autocatalytic random scission and (E) autocatalytic end scission.

6.4.1 Case study A

Beslikas et al. [25] carried out a set of degradation experiments using thin films of semi-crystalline poly(lactide) in phosphate buffer solution pH 7.2 at 50°C. The samples had an initial M_n of 120000 g mol^{-1} and an initial crystallinity of 56.5%. The thickness of the films is not given in the publication. It is set as 50 μm in the model here, although the thickness does not affect the conclusions. Their experimental results are reproduced using discrete symbols in Fig. 6.6, in which normalised number-averaged molecular weight, degree of crystallinity and mass loss are shown as functions of time. Significant mass loss while M_n > 5000 g mol^{-1} indicates that end scission must have happened. However a gentle deceleration can be observed on the molecular weight - time curve, which indicates random scission also occurred. A plot of ($1/M_n$) versus time is not linear and an initial delay on the molecular weight - time curve can be observed, which indicates that strong autocatalytic hydrolysis was in operation. It can therefore be concluded that the degradation is by a combination of autocatalytic random and autocatalytic end scission.

The best fitting between the mathematical model and the data is shown in Fig. 6.6 using solid lines. The fitting parameters are provided in Table 6.1. It is not possible to achieve an equally good fitting with a different set of hydrolysis mechanisms. Both crystallisation and diffusion of small chains are included in the numerical model. Crystallite size V_c is estimated from the literature [52]. It can be observed that the mathematical model can fit the data very well for the average molecular weight and degree of crystallinity and quite well for mass loss. The best fit is achieved by $k_{r1} = k_{e1} = 0$, which indicates that the hydrolysis is fully autocatalytic, and supports the qualitative analysis. The reaction rate ratio of $k_{e2}/k_{r2} = 7500$ indicates that end scission occurs much faster than random scission. The high rate of end scission is necessary to produce the level of mass loss observed in the experiment. However it is very important to point out that the relatively small but finite random scission rate has a major effect on the molecular weight reduction. The dashed line in Fig. 6.6 shows the model prediction using identical set of parameters except that k_{r2} was set as zero. It can be observed that the small amount of random scission has a large effect on both molecular weight reduction and mass loss. A fitting to mass loss may be achieved without random scission by increasing k_{e2}, but a fitting of molecular weight is not possible. Similarly, a fitting to mass loss is only possible if end scission is included. Both random and end scission are required to fit the data. It can be observed that agreement between the model prediction and experimental data for the mass loss

curve is relatively poor. The agreement can be improved by modifying the expression for the diffusion coefficient.

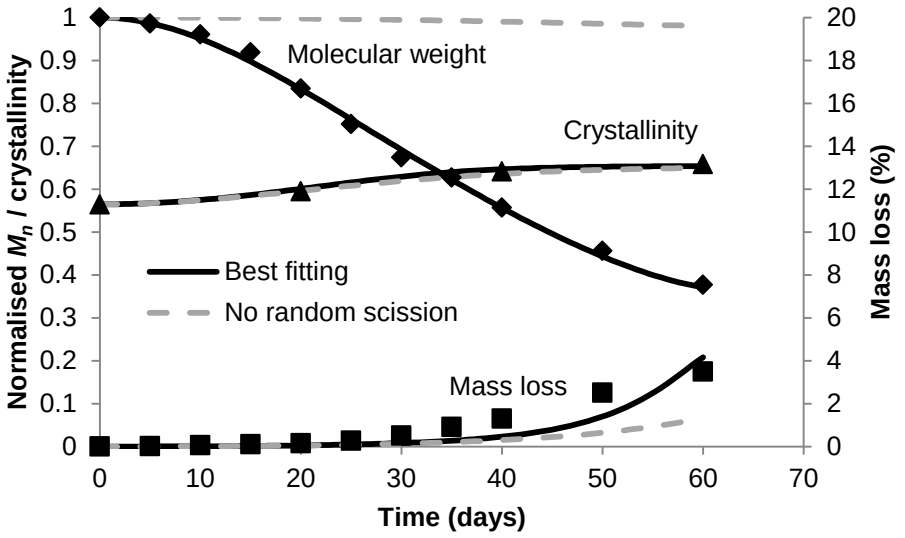

Fig. 6.6 A model fitting of molecular weight, crystallinity and mass loss for combined autocatalytic random scission and autocatalytic end scission as suggested by the qualitative analysis (solid black lines). For comparison, a fitting without random scission also included (dashed grey lines). Discrete symbols indicate experimental data [25].

Model parameters	units	Case study A (zero monomer)	Case study A (1% monomer)	Case study B
M_0	g mol^{-1}	72	72	65 [(a)]
k_{r1}	day^{-1}	0	0	0
k_{r2}	[mol^{-1}m^3]$^{0.5}$day^{-1}	3.0 x10^{-6}	0.13 x10^{-6}	8.5 x10^{-6}
k_{e1}	day^{-1}	0	0	1.26 x10^5*k_{r1}
k_{e2}	[mol^{-1}m^3]$^{0.5}$day^{-1}	7500*k_{r2}	40000*k_{r2}	0
$N_{chains0}$	mol m^{-3}	10.4	10.4	55
D_0	m^2 day^{-1}	2.5 x10^{-11}	4.0 x10^{-13}	1.6 x10^{-15}
D_{pore}	m^2 day^{-1}	2.5 x10^{-7}	4.0 x10^{-9}	1.6 x10^{-11}
Initial porosity	no units	0	0	0
C_{e0}	mol^{-1}m^3	17300	17300	17,300
ω	mol^{-1}m^3	17300	17300	17,300
X_{max}	no units	0.655	0.655	0
p_x	no units	0.004	0.0006	0
V_c	m^3	4.19 x10^{-24}	4.19 x10^{-24}	0

(a) Molar mass is taken as the average of poly(lactide) and poly(glycolide)

Table 6.1 Values of the model parameters used in the fittings

Residual monomer can have a significant effect on the degradation trends as discussed in the next chapter. However most of the early experimental studies did not report the amount of residual monomers in their samples. In order to demonstrate that the model and qualitative analysis scheme are still valid if the samples contain residual

monomers, the fitting is repeated with an assumed initial monomer concentration of 1%. The repeated best fitting is shown in Fig. 6.7 and compared with the original fitting assuming zero monomer content. The same combination of hydrolysis mechanisms (k_{r1} = k_{e1} = 0) is required in order to get the best fitting, which is of similar quality to the original. Several parameters needed to be modified due to the initial catalyst and their values are given in Table 6.1. The hydrolysis reaction rate is reduced due to the extra initial catalyst, the ratio of end:random scission is increased, the diffusion coefficient is reduced, and a value of n = 0.75 is required. A more comprehensive discussion is presented in the next chapter of this thesis. The ability of the qualitative scheme was not affected by the uncertainty that exists due to residual monomer not being measured.

The qualitative analysis scheme was able to identify the hydrolysis mechanisms which were required in order to achieve a good fitting of the model to the experimental data.

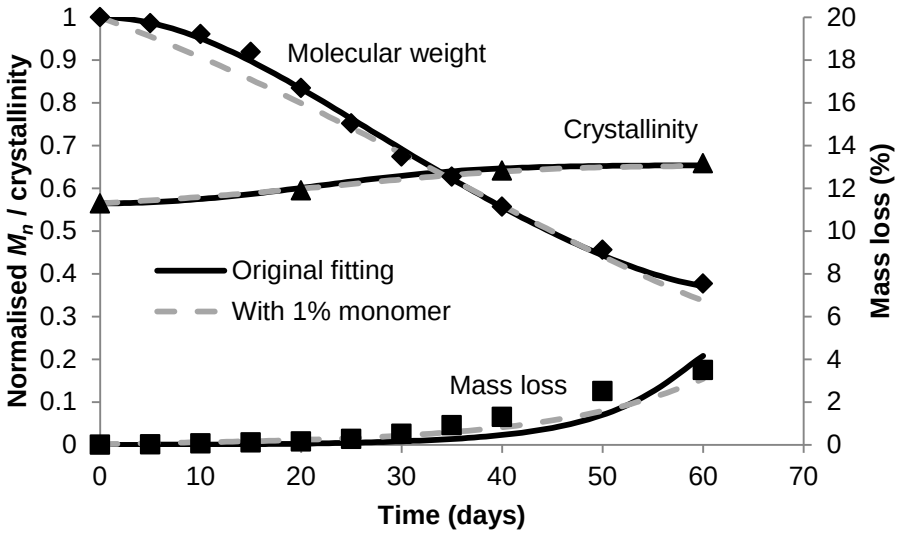

Fig. 6.7 A re-fitting of the experimental data of Beslikas et al. [25] for an assumption of 1% initial monomer (dashed grey lines). The original fitting from Fig. 6.6. with effectively zero initial monomer (solid black lines) is included for reference.

6.4.2 Case study B

Batycky et al. [26] carried out degradation experiments of drug-encapsulating microspheres made of poly(DL-lactide-co-glycolide) 50:50. The samples are amorphous throughout, had an initial M_n of 20500 and were of radius 10 μm. Their data are reproduced in Fig. 6.8 for normalised number averaged molecular weight and mass loss as functions of time. From the figure it can be observed that there is clear deceleration on the molecular weight - time curve indicating random scission. There is

an initial delay in the molecular weight reduction and therefore a plot of ($1/M_n$) versus time is not linear, which indicates autocatalytic random scission. However, the delay is less significant compared to case study A, perhaps suggesting a noncatalytic hydrolysis contribution. The mass loss is significant while M_n > 5000 g mol^{-1} indicating a large end scission rate. The degradation is therefore through a combination of autocatalytic random and noncatalytic end scission. Batycky et al. [26] also used a mathematical model to determine whether end or random scission was dominant and concluded that a combination of both mechanisms was required to fit their data.

The solid lines in Fig. 6.8 show the best fitting of the model. All the parameters used in the fitting are provided in Table 6.1. Again it can be observed that the model is able to fit the experimental data very well. The best fit was obtained by setting $k_{r1} = k_{e2} = 0$, which indicates autocatalytic random and noncatalytic end scission, and $k_{e1} / k_{r2} = 1.26 \times 10^5$, which indicates end scission occurs much faster than random scission. Similar to Case A, the large end scission rate is necessary for the observed mass loss and a similar fitting cannot be achieved by using a different combination of hydrolysis mechanisms. The small but finite rate of random scission is critical to the molecular weight reduction. The dashed lines in Fig. 6.8 show the model prediction using an identical set of parameters except that k_{r1} was set to zero. As with Case A, it can be observed that the small amount of random scission effects both molecular weight reduction and mass loss. Random scission is again required to achieve a fitting to the experimental data for molecular weight and end scission is required for mass loss. The values of diffusion coefficients D_0 and D_{pore} are chosen to give the best model fitting. They give an indication of the polymer diffusion coefficients. Significant variation is to be expected between different setups since many factors affect diffusion. For example, the experiments of Yoon et al. [98] found diffusion coefficients to be 3 orders of magnitude greater for water molecules in poly(lactide) than poly(glycolide). Again the qualitative analysis scheme has been shown to successfully identify which hydrolysis mechanisms played a critical role during the degradation experiments.

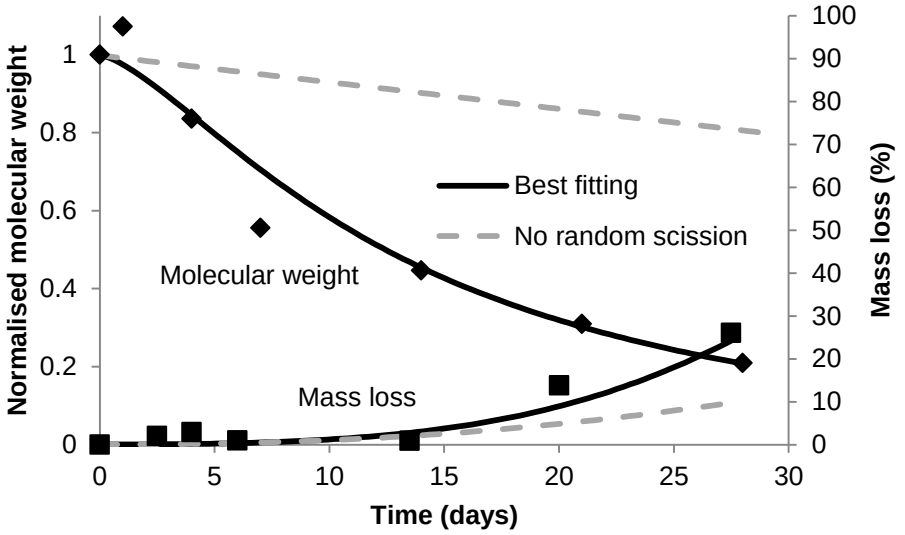

Fig. 6.8 A model fitting using a combination of autocatalytic random scission and noncatalytic end scission (solid black lines) as suggested by the qualitative analysis. A fitting without random scission is included for reference (dashed grey lines). Experimental data [26] for molecular weight and mass loss are discrete symbols.

6.5 Review of hydrolysis mechanisms for experimental data available in the literature

The qualitative analysis is applied to experimental data of 31 previous publications, which are obtained from the literature [1-31]. Table 6.2 lists the identified hydrolysis mechanisms for each individual paper. Actual fittings with the mathematical model are also performed for half of the cases as indicated in the table. A similar level of fitting accuracy as shown in Section 6.4 is obtained for all these cases. Experimental details such as polymer type, initial molecular weight and minimum dimension of the samples are also provided. The following conclusions can be drawn from the analysis:

- A combination of random and end scission is identified for almost all the data.
- Significant molecular weight reduction is always due to random scission.
- Mass loss is due to end scission.
- Autocatalytic random scission is required for molecular weight reduction in almost all publications.

Table 6.2 identifies the hydrolysis mechanisms which are required in order for a fitting to be achieved. Naturally, the best fitting will be achieved by allowing the model the flexibility to include all hydrolysis mechanisms to a greater or lesser extent.

An important finding is that a good fitting cannot be achieved without autocatalytic random scission in most cases. Since the analysis found a mixture of autocatalytic and noncatalytic hydrolysis, it is likely that both types of hydrolysis mechanism occur depending of the setup of a particular experiment. However because high residual monomers make the degradation appear to be noncatalytic, it cannot be ruled out that the cases the analysis identified as noncatalytic are in fact also autocatalytic if residual monomers were present. There have been several experimental publications which suggest autocatalytic hydrolysis plays a significant role in degradation under specific conditions. In particular, heterogeneous degradation of large samples has been attributed to autocatalysis [14, 15, 22, 27, 41, 42], as has the accelerated degradation of samples with high residual monomer [18, 23], along with the accelerated degradation of polymers with carboxylic acid end groups versus benzyl alcohol end groups [27]. However, the findings of the analysis in Table 6.2 suggest that autocatalytic hydrolysis has a more important role than noncatalytic hydrolysis over a very broad range of conditions. The experiments considered in the analysis vary greatly in factors such as sample size and shape, initial molecular weight, polymer or copolymer type, buffer solution type and temperature, crystallinity, and the rate of degradation. But the model almost always suggests that autocatalytic hydrolysis occurs. It is important to note that since end scission is expected, the monomers which result from end scission control the rate of autocatalytic random scission, and therefore the rate of M_n reduction. This is due to the fact that the number of monomers is significantly greater than oligomers, as discussed in Section 6.3. Since end scission has little or no effect on molecular weight, models which derive the acid catalyst concentration from the value of molecular weight do not consider the expected situation that end scission controls the concentration of acid catalyst. Also, an alternative interpretation of the findings of Antheunis et al. [27] that carboxylic acid end groups accelerate degradation versus benzyl alcohol end groups could be that the benzyl alcohol end groups are more resistant to end scission, and hence the initial production of monomers, and therefore catalyst, is retarded.

Another important finding is that end scission is required in order to achieve a good fitting in most cases.

In the most practical polymers, the initial molecular weight is too large for random scission to produce enough oligomers by chance in order to give the observed mass loss. However random scission is crucial in order to give the observed molecular weight reduction. Considering the experimental data for mass loss presented in Fig. 6.6

and Fig. 6.8 [25, 26], for the molecular weight to reduce by 67% only two random scissions per chain are required. It is impossible for this number of random scissions to produce 3% and 15% mass of oligomers by chance to give the observed mass loss given that the initial chains contain 1667 and 315 polymer units respectively. If there is no end scission, the observed mass loss would require that the polymer chains become water-soluble at M_n≈14000 and M_n≈2600 g mol^{-1} respectively. These values are much larger than those typically found in the literature, which may be in the region of <1000 g mol^{-1} [27, 43, 44]. It can be generally concluded that ester bonds towards the end of polymer chains are more susceptible to hydrolysis than those in the middle. If end scission is due to the acidic chain end folding back on itself, it may be the case that a number of bonds near the chain end can be cleaved. Experimental measurements of lactic acid monomers would not identify oligomers produced by this type of end scission, and therefore may falsely be interpreted as evidence for random scission.

				Scission type				
				Random scission		**End scission**		
Ref	**Polymer type**	**Initial M_n (kg mol^{-1})**	**Minimum size (mm)**	**Auto-catalytic**	**Non-catalytic**	**Auto-catalytic**	**Non-catalytic**	**Fitting carried out?**
[1]	PLA 70L:30L,D	290	1	YES		ONE OF THESE TWO		YES
[2]	PLA - L, D or L/D	500	0.1	YES		MAYBE	MAYBE	YES
[3]	PLGA 50DL:50G	10.5	N/A	YES		ONE OF THESE TWO		YES
[4]	PLGA	33	0.05	YES		ONE OF THESE TWO		NO ATTEMPT
[5]	PLLA	550	0.05	YES		ONE OF THESE TWO		NO ATTEMPT
[6]	PLLA	155	0.8	YES		ONE OF THESE TWO		YES
[7]	PLLA	166	0.8	YES	MAYBE	ONE OF THESE TWO		YES
[8]	PLLA	27-177	1.5-3	YES		ONE OF THESE TWO		YES
[9]	PLA - L, D or L/D	90	0.05	YES		YES		YES
[10]	PLA - L, D or L/D	450	0.05	YES		YES		NO ATTEMPT
[11]	PLLA	45	0.033	MAYBE	LIKELY		YES	YES
[12]	PLA 50L:50D	450	0.05	YES		ONE OF THESE TWO		YES
[13]	PLGA - 50DL:50G	14	0.2	YES	MAYBE		YES	NO ATTEMPT
[14]	PDLLA	85	1.5	YES		YES		NO ATTEMPT
[15]	PLLA	72	2	MAYBE	LIKELY		YES	NO ATTEMPT
[16]	PLGA	53	0.2	YES		ONE OF THESE TWO		NO ATTEMPT
[17]	PLLA	550	0.05	YES		YES		NO ATTEMPT
[18]	PLGA 85:15	IV = 1.4dl/g	1.6-3.4	YES		YES		YES
[19]	PLA 96L:4D	37	2.6	YES		ONE OF THESE TWO		NO ATTEMPT
[20]	PLA 70L:30DL	≈20	2	YES		ONE OF THESE TWO		NO ATTEMPT
[21]	90PLA:10PCL	28	0.4	YES	MAYBE		YES	NO ATTEMPT
[22]	PDLLA	20-34	2	YES		ONE OF THESE TWO		YES
[23]	PDLLA	10	0.5	YES		YES		NO ATTEMPT
[24]	PLGA 50:50	28	0.0005-0.022	MAYBE	LIKELY	ONE OF THESE TWO		NO ATTEMPT
[25]	PLLA	120	thin film	YES		YES		YES
[26]	PLGA 50:50	20	microsphere	YES			YES	YES
[27, 28]	PLA, PLGA, PCL	10	1.4-2.3	YES	MAYBE	MAYBE	MAYBE	YES
[29]	PLGA	40	0.05	YES	MAYBE	MAYBE	MAYBE	YES
[30]	PDLA	100	0.1	YES		YES		YES
[31]	PLLA	160	2	MAYBE	LIKELY	MAYBE	MAYBE	NO ATTEMPT

Table 6.2 The qualitative analysis scheme and model are used on a number of degradation experiments to determine the dominant hydrolysis mechanisms

6.6 Conclusions

The mathematical model was presented that considers degradation by the individual hydrolysis mechanisms: noncatalytic random scission, autocatalytic random scission, noncatalytic end scission and autocatalytic end scission. The model was able to fit all experimental degradation data at hand. Simple qualitative trends in the degradation of molecular weight and mass loss were found to relate to the underlying hydrolysis mechanisms. These trends are that: (i) a deceleration of molecular weight reduction versus time indicates random scission whereas a lack of the deceleration indicates end scission; (ii) autocatalytic hydrolysis is indicated by a nonlinear relationship between ($1/M_n$) and time; (iii) mass loss while the polymer is still medium to high molecular weight indicates end scission; and (iv) a linear increase in mass loss with time indicates noncatalytic end scission. The experimental degradation data from 31 publications was analysed to identify the most likely hydrolysis mechanisms, using either the qualitative analysis mentioned above or detailed model fittings. The analysis found that: (i) a combination of random and end scission is almost always predicted to occur; (ii) molecular weight reduction is always due to random scission; (iii) mass loss is due to end scission; and (iv) autocatalytic hydrolysis is expected more often than noncatalytic hydrolysis. The effects of initial molecular weight and residual monomer are important but are not investigated in this chapter in order to maintain simplicity. They are analysed in detail in the next chapter.

Chapter 7: The effects of initial molecular weight and residual monomer on degradation mechanisms of bioresorbable polyesters

The mathematical model that is presented in Chapter 5 is extended in the previous chapter in order to allow the effects of individual hydrolysis mechanisms to be studied in detail. The same model is used in this chapter in order to analyse the effects of initial molecular weight and residual monomer in biodegradable polymers. These are both important factors, which are not currently fully understood. Residual monomer is of particular importance and has received more attention in the literature recently. The use of the mathematical model to increase current understanding is of great interest to the biomaterials field. This chapter has been published in Acta Biomaterialia [99].

7.1 Introduction

Initial molecular weight significantly affects degradation of bioresorbable polymers, as has been shown by several experimental publications [8, 29-31, 88, 89]. If the initial molecular weight of biodegradable polymers varies by an order of magnitude, so too does the number of polymer chains and therefore the number of scissions required to halve molecular weight. In addition, the ratio of end scission to random scission is likely to be higher for lower molecular weight samples, which have a higher ratio of bonds at the chain ends. Mass loss may also be affected by initial molecular weight since more monomers will be produced if there is a greater number of chain ends, due to a greater rate of end scission. Experimental results in which samples of different initial molecular weights show the same trends should actually be interpreted as evidence for different rates of chain scission. The effect of initial molecular weight depends of the type of hydrolysis, including noncatalytic random scission, autocatalytic random scission, noncatalytic end scission and autocatalytic end scission. These hydrolysis mechanisms are discussed in detail in the previous chapter of this thesis, using a mathematical model. The mathematical model simulates bulk mass loss due to the diffusion of monomers or oligomers out of the polymer. Significant mass loss due to surface erosion is not typically expected for the polymers considered in this chapter. In addition, substantial mass loss may occur when the polymer begins to break apart in the very late stages of degradation, by which time the model is no longer valid. A monomer is produced by each end scission whereas oligomers are produced when a random scission occurs near a chain end. One aim of this chapter is to understand the effects

of initial molecular weight and relate them to the fundamental hydrolysis mechanisms. Simulations are conducted using the mathematical model that is presented in the previous chapter of this thesis.

A polymer may contain residual monomer that remains from polymerisation or is thermally generated from processing techniques such as melt extrusion. The initial monomer content in biodegradable polymers has been shown to have an impact on the degradation trends [18, 23, 87, 88]. In all experiments of which the author of this thesis is aware, the rate of degradation has been accelerated by an increased initial monomer content. The acceleration can be substantial. In the experiments of Paakinaho et al. [18] residual monomers accelerated the rate of degradation of inherent viscosity and strength by approximately one order of magnitude. The experimental data in the literature [18, 23, 87, 88] support the theory of autocatalysis, in which the degradation is catalysed by the acid chain ends of residual monomers. The initial monomer is not expected to affect degradation that is purely noncatalytic in nature. In this chapter, the effect of residual monomer is analysed by simulations with the mathematical model detailed in the previous chapter. It should be noted that many of the experimental degradation studies before the year 2000 could have high residual monomer contents, due to their processing conditions, although this was rarely measured and thus not detailed in the publications. It is of critical importance that residual monomer is measured or removed for future experiments of biodegradable polymers in order for their degradation characteristics to be fully analysed.

Initial molecular weight and residual monomer were chosen for analysis because they have a significant effect on degradation and are not fully understood. As a result of the lack of clear understanding, these factors are often not discussed in the analysis of experimental data. The simple trends identified in this work can be used to estimate the effects of both factors. The mathematical model is ideally suited for the analysis of initial molecular weight and initial monomer content because both factors are directly implemented in it. Initial molecular weight is almost always stated in experimental publications. Therefore the findings of this chapter can be used when analysing historical experimental data. Although residual monomer is not always measured, it can be estimated to some degree if polymer processing conditions are known in detail, and it has been measured more often in recent years.

In this chapter the effects of initial molecular weight and residual monomers are modelled, neither of which are fully understood at present. The mathematical model, presented in the previous chapter, is fitted to experimental data containing various weight fractions of initial monomer, and also to experimental data containing various initial molecular weights. The experimental data discussed in this chapter are for poly(lactide) or poly(glycolide) homo- and copolymers because a large proportion of experimental publications consider these polymers in the literature. The fittings serve to demonstrate the ability of the model to consider both factors and to relate the degradation trends to the underlying hydrolysis mechanisms. The author is not aware of any models for chain scission of biodegradable polymers that have included initial monomer content to date. It should be noted that the mathematical model used here is purposely over complicated. The intention here is to use the model to (a) identify the individual hydrolysis mechanisms that are prominent in experimental studies and (b) understand the effect of various factors with regards to specific hydrolysis mechanisms. Once the effects of each individual factor are understood, it is then possible to simplify the model by eliminating the unimportant factors. The purpose of simulations in this chapter is to understand experimental results rather than to predict the degradation based on simple information such as the polymer type, polymer microstructure, molecular weight distribution and degradation medium.

7.2 The mathematical model

The mathematical hydrolysis model is described in the previous chapter of this thesis. Eqs. 7.1 to 7.5 here are only repeated to help explain how initial molecular weight and residual monomer affect the model. All the model parameters and units are defined at the start of this thesis for reference. The rate of random scission R_{rs} is given by

$$\frac{dR_{rs}}{dt} = k_{r1}C_e + k_{r2}C_e\left(\frac{C_{acid}}{1-X_c}\right)^n \qquad 7.1$$

and the rate of end scission R_{es} is given by

$$\frac{dR_{es}}{dt} = k_{e1}C_{end} + k_{e2}C_{end}\left(\frac{C_{acid}}{1-X_c}\right)^n \qquad 7.2$$

which differs from Eq. 7.1 in that the reactant is chain ends C_{end} for end scission instead of amorphous ester bonds C_e for random scission. Separate reaction constants are used for noncatalytic random scission k_{r1}, autocatalytic random scission k_{r2}, noncatalytic end scission k_{e1}, and autocatalytic end scission k_{e2}. Initial molecular weight affects the rate of end scission from the outset since for a lower initial molecular weight there are more initial chains N_{chain0} and therefore more chain ends as given by

$$C_{end} = 2N_{chain} = 2N_{chainO} + 2\left(R_{rs} - \left(R_{ol}/m\right)\right) \quad 7.3$$

in which the concentration of random scissions R_{rs} and ester units in oligomers R_{ol} are both zero at the start of degradation. The rate of end scission therefore increases linearly with the number of chains and inversely with initial molecular weight. The rate of random scission in Eq. 7.1 does not increase in the same manner because it is not directly dependent on the number of chain ends. The ratio of end scission to random scission therefore increases. If molecular weight reduction is due to random scission and mass loss is due to end scission as suggested in the previous chapter of this thesis, mass loss may be expected to occur earlier for a lower initial molecular weight. A greater rate of end scission results in more monomers C_m and therefore a greater concentration of acid catalyst C_{acid} as given by

$$C_{acid} = C_m + \left(C_{ol}/m\right) \quad 7.4$$

This means the rate of autocatalytic hydrolysis increases, for both random and end scission, and the ratio of autocatalytic to noncatalytic scissions increases. Another major effect of increasing the value of N_{chain0}, due to lower initial molecular weight, is that the relative increase of N_{chain} due to each random scission is reduced. In other words, increasing the terms in brackets on the right hand side of Eq. 7.3 during degradation becomes less significant as N_{chain0} increases. This affects the degradation of number averaged molecular weight, calculated by

$$M_n = \frac{\left(C_e + \omega X_c\right)M_0}{N_{chain}} \quad 7.5$$

which depends primarily on the increase of N_{chain}. For a lower initial molecular weight the effect of each random scission on M_n is reduced. The balance between an

increased rate of random scission and reduced relative effect of each random scission depends on the values of the reaction rate constants k_{r1}, k_{r2}, k_{e1} and k_{e2}.

As the initial monomer content increases, the initial concentration of acid catalyst also increases since C_m increases in Eq. 7.4. This results in two main effects: 1) the rate of autocatalytic chain scission increases, and so too therefore does the rate of M_n reduction and ratio of autocatalytic to noncatalytic hydrolysis, and 2) the relative increase in C_{acid} for the same number of scissions is reduced since C_m has a larger initial value in Eq. 7.4. As a result of point 2, the rate of autocatalytic random scission does not increase to such a great extent during degradation. Point 1 may shift the molecular weight - time curve, as discussed in the previous chapter, from noncatalytic to autocatalytic in appearance. Point 2 may have the opposite effect. The balance between these effects depends on the reaction rate constants k_{r1}, k_{r2}, k_{e1} and k_{e2}.

7.3 The effect of initial molecular weight

The effect of initial molecular weight on the degradation of molecular weight and mass loss is analysed for several different types of hydrolysis including noncatalytic random scission, autocatalytic random scission, noncatalytic end scission and autocatalytic end scission. Molecular weight degradation is characterised by the molecular weight half-life. It is often the case that polymer samples show zero mass loss for a long period at the start of degradation [5, 7, 9, 10]. An indication of the likely duration of this delay before mass loss onset is characterised here by the time taken for water-soluble monomers and oligomers to account for 10% of the total polymer weight. To simplify the results, the simulations are amorphous unless fitting experimental data for crystallinity. Similarly, diffusion of water-soluble small chains has been previously studied by Wang et al. [50], and hence is not considered here unless fitting experimental data for mass loss. The model is also fitted to experimental data for various initial M_n, which is used here to indicate the molecular weight of the samples at the start of degradation, after all processing and sterilisation. Model constants that are used for all simulations in this chapter, unless otherwise stated, are given in Table 7.1. As in the simulations in the previous chapter of this thesis, the value of initial monomer is set as zero ($10^{-10}\,C_{e0}$ or 10^{-8} wt.% for numerical reasons) for all simulations unless measured experimentally. This value is not varied in this section in order to focus on the effect of initial molecular weight. The accuracy of fittings to experimental data is not affected if a high concentration of initial monomer is assumed as demonstrated the

previous chapter. All parameters related to crystallinity are set to zero for amorphous simulations.

Constant	Units	Value
C_{e0}	mol m^{-3}	17300
n	no units	0.5
M_0	g mol^{-1}	72
α	no units	28
β	no units	2
m	no units	4
Variables	**Units**	**Initial Values**
R_{ol} R_{rs} R_{es} R_s C_{ol}	mol m^{-3}	0
R_m C_m	mol m^{-3}	10^{-10} C_{e0}
C_e	mol m^{-3}	C_{e0} - (C_m + ωX_c)

Table 7.1 Model constants and initial variable values used in simulations in this chapter

7.3.1 Simulations to identify the effect of initial molecular weight on molecular weight reduction

Scenarios for the effect of initial M_n on the molecular weight half-life for each individual hydrolysis mechanism are shown in Fig. 7.1 Each time initial molecular weight is halved the M_n half-life is halved for end scission (k_{r1}=k_{r2}=0), doubled for noncatalytic random scission (k_{r2}=k_{e1}=k_{e2}=0), and increased by 10-15% for autocatalytic random scission (k_{r1}=k_{e1}=k_{e2}=0). For noncatalytic random scission, samples of different initial molecular weight have the same rate of chain cleavage. However, polymers with higher initial M_n have fewer chains, and hence the effect of each random scission on molecular weight is greater. There is an inverse relationship between M_n half-life and initial molecular weight. In autocatalytic random scission, this effect is offset by the fact that for a lower initial molecular weight more oligomers are produced, since more scissions are required to equally reduce M_n, which accelerate the rate of chain scission. For pure end scission the M_n half-life increases linearly with initial M_n.

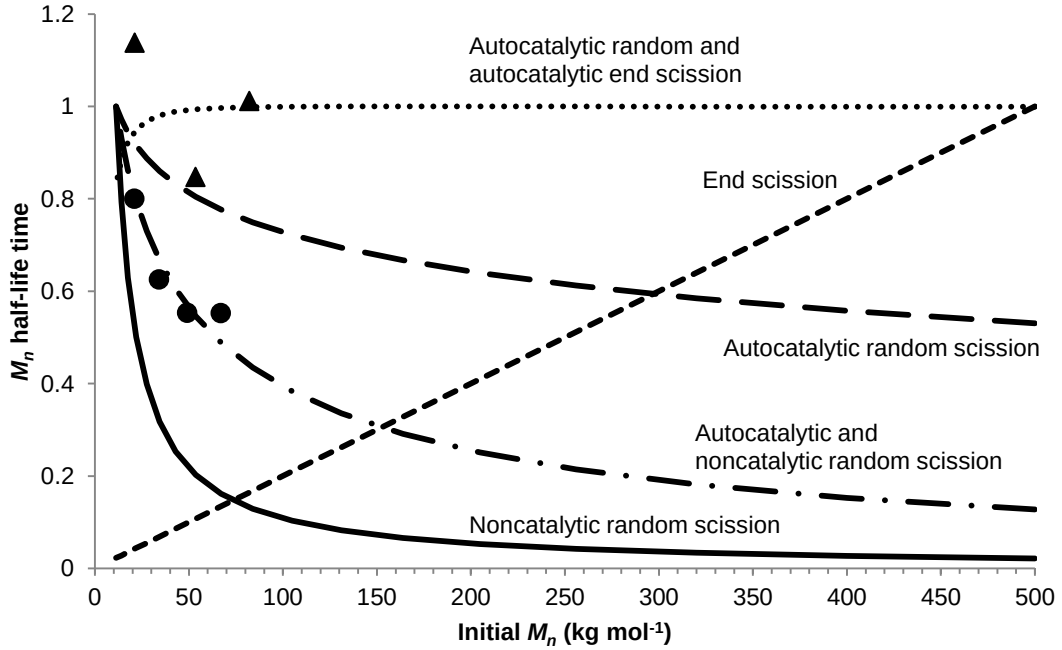

Fig. 7.1 Scenarios for M_n half-life versus initial molecular weight for various theories of hydrolysis: noncatalytic random (solid); autocatalytic random (long dash); a combination of autocatalytic and noncatalytic random (k_{r2}/k_{r1}=10, dash-dot); either autocatalytic or noncatalytic end (short dash); and a combination of autocatalytic random and autocatalytic end (k_{e2}/k_{r2} = 3000, dotted). Experimental data for poly(lactide-co-glycolide) by Raman et al. [29] (circles) and poly(lactide) by Pitt et al. [30] (triangles) are included for reference.

Experimental data by Raman et al. [29] and Pitt et al. [30] are included in the figure. The data points are arbitrarily normalised to suit the existing curves. The curve for combined autocatalytic and noncatalytic random scission (k_{e1}=k_{e2}=0) has the reaction rate ratio k_{r2}/k_{r1}=10 and the curve for combined autocatalytic random and autocatalytic end scission (k_{r1}=k_{e1}=0) has the reaction rate ratio k_{e2}/k_{r2}=3000. The same reaction rate ratios are used in the fittings of the model to the experimental data in the next section. The autocatalytic random scission curve may be interpreted to fit the data of Pitt et al. [30], as opposed to a combination of random and end scission, but mass loss data does not support this theory as discussed shortly. There is almost no dependence of M_n half-life on initial molecular weight for a combination of autocatalytic random and autocatalytic end scission. The effect of increasing the rate of end scission at a lower initial M_n, and therefore the rate of autocatalytic random scission, offsets the effect of more random scissions being required to reduce normalised molecular weight.

7.3.2 Simulations to identify the effect of initial molecular weight on mass loss

Fig. 7.2 shows scenarios for the effect of initial molecular weight on the time taken for 10% of the total polymer weight to be water-soluble for various hydrolysis mechanisms. For end scission (k_{r1}=k_{r2}=0), the rate of production of monomers is linearly related to the number of chain ends, and thus the time taken for monomers to account for 10% of the polymer increases linearly with initial molecular weight. For random scission however (k_{e1}=k_{e2}=0), initial molecular weight has negligible effect because the number of random scissions required to reduce M_n from a typical high initial value (i.e. $3x10^5$ g mol^{-1}) to a typical low initial value (i.e. $3x10^4$ g mol^{-1}) is small compared to the number of scissions required to convert 10% of the polymer to oligomers. The trends are not affected by whether hydrolysis is noncatalytic or autocatalytic for either random or end scission. A curve for combined autocatalytic random and autocatalytic end scission (k_{r1}=k_{e1}=0) is shown for the reaction rate ratio k_{e2}/k_{r2}=3000, which is the same as that used in the fitting of the model to the experimental data of Pitt et al. [30] in the next section. It could be argued that the experimental data points may fit to the end scission curve if they are normalised to an alternative value. However, the M_n half-life data from the same experiments, shown on Fig. 7.1, do not resemble the curve for end scission in that figure.

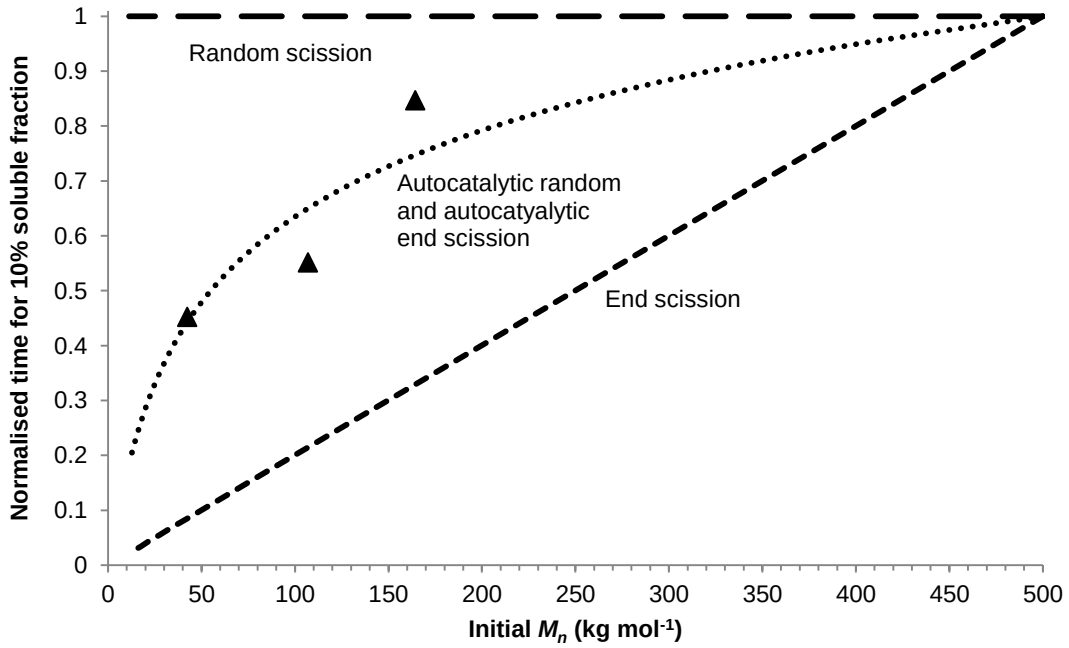

Fig. 7.2 Scenarios for the time until 10% of the polymer is water-soluble versus initial molecular weight is shown for various theories of hydrolysis: random scission (long dash), end scission (short dash), and an autocatalytic combination of both with a reaction rate ratio of k_{e2}/k_{r2} = 3000 (dotted). Experimental data for poly(lactide) by Pitt et al. [30] (triangles) are included for reference.

7.3.3 Fitting the model to experimental data

Having identified the underlying mechanism, the model is used to fit the experimental data of Raman et al. [29] and Pitt et al. [30], which both consider the effect of initial molecular weight. The reaction rate ratios that are used in the fittings are also used for simulations in Fig. 7.1 and Fig. 7.2. Raman et al. [29] conducted degradation experiments on amorphous 50 μm poly(DL-lactide-co-glycolide) microspheres of various initial molecular weights in phosphate buffer solution (PBS) pH 7.4 at 37°C. The initial molecular weights were 67000, 49000, 34000 and 21000 g mol^{-1}, for which the values of N_{chain0} in the model are 16.8, 22.9, 33.0 and 53.4 mol m^{-3} respectively. The model setup is the same as the previous section and Table 7.1 except M_0=65 g mol^{-1}, which is the average molar mass of poly(lactide) and poly(glycolide). Fig. 7.3 shows that the model is able to fit the experimental data for a combination of noncatalytic and autocatalytic random scission as indicated by Fig. 7.1 The reaction rates are k_{r1} = 3x10^{-5} day^{-1}, k_{r2} = 3x10^{-4} $[mol^{-1}m^3]^{0.5}day^{-1}$ and k_{e1} = k_{e2} = 0. The same model parameters are used for all data sets except for N_{chain0}, which represents initial M_n. This demonstrates the ability of the model to consider the effect of initial M_n. The fitting must use a combination of autocatalytic and noncatalytic random scission but cannot be improved by including end scission. For noncatalytic random scission alone (k_{r2}=k_{e1}=k_{e2}=0), M_n degrades too quickly for the samples with high initial M_n, and for autocatalytic random scission alone (k_{r1}=k_{e1}=k_{e2}=0), M_n degrades too slowly for the samples with high initial M_n.

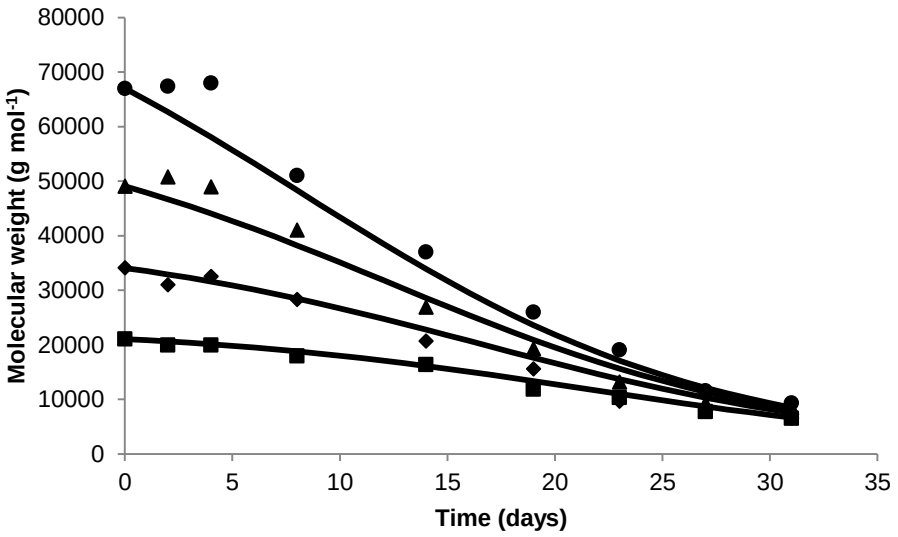

Fig. 7.3 Model fitting of molecular weight versus time for a combination of noncatalytic random and autocatalytic random scission. Discrete points represent experimental data [29] for various initial molecular weights and solid lines represent the model fitting.

Poly(DL-lactide) films of approximately 0.1 mm thickness were degraded *in vivo* by Pitt et al. [30]. The values of initial number averaged molecular weight were approximately 42000, 107000 and 164000 g mol^{-1}, for which the values of N_{chain0} in the model are 29.3, 11.6 and 7.57 mol m^{-3} respectively. All other parameters are the same for all three data sets. A fitting of the mathematical model for a combination of autocatalytic end scission and autocatalytic random scission is shown in Fig. 7.4. The model setup is given in Table 7.1. Simulations are amorphous throughout, and thus all crystallinity terms are set to zero. Diffusion is included in order model mass loss and the diffusion coefficients are $D_0 = 10^{-11}$ m^2 $week^{-1}$ and $D_{pore} = 10^{-7}$ m^2 $week^{-1}$. Initial porosity is set to zero. The polymer film is represented by 200 finite difference nodes. Reaction rates are k_{r2} = 1.25×10^{-5} $week^{-1}$, $k_{e2} = 3.75 \times 10^{-2}$ $[mol^{-1}m^3]^{0.5}week^{-1}$ and $k_{r1} = k_{e1} = 0$. The experimental samples have very similar M_n half-lives but mass loss occurs earlier for samples with lower initial M_n. The model is able to simulate these degradation behaviours by using a combination of end scission and random scission as would be identified by simple analysis of Fig. 7.1 and Fig. 7.2. Mass loss data for the model is not shown to a high percentage because the model is not designed for high mass loss, at which time parts of the polymer may break away and the water-soluble chains may be able to diffuse through cracks in the polymer as opposed to through the polymer material.

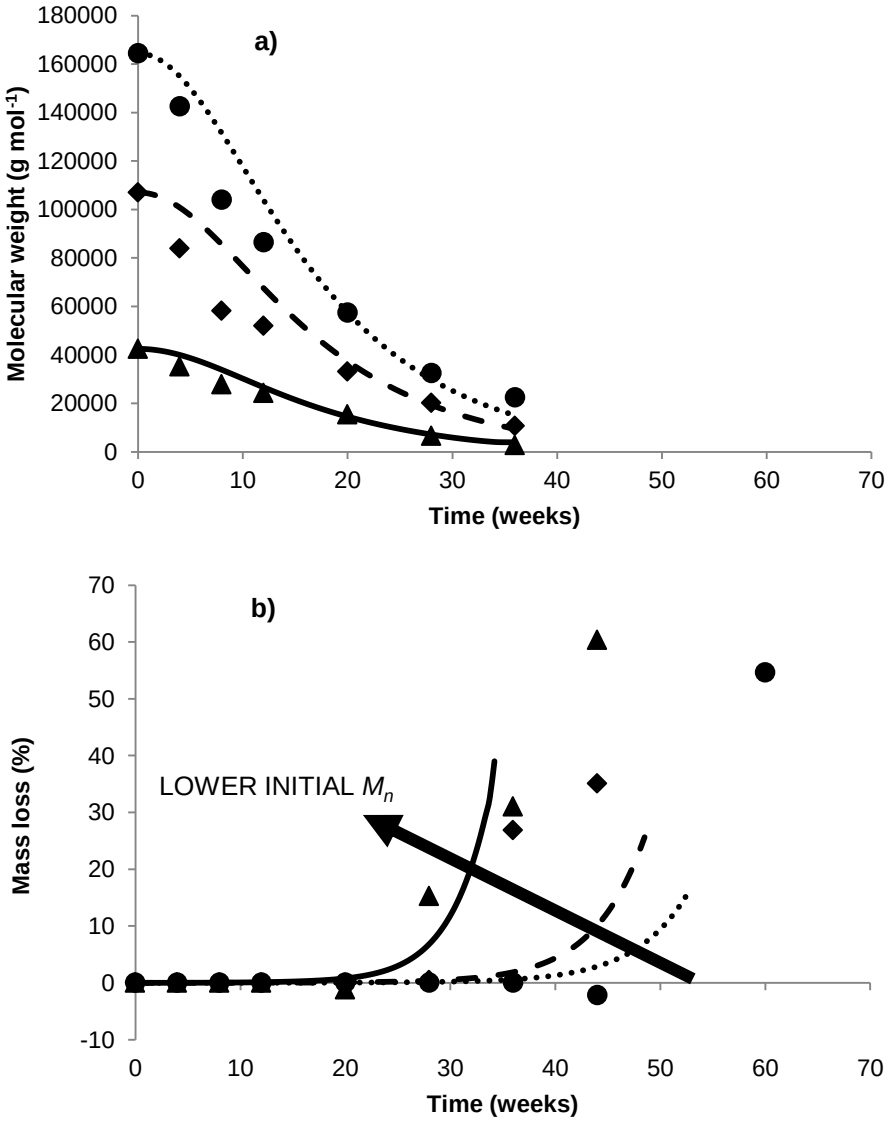

Fig. 7.4 Model fitting of a) molecular weight and b) mass loss versus time for a combination of autocatalytic random and autocatalytic end scission. Lines represent the model fitting and discrete points represent experimental data [30] for various initial M_n: 42000 (triangle, solid line), 107000 (diamond, dashed line) and 164000 g mol^{-1} (circle, dotted line).

The analyses on M_n half-life and time to mass loss onset in Fig. 7.1 and Fig. 7.2 do not consider the shape of the molecular weight - time curves. As discussed in the previous chapter of this thesis, the shape depends strongly on the type of hydrolysis. The fittings here must use the correct combination of hydrolysis mechanisms to 1) model the differences between degradation of samples with different initial molecular weights, and 2) model the shape of the molecular weight - time curves. The shapes of the molecular weight - time curves in Fig. 7.3 and Fig. 7.4 bear a good resemblance to the experimental data. The fittings for both sets of data are shown with normalised molecular weight in Fig. 7.5. This figure emphasises the trend seen in Fig. 7.1 that in

the experiments of Pitt et al. [30] (Fig. 7.5 (b)) all samples degrade at a similar rate for normalised M_n, regardless of initial molecular weight, whereas in the experiments of Raman et al. [29] (Fig. 7.5 (a)) there is a reduced rate of M_n degradation for samples with lower initial molecular weight. In the fittings to both sets of experimental data, the model finds a significantly increased rate of random chain scission in the samples of lower initial molecular weight. This is due to greater production of oligomers or monomers and is necessary in order to prevent the molecular weight of the high initial molecular weight samples reducing too quickly compared to the low initial molecular weight samples. For a combination of autocatalytic and noncatalytic hydrolysis, the samples of lower initial molecular weight therefore have a greater ratio of autocatalytic to noncatalytic hydrolysis, which can be seen in the slight shift of curves in Fig. 7.5 (a) from a noncatalytic shape to an autocatalytic shape, as detailed in the previous chapter of this thesis.

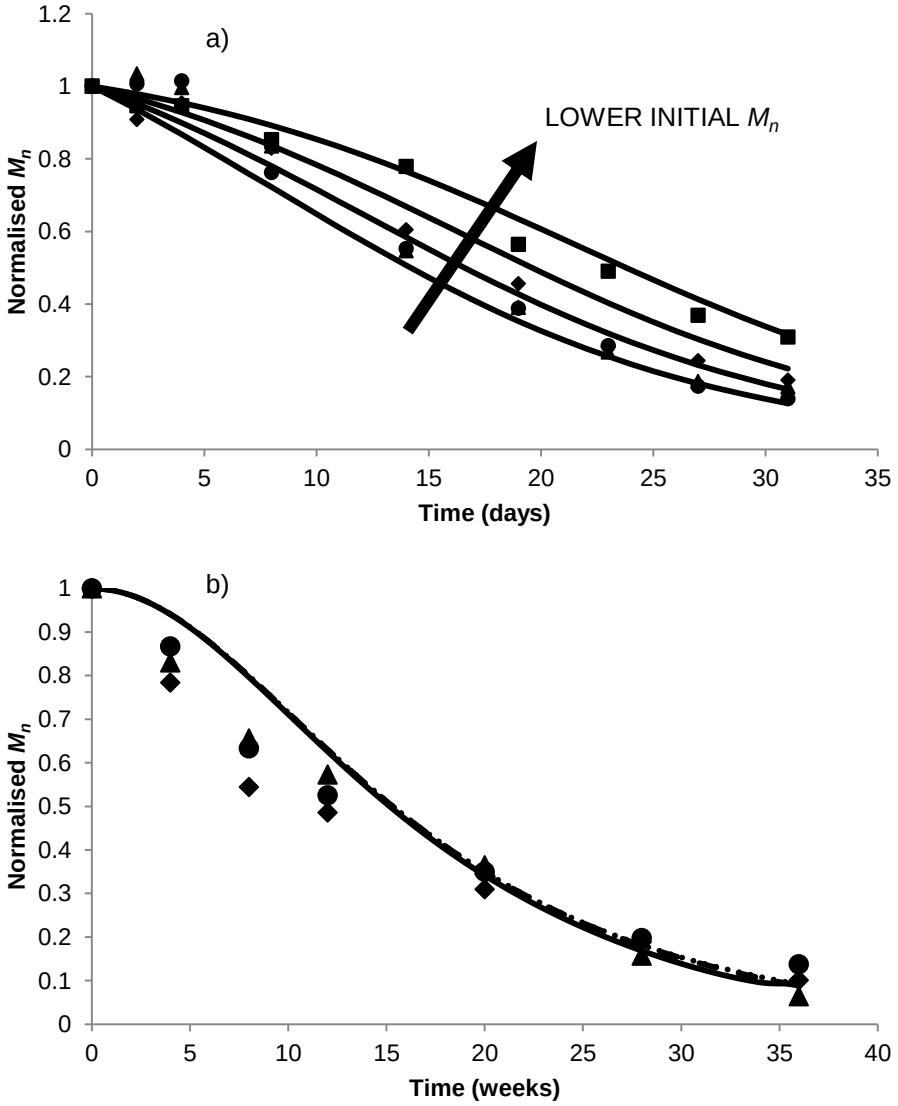

Fig. 7.5 Alternative presentation with normalised M_n for a) the fitting shown in Fig. 7.3 and b) the fitting shown in Fig. 7.4. The shapes of discrete symbols and line types are the same as used previously.

7.3.4 Review of other publications for the effect of initial molecular weight

The two sets of experimental data that have already been discussed [29, 30] demonstrated different effects of initial M_n. Other publications which also consider initial molecular weight are discussed here. Migliaresi et al. [8] studied the degradation of 3 mm rods of amorphous poly(L-lactide) with initial weight average molecular weights of 27000 and 177000 g mol^{-1} in Ringer solution at 37°C. The molecular weight half-lives were approximately 100 days for both samples, and thus Fig. 7.1 suggests a combination of autocatalytic random scission and autocatalytic end scission may give a good fitting of the model to experimental data. Huttunen [88] compared the degradation of 4 mm rods of poly(L-lactide-co-D-lactide) 96L:4D and poly(L-lactide-co-

DL-lactide) 80L:20DL in PBS pH 7.4 at 37°C with initial inherent viscosities varying from 1.45 to 4.98 dl g^{-1}. The experimental data is only given for the early stages of degradation but the inherent viscosity half-lives are similar for all samples, or perhaps slightly shorter for the samples with lower initial inherent viscosities. By comparison to Fig. 7.1, it can be seen that a good fitting may be achieved by a combination of autocatalytic random scission and autocatalytic end scission. Witschi and Doelker [100] conducted experiments on 3-5 μm microspheres of poly(lactide-co-glycolide) 50:50 in PBS pH 7.4 at 37°C. The samples identified as RG-502 SD/WOW and RG-504 SD/WOW have the same copolymer ratio but different initial number average molecular weights of ≈6750 and ≈13000 g mol^{-1} respectively. The lower molecular weight samples have similar or slightly longer M_n half-lives, which suggests autocatalytic random scission is likely according to Fig. 7.1. Grizzi, Li and Vert [22, 41] conducted degradation experiments of 2mm thick poly(DL-lactide-co-L-lactide) plates in PBS pH 7.4 at 37°C. The polymers had initial weight average molecular weights of approximately 43000 and 65000 g mol^{-1}. The time to the onset of mass loss is 5-9 weeks for the 43000 g mol^{-1} sample and ≈7 weeks for the 65000 g mol^{-1} experiment. Given that the onset of mass loss occurs at similar times for both samples, Fig. 7.2 suggests that random scission without end scission is likely. Molecular weight data for the 65000 g mol^{-1} sample is too infrequent for comparison to Fig. 7.1. Pistner et al. [31] carried out degradation experiments of 2 mm thick amorphous poly(L-lactide) rods *in vivo* with initial number average molecular weights of 132000 and 197000 g mol^{-1}. There is an approximately inverse relationship between M_n half-life and initial molecular weight, which suggests noncatalytic random scission is dominant according to Fig. 7.1. Both samples begin to demonstrate mass loss at 42.5 weeks, which suggests random scission is responsible for mass loss according to Fig. 7.2. Hyon et al. [23] conducted experiments for the degradation of 0.5 mm strips of poly(DL-lactide) with initial weight average molecular weights of 7000, 12000 and 43000 g mol^{-1}. The samples were manufactured via different techniques and were expected to have varying concentrations of residual monomer, which significantly affects degradation. Caution must therefore be taken when analysing the effect of initial molecular weight. The increased rate of degradation for lower molecular weight samples was attributed to an increased initial concentration of residual monomers. The effect of residual monomer is discussed in the next section of this chapter, the findings of which agree with that theory. In the experiments, samples with lower initial M_n demonstrated shorter M_n half-lives and more accelerated mass loss. These trends are expected for a combination of autocatalytic random scission and autocatalytic end scission according to Fig. 7.1 and

Fig. 7.2. It may be the case that both initial molecular weight and residual monomer affected the results in a similar manner.

In the above analysis, the hydrolysis mechanisms suggested by comparison of experimental data to Fig. 7.1 and Fig. 7.2 agree with those suggested in the previous chapter of this thesis. This supports the trends identified in Fig. 7.1 and Fig. 7.2 along with ability of the model to consider the effect of initial molecular weight. It also supports the findings in the previous chapter that random scission is responsible for the reduction of molecular weight and that autocatalytic hydrolysis may be more prevalent in degradation experiments than noncatalytic hydrolysis. One set of experiments that do not fit the expected trends predicted by the model are those of Park [89], which consider 10 μm microspheres of poly(DL-lactide). The degradation rate of a high molecular weight sample was negligible compared to that of a low molecular weight sample. However, the values of initial number average molecular weight (900-1300 g mol^{-1}) are orders of magnitude lower than typical experimental poly(lactide), which resulted in one sample being beneath the glass transition temperature. The samples also contained high quantities of low molecular weight chains, which may have significantly affected hydrolysis in a similar manner to that discussed in the next section for residual monomers.

7.4 The effect of residual monomers

Residual monomer significantly affects degradation if autocatalytic hydrolysis is assumed to occur [18, 23]. Noncatalytic hydrolysis will by definition be unaffected. The model is used here to predict the effect of initial monomer content on the molecular weight half-life for autocatalytic hydrolysis. The model is also fitted to experimental data to demonstrate the ability of the model to consider residual monomer.

The effect of initial monomer content on the M_n half-life is shown in Fig. 7.6 for autocatalytic random scission, autocatalytic end scission, and a combination of both with reaction rate ratios k_{e2}/k_{r2} =10, 10^2, $3x10^2$ and 10^3. The model setup is the same as that given in Table 7.1 except the initial monomer fraction varies from $C_m = R_m = 10^{-1}$ C_{e0} to 10^{-7} C_{e0}. The noncatalytic reaction rates are set to zero (k_{r1}=k_{e1}=0) and N_{chain0} = 42.4 mol m^{-3}. The simulation is assumed to be amorphous throughout with no diffusion, and hence all model parameters related to crystallinity and diffusion are set to zero. If molecular weight reduces due to random scission (as is the case in curves A-E in Fig. 7.6) there is an inverse square root law relationship between M_n half-life and initial monomer fraction above a critical monomer content, which depends on the ratio of end

scission to random scission. This relationship can be derived analytically from the mathematical model. Experimental data for the inherent viscosity half-life of poly(lactide-co-glycolide) with various initial monomer contents [18] is included in the figure and can be seen to follow the predicted trend for autocatalytic random scission and autocatalytic end scission until the initial monomer content is increased above 2%. The reaction rate ratio for the dotted line is the same as that used in the fitting of the model to the experimental data for molecular weight, crystallinity and mass loss later in this section (k_{e2}/k_{r2} = 3x10^2). It can be seen to fit through the experimental data points well. The model appears to be suitable for initial monomer contents up to 2% in Fig. 7.6, a value for which the initial monomer content due to typical processing techniques can and should fall well below in order to ensure that products display reliable and repeatable *in vivo* behaviour. According to the literature, the release of monomers from biodegradable polymers causes a decrease in pH in the tissue adjacent to the product, which has been suggested to have adverse effects in clinical applications [34-38]. Therefore it is advisable to minimise the initial monomer content to enhance biocompatibility. The cause of the two samples with highest initial monomer contents having lower than predicted M_n half-lives cannot be explained by the model. It may be due to factors that are out of scope for the model such as changes in the polymer structure or the development of monomer-filled pores, as found in a previous study [23]. The mathematical model assumes that monomers are evenly distributed amongst the amorphous phase.

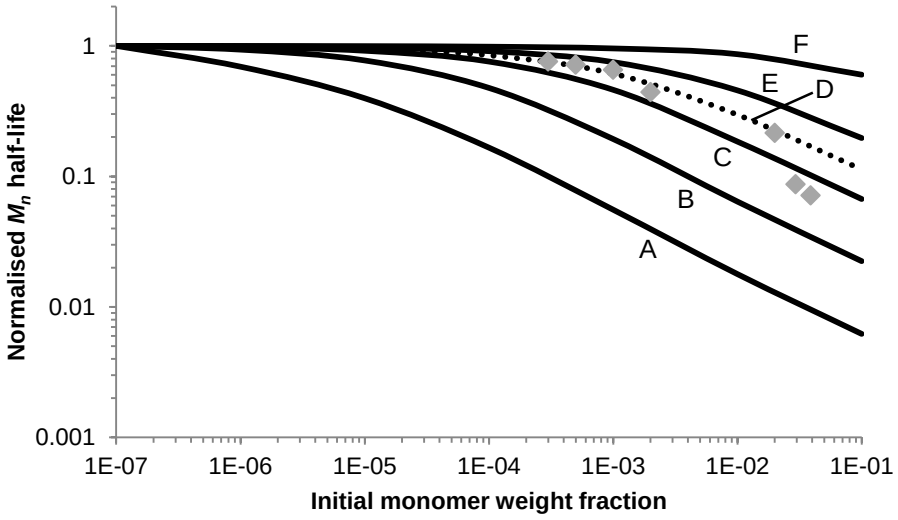

Fig. 7.6 Time to halve molecular weight versus initial monomer weight fraction for autocatalytic hydrolysis varying from random scission (A) to end scission (F). The end:random scission rate ratios (k_{e2}/k_{r2}) for combined simulations are 10 (B), 100 (C), 300 (D) and 1000 (E). Discrete points are experimental data [18].

To test the ability of the mathematical model to incorporate initial monomer fraction, it is fitted to the experimental data of Paakinaho et al. [18] for inherent viscosity, crystallinity and mass loss. In the experiments, 1.6mm poly(L-lactide-co-glycolide) 85L:15G rods containing different fractions of initial monomer were degraded in 37°C Sörensen buffer solution. The initial monomer contents were 0.03%, 0.05%, 0.1% and 0.2%, for which initial crystallinity X_c = 0.029, 0.067, 0.035 and 0.033 and N_{chain0} = 42.4, 46.9, 52.4 and 46.9 respectively. These values are derived from experimental measurements. The values of N_{chain0} represent initial molecular weights of 2.94, 2.66, 2.38 and 2.66 x10^4 g mol^{-1}. These values are estimated through a linear relationship to initial inherent viscosity of M_n = 27900 I.V. – 6890, in which the units of M_n and I.V. are g mol^{-1} and dL g^{-1}. It is the linear best fit for 22 data points of poly(L/D lactide) 96/4 with I.V. < 4 dL g^{-1} [87, 101]. The values of all other model parameters do not vary between the data sets and are given in Table 7.1 and Table 7.2 except C_m = R_m = C_{e0} x 0.003, 0.005, 0.01 and 0.02 mol m^{-3} to reflect residual monomer and a value of n = 0.67 gives the best fitting. The initial values of porosity and extended crystallinity are zero. There are 200 finite difference nodes to represent the rod diameter. Diffusion is included in the model in order to model mass loss due to small water-soluble chains leaving the polymer. The model is only being fitted to the four samples in which the monomer was produced during processing, and for which mass loss was measured. In the other three samples, the monomer was added manually and may have a slightly different effect on degradation if, for example, monomer-filled pores develop as previously seen [23]. In the fitting, the reduction of normalised molecular weight (mathematical model) is compared to normalised inherent viscosity (experimental data) since molecular weight was not measured. The model is able to fit the data as can be seen in the fitting in Fig. 7.7. That the same set of model parameters is used for all samples demonstrates the ability of the model to simulate the effect of initial monomer at least up to 0.2%. In the fitting, the noncatalytic reaction rates can be set to zero, which suggests that chain cleavage due to noncatalytic hydrolysis is negligible compared to that of autocatalytic hydrolysis. This is to be expected since the initial monomers greatly increase the rate of autocatalytic scission, as can be seen in Fig. 7.6. by the effect of initial monomer on the molecular weight half-life. The fittings of M_n to inherent viscosity are shown together in Fig. 7.8. The experimental data for the 2-4% initial monomer samples, to which the model is not fitted, are also included for reference. As the initial monomer weight fraction increases, the catalysing carboxylic chain ends, which are produced during hydrolysis, make up a smaller fraction of the total concentration of catalyst. As a result, the catalyst, and therefore the rate of chain scission, does not increase to such an

extent during degradation and the molecular weight - time curves shift from autocatalytic (degradation rate accelerating) towards noncatalytic in appearance, as shown in Fig. 6.1 in the previous chapter. Although the molecular weight - time curves shift towards noncatalytic in appearance, the results still support a theory of autocatalytic hydrolysis because the monomers catalyse the hydrolysis. It is simply the case that the negligible increase in catalyst during degradation results in a similar trend to noncatalytic hydrolysis. One remarkable interpretation of this could be that many experimental publications which appear to demonstrate noncatalytic hydrolysis may have actually undergone autocatalytic hydrolysis but contained high residual monomer. Paakinaho et al. [18] even found the concentration of monomer catalyst to decrease during degradation. This is why the rate of M_n reduction for the 4% sample decelerates to an even greater extent than the curve for noncatalytic random scission in Fig. 6.1 in the previous chapter. In the experiments of Paakinaho et al. [18], the monomer diffused out of the 4% sample at a much greater rate than the 2%, which can be explained by Fick's law for diffusion, in which the rate of diffusion is dependent on the concentration gradient. Therefore it is plausible that the monomer does not diffuse out rapidly in samples with low residual monomer contents such as those of Paakinaho in the range of 0.03-0.2%. It should be noted that if the residual monomer catalyst is assumed to diffuse out of the polymer in the first few weeks, there may still be long term effects because the chain scissions in the first few weeks lead to more chain ends and therefore a greater rate of end scission throughout the duration of degradation.

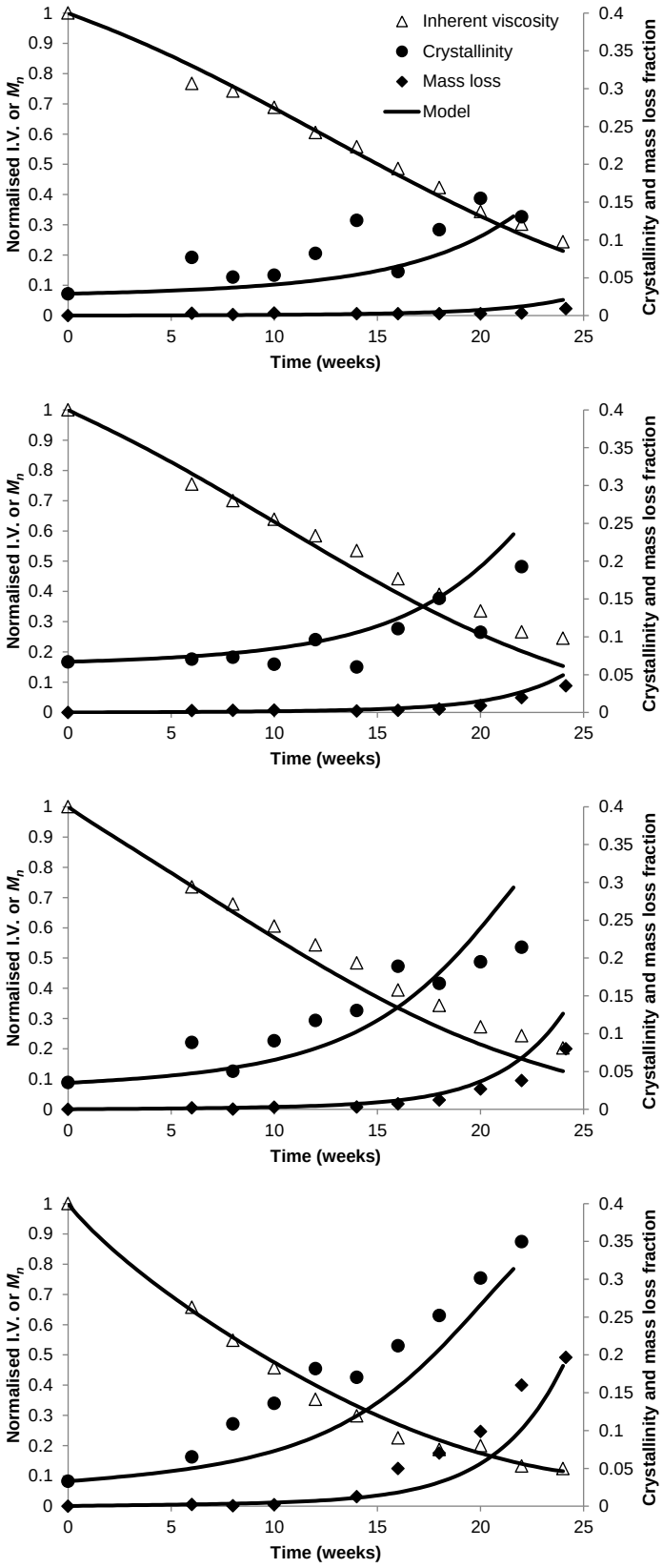

Fig. 7.7 Model fitting to the experimental data [18] with an assumption of a combination of autocatalytic random scission and autocatalytic end scission. Initial monomer contents are a) 0.03%, b) 0.05%, c) 0.1% and d) 0.2%.

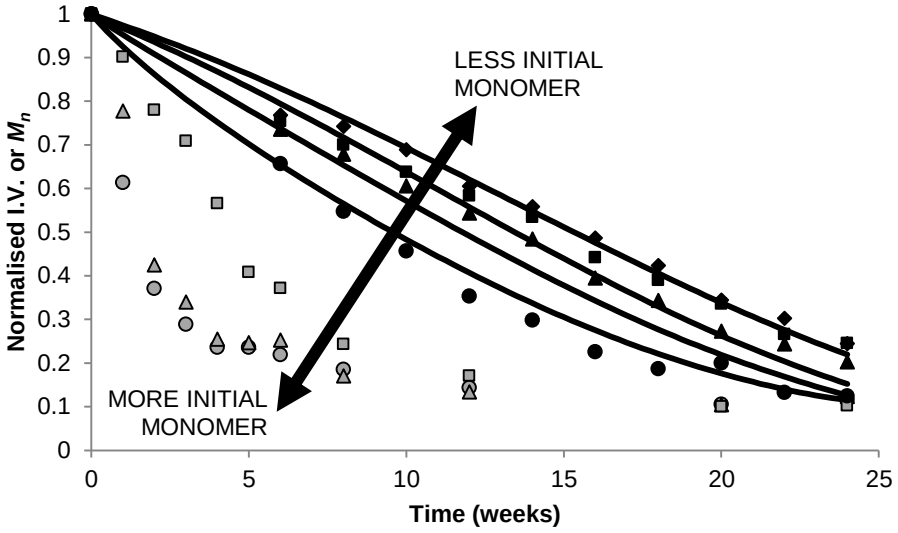

Fig. 7.8 Alternative presentation for the fitting shown in Fig. 7.7. Additional experimental data by Paakinaho et al. [18] is included for three samples with higher initial monomer contents. Initial monomer wt.% are 0.03% (black diamond), 0.05% (black square), 0.1% (black triangle), 0.2% (black circle), 2% (grey square), 3% (grey triangle) and 4% (grey circle).

Parameter	Units	Value	Parameter	Units	Value
C_{e0}	mol m^{-3}	1.73 x10^{4}	M_0	g mol^{-1}	72
D_0	m^2 day^{-1}	2 x10^{-9}	ω	mol m^{-3}	1.73 x10^{4}
D_{pore}	m^2 day^{-1}	2 x10^{-5}	X_{max}	-	0.45
k_{r2}	$[mol^{-1}m^3]^{0.5}day^{-1}$	3.4 x10^{-6}	p_x	-	2 x10^{-4}
k_{e2}	$[mol^{-1}m^3]^{0.5}day^{-1}$	300*k_{r1}	V_c	m^3	4.19 x10^{-4}
k_{e1}, k_{r1}	day^{-1}	0	η_A	mol^{-1}	6.02 x10^{23}

Table 7.2 Parameters used by the model in the data fitting

7.5 Conclusions

The mathematical model presented in the previous chapter of this thesis was used to analyse the effect of initial molecular weight. Various hydrolysis mechanisms were considered, including noncatalytic random scission, autocatalytic random scission, noncatalytic end scission and autocatalytic end scission. It was found that an increase in initial molecular weight resulted in a decreased molecular weight half-life in the case of random scission. The decrease was greater for noncatalytic hydrolysis than autocatalytic hydrolysis. In contrast, for end scission, increasing initial molecular weight resulted in an increased molecular weight half-life. The time taken for significant mass loss increased as initial molecular weight increased if mass loss was attributed to end scission. However, mass loss due to random scission was unaffected by initial molecular weight. The model was able to fit experimental data [29, 30] for molecular weight reduction and mass loss for samples with different initial molecular weights. For the most common combination of hydrolysis mechanisms identified for a large number of data sets in the previous chapter, autocatalytic random scission and autocatalytic end scission, initial molecular weight did not typically affect the molecular weight half-life, although the rate of chain cleavage was affected.

The effect of residual monomer on the degradation was also analysed. For autocatalytic hydrolysis, an inverse square root law was found to relate molecular weight half-life to initial molecular weight. This trend was also identified in experimental data [18] for degradation of samples with different residual monomer contents defined by measurements. The model was able to fit this experimental data by only varying the initial monomer content between fittings. It was found that experimental results for samples with high concentrations of residual monomer may demonstrate similar degradation trends to those expected for noncatalytic hydrolysis.

Part 3: Modelling the change in Young's modulus of degrading polymers

The mechanical properties of medical fixation devices are of great importance throughout their lifetime to ensure that they provide the optimal level of mechanical support. Currently, no models exist for the degradation of mechanical properties of glassy polymers and hence device designs cannot be fully optimised for individual patients' needs. It is necessary for mathematical models to be developed for the degradation of Young's modulus and other mechanical properties. In part 3 of this thesis, a new atomistic modelling technique is presented to analyse mechanical properties of poly(lactide) and the effect of chain scission on mechanical properties. This understanding is implemented into the mathematical model presented in part 2 of this thesis to give an overall model for Young's modulus degradation.

Chapter 8: Theory and validation of an atomic finite element model for poly(lactide)

The mathematical models presented in Chapters 4 to 7 of this thesis consider numerical analysis of chain scission in order to model the degradation of molecular weight and increases in polymer crystallinity. Currently, there is no atomistic model in the literature which relates chain scission to mechanical properties in a biodegradable polymer during degradation. In order to develop such a relationship, atomic studies are conducted over the next three chapters of this thesis. In this chapter, a new atomic simulation technique is presented which offers significant computational benefits over existing methods such as molecular dynamics. In Chapter 9, atomic simulations are conducted in order to analyse the mechanical properties of biodegradable polymers during degradation by hydrolytic polymer chain scission. In Chapter 10, a model is presented to relate change in Young's modulus to polymer chain scission and crystallinity. A large part of this chapter is included in a publication draft [102].

8.1 Introduction

In molecular dynamics (MD) simulations, potential energy equations are used to calculate the instantaneous forces applied by the atoms to one another at discrete time intervals. The forces result in acceleration of the atoms and for each time step, the speed and distance travelled by each atom can be calculated. Based on this information, the new atom positions are derived which leads to a new set of forces being calculated and the cycle repeats. The MD potential energy equations simulate the interactions between atoms due to covalent bonds present in polymer chains and also due to long range van der Waals and Coulomb interactions; the latter two of which are referred to together as nonbond interactions. MD simulations have been used extensively to model material properties at the atomic scale. However, the simulations have high computational demands so the analysis of large atomic structures, including amorphous polymers, is difficult even on a super computer. This chapter presents an atomic finite element method (AFEM), which models a polymer at the atomic scale according to MD interatomic potential energy equations. In the AFEM simulations, the forces required to move atoms relative to one another are represented by atomic finite elements. After boundary conditions are applied to an atomic structure, including the application of a force or strain to the overall structure, the final positions of atoms are

calculated by minimising the total potential energy of the system. The new atomic coordinates are used to determine the overall Young's modulus of the material being modelled. This AFEM technique is much less computationally demanding than molecular dynamics, and hence suitable for the modelling of large amorphous polymer structures. In this chapter, firstly the MD potential energy equations are explained. Then the atomic finite element theory is presented, from the principle of minimum potential energy. Finally, several validations of the method and its corresponding computer code are included.

8.2 Molecular dynamics interatomic potential energy

In molecular dynamics, the interactions between atoms are described by molecular dynamics force fields, which relate atomic coordinates to potential energy. For example, the potential energy for a pair of covalently bonded atoms is a function of the atomic separation. Force fields vary greatly by application; in the analysis of a regularly repeating structure such as diamond, the simulations may analyse just a few atoms which are considered to repeat periodically over an infinite distance. Therefore, the computational demands are much lower than for more complex molecular structures, As a result, the force fields can represent the interatomic potentials with a higher degree of complexity. For example, the potential energy for interatomic separation may take the exponential Morse potential instead of a simple harmonic potential. The PLAFF2 force field was developed by McAliley specifically for poly(lactide) and was supplied as supplementary information with his thesis [85]. Fig. 8.1 shows the different types of main chain deformation schematically, including how they may represent a section of a polymer chain. In the force field, potential energy is calculated for covalently bonded atoms based on interatomic separation (the bond-stretch potential energy), the angle between adjacent bonds (the bond-angle potential energy) and rotation of the polymer chain about a bond (the bond-dihedral potential energy). There is also potential energy associated with the interatomic separation of atoms that are not covalently bonded (the nonbond potential energy). The bond-stretch and nonbond potential energy functions consider pairs of atoms, while the potential energy functions for bond-angle and bond-dihedral consider groups of three and four atoms respectively.

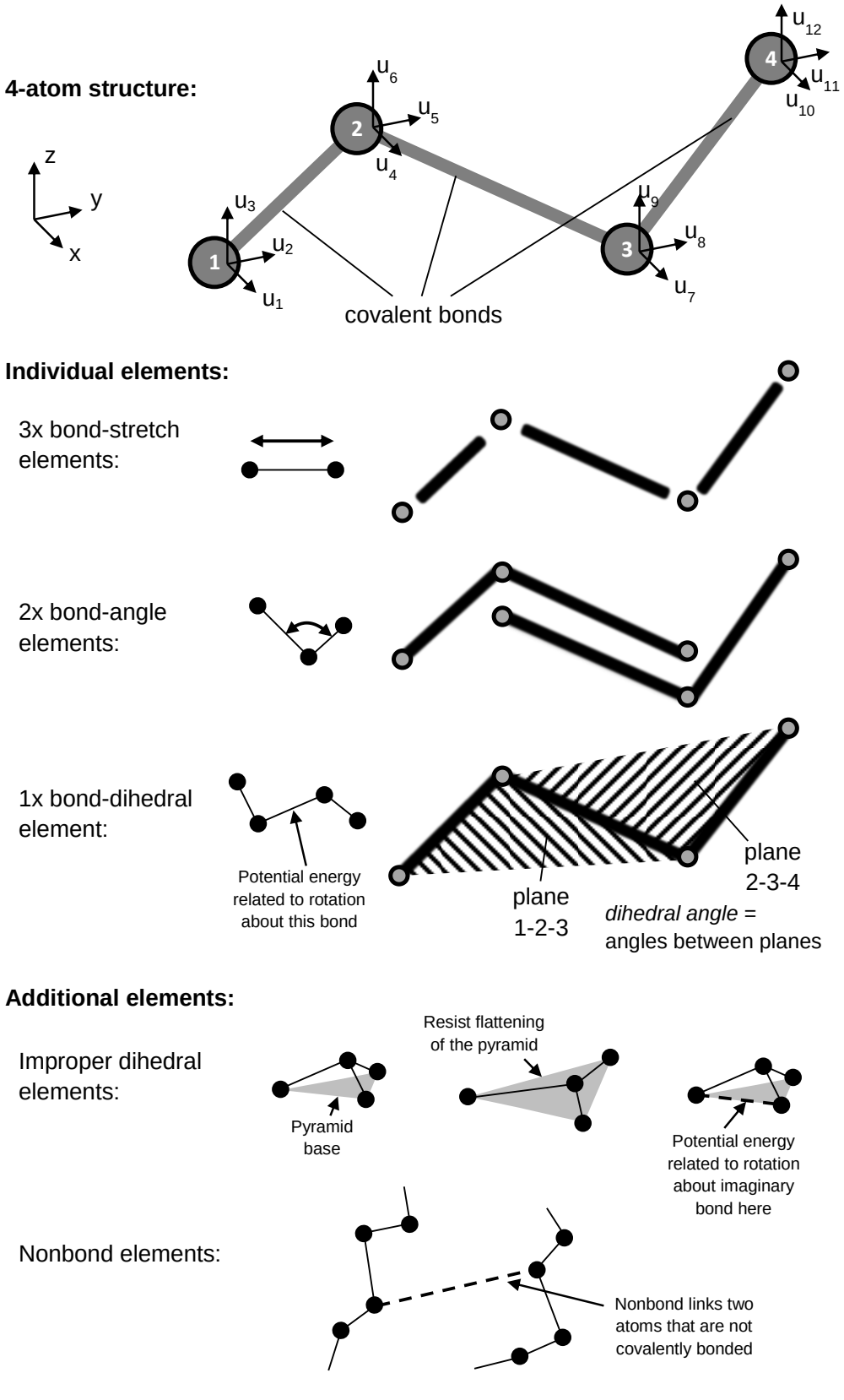

Fig. 8.1 Schematic of the interatomic potential energy terms: bond-stretch, bond-angle, bond-dihedrals, which are divided into proper and improper dihedrals, and nonbonds.

8.2.1 Minimisation of the total potential energy

The simulations in this thesis consider the potential energy of a representative unit cell of polymer, which contains several polymer chains. The total potential energy of the unit cell, V_{MD} (kJ mol^{-1}), according to the PLAFF2 force field is given in Eq. 8.1 as

$$V_{MD} = \sum_{\substack{bonds \\ i,j}} V_b + \sum_{\substack{angles \\ i,j,k}} V_a + \sum_{\substack{dihedrals \\ i,j,k,l}} V_d + \sum_{\substack{nonbonds \\ i,j}} V_{nb} - Fu \qquad 8.1$$

which is the sum of potential energies for all bond-stretch, V_b, bond-angle, V_a, bond-dihedral, V_d, and nonbonded, V_{nb} (all kJ mol^{-1}), atomic interactions. The term Fu is the applied work due to an externally applied force, F (N), and the displacement where F is applied, u (nm). In molecular dynamics, the term “relaxed structure” refers to a structure in which the atomic coordinates are found such that total potential energy is at a minimum; it is the configuration that the force field suggests is likely to exist in a real material. In order to find the relaxed structure through MD simulations, the simulations need to run for a duration that enables the atoms to naturally move to their most relaxed coordinates. At this time, the total potential energy given in Eq. 8.1 is at a minimum. Since the simulations are dynamic, the atoms will actually oscillate about their relaxed coordinates. The degree of oscillation depends on the temperature of the simulation. In molecular statics simulations, the atoms have no velocity, and hence they do not oscillate and do not naturally converge to a relaxed configuration. Instead, the atomic coordinates may be iterated by methods including random iteration, iteration according to a probability distribution, or iteration along the steepest gradient of potential energy. The procedure finishes when the total potential energy, or its rate of change, falls below a threshold value. Young’s modulus may be calculated by the minimisation of total potential energy in molecular dynamics or molecular statics simulations. This is typically achieved by the application of a remote force or displacement to the boundary of the representative polymer unit, and the minimisation of potential energy in order to find the new atomic coordinates for all atoms; Young’s modulus can be calculated by relating the force that is applied to the resulting strain or vice versa.

8.2.2 The PLAFF2 molecular dynamics force field

The PLAFF2 force field was developed by McAliley [85] in order to model poly(lactide). It gives potential energy functions for bond-stretch, bond-angles, bond-dihedrals and nonbonds as discussed in relation to Fig. 8.1. The potential energy functions of

PLAFF2 are explained in detail in this section. They consist: (i) of harmonic potentials for bond-stretch and bond-angle potentials; (ii) of the periodic dihedral function and Ryckaert-Bellemans expansion for bond-dihedrals; and (iii) of Lennard-Jones and Coulomb interactions for nonbond potential energy. In the PLAFF2 force field, and the thesis describing its development [85], the atoms in poly(lactide) polymer repeat units were identified according to the notation given in Fig. 8.2.

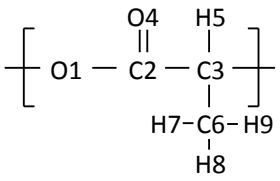

Fig. 8.2 The atoms of a poly(lactide) polymer chain unit are identified using the same notation as that used by McAliley in the development of PLAFF2.

The PLAFF2 force field is supplied as supplementary information with McAliley's thesis [85] in a format suitable for the molecular dynamics package Gromacs. The manual for Gromacs [103] gives details of the force field file format and the potential energy functions which are described in Eqs. 8.2 - 8.8.

Bond-stretch potential energy, V_b, of two covalently bonded atoms is given by

$$V_b = \tfrac{1}{2} k_b \left(r_{ij} - r_0\right)^2 \qquad 8.2$$

in which k_b (kJ mol^{-1} nm^{-2}) is the bond-stretch force constant, r_{ij} (nm) is the atomic separation, and r_0 (nm) is the equilibrium atomic separation.

Bond-angle potential energy, V_a, can be calculated as

$$V_a = \tfrac{1}{2} k_a \left(\theta - \theta_0\right)^2 \qquad 8.3$$

in which k_a (kJ mol^{-1} rad^{-2}) is the bond-angle force constant, θ (rad) is the angle between atoms i, j, k, and the equilibrium angle is θ_0 (rad).

Bond-dihedral potential energy, V_d, in PLAFF2 includes both proper and improper dihedrals which are shown schematically in Fig. 8.1. Proper dihedrals consider atoms which are covalently bonded in series. Their potential energy is related to rotation about the covalent bond between the middle two atoms. Improper dihedrals in PLAFF2 consider four atoms of which three are all covalently bonded to a central atom. These can be considered to be in the form of a pyramid as shown in Fig. 8.1, and the potential energy function is related to rotation about one of the bottom edges of the pyramid even though there is not a covalent bond along that edge. Potential energy for proper dihedrals can be considered to prevent the polymer chain from twisting freely and improper dihedrals are often used to keep chemical groups planar such as the carbonyl group in poly(lactide). In PLAFF2, improper dihedrals are recorded in the force field in a manner which enables them to be implemented as proper dihedrals. To simplify the explanation here, only proper dihedrals are described. For a set of four atoms, i, j, k, l, covalently bonded in series, the dihedral angle, Φ (rad), is defined as the angle between the plane of atoms i, j, k, and the plane of atoms j, k, l. The angle is defined according to the IUPAC/IUB convention such that an angle of zero corresponds to the cis configuration with atoms i and l on the same side. The Ryckaert-Bellemans dihedral potential energy, $V_{d(Ryckaert\text{-}Bellemans)}$ (kJ mol^{-1}), is

$$V_{d(Ryckaert-Bellemans)} = \sum_{n=0}^{5} C_n \left(\cos\left(\phi - 180°\right)\right) \qquad 8.4$$

in which C_n (kJ mol^{-1}) are six Ryckaert-Bellemans coefficients. In addition to the Ryckaert-Bellemans dihedral function, PLAFF2 utilises the periodic dihedral function which gives the periodic dihedral potential energy, $V_{d(periodic)}$ (kJ mol^{-1}), as

$$V_{d(periodic)} = \tfrac{1}{2} k_d \left(1 + \cos\left(n_\phi \phi - \phi_0\right)\right)^2 \qquad 8.5$$

in which k_d (kJ mol^{-1} rad^{-2}) is the periodic dihedral force constant, Φ_0 (rad) is the phase shift and n_Φ (no units) is the multiplicity which dictates the number of peaks in the potential energy one complete rotation of the bond.

Nonbond potential energy, V_{nb}, is calculated as the sum of Lennard-Jones potential energy, $V_{Lennard\text{-}Jones}$ (kJ mol^{-1}), and Coulomb interaction potential energy, $V_{Coulomb}$ (kJ mol^{-1}), as given by

$$V_{nb} = V_{Lennard\text{–}Jones} + V_{Coulomb}. \tag{8.6}$$

The Lennard-Jones potential energy accounts for the long range attractive van der Waals interactions and the short range Pauli repulsion due to overlapping electron orbitals. It can be calculated as

$$V_{Lennard\text{–}Jones} = 4\sqrt{\varepsilon_{ii}\varepsilon_{jj}}\left(\left(\frac{\sqrt{\sigma_{ii}\sigma_{jj}}}{r_{ij}}\right)^{12} - \left(\frac{\sqrt{\sigma_{ii}\sigma_{jj}}}{r_{ij}}\right)^{6}\right) \tag{8.7}$$

in which r_{ij} (nm) is the interatomic separation, ε_{ii} and ε_{jj} (kJ mol^{-1}) are the Lennard-Jones well-depth parameters for atoms i and j respectively, and σ_{ii} and σ_{jj} (nm) are the Lennard-Jones radii for atoms i and j respectively. Each type of atom has its own well-depth and radii parameters so in order to calculate the Lennard-Jones interaction between two different atoms the two sets of parameters must be combined. The terms $\sqrt{\varepsilon_{ii}\varepsilon_{jj}}$ and $\sqrt{\sigma_{ii}\sigma_{jj}}$ in Eq. 8.8 indicate that the Lennard-Jones well-depth and Lennard-Jones radii parameters for a nonbond between atoms i and j are calculated as the geometric mean of the individual atoms' parameters.

The Coulomb interaction potential energy accounts for the attraction or repulsion of atoms due to their permanent charge and is given by

$$V_{Coulomb} = \frac{1}{4\pi\varepsilon_0}\left(\frac{q_i q_j}{r_{ij}}\right) \tag{8.8}$$

in which ε_0 (F m^{-1}) is the electric constant, q_i and q_j (units of elementary charge) are electric charges for atoms i and j respectively. In the PLAFF2 force field, the nonbond potential energy function does not apply to atoms that are separated by just one or two covalent bonds since the repulsive forces become too great. Also, nonbonds between atoms that are separated by exactly 3 covalent bonds have their potential energy contribution halved.

8.2.3 Validation of the nonbond potential energy equation form and units

McAliley supplied plots of nonbond potential energy functions versus interatomic separation for OPLS and CHARM force fields (on which PLAFF2 is based) in the appendix of his thesis. These OPLS plots are reproduced in order to check that the force field parameter values and units are interpreted correctly along with the form of the potential energy in Eqs. 8.6 - 8.8. The potential energy functions for a nonbond between the carbonyl carbon (C2) and oxygen (O4) atoms in poly(lactide) repeat units are shown in Fig. 8.3. The OPLS force field is used in Eq. 8.6 generate the plot in Fig. 8.3 a) which can be seen to replicate the plot produced my McAliley in Fig. 8.3 b). The agreement indicates that the nonbond terms of the force field are being implemented correctly.

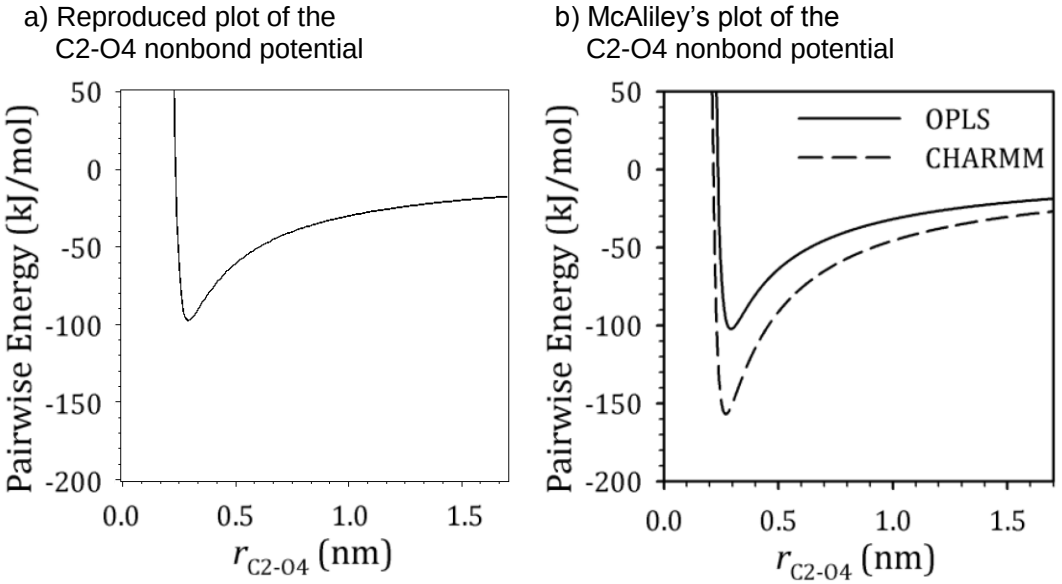

Fig. 8.3 a) the OPLS force field is used to produce a plot of the C2-O4 nonbond potential energy function which is a good replica of b) the plot of the same potential energy function taken from the appendix of McAliley's thesis [85] with permission via the Copyright Clearance Centre.

8.3 Atomic finite element method (AFEM)

The bond-dihedral and nonbond terms in the molecular dynamics total potential energy equation in Eq. 8.1 are nonlinear, and hence the rate of change in potential energy varies with deformation. Due to the nonlinearity, iterative simulation techniques are necessary, such as molecular dynamics or molecular statics. In the atomic finite element method (AFEM) presented here, the displaced atomic coordinates that result from an externally applied strain are calculated in a single computation step. The reduced computational demands, versus iterative simulations, enable the analysis of structures containing a greater number of atoms. This is particularly beneficial for the analysis of polymers, in which a single molecule may contain over 10000 atoms.

There are three main aspects to the work presented in Section 8.3 here: firstly, in Section 8.3.1, the minimisation of total potential energy in the context of the atomic finite element method is presented; secondly, in Section 8.3.2, the nonlinear potential energy terms are adapted into a quadratic form, which enables static linear analysis for AFEM; thirdly, in Sections 8.3.3 to 8.3.5, the finite elements which represent the potential energies for bond-stretch, bond-angle, bond-dihedral and nonbonds are derived from the theory of minimum potential energy. Details of the AFEM program setup are given in Section 8.3.6.

8.3.1 Minimisation of total potential energy

The total potential energy V_{MD}, given in Eq. 8.1, is adapted here to enable static linear analysis. The adapted total potential energy of the unit cell, V_{MD_FEM} (kJ mol^{-1}), is given by Eq. 8.9 as

$$V_{MD\_FEM} = \sum_{\substack{bonds \\ i,j}} V_b + \sum_{\substack{angles \\ i,j,k}} V_a + \sum_{\substack{dihedrals \\ i,j,k,l}} V_{d\_FEM} + \sum_{\substack{nonbonds \\ i,j}} V_{nb\_FEM} - Fu \qquad 8.9$$

in which V_{d_FEM} (kJ mol^{-1}) is the adapted bond-dihedral potential energy and V_{nb_FEM} (kJ mol^{-1}) is the adapted nonbond potential energy. Other terms are unchanged from Eq. 8.1. In AFEM, the atomic displacements, u_i (nm), are found in order to minimise total potential energy in Eq. 8.9. As with any mathematical function, the value of potential energy is at a minimum when its derivative is zero according to

$$\frac{d\left(V_{MD\_FEM}\right)}{d\left(u_i\right)} = 0 . \qquad 8.10$$

For 3D simulations, each atom in the unit cell has 3 displacement terms in x, y and z. Therefore, the number of linear equations given by the differentiation in Eq. 8.10 is equal to three times the number of atoms in the unit cell. These linear equations can be written in matrix form in Eq. 8.11 as

$$[K][d] = [F]. \qquad 8.11$$

The displacement matrix [d] is a column matrix containing all the displacement terms u_i. The force matrix [F] is a column matrix containing the Cartesian forces that are externally applied to each atom. The global stiffness matrix [K] relates the displacement of each atom to the applied forces. The system of linear equations can be solved by inverting the stiffness matrix and solving for displacements u_i in [d]. This gives the values of u_i for all atoms in order to satisfy Eq. 8.10 and minimise total potential energy. AFEM uses atomic finite elements to represent the individual interatomic potentials between atoms, according to a molecular dynamics force field. Fig. 8.1 shows how covalent bond elements fit into a simple structure containing 4 atoms. There is one finite element for each potential energy term that is considered. For the chosen MD force field (PLAFF2), four different types of finite element are required in the atomic scale simulations. These are:

- The bond-stretch element, which represents the interatomic separation of two covalently bonded atoms;
- The bond-angle element, which represents the angle between two covalent bonds;
- The bond-dihedral element, which represents rotation about a covalent bond and improper dihedrals;
- And the nonbond element for the interatomic separation of two atoms that are not covalently bonded.

Due to the large number of potential energy terms that are summed for the total potential energy in Eq. 8.9, the task of deriving this summation and differentiating by each atomic displacement u_i is complicated. Rather than consider the entire equation for total potential energy, the stiffness matrix [K] can be built up directly by considering

each element in isolation. This is called the Direct Stiffness Method. The differential, according to Eq. 8.10, is conducted for each potential energy term. For bond-stretch and nonbond terms, the atomic finite element contains 2 atoms and a total of 6 Cartesian displacements, u_i, as shown in Fig. 8.1. The differential with respect to u_i therefore results in 6 linear equations. For bond-angle and bond-dihedral terms, there are 9 and 12 equations respectively. As with the total potential energy differential in Eq. 8.11, the single element differential can be written in matrix form as

$$[K_e][d_e]=[F_e] \tag{8.12}$$

in which $[K_e]$ is the element stiffness matrix, $[d_e]$ is the element displacement matrix and $[F_e]$ is the element force matrix. Element stiffness matrices are assembled into the global stiffness matrix via the Direct Stiffness Method. The theory for the development of element stiffness matrices for bond-stretch and nonbond elements is presented in Section 8.3.3. Bond-angle elements are presented in Section 8.3.4 and bond-dihedral elements are presented in Section 8.3.5.

Temperature is represented in molecular dynamics by the velocity of the atoms. Since the AFEM simulations are static and the atoms have no velocity and the temperature is effectively 0 Kelvin. One of the assumptions in AFEM is that the initial potential energies of the bonds are at a minimum. Therefore it is appropriate to use an atomic structure that has been relaxed by molecular dynamics simulations so that the unbalanced internal forces (between atoms) are minimised. In the simulations for Young's modulus conducted in this thesis, the initial atomic structure for amorphous poly(lactide) was found by McAliley through molecular dynamics simulations and supplied as additional information with his PhD thesis [85].

8.3.2 Adaptation of the MD Potential energies terms for AFEM

The molecular dynamics bond-stretch and bond-angle potential energy terms in the PLAFF2 force field take the harmonic form as given in Eqs. 8.2 and 8.3. To enable static linear finite element analysis, the bond-dihedral and nonbond potential energy terms are adapted from the more complex forms used in PLAFF2, to also take the harmonic form, according to

$$V_{el} = \tfrac{1}{2} k_{el} d_{el}^{\ 2} \tag{8.13}$$

in which V_{el} is potential energy (kJ mol^{-1}) and k_{el} is the force constant (kJ mol^{-1} nm^{-2} for linear displacement or kJ mol^{-1} rad^{-2} for angular displacement). Eq. 8.13 can describe all the potential energies. The subscript *el* is:

- *b*, to represent bond-stretch potential energy
- *a*, to represent bond-angle potential energy
- *d_FEM*, to represent bond-dihedral potential energy
- and *nb_FEM*, to represent nonbond potential energy.

d_{el} is the change in length (nm) for bond-stretch and nonbond elements, or change in angle (rad) for bond-angle and bond-dihedral elements. The change in length or angle is due to the displacements of atoms contained within the element, u_i. For static linear finite element analysis, the potential energies are zero in the initial atomic configuration, before a displacement is externally applied to the unit cell.

The double derivative of potential energy V_{el} with respect to change in length or angle d_{el} gives the finite element stiffness k_{el}

$$\frac{d\left(V_{el}\right)}{d\left(d_{el}\right)} = k_{el} d_{el} \qquad 8.14$$

and

$$\frac{d^2\left(V_{el}\right)}{d\left(d_{el}\right)^2} = k_{el} \,. \qquad 8.15$$

Since the PLAFF2 force field uses a harmonic form of bond-stretch and bond-angle potential energy, the values k_b and k_a are explicitly given in Eqs. 8.2 and 8.3. For the bond-dihedral and nonbond potential energy terms however, the values of k_{d_FEM} and k_{nb_FEM} are not explicitly given in PLAFF2. They are derived here for use in the harmonic potential energy in AFEM by twice differentiating the PLAFF2 potential energy terms for bond-dihedrals and nonbonds with respect to length or angle.

Differentiation of bond dihedral potential energy for k_{d_FEM}

There are two types of bond-dihedral potential energy: the Ryckaert-Bellemans and periodic types as given in Eqs. 8.3 and 8.4. The Ryckaert-Bellemans potential energy function is written in expanded form along with the single and double derivatives with respect to the dihedral angle, Φ, in Eqs. 8.16 - 8.18 as

$$V_{d(Ryckaert-Bellemans)} = C0 + C1\cos(\Phi) + C2\cos(\Phi)^2 + C3\cos(\Phi)^3 + C4\cos(\Phi)^4 + C5\cos(\Phi)^5 \quad 8.16$$

$$\frac{dV_{d(Ryckaert-Bellemans)}}{d\Phi} = -C1\sin(\Phi) - 2\,C2\cos(\Phi)\sin(\Phi) - 3\,C3\cos(\Phi)^2\sin(\Phi) - 4\,C4\cos(\Phi)^3\sin(\Phi) - 5\,C5\cos(\Phi)^4\sin(\Phi) \quad 8.17$$

$$\frac{d^2V_{d(Ryckaert-Bellemans)}}{d\Phi^2} = -C1\cos(\Phi) + 2\,C2\sin(\Phi)^2 - 2\,C2\cos(\Phi)^2 + 6\,C3\cos(\Phi)\sin(\Phi)^2 - 3\,C3\cos(\Phi)^3 + 12\,C4\cos(\Phi)^2\sin(\Phi)^2 - 4\,C4\cos(\Phi)^4 + 20\,C5\cos(\Phi)^3\sin(\Phi)^2 - 5\,C5\cos(\Phi)^5 \quad 8.18$$

The periodic dihedral potential energy function and the single and double derivatives with respect to the dihedral angle are calculated in Eqs. 8.19 - 8.21 as

$$V_{d(periodic)} = k_d\left(1 + \cos\left(n\Phi - \Phi_0\right)\right) \quad 8.19$$

$$\frac{dV_{d(periodic)}}{d\Phi} = -k_d\sin\left(n\Phi - \Phi_0\right)n \quad 8.20$$

$$\frac{d^2V_{d(periodic)}}{d\Phi^2} = -k_d\cos\left(n\Phi - \Phi_0\right)n^2 \quad 8.21$$

In order to calculate the AFEM bond-dihedral element stiffness k_{d_FEM}, the initial value of the dihedral angle Φ must be calculated according to IUPAC/IUB convention, as identified in Fig. 8.4. It must not be normalised between 0 and +180 degrees since the torsion potential energy of a bond may not be symmetrical about 0 degrees. The method described in Eqs. 8.22 - 8.26 is based on the documentation supplied with the

PumMa molecular dynamics package [104]. The vector $\bar{n}_{ijk}$ normal to the plane through atoms i, j and k is given by

$$\hat{n}_{ijk} = r_{ij} \times r_{jk} \tag{8.22}$$

in which $\bar{r}_{ij}$ is the vector from atoms i to j and $\bar{r}_{jk}$ is the vector from atoms j to k. Similarly, the vector $\bar{n}_{jkl}$ normal to the plane through atoms j, k and l is given by

$$\hat{n}_{jkl} = r_{jk} \times r_{kl} \tag{8.23}$$

in which $\bar{r}_{kl}$ is the vector from atoms k to l. The sine and cosine of the torsion angle are defined as

$$\sin\phi = \frac{\left(\hat{n}_{ijk} \times \hat{n}_{jkl}\right) \cdot r_{jk}}{\left|\hat{n}_{ijk}\right|\left|\hat{n}_{jkl}\right|\left|r_{jk}\right|} = \frac{\left(\hat{n}_{jkl} \cdot r_{ij}\right) \times r_{jk}}{\left|\hat{n}_{ijk}\right|\left|\hat{n}_{jkl}\right|} \tag{8.24}$$

and

$$\cos\phi = \frac{\hat{n}_{ijk} \cdot \hat{n}_{jkl}}{\left|\hat{n}_{ijk}\right|\left|\hat{n}_{jkl}\right|}. \tag{8.25}$$

The dihedral angle can then be calculated as

$$\phi = -a\tan\left(\frac{\sin\phi}{\cos\phi}\right). \tag{8.26}$$

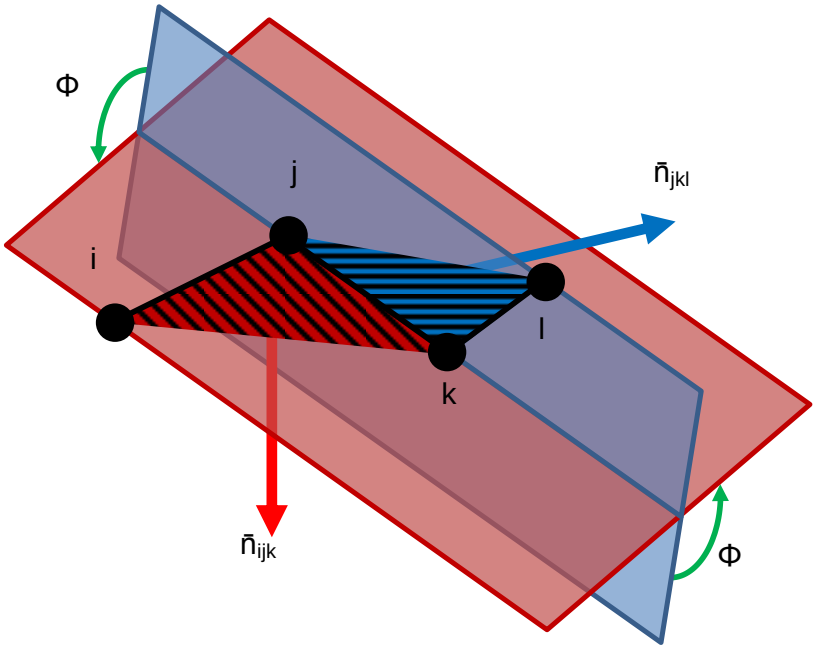

Fig. 8.4 A Schematic of a bond-dihedral element for atoms i, j, k and l. The initial angle that should be used to find the element stiffness is shown as Φ.

Differentiation of nonbond potential energy for k_{nb_FEM}

The potential energy of nonbonded interactions between two atoms is given by the sum of the Lennard-Jones and coulomb interaction potential energies. This potential energy is given in Eq. 8.27 and the derivatives with respect to length of the nonbond are given in Eqs. 8.28 and 8.29 as

$$V_{nb} = \frac{1}{4}\frac{q_i q_j}{\pi\varepsilon_0 r_{ij}} + 4\sqrt{\varepsilon_i \varepsilon_j}\left(\frac{\sigma_{ii}^6 \sigma_{jj}^6}{r_{ij}^{12}} - \frac{\sigma_{ii}^3 \sigma_{jj}^3}{r_{ij}^6}\right) \tag{8.27}$$

$$\frac{dV_{nb}}{dr_{ij}} = -\frac{1}{4}\frac{q_i q_j}{\pi\varepsilon_0 r_{ij}^2} + 4\sqrt{\varepsilon_i \varepsilon_j}\left(-\frac{12\,\sigma_{ii}^6 \sigma_{jj}^6}{r_{ij}^{13}} + \frac{6\,\sigma_{ii}^3 \sigma_{jj}^3}{r_{ij}^7}\right) \tag{8.28}$$

$$\frac{d^2V_{nb}}{dr_{ij}^2} = \frac{1}{2}\frac{q_i q_j}{\pi\varepsilon_0 r_{ij}^3} + 4\sqrt{\varepsilon_i \varepsilon_j}\left(\frac{156\,\sigma_{ii}^6 \sigma_{jj}^6}{r_{ij}^{14}} - \frac{42\,\sigma_{ii}^3 \sigma_{jj}^3}{r_{ij}^8}\right) \tag{8.29}$$

The nonbond force constant is calculated in Eq. 8.29 based on interatomic separation r_{ij}. For each of the bond-dihedral and nonbond AFEM elements in a unit cell, the force

constants must be calculated based on the particular atomic configuration, whereas the bond-stretch and bond-angle force constants do not depend on the length or angle of the elements. All force constants are assumed to be constant during AFEM simulations, which are limited to small strains. If the force constants were permitted to change during the deformation, nonlinear simulations would be required, thereby diminishing the computational benefits of AFEM over molecular dynamics and molecular statics simulations.

Fig. 8.5 shows plots for the potential energy along with its first and second derivatives versus the interatomic separation for a nonbond between carbonyl carbon and carbonyl oxygen atoms, identified as C2 and O4 in Fig. 8.2. The first derivative gives the interatomic force that the nonbonded atoms apply to one another. The second derivative gives the force constant, which is the atomic finite element stiffness. As can be seen, at short interatomic separations the atoms apply a positive interatomic force to each other, which indicates repulsion due to electron orbital overlap. At the equilibrium interatomic distance, which is 0.294 nm for this C2 and O4 nonbond, the interatomic force is zero because the atoms' attraction and repulsion perfectly balance. As the interatomic separation increases further, the atoms apply an attractive interatomic force to each other and a force must be applied to sustain the interatomic separation. At the interatomic separation highlighted by the vertical dashed line in the figure, the nonbond effectively breaks because further elongation of the nonbond results in less force being required to sustain the separation, therefore the atomic finite element stiffness changes from a positive to a negative value. For the AFEM simulations used to analyse the poly(lactide) polymer structure in this thesis, nonbond elements with negative stiffness are considered to represent broken bonds and therefore are not included in the simulations. A similar trend occurs for dihedrals but as opposed to nonbonds, where there is a threshold interatomic separation above which stiffness is negative, there are angular ranges in which the dihedral stiffness is negative. In these ranges, the dihedral potential energy function represents an atomic state in which changes to the dihedral angle are not resisted. Therefore bond-dihedral atomic finite elements with a negative stiffness are also excluded from the simulations. In the PLAFF2 force field, the potential energy contribution from nonbonds that connect atoms separated by exactly 3 covalent bonds is halved. Therefore the atomic finite element stiffness for those nonbonds is also halved.

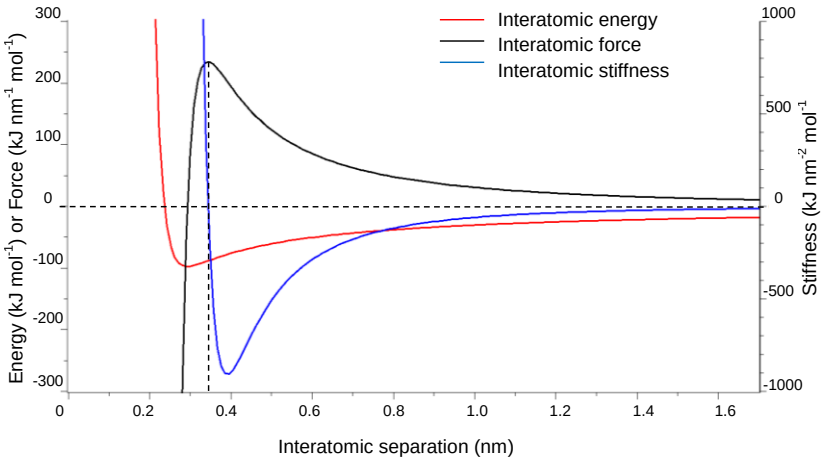

Fig. 8.5 The PLAFF2 nonbond potential energy is shown for a nonbond between a carbonyl carbon and carbonyl oxygen atoms in poly(lactide). The single and double derivatives, with respect to interatomic separation, indicate interatomic force and atomic finite element stiffness respectively.

8.3.3 Development of the bond-stretch and nonbond AFEM elements

As described in Eq. 8.10, the total potential energy is minimised when its derivative with respect to atomic displacement is equal to zero. In the next three sections, potential energy terms are differentiated in order to find the element stiffness matrices, as discussed in relation to Eq. 8.12. There are three types of element: 1) bond-stretch elements, which have the same form as nonbond elements and consider interatomic separation, 2) bond-angle elements and 3) bond-dihedral elements, which are valid for both proper and improper bond-dihedral potential energy functions. Following the format of the molecular dynamics force field PLAFF2, the potential energy of an atomic finite element, V_{el}, is given by Eq. 8.13 in terms of change in length or angle of the element, d_{el}. In order to enable differentiation with respect to atomic displacement u_i, V_{el} is presented in terms of u_i as opposed to d_{el}.

The bond-stretch and nonbond elements both relate potential energy to interatomic separation and hence the discussion here regarding Eqs. 8.30 - 8.37 applies to both elements. A bond-stretch element is shown in Fig. 8.6 before and after displacements of the atoms result in elongation of the element. The vector displacement of atom A, $\bar{u}_A$, is given by

$$\bar{u}_A = \begin{pmatrix} u_1 \\ u_2 \\ u_3 \end{pmatrix} \qquad 8.30$$

in which u_1, u_2 and u_3 are the Cartesian x, y, z scalar atomic displacements. Similarly the displacement of atom B, $\bar{u}_B$, is given by

$$\bar{u}_B = \begin{pmatrix} u_4 \\ u_5 \\ u_6 \end{pmatrix}. \qquad 8.31$$

The component of $\bar{u}_B$ along the vector $\bar{r}_{AB}$ from atom A to atom B causes an elongation of the element, ΔL_B, and is given by the dot product of both vectors. In contrast, the component of $\bar{u}_A$ along $\bar{r}_{AB}$ causes a change in length, ΔL_A, which is a reduction rather than elongation of the element length as shown in the figure. Therefore the total elongation of the element, ΔL_{AB}, is given by

$$\Delta L_{AB} = \bar{u}_B \cdot \bar{r}_{AB} - \bar{u}_A \cdot \bar{r}_{AB}. \qquad 8.32$$

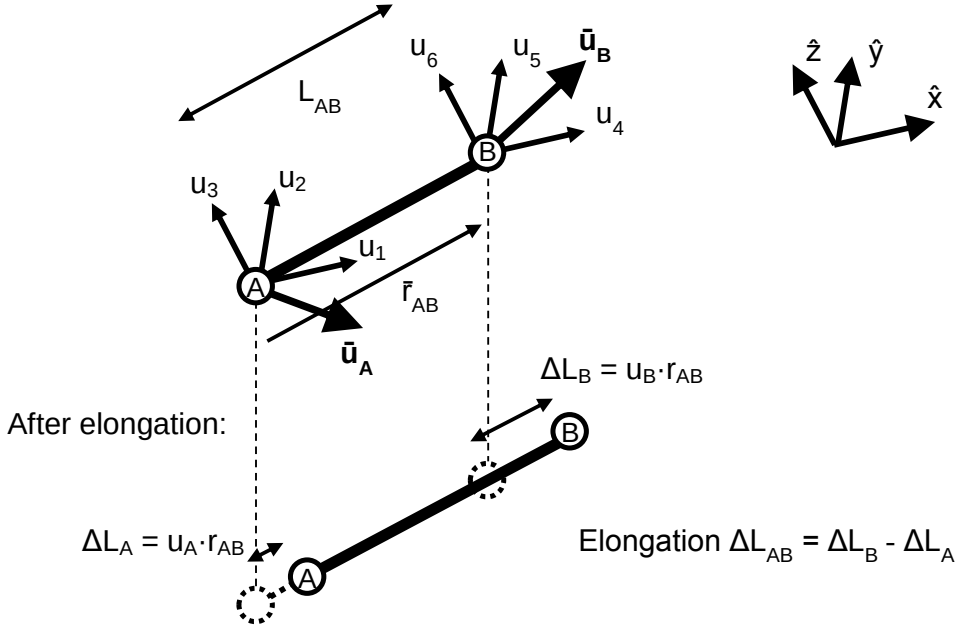

Fig. 8.6 Schematic of a bond-stretch element in AFEM containing 2 atoms. The displacements of both atoms contribute to overall elongation of the element.

For AFEM simulations, it is necessary to consider Eq. 8.1 in terms of the individual scalar atomic displacement u_1 to u_6. The term α_i is used to indicate the effect of the ith atomic displacement on the overall element elongation, such that total elongation of the element can be described by

$$\Delta L_{AB} = \sum_{i=1-6} \alpha_i u_i \qquad 8.33$$

which is the sum of all the atomic displacements multiplied by their individual effects on overall element elongation. The six α_i terms can be found by differentiating Eq. 8.32 by the six u_i terms according to

$$\alpha_i = \frac{d\left(\Delta L_{AB}\right)}{d\left(u_i\right)}. \qquad 8.34$$

The interatomic potential energy of the element, is found by substituting ΔL_{AB} into Eq. 8.13 as d_{el} to give

$$V_{el} = \tfrac{1}{2} k_{el} \left(\sum_{i=1-6} \alpha_i u_i \right)^2 \qquad 8.35$$

which is differentiated with respect to u_i, when minimising total potential energy in Eq. 8.10. This differentiation gives the element stiffness matrix, as discussed in relation to Eq. 8.12. The ith linear equation that results from the differentiation can be written in matrix form as

$$\frac{dV_{el}}{du_i} = k_{el}\alpha_i \begin{bmatrix} \alpha_1 & \alpha_2 & \alpha_3 & \alpha_4 & \alpha_5 & \alpha_6 \end{bmatrix} \begin{bmatrix} u_1 \\ u_2 \\ u_3 \\ u_4 \\ u_5 \\ u_6 \end{bmatrix}. \qquad 8.36$$

where $k_{el}\alpha_i[\alpha]$ is the ith row of the element stiffness matrix. By differentiating Eq. 8.35 with respect to each of the six atomic displacements individually, each row of the stiffness matrix is found. The whole 6 x 6 element stiffness matrix can be derived as

$$k_{el}\begin{bmatrix} \alpha_1\alpha_1 & \alpha_1\alpha_2 & \dots & \alpha_1\alpha_6 \\ \alpha_1\alpha_2 & \alpha_2\alpha_2 & \dots & \alpha_2\alpha_6 \\ \vdots & \vdots & \ddots & \vdots \\ \alpha_1\alpha_6 & \alpha_2\alpha_6 & \cdots & \alpha_6\alpha_6 \end{bmatrix} \qquad 8.37$$

which can be substituted into the global stiffness matrix using the Direct Stiffness Method.

8.3.4 Development of the bond-angle AFEM element

Fig. 8.7 shows a bond-angle element for which change to the angle between three atoms is considered. As with the bond-stretch element above, the atomic displacements must be related to change in bond-angle in order to derive the element stiffness matrix. This derivation is described here in relation to Eqs. 8.38 - 8.48.

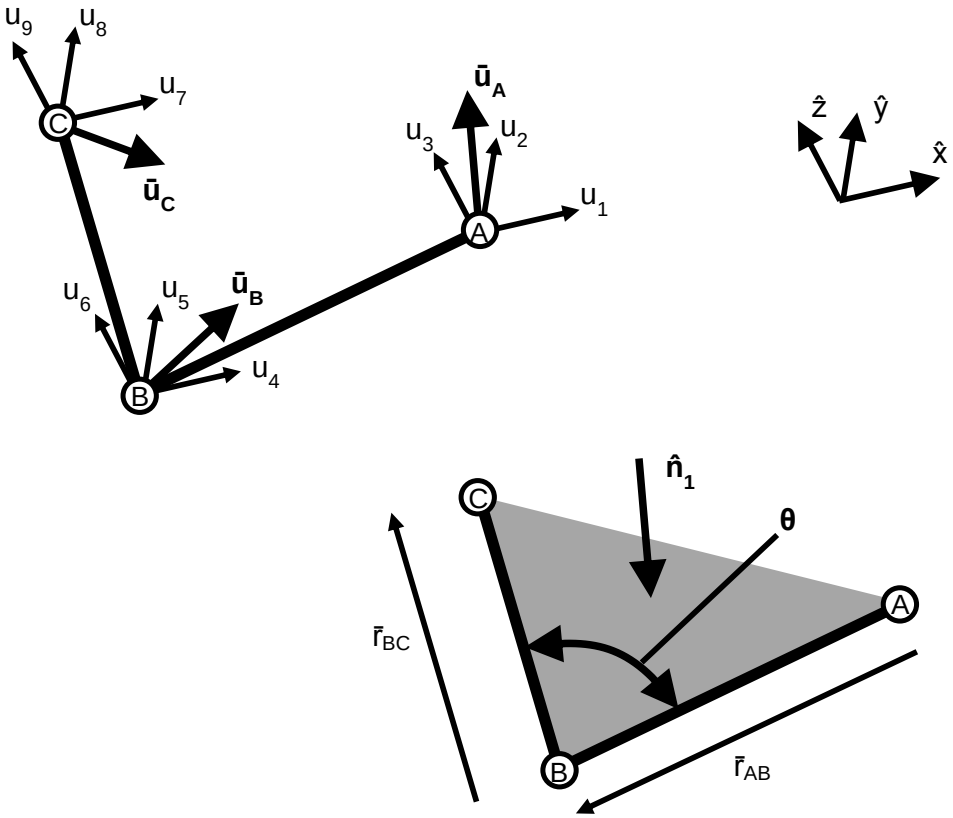

Fig. 8.7 Schematic of a bond-angle element for 3 atoms.

The vector displacements of each atom, $\bar{u}_A$, $\bar{u}_B$, $\bar{u}_C$, consist of three Cartesian scalar atomic displacements according to

$$\bar{u}_A = \begin{pmatrix} u_1 \\ u_2 \\ u_3 \end{pmatrix} \qquad \bar{u}_B = \begin{pmatrix} u_4 \\ u_5 \\ u_6 \end{pmatrix} \qquad \bar{u}_C = \begin{pmatrix} u_7 \\ u_8 \\ u_9 \end{pmatrix} \tag{8.38}$$

To relate the atomic vector displacements to change in bond-angle, θ, it is convenient to view the structure along the $\hat{n}_1$ vector in Fig. 8.7 which is normal to the plane of the three atoms. Fig. 8.8 shows this view of the element. The angles between the vectors $\bar{r}_{AB}$ and $\bar{r}_{BC}$ and the arbitrary reference in Fig. 8.8 are θ_A and θ_C respectively. They can be used to express the overall bond-angle as

$$\theta = \theta_C - \theta_A . \tag{8.39}$$

The unit vectors $\hat{n}_A$ and $\hat{n}_C$ in the figure lie in the $\hat{n}_1$ plane and are normal to the vectors $\bar{r}_{AB}$ and $\bar{r}_{BC}$ respectively. For small displacements, the effect of the vector atomic displacement $\bar{u}_A$ of atom A on the angle θ_A in radians is given by

$$\Delta\theta_A = \frac{\bar{u}_A \cdot \hat{n}_A}{|\bar{r}_{AB}|} \tag{8.40}$$

and similarly the effect of $\bar{u}_C$ on θ_C is

$$\Delta\theta_C = \frac{\bar{u}_C \cdot \hat{n}_C}{|\bar{r}_{BC}|} . \tag{8.41}$$

The displacement of atom B affects both θ_A and θ_C according to

$$\Delta\theta_A = -\frac{\bar{u}_B \cdot \hat{n}_A}{|\bar{r}_{AB}|} \tag{8.42}$$

and

$$\Delta\theta_C = -\frac{\bar{u}_B \cdot \hat{n}_C}{\left|\bar{r}_{BC}\right|}. \qquad 8.43$$

Eqs. 8.39 - 8.43 combine to give the total change in bond-angle in terms of the vector atomic displacements as

$$\Delta\theta = \frac{\bar{u}_A \cdot \hat{n}_A}{\left|\bar{r}_{AB}\right|} - \frac{\bar{u}_B \cdot \hat{n}_A}{\left|\bar{r}_{AB}\right|} - \frac{\bar{u}_B \cdot \hat{n}_C}{\left|\bar{r}_{BC}\right|} + \frac{\bar{u}_C \cdot \hat{n}_C}{\left|\bar{r}_{BC}\right|}. \qquad 8.44$$

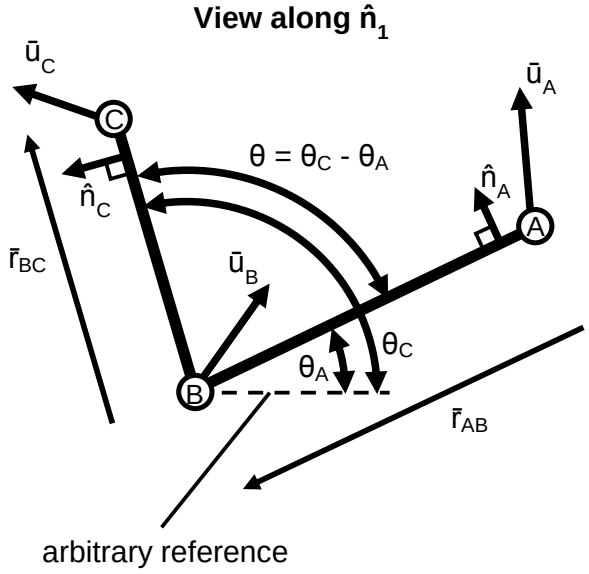

Fig. 8.8 View along the vector $\bar{n}_1$ in Fig. 8.7.

For the purposes of AFEM, it is useful to consider changes to the bond-angle in terms of the Cartesian scalar atomic displacements u_1 to u_9. The $\bar{u}_A$, $\bar{u}_B$ and $\bar{u}_C$ vector terms in Eq. 8.44 can simply be replaced by their respective scalar displacements as given in Eq. 8.38. As with the bond-stretch element theory above, Eq. 8.44 can be differentiated by the nine atomic displacements in order to find their individual effects, α_i, on the bond-angle according to

$$\alpha_i = \frac{d(\Delta\theta)}{d(u_i)}. \qquad 8.45$$

The total change in angle can then be simply rewritten as the sum of the nine atomic displacements multiplied by their effect on the overall bond-angle according to

$$\Delta\theta = \sum_{i=1-9} \alpha_i u_i \ . \qquad 8.46$$

By substituting $\Delta\theta$ into Eq. 8.13 as d_{el}, the element potential energy is given by

$$V_{el} = \tfrac{1}{2} k_{el} \left(\sum_{i=1-9} \alpha_i u_i \right)^2 \qquad 8.47$$

which is differentiated with respect to the nine atomic displacements to satisfy Eq. 8.10 for the minimisation of total potential energy. As is demonstrated for a bond-stretch element in Eqs. 8.35 - 8.37 above, the differentiation produces the element stiffness matrix. For a bond-angle element, this matrix is a 9 x 9 matrix which takes the form

$$k_{el} \begin{bmatrix} \alpha_1\alpha_1 & \alpha_1\alpha_2 & \dots & \alpha_1\alpha_9 \\ \alpha_1\alpha_2 & \alpha_2\alpha_2 & \dots & \alpha_2\alpha_9 \\ \vdots & \vdots & \ddots & \vdots \\ \alpha_1\alpha_9 & \alpha_2\alpha_9 & \cdots & \alpha_9\alpha_9 \end{bmatrix} . \qquad 8.48$$

8.3.5 Development of the bond-dihedral AFEM element

Fig. 8.9 shows a bond-dihedral element which relates the change in the dihedral angle to increase in potential energy. For four atoms, A, B, C, D, the bond-dihedral potential energy in the MD force field considers the dihedral angle Φ which is defined as the angle between the ABC plane and the BCD plane. The deformation is similar to a mechanical torsion spring as shown in the bottom left of the figure. Eqs. 8.49 - 8.63 demonstrate the theory of an AFEM bond-dihedral element, which is valid for both proper and improper dihedral potential energy functions in PLAFF2.

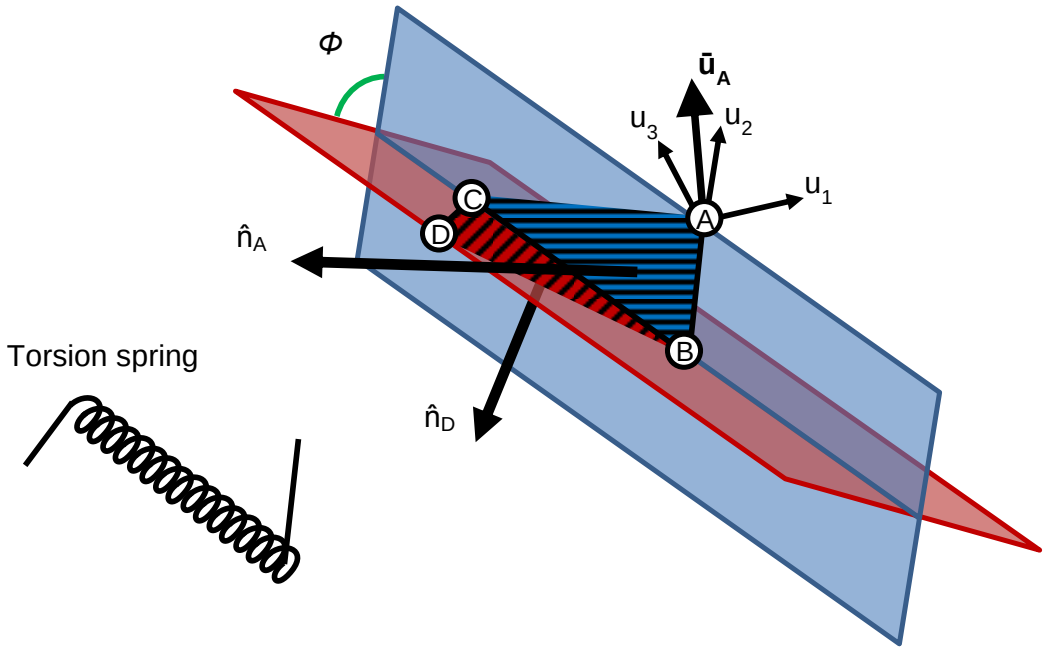

Fig. 8.9 Schematic of a bond-dihedral element for 4 atoms. Changes to the dihedral angle Φ between the planes of atoms A, B, C and B, C, D are considered in AFEM.

As with bond-stretch and bond-angle elements, there are three Cartesian scalar atomic displacements for each atom. These combine as vector displacements for each atom A, B, C and D, which are $\bar{u}_A$, $\bar{u}_B$, $\bar{u}_C$ and $\bar{u}_D$, respectively, according to

$$\bar{u}_A = \begin{pmatrix} u_1 \\ u_2 \\ u_3 \end{pmatrix} \qquad \bar{u}_B = \begin{pmatrix} u_4 \\ u_5 \\ u_6 \end{pmatrix} \qquad \bar{u}_C = \begin{pmatrix} u_7 \\ u_8 \\ u_9 \end{pmatrix} \qquad \bar{u}_D = \begin{pmatrix} u_{10} \\ u_{11} \\ u_{12} \end{pmatrix} \tag{8.49}$$

In Fig. 8.9, the dihedral angle is shown as the angle between the planes defined by the $\hat{n}_A$ and $\hat{n}_D$ vectors. These vectors are given by

$$\hat{n}_A = \frac{\bar{r}_A \times \bar{r}_{BC}}{\left|\bar{r}_A \times \bar{r}_{BC}\right|} \quad \text{and} \quad \hat{n}_D = \frac{\bar{r}_D \times \bar{r}_{BC}}{\left|\bar{r}_D \times \bar{r}_{BC}\right|} \tag{8.50}$$

in which $\bar{r}_A$ is the vector from atom B to A, $\bar{r}_{BC}$ is the vector from atom B to C, and $\bar{r}_D$ is the vector from atom C to D, as shown in Fig. 8.10 (a).

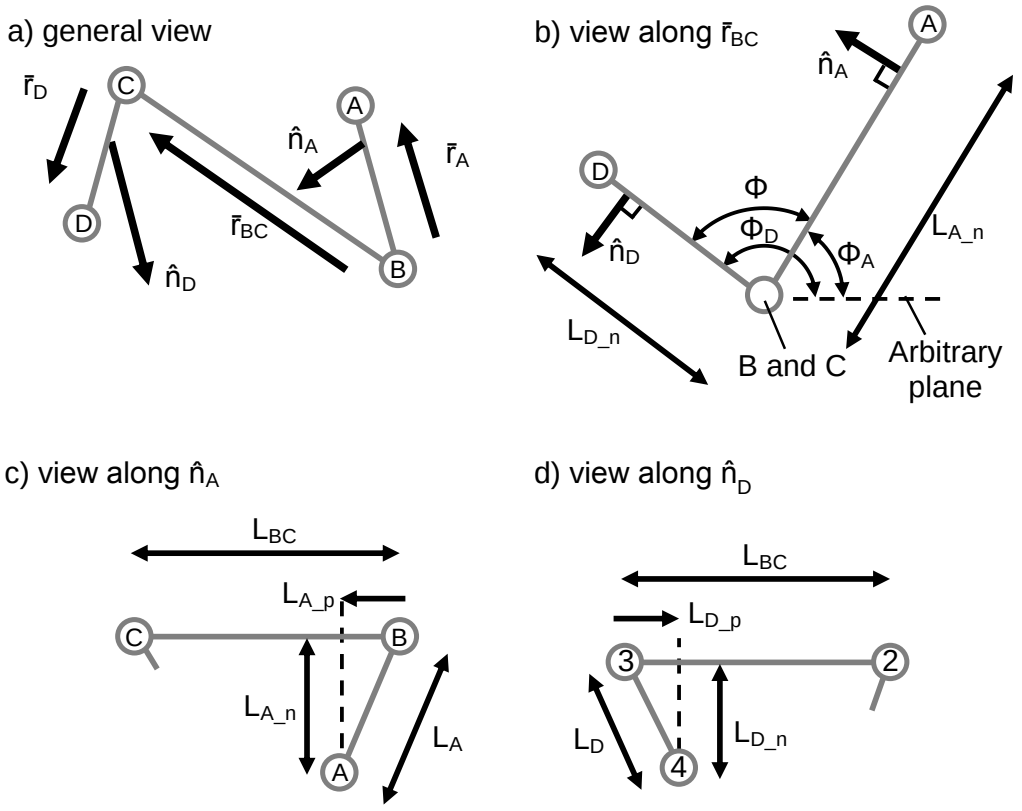

Fig. 8.10 Definitions of lengths, vectors and angles that are used in the differentiation of the bond-dihedral element for the purpose of minimisation of total potential energy.

As with the bond-angle element, the Cartesian atomic displacements need to be related to change in element angle since the strain energy of the element depends on the change in angle. To relate a vector displacement of each atom ($\bar{u}_A$ to $\bar{u}_D$) to change in dihedral angle, it is helpful to view the structure along the $\bar{r}_{23}$ vector, as shown in Fig. 8.10 (b). The dihedral angle can be considered as the difference between the angles that the planes defined by $\hat{n}_A$ and $\hat{n}_D$ make with the arbitrary plane according to

$$\phi = \phi_D - \phi_A . \qquad 8.51$$

Similarly, changes in the dihedral angle due to deformation of the bond-dihedral element may be expressed as

$$\Delta\phi = \Delta\phi_D - \Delta\phi_A . \qquad 8.52$$

For small displacements, the change in angle Φ_A in radians due to the vector displacement $\bar{u}_A$ of atom A is

$$\Delta\phi_A = \frac{\bar{u}_{A\cdot} \cdot \hat{n}_A}{L_{A\_n}} . \qquad 8.53$$

in which L_{A_n} is the perpendicular distance of atom A from the vector $\bar{r}_{BC}$ as shown in Fig. 8.10 (c). Similarly, the change in angle Φ_D due to displacement of atom D is

$$\Delta\phi_D = \frac{\bar{u}_D \cdot \hat{n}_D}{L_{D\_n}} \qquad 8.54$$

where L_{D_n} is defined in Fig. 8.10 (d). For atoms B and C, the relationship between their atomic displacement and change in dihedral angle is complicated by the fact their displacement leads to a change in the vector $\bar{r}_{BC}$. Fig. 8.11 (a) shows a view along $\bar{r}_{BC}$ with atoms A, B and C all in the horizontal plane. The arbitrary plane shown in Fig. 8.10 (b) is also chosen to contain atoms A, B and C so the angle Φ_A is equal to zero in Fig. 8.11 (a). The horizontal component of a displacement $\bar{u}_B$ of atom B in Fig. 8.11 (a) has no effect on the angle Φ_A. This is because the plane ABC is unaffected by atomic displacement within the plane. Only the $\hat{n}_A$ component of the displacement of node B, given by $\bar{u}_B \cdot \hat{n}_A$, affects the angle. The change in vector $\bar{r}_{BC}$ due to $\bar{u}_B$ can be considered to produce an effective displacement of atom A; this is because in the view along the new vector $\bar{r}_{BC}$, the position of atom A is different than when viewing down the original vector $\bar{r}_{BC}$.

Fig. 8.11 (b) shows a side view with nodes A, B and C in the horizontal plane. Fig. 8.11 (c) and (d) show the effect of displacement of atom B from the side view and the post-displacement $\bar{r}_{BC}$ view.

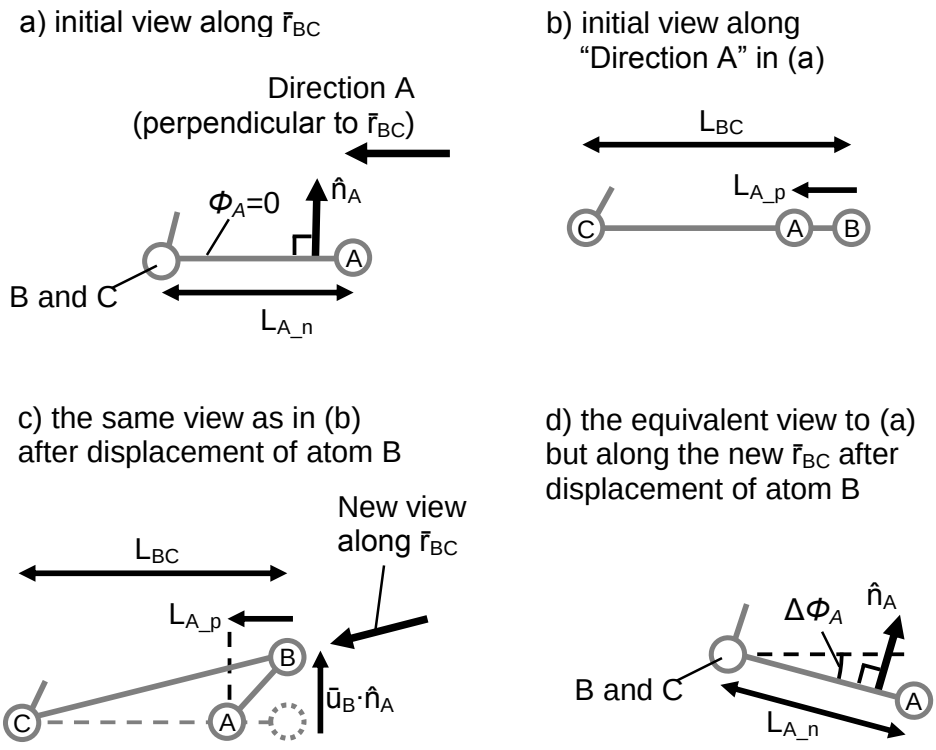

Fig. 8.11 Schematic of the change in angle Φ_A due to a displacement of atom B while atoms A and C remain stationary.

For small displacements, the relationship between displacement $\bar{u}_B$ and change in angle Φ_A in radians is

$$\Delta\phi_A = -\frac{\bar{u}_B \cdot \hat{n}_A}{L_{A\_n}}\left(\frac{L_{BC} - L_{A\_P}}{L_{BC}}\right) \qquad 8.55$$

in which the terms L_{BC} and L_{A_p} are shown in Fig. 8.11. This is very similar to Eq. 8.53 with the addition of the terms in brackets which are equal to the distance (along $\bar{r}_{BC}$) between atoms A and C, divided by the distance (along $\bar{r}_{BC}$) between atoms B and C. These terms are necessary because if atoms A and C are close in Fig. 8.11 (c), the effect of displacement of atom B on Φ_A reduces, while if atoms B and C are closer the effect of $\bar{u}_B$ is magnified. The distance L_{A_p} is direction and has a sign convention such that it is positive when the angle ABC is less than 90°. The minus sign at the beginning of the equation results from the fact that if $\bar{u}_B$ is positive in the $\hat{n}_A$ direction, the change in Φ_A is negative. In a similar manner, the change in angle Φ_A due to displacement $\bar{u}_C$ of atom C can be calculated as

$$\Delta\phi_A = -\frac{\bar{u}_C \cdot \hat{n}_A}{L_{A\_n}}\left(\frac{L_{A\_P}}{L_{BC}}\right) \tag{8.56}$$

and the change in angle Φ_D due to displacements $\bar{u}_B$ and $\bar{u}_C$ respectively are

$$\Delta\phi_D = -\frac{\bar{u}_B \cdot \hat{n}_D}{L_{D\_n}}\left(\frac{L_{D\_P}}{L_{BC}}\right) \tag{8.57}$$

and

$$\Delta\phi_D = -\frac{\bar{u}_C \cdot \hat{n}_D}{L_{D\_n}}\left(\frac{L_{BC} - L_{D\_P}}{L_{BC}}\right). \tag{8.58}$$

As with L_{A_p}, the sign convention for L_{D_p} is that it is positive when the angle BCD is less than 90°. Aside from L_{A_p} and L_{D_p} all lengths discussed here take positive values. The six relationships in Eqs. 8.53 - 8.58 between atomic displacement and change in angles Φ_A and Φ_D all contribute towards the overall change in dihedral angle, given in Eq. 8.52, which can be expressed in terms of atomic displacements as

$$\begin{aligned}\Delta\phi &= \Delta\phi_D - \Delta\phi_A = \\ &\left(\frac{\bar{u}_D \cdot \hat{n}_D}{L_{D\_n}} - \frac{\bar{u}_B \cdot \hat{n}_D}{L_{D\_n}}\left(\frac{L_{D\_P}}{L_{BC}}\right) - \frac{\bar{u}_C \cdot \hat{n}_D}{L_{D\_n}}\left(\frac{L_{BC} - L_{D\_P}}{L_{BC}}\right)\right) \\ &-\left(\frac{\bar{u}_{A\cdot} \cdot \hat{n}_A}{L_{A\_n}} - \frac{\bar{u}_C \cdot \hat{n}_A}{L_{A\_n}}\left(\frac{L_{A\_P}}{L_{BC}}\right) - \frac{\bar{u}_B \cdot \hat{n}_A}{L_{A\_n}}\left(\frac{L_{BC} - L_{A\_P}}{L_{BC}}\right)\right)\end{aligned} \tag{8.59}$$

Each of the vector atomic displacements $\bar{u}_A$, $\bar{u}_B$, $\bar{u}_C$, $\bar{u}_D$ in Eq. 8.59 consist of three Cartesian scalar atomic displacements as described in Eq. 8.49 above. Therefore Eq. 8.59 can be written in terms of the 12 atomic displacements u_1 to u_{12}. As demonstrated for the bond-stretch and bond-angle elements, the equation for $\Delta\Phi$ can be differentiated with respect to the 12 atomic displacements in order to determine the individual effect , α_i, of each displacement on the dihedral angle, Φ, according to

$$\alpha_i = \frac{d(\Delta\phi)}{d(u_i)}. \tag{8.60}$$

Then the total change in dihedral angle can be calculated as

$$\Delta\phi = \sum_{i=1-12} \alpha_i u_i \ . \qquad 8.61$$

which can be substituted into Eq. 8.13 to give the element potential energy as

$$V_{el} = \tfrac{1}{2} k_{el} \left(\sum_{i=1-12} \alpha_i u_i \right)^2 . \qquad 8.62$$

The potential energy is differentiated with respect to the twelve atomic displacements according to Eq. 8.10, for total potential energy minimisation. As is demonstrated for bond-stretch and bond-angle element stiffness matrices above, the differentiation produces the 12 x 12 element stiffness matrix as given by

$$k_{el} \begin{bmatrix} \alpha_1\alpha_1 & \alpha_1\alpha_2 & \cdots & \alpha_1\alpha_{12} \\ \alpha_1\alpha_2 & \alpha_2\alpha_2 & \cdots & \alpha_2\alpha_{12} \\ \vdots & \vdots & \ddots & \vdots \\ \alpha_1\alpha_{12} & \alpha_2\alpha_{12} & \cdots & \alpha_{12}\alpha_{12} \end{bmatrix} . \qquad 8.63$$

8.3.6 The AFEM program setup

A dedicated Visual Basic program is created in this thesis to run the AFEM simulations. The program incorporates MATLAB scripts and completes the following tasks:

1. Import a polymer structure file containing the atomic coordinates.
2. Analyse the structure to identify the AFEM elements based on the MD force field PLAFF2.
3. Build the local stiffness matrices and the global stiffness matrix.
4. Include boundary conditions to represent an applied strain.
5. Solve the simultaneous equations in order to calculate the final atomic coordinates after the structure has been strained.
6. Calculate the increase in interatomic potential energy in each AFEM element based on the calculated atomic displacements, in order to determine Young's modulus.

Steps 1-3 and 6 are conducted in a Visual Basic environment while steps 4-5 are conducted in MATLAB.

The nonbond potential energy function theoretically applies to all atom pairs in a polymer. However, this requires an infinitely large number of elements to be considered. The long range nature of the nonbonds is often incorporated through Ewald summation techniques in molecular dynamics simulations but these techniques do not translate well to AFEM. In order to ensure reasonable computational requirements, it is necessary to limit the maximum distance that is considered for nonbonds, referred to as the nonbond cut-off distance. Nonbond elements are only included for atom pairs that have an interatomic separation less than the nonbond cut-off distance. For the simulations of a poly(lactide) structure in this thesis a nonbond cut-off distance of 0.95 nm is used, since this value is frequently employed in molecular dynamics studies. The nonbond cut-off distance is varied in some simulations, which specifically investigate the importance of nonbond cut-off distance.

8.3.6.1 Calculation of Young's modulus from potential energy increase

As a result of an applied displacement, the interatomic potential energy increases. This increase represents strain energy and is used to calculate Young's modulus according to the method described in Eqs. 8.64 - 8.66. The total strain energy in a structure can be found by summing up the individual elements' strain energies after deformation. For a unit cell of continuous material that is uniaxially strained, the strain energy stored in the material, U, is equal to the work that is applied to the material. It is given by

$$U = \tfrac{1}{2} F u \qquad 8.64$$

where F is the force applied to the unit cell boundary and u is the cell elongation that results from the applied force. The stress in the direction of applied force, σ, can be calculated using Eq. 8.64 as

$$\sigma = \frac{F}{A} = \frac{U}{\tfrac{1}{2} A u} \qquad 8.65$$

where A is the cross-sectional area of the unit cell, perpendicular to the applied force. The strain is equal to the unit cell elongation u divided by the unit cell length L. Young's modulus can therefore be calculated as stress divided by strain according to

$$E = \frac{\left(\frac{U}{\frac{1}{2}Au}\right)}{\left(\frac{u}{L}\right)} = \frac{UL}{\frac{1}{2}Au^2} \qquad 8.66$$

8.3.6.2 Periodic boundary conditions

Periodic boundary conditions are used to enable large structures to be represented by a smaller repeating unit cell, which repeats in all directions to infinity. For molecular dynamics and AFEM simulations, this means a large structure of many atoms can be simulated while the actual number of degrees of freedom being considered is much smaller; only those in one of the unit cells. As a result, the number of linear equations that results from the differentiation of total potential energy in Eq. 8.10 is lower, which is necessary to ensure reasonable computation requirements. The unit cell being modelled is referred to as the "central unit cell" while all others are referred to as periodic images. Periodic boundary conditions are used to represent the interactions between atoms in the central unit cell and atoms in the surrounding unit cell images. The displacements of atoms in the unit cell images are identical, within their respective unit cells, to those in the central unit cell. Elongation or contraction of the central unit cell causes all periodic unit cells to displace in order to maintain the periodic cell boundaries. For each of the three Cartesian directions, there is a displacement of the unit cell boundary, u_{cell}. For an applied force, F, to the unit cell boundary, u_{cell} is found in order to minimise total potential energy. For 3D simulations, the two values of u_{cell} that are calculated perpendicular to the direction of applied force or displacement indicate Poisson's ratio. Since the three u_{cell} terms are found in order to minimise potential energy, the differential of the total potential energy equation with respect to these u_{cell} terms must equal zero, as for u_i terms in Eq. 8.10. This gives three extra linear equations and therefore the global stiffness matrix increases in size by 3 rows and columns. When applying boundary conditions for the purpose of solving the series of linear equations, the u_{cell} terms may be set manually in order to represent an applied displacement to the unit cell boundary.

8.4 Validation of AFEM

Tests are performed here to validate individual aspects of the AFEM simulation. The bond-angle and bond-dihedral elements are utilised in a simple structure to ensure that they are resisting deformation in the correct manner. Another simple structure is used to validate that the periodic boundary conditions and values of Poisson's ratio are being identified in AFEM correctly. A portion of an atomic structure for crystalline poly(lactide) is analysed using the AFEM program presented in this thesis and an existing FEA program to ensure the results are the same. Finally, in order to check that the AFEM program is minimising the finite element potential energy correctly, the atomic displacements found by the AFEM program are modified to ensure that potential energy increases as a result.

8.4.1 Validation of the bond-angle and bond-dihedral AFEM elements

In order to validate the implementation of bond-angle elements, a simple 4-atom structure as shown in Fig. 8.12 is used. There are three bond-stretch elements between atoms 1-2, 2-3 and 3-4. The lengths of all of these elements are 1 m and have a stiffness of 1 J m^{-2}, which is equivalent to 1 N m^{-1}. The large values are used to simplify manual analysis in these preliminary tests. There are 2 bond-angle elements, between atoms 1-2-3 and 2-3-4, which both have initial angles of 90° and a stiffness of 1 J rad^{-1}, which is equivalent to 1 Nm rad^{-1}. A y-displacement of 0.06m is applied to atom 4, which is equivalent to 6% of the structure's y dimension. Atom 3 is free to displace in the y direction in order to minimise potential energy according to the AFEM method.

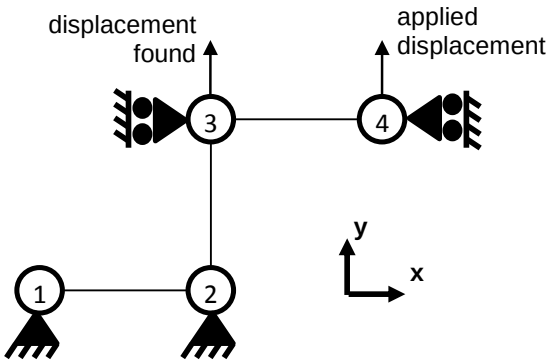

Fig. 8.12 A simple 4-atom structure is used to validate the bond-angle elements. Atoms 1 and 2 are fixed, atom 3 is free to displace in the y direction only, and atom 4 is manually displaced in the y direction and fixed in the x direction.

The results of the AFEM simulation are shown in Fig. 8.13. A displacement in the y-direction of 0.03 m is found for atom 3. The displacement of atom 4 is accommodated by elongation of the bond-stretch element between atoms 2-3 along with an increase in the angle of the bond-angle element between atoms 2-3-4. For small displacements, the change in angle of the bond element 2-3-4 can be calculated as the y-displacement of atom 4 relative to atom 3 divided by the distance between atom 3 and 4. Therefore the AFEM simulation finds the change is bond-angle to be 0.03 rad. Given the stiffness of the element is 1 Nm rad^{-1}, a torque of 1 Nm is required in order to achieve the atomic displacement found; this equates to a y-direction force of 0.03 N being applied to atom 4. This force is transferred through the bond-stretch element 2-3 to the fix constraint at atom 2. Therefore the bond-stretch element 2-3 must elongate by 0.03 m, given it has stiffness of 1 N m^{-1}. This elongation is found by the AFEM simulation which indicates that the AFEM simulation is correctly implementing bond-stretch and bond-angle elements.

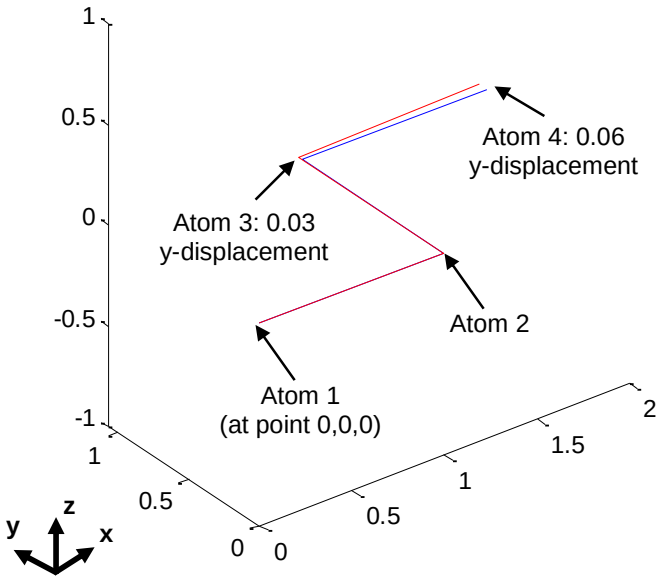

Fig. 8.13 Results of the AFEM simulations for the simple 4-atom structure shown in Fig. 8.12. The original structure (blue) displaces to the deformed structure (red).

In order to test the bond-dihedral AFEM element, the position of atom 4 is changed to be directly above atom 3 in the z direction rather than being in the positive x direction. The same bond-stretch and bond-angle elements exist as are used in the previous test shown in Fig. 8.13. In addition to those elements, a bond-dihedral element is included between atoms 1-2-3-4. The stiffness of the bond-dihedral element is 1 Nm rad^{-1} which is the same as the bond-angle element. Fig. 8.14 shows the structure before and after

the AFEM simulations for an applied displacement of atom 4 in the x-direction of 10% of the overall structure size in the x-direction. This displacement can be accommodated by elongation of bond-stretch element 1-2, increase in the angle of bond-angle element 1-2-3, and increase in the angle of the bond-dihedral element 1-2-3-4. The displacement of atoms 2, 3 and 4 together causes elongation of the bond-stretch element, the displacement of atoms 3 and 4 together causes an increase in the angle of the bond-angle element, and displacement of atom 4 in isolation causes an increase in the angle of the bond-dihedral element. As discussed in relation to Fig. 8.13, the stiffness used for the bond-stretch and bond-angle elements, and the distance of 1m between atoms, means that the overall x-displacement accommodated by the bond-stretch and bond-angle elements is equal for the same force. Therefore the x-displacement of atom 2 relative to atom 1 is expected to be the same and the x-displacement of atom 3 relative to atom 2. The isolated displacement of atom 4 in the x direction causes the bond-dihedral angle to increase but does not affect the elongation of bond-stretch element 1-2 or bond-angle element 1-2-3. For a very weak bond-dihedral stiffness, all y-displacement is expected to be accommodated by the displacement of atom 4 alone; for a rigid bond-dihedral, the x-displacement of atoms 3 and 4 should be equal. For small displacements, the increase in radians of the bond-dihedral angle is equal to the displacement of atom 4 in metres since the distance between atoms 3 and 4 is unity. Therefore the stiffness of the bond-dihedral elements of 1 Nm rad^{-1} provides an effective resistance to the displacement of atom 4 relative to atom 3 of 1 N m^{-1}. This resistance is the same as bond-stretch element 1-2's resistance to displacement of atom 2 relative to atom 1, in the x direction. It is also equal to the resistance of atom 3 relative to atom 2, due to the bond-angle element. As a result, the displacement of atom 4 relative to atom 3 should be the same as the displacement of atom 3 relative to atom 2 and of atom 2 relative to atom 1; all with respect to x direction displacements. The AFEM simulation finds x-displacements of atoms 2, 3 and 4 to be 0.0333, 0.0667 and 0.1 m respectively, which agrees with the above analysis. Therefore the AFEM simulation is successfully implementing the bond-stretch, bond-angle and bond-dihedral elements.

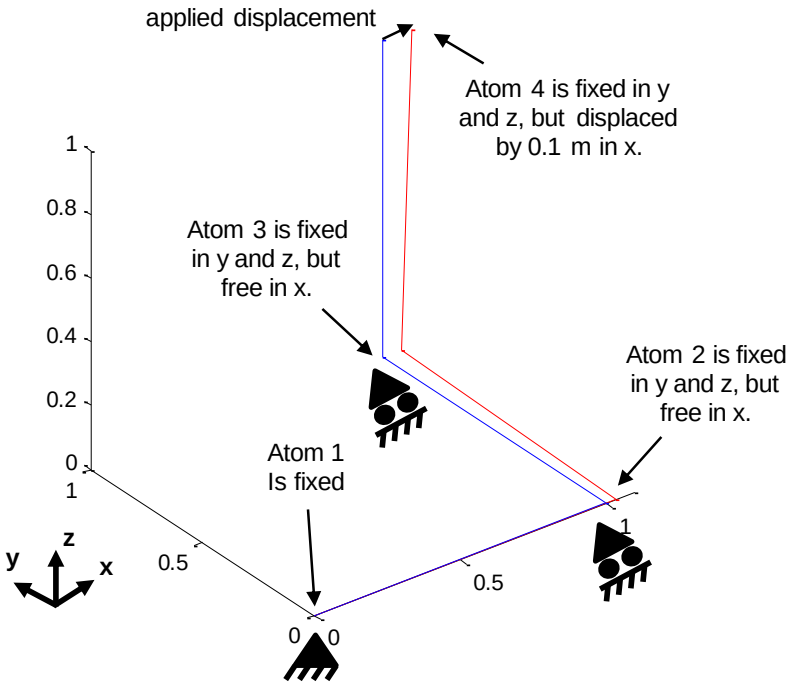

Fig. 8.14 A simple 4-atom structure (blue) displaces to the deformed structure (red) during AFEM simulations.

8.4.2 Validation of the periodic boundary conditions and Poisson's ratio

To test the periodic boundary conditions of AFEM simulations, a simple unit cell containing 6 atoms as shown in Fig. 8.15 (a) is strained in the z direction by manually setting u_{cell} for the z dimension of the unit cell. The atoms are linked by nonbond AFEM elements which are assigned a stiffness of $1x10^{-9}$ N nm^{-1} and the distance between the atoms is 0.1nm. The unit cell dimensions are therefore 0.1x0.1x0.6 nm. There are 5 nonbonds that are non-periodic which are coloured blue in Fig. 8.15 (a), whereas the periodic AFEM elements are coloured red. Atom 6 at the top of the unit cell is periodically connected to an image of atom 1 at the bottom of the adjacent unit cell image in the positive z direction. Similarly, atom 1 in the figure is bonded to an image of atom 6 in the adjacent unit cell image in the negative z direction. All atoms are bonded to four periodic versions of themselves in the adjacent unit cell images in the x and y directions. Bond-angle elements are also included to prevent the structure from being free to skew without resistance.

The Young's modulus value calculated by the AFEM program is 10GPa, which can be manually checked according to Eq. 8.66. The initial structure (red) is shown in Fig. 8.15 (b) along with the displaced structure (blue) offset to the right. For a 10% strain (u_{cell} =

0.06 nm), the individual element displacement is expected to be 0.01 nm. The strain energy of each vertical element is therefore

$$U = \tfrac{1}{2} k_{el} d_{el}^{\ 2} = \tfrac{1}{2} 1x10^{-9} 0.01^2 = 5x10^{-14} \text{ N nm.} \quad 8.67$$

There are 5 non-periodic and 2 periodic elements which all contain this strain energy so the total strain energy is 30 x10^{-14} N nm. By substituting this value into Eq. 8.66, along with L_z=0.6 nm, A_z=0.01 nm^2 and d_z=0.06 nm, Young's modulus is calculated as

$$E = \frac{UL_z}{\tfrac{1}{2} A_z d_z^{\ 2}} = \frac{30x10^{-14} * 0.6}{\tfrac{1}{2} * 0.1^2 * 0.06^2} = 1x10^{-8} \text{ N nm}^{-2}. \quad 8.68$$

The Young's modulus is therefore calculated as 1x10^{10} N m^{-2} which is 10GPa as found by the AFEM simulation. This value of Young's modulus can also be checked by simple force mechanics. This simulation indicates that the AFEM simulations are being completed successfully and that the calculation of Young's modulus is correct.

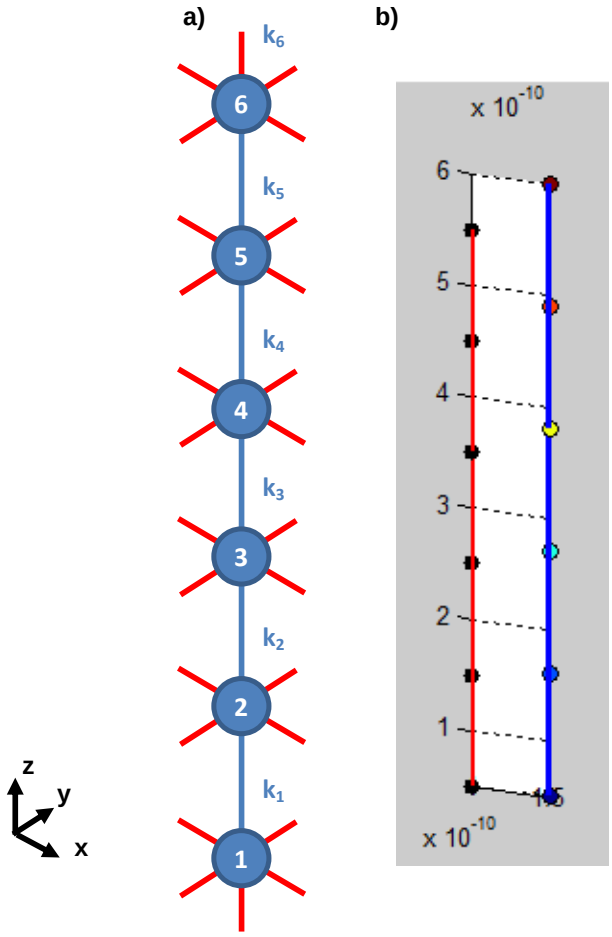

Fig. 8.15 The periodic boundary conditions are tested for a unit cell containing 6 evenly spaced atoms. (a) shows the unit cell atomic structure in which periodic (red) and non-periodic (blue) AFEM nonbond elements are used to connect all atoms to the adjacent atoms in the x, y and z directions. (b) shows the initial (red) and displaced (offset blue) atomic coordinates used/found in the AFEM simulation.

To validate the ability of the AFEM simulations to consider periodic boundary conditions in 3D, and the ability to identify the correct values of Poisson's ratio, an atomic grid structure is used as shown in Fig. 8.16 with diagonal elements. The atoms are arranged in a 3D grid and the central unit cell contains 8 atoms which make up the corners of a cube. Nonbonds are used in the simulations to connect the atoms. Each atom in a grid is nonbonded to the 26 neighbouring atoms in the x, y, z and diagonal directions. The diagonal elements which effectively lie on the faces of the cube, rather than passing through the centre of the cube, are not shown in Fig. 8.16 (a) and (b) for clarity in the images. The effective cube that is outlined by the non-periodic elements in Fig. 8.16 (a) lies in the centre of the cubic periodic unit cell, which is twice as big in all dimensions, as shown in Fig. 8.16 (c). The deformation of the structure when Poisson's

ratio is constrained to be zero can be seen in Fig. 8.16 (d), which is achieved by setting u_{cell} in the x and y direction to be zero.

a) only non-periodic elements:

b) periodic (blue) and non-periodic (red) elements:

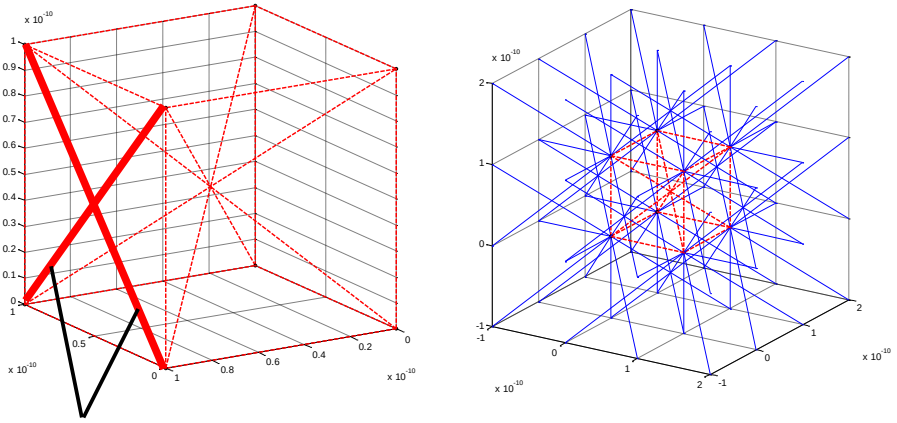

These diagonal elements, which are effectively "cube-face" rather than "through-cube" diagonals, do exist but are not shown in (a) and (b) for clarity.

c) view from above showing the periodic cell boundaries:

d) the unit cell before (red) and after (blue) strain with all non-periodic elements:

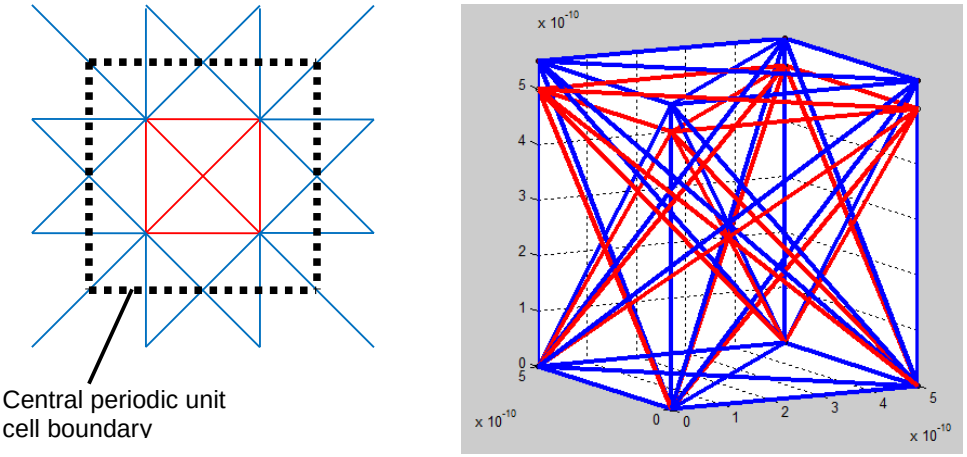

Fig. 8.16 The test atomic structure is shown with only non-periodic elements (a) and with both periodic and non-periodic elements (b). The boundaries of the central unit cell are shown in (c) and the non-periodic elements are shown before and after strain in (d). Some diagonal elements are missing in (a) and (b) as indicated for clarity.

To test the ability of the AFEM simulation to determine Poisson's ratio, the "through-cube" diagonal elements shown in Fig. 8.16 (a) and (c) are set to be three orders of magnitude stiffer than the other elements. The simulations therefore find the deformation which accommodates the 10% applied strain but does not result in changes to the length of the stiff diagonal elements. The results are shown in Fig. 8.17

(a) from a general viewpoint and Fig. 8.17 (b) when view from above. The atomic displacements demonstrate an overall contraction in the x and y directions. The values of u_{cell} in the x and y directions are found in the solution during AFEM rather than set manually. They are found to be negative and half the magnitude of u_{cell} in the z direction which indicates a value of Poisson's ratio of 50%. This value allows the stiff diagonal elements to rotate towards the direction of applied strain rather than elongate, which can be verified by simple trigonometric analysis.

An additional method of validation of periodic boundary conditions is to increase the size of the unit cell to include more atoms and check that the results are unaffected. This validation method is used for the crystalline poly(lactide) structure which is detailed and analysed by AFEM simulations in Chapter 9. In this section, the AFEM simulations have been validated to be able to implement periodic boundary conditions and correctly identify Poisson's ratio.

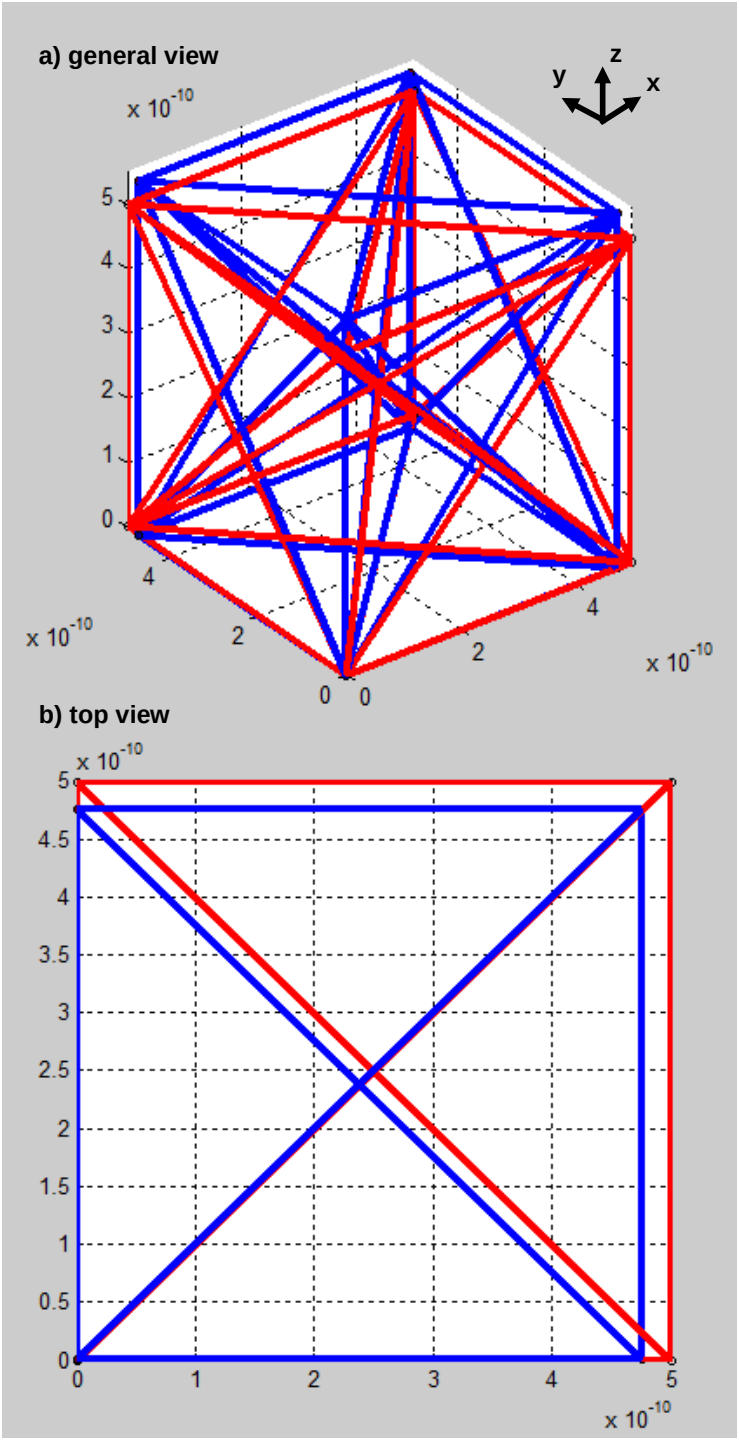

Fig. 8.17 The periodic structure before (red) and after (blue) deformation is shown from a general viewpoint (a) and from above (b). The through-cube diagonals are set to be three orders of magnitude stiffer than the other elements so Poisson's ratio is correctly found to avoid strain in these elements.

8.4.3 Validation of the AFEM program by comparison to a freely available FORTRAN FEA beam program

To further validate the AFEM method presented in this thesis, a simple structure is analysed using both AFEM simulations and a FORTRAN-based finite element analysis program, which utilises standard FEA beam elements and is supplied with Smith and Griffith's text book [105]. The results generated by the two methods are compared and must be in agreement. The 4-atom structure shown in Fig. 8.18 is used in the simulations, for which the atomic coordinates are derived from a sample poly(lactide) structure and are given in Table 8.1. There are covalent bonds between atoms 1-2, 2-3 and 3-4. The boundary conditions of the simulations are: a displacement of 1e-15 m is applied to atom 1 in the z direction and it is constrained in the x and y directions; atom 2 is unconstrained; atom 3 is constrained in x but free in y and z; and atom 4 is fully fixed.

Atom	x (m)	y (m)	z (m)
1	-9.35E-11	4.03E-11	-1.21E-09
2	2.32E-11	3.61E-11	-1.24E-09
3	9.40E-11	1.10E-10	-1.35E-09
4	1.41E-10	2.45E-10	-1.30E-09

Table 8.1 Coordinates of the atoms in the simulations

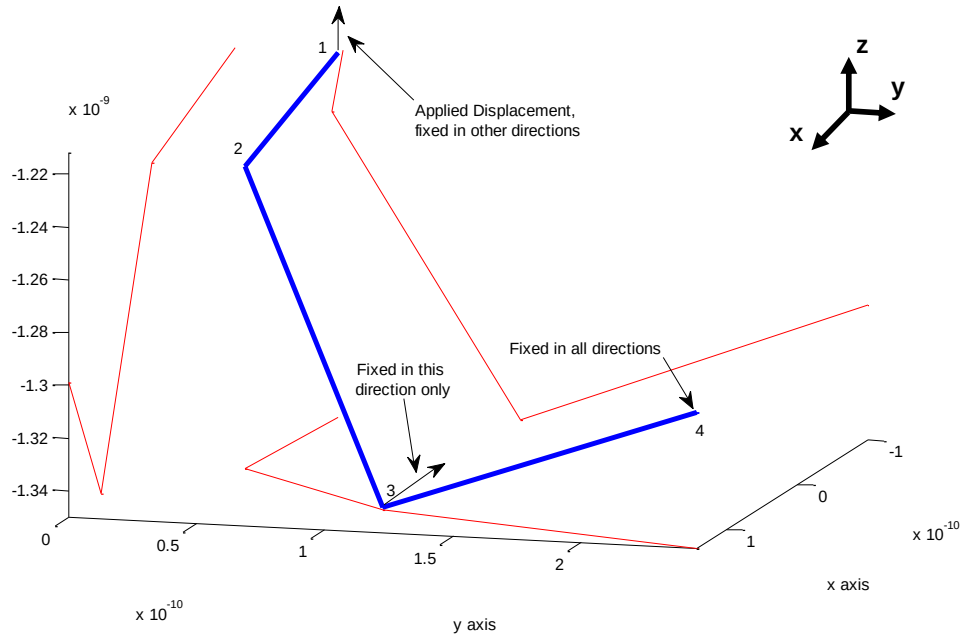

Fig. 8.18 A simple 4-atom structure is shown in blue. Projections of the structure are shown in red on planes normal to the x, y and z dimensions. Atom 1 is displaced in the z direction, atom 3 is constrained in y and z but free in x and atom 4 is fully fixed.

In the AFEM structure there are 3 bond-stretch elements, 2 bond-angle elements and 1 bond-dihedral element. For the FEA beam-element simulations, three regular FEA beam elements are used between atoms 1-2, 2-3 and 3-4. These beam elements resist deformation by elongation, bending, or twisting of the elements. The force field parameters are derived from the PLAFF2 force field as given in Table 8.2. These AFEM stiffnesses need to be translated into input parameters for the stiffness of the beams used in the FEA beam-element simulation, which is described here with Eqs. 8.69 - 8.72. The bond-angle AFEM elements are set to be infinitely stiff in order to allow the FEA beam-element program [105] to represent AFEM correctly as discussed shortly.

AFEM element type	Atoms	Stiffness	Units
Bond-stretch	1-2	1.58E+03	J m^{-2}
Bond-stretch	2-3	8.81E+02	J m^{-2}
Bond-stretch	3-4	7.45E+02	J m^{-2}
Bond-angle	1-2-3	≡ infinity	J rad^{-2}
Bond-angle	2-3-4	≡ infinity	J rad^{-2}
Bond-dihedral	1-2-3-4	7.94E-20	J rad^{-2}

Table 8.2 AFEM elements' stiffnesses in the structure

When considering elongation of the beam elements, the force *F* that must be applied to the beam in order to achieve a displacement of the end of the beam u_b is given by

$$F = \frac{EA}{L} u_b \qquad 8.69$$

in which *A* is the cross sectional area of the beam, *L* is the length of the beam, and *E* is the value of Young's modulus of the beam material. Therefore in order for the beam element to have the same stiffness as the AFEM bond-stretch element, the term EA/L must be equal to the AFEM bond-stretch element stiffness, k_b. The FEA beam-element program [105] automatically includes the length of the beam based on the atomic coordinates. Therefore the input to the FEA beam-element program [105] for beam stiffness, referred to as k_{EA}, is equal to

$$k_{EA} = EA = k_b L \qquad 8.70$$

The stiffnesses of the AFEM bond-stretch elements are therefore multiplied by the bond length in order to determine the stiffness value to use in the FEA beam-element program [105]. The units of k_{EA} are J m^{-1} rather than J m^{-2} for AFEM bond-stretch elements.

For beam bending, the input to the FEA beam-element program [105] represents the Young's modulus of the beam material multiplied by the second moment of area of the beam. There is no potential energy function in the molecular dynamics force field that is equivalent to bending of a beam between two atoms. The bond-angle term refers to the angle between bonds based on the angle between straight vectors through the atoms, which effectively means the beams must remain straight and therefore in beam bending theory the bending stiffness must be infinite. Similarly, the FEA beam-element program [105] considers the joints between beams to be rigid (the angle between beams at the node points are fixed) therefore the angle between two bonds cannot change. The value of bond-angle AFEM element stiffness is therefore set to effectively infinity as detailed in Table 8.2. For the stiffness inputs just described, neither the AFEM simulation nor the FEA beam-element simulation allow the angle between bonds to change or allow the bond to bend along its length.

For the translation of the bond-dihedral stiffness from AFEM to the FEA beam-element program [105], a similar approach to that for the bond-stretch elements is required. In beam bending theory, the torque T is related to torsion in the beam along the beam according to

$$T = \frac{GJ}{L}\alpha_t \qquad 8.71$$

where G is shear modulus of elasticity, J is the polar moment of inertia, L is the length of the beam and α_t is the torsion angle. For the AFEM bond-dihedral element however, the stiffness of the element k_{d_FEM} has units of J rad^{-2} and torque is given by direct multiplication of this stiffness with angular displacement; there is no dependency on the length of the bond about which rotation is being considered. Therefore the stiffness of the AFEM bond-dihedral element is equal to GJ/L. Since the FEA beam-element program [105] automatically considers the length of the bond, the input to the program for beam torsional stiffness, k_{GJ}, is given by

$$k_{GJ} = GJ = k_{d\_FEM} L \qquad 8.72$$

where L is the length of the covalent bond about which rotation is considered for the bond-dihedral element: the distance between the 2nd and 3rd atoms of the element. In the AFEM simulation, there is only one bond-dihedral element, which considers rotation about the bond between atoms 2 and 3. The rotation about the other two covalent bonds is not considered and therefore the torsional stiffness k_{GJ} of the beam between atoms 1-2 and 3-4 is set to be zero.

The results of the AFEM and FEA beam-element simulations are shown in Table 8.3 for displacement and applied (external) force. The terms that can be considered as non-zero are formatted in bold italic. Both simulations give the same results which validates the ability of the AFEM program to build element stiffness matrices, assemble them into a global stiffness matrix, apply boundary conditions, and solve the equations/matrices. The results are sensible since the externally applied forces balance to zero in all directions and external forces are only found to occur where boundary conditions are set. The FEA beam-element program solution also includes rotational displacements of nodes and external torques that are applied to nodes because the nodes are considered to be rigid joints. The nodes are found to rotate, which allows the central beam to undergo torsion, but no external nodal-torques are found because none of the atoms are constrained from rotation. Neither nodal-rotation nor applied nodal-torque are represented in the AFEM method because the elements represent molecular dynamics force field equations rather than solid body beams.

Atom	Direction	Displacement in AFEM (m)	Displacement in FORTRAN (m)	External Force in AFEM (N)	External Force in FORTRAN (N)
1	x	-7.83E-75	0.00E+00	***7.83E-15***	***7.83E-15***
1	y	-6.84E-75	0.00E+00	***6.84E-15***	***6.84E-15***
1	z	2.91E-75	0.00E+00	***-2.91E-15***	***-2.91E-15***
2	x	***-7.75E-17***	***-7.75E-17***	0.00E+00	0.00E+00
2	y	***-3.30E-16***	***-3.30E-16***	0.00E+00	0.00E+00
2	z	***-2.97E-16***	***-2.97E-16***	-3.31E-24	0.00E+00
3	x	1.31E-84	0.00E+00	0.00E+00	0.00E+00
3	y	***3.13E-16***	***3.13E-16***	0.00E+00	0.00E+00
3	z	***1.83E-16***	***1.83E-16***	1.99E-23	0.00E+00
4	x	7.83E-75	0.00E+00	***-7.83E-15***	***-7.83E-15***
4	y	6.84E-75	0.00E+00	***-6.84E-15***	***-6.84E-15***
4	z	***1.00E-15***	***1.00E-15***	***2.91E-15***	***2.91E-15***

Table 8.3 Results for displacements and required forces of the structure shown in Fig. 8.18 after displacement of atom 4 in the z direction. Terms that can be considered as non-zero are formatted in bold italic.

The technique of validating the AFEM method by comparison to the FEA beam-element program [105] results is also used for a much larger structure which represents a section of poly(lactide) crystalline chain. The structure used is shown in Fig. 8.19. Atom 79 is fixed in all 3 dimensions, atom 19 is fixed in the x/y directions, and atom 1 is fixed in x/y and displaced by $1x10^{-10}$ m in the z direction. The AFEM stiffnesses are derived from the PLAFF2 force field and are translated to elongation, bending and torsional stiffnesses for the beam-element-based FEA simulations as described in the previous study related to Fig. 8.18. Beam elongation stiffnesses are determined from the AFEM bond-stretch stiffness through Eq. 8.70. The AFEM bond-angle stiffness and the beam-bending stiffness are set to be infinitely stiff. In order to translate the AFEM bond-dihedral elements to beam torsional stiffness, only one bond-dihedral element can exist for each covalent bond about which rotation is considered. Therefore bond-dihedral elements are only included in the simulations if all four atoms of the element lie on the main polymer backbone. Beam stiffnesses for torsion are derived from the AFEM bond-dihedral stiffness according Eq. 8.72 for bond-dihedrals on the polymer backbone.

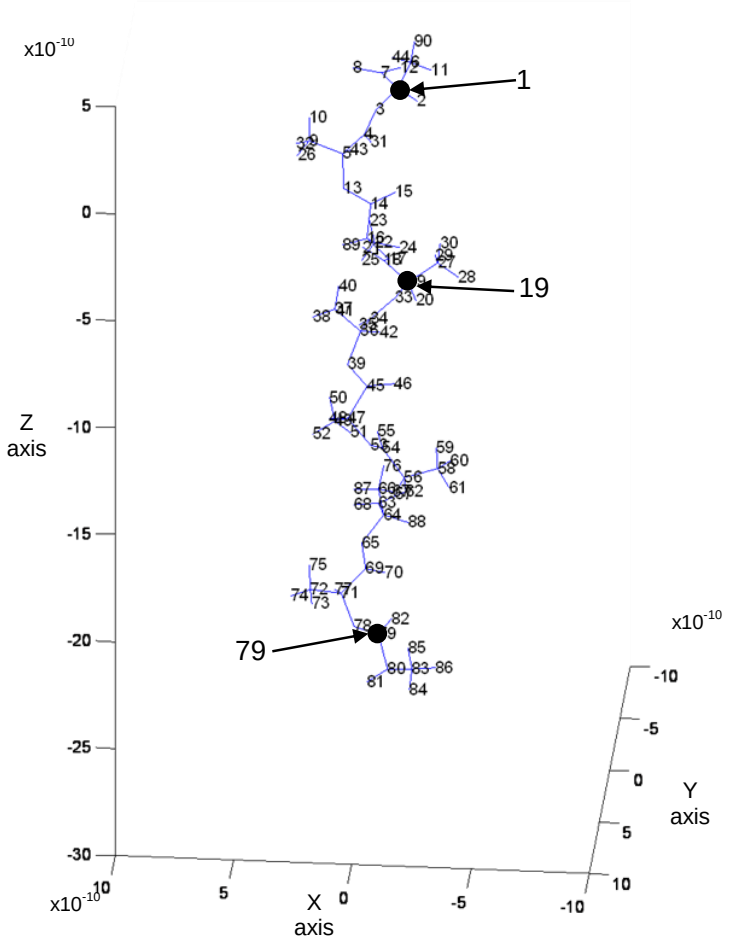

Fig. 8.19 The poly(lactide) chain used in simulations with atoms numbered from 1 to 90. Atom 79 is fixed in x/y/z, atom 19 is fixed in x/y, and atom 1 is fixed in x/y and displaced by $1x10^{-10}$ m in z.

The results of the AFEM simulation are shown in Fig. 8.20. The external z-direction force that must be applied to atom 1 is calculated as 1.802e-11 N in the AFEM simulation. The force in the z-direction calculated for atoms 19 is zero because it is not constrained in the z-direction. The external force calculated for atom 79 is 1.802e-11 N in the negative z-direction. Therefore the externally applied z-direction forces balance. In the FEA beam-element simulation, the same forces are found. Also, both AFEM and the FEA beam-element program [105] find the same displacements of all atoms. These results validate the ability of the AFEM program. The deformation of the structure is not representative of the deformation that may be expected for a real poly(lactide) chain because many of the bond-dihedral elements are set to infinitely low stiffness and nonbonds are not included. The large deformations in x and y directions are due to the bond-dihedral elements being the much weaker than the bond-stretch elements. It is more favourable for the structure to deform by rotation about bonds than by simple elongation of bonds. Such large deformations are shown for visual clarity and are

acceptable for validation purposes in which the scale of the deformation has no effect. However, for simulations that represent a real material, only small deformations are valid.

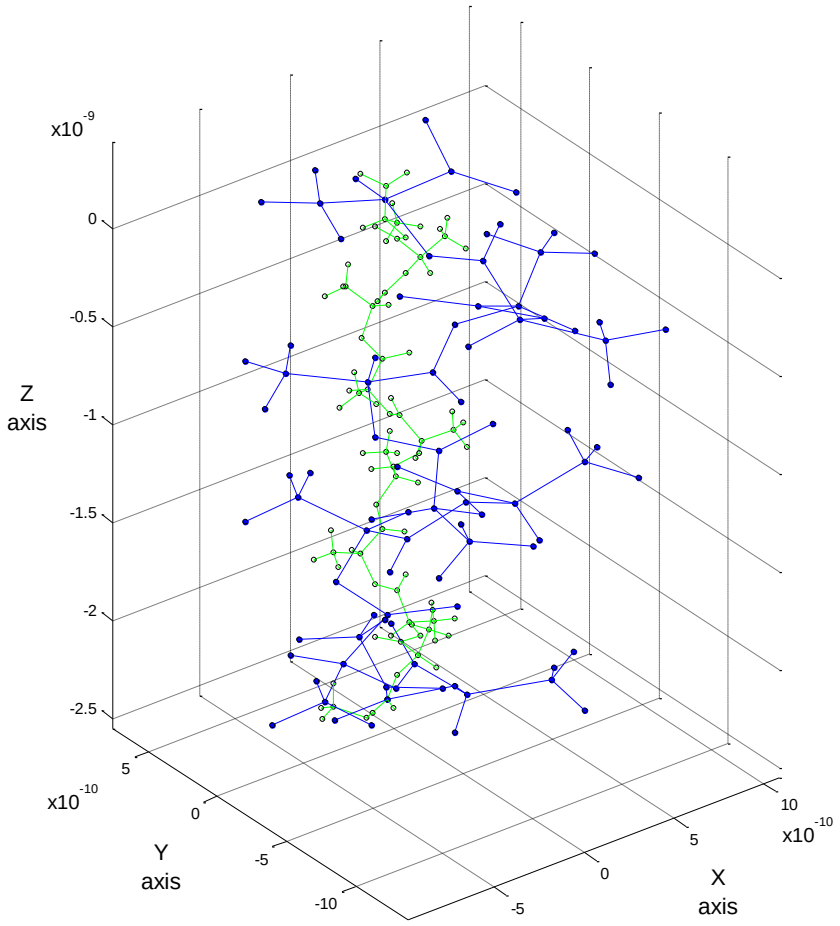

Fig. 8.20 The poly(lactide) chain is shown in the original (green) configuration and the deformed (blue) configuration after a displacement is applied to the structure.

8.4.4 Validation that the optimal displacements are found by AFEM

The AFEM method must find the optimal atomic positions that result from an applied strain to an atomic structure. In these positions, the potential energy sum for all AFEM elements should be at a minimum. This sum is equal to the work done by an applied force to the unit cell, *Fu* in Eq. 8.9 above. To validate that the AFEM simulation is working correctly, the calculated displacements are manually modified. If the optimal displacements are correctly found, before the manual modification, the potential energy sum for all AFEM elements must increase as a result of the manual modification to the atomic displacement results file. A sample crystalline poly(lactide) structure, similar to the one shown in Fig. 8.19 but with 180 atoms, is analysed using the AFEM method to

find the atomic displacements. Periodic boundary conditions are used, Poisson's ratio is calculated in the AFEM simulation, and all AFEM elements are included: bond-stretch, bond-angles, bond-dihedral (both proper and improper) and nonbond elements. The result for displacement of atom 172 is manually modified by a small amount in the positive and negative x, y and z directions. The resulting potential energy sums for all elements in the structure are given in Table 8.4. As can be seen, any manual modification to the calculated displacement value leads to an increase in potential energy. This indicates that the AFEM simulation is correctly finding the atomic displacements to minimise total potential energy, which therefore supports the ability of the AFEM simulations (i) to implement all element types, (ii) to implement periodic boundary conditions, and (iii) to determine Poisson's ratio successfully.

Test description	Strain energy (J)
No modification to AFEM displacement results	5.61383E-19
x-displacement of atom 172 varied +0.01E-11 m	5.61385E-19
x-displacement of atom 172 varied -0.01E-11 m	5.61385E-19
y-displacement of atom 172 varied +0.01E-11 m	5.61386E-19
y-displacement of atom 172 varied -0.01E-11 m	5.61386E-19
z-displacement of atom 172 varied +0.01E-11 m	5.61389E-19
z-displacement of atom 172 varied -0.01E-11 m	5.61389E-19

Table 8.4 The strain energy of the structure increases when the AFEM simulation results for atomic displacement are manually modified slightly in x, y and z directions, which indicates that the optimal displacements have been found.

8.5 Conclusions

The theory of minimisation of total potential energy was presented in the context of molecular dynamics and finite element analysis. The molecular dynamics force field PLAFF2, which was specifically developed for poly(lactide) [85], was used to develop the atomic finite element method, AFEM, for static linear analysis of poly(lactide). During AFEM simulations the following steps are taken:

1. Determine the atomic coordinates from a molecular dynamics polymer structure file and represent the polymer with AFEM elements.
2. Apply boundary conditions to represent an applied strain.
3. Solve the simultaneous equations in AFEM in order to minimise total potential energy and calculate the final atomic coordinates after the structure has been strained.
4. Calculate the potential energy increase of all AFEM elements in the polymer, based on the calculated atomic displacements, and therefore determine the value of Young's modulus for the polymer.

Three types of finite elements were presented to represent the potential energy functions in the molecular dynamics force field PLAFF2 [85]. The finite element stiffness matrices were presented for these elements which contain two, three, or four atoms, each with three degrees of freedom. Periodic boundary conditions and the method of identifying Poisson's ratio were incorporated in the AFEM simulation technique. The potential energy functions in PLAFF2 [85] are given in terms of interatomic separation of atoms or the angle between atoms. Those potential energy functions were translated to be in terms of atomic displacement in order to be suitable for AFEM. The values of stiffness used in the finite elements were derived from the force field. Several validations of individual aspects of the AFEM simulation technique were performed.

Chapter 9: Atomic analysis for the mechanical properties of poly(lactide) and the effect of chain scission

The atomic finite element method (AFEM) that was presented in the previous chapter of this thesis is used in this chapter to analyse amorphous and crystalline poly(lactide) structures. The mechanical properties are analysed with and without polymer chain scissions, which simulate biodegradation. Along with overall material properties, the atomic-scale transfer of force through a strained polymer is analysed. The simulation setup is also varied to identify the most important factors that affect mechanical properties. The effect of chain scission on the overall polymer Young's modulus is analysed. Finally, the local atomic-scale effect of chain scission on the interatomic transfer of force through a strained polymer is investigated. A large part of this chapter is included in publication drafts [102, 106].

9.1 Introduction

The degradation of the Young's modulus of biodegradable polymers is of great interest because medical devices constructed from these polymers are used in mechanical applications including structural support for broken bones. The critical review of mechanical properties in Chapter 2 found that molecular weight reduction, due to chain scission, plays a critical role in the degradation of mechanical properties. However, the precise effect of chain scissions is not well understood at present. The AFEM simulation technique is discussed in detail in Chapter 8. It allows atomic analysis of biodegradable polymers and is used in this chapter to further the understanding of how mechanical properties are affected by chain scission. Interatomic potential energy functions for covalent bonds and nonbonded interactions, which are taken from the PLAFF2 molecular dynamics force field for poly(lactide) [85], are used in atomic finite element analysis simulations. The AFEM simulation technique is greatly more computationally efficient than molecular dynamics (MD) simulations, which allows the analysis of polymer chain scission in large amorphous polymer structures. In AFEM, there are four main types of elements: three are used to simulate covalent bonds while the fourth represents nonbonded interactions including Lennard-Jones and Coulomb interactions. The three covalent bond elements are referred to as bond-stretch, bond-angle and bond-dihedral elements. They model the covalent bonds' stiffness with respect to interatomic separation of two covalently bonded atoms, the angle between

two covalent bonds, and the rotation of a polymer chain about a covalent bond, respectively. During the AFEM simulations, a strain is applied to the atomic structure and the resulting interatomic potential energy increase, which represents strain energy, in the AFEM simulations is used to identify Young's modulus for the polymer. Since the simulations are for static analysis, the magnitude of applied strain does not affect the calculation of Young's modulus. A value of 10% strain is used for the displayed results to ensure clarity in the images. In this chapter, the application of AFEM for crystalline and amorphous poly(lactide) structures is demonstrated and the relationship between Young's modulus and molecular weight, utilising a large number of scissions, is analysed; this relationship is compared to the trends found for experimental data in the critical review of mechanical properties in Chapter 2. Also, the AFEM results are analysed to investigate the local atomic-scale effects of individual chain scissions in terms of the force transferred through the polymer by individual atoms.

9.2 The crystalline and amorphous unit cells

The AFEM simulations import atomic coordinates from molecular dynamics polymer structure files. The coordinates are given for a central unit cell which repeats periodically in x, y and z directions to infinity. The repeats of this central unit cell are called images. Periodic boundary conditions mean an infinitely large structure can be represented by a few atoms in the central cell. This type of analysis is necessary since atomic simulations are computationally demanding and not suitable for a very large number of atoms. Periodic boundary conditions are used in the AFEM simulations in order to represent the fact that opposite sides of the central unit cell are effectively connected to each other in the adjacent unit cell images. If the central unit cell expands, all of the surrounding unit cell images also expand and are pushed outwards. In this thesis, both crystalline and amorphous polymer structures are analysed. The crystalline unit cell has been subject to several studies which optimise the atomic coordinates [53-56]. The crystalline structure used in this thesis is the most recent in the literature, proposed by Sasaki and Asakura [56]. For AFEM simulations, the unit cell of 180 atoms is repeated once in each of the x, y and z directions in order to achieve a unit cell containing 1440 atoms; this larger unit cell is desired for the analysis of chain scission in this thesis. Fig. 9.1 shows the unit cell used for AFEM simulations which contains 1440 atoms. The unit cell effectively contains 8 helical chains, which are aligned in the z direction, each with 20 repeat polymer units. The top of each chain is covalently bonded to the bottom of the same respective chain in the unit cell image that is adjacent and directly above. Therefore the chains have an infinitely large molecular

weight. Some chains lie on the x or y boundaries of the central unit cell and therefore contain atoms which are covalently bonded across these boundaries too. The unit cell has dimensions of 2.132 nm, 1.232 nm and 5.776 nm in the x, y and z directions respectively.

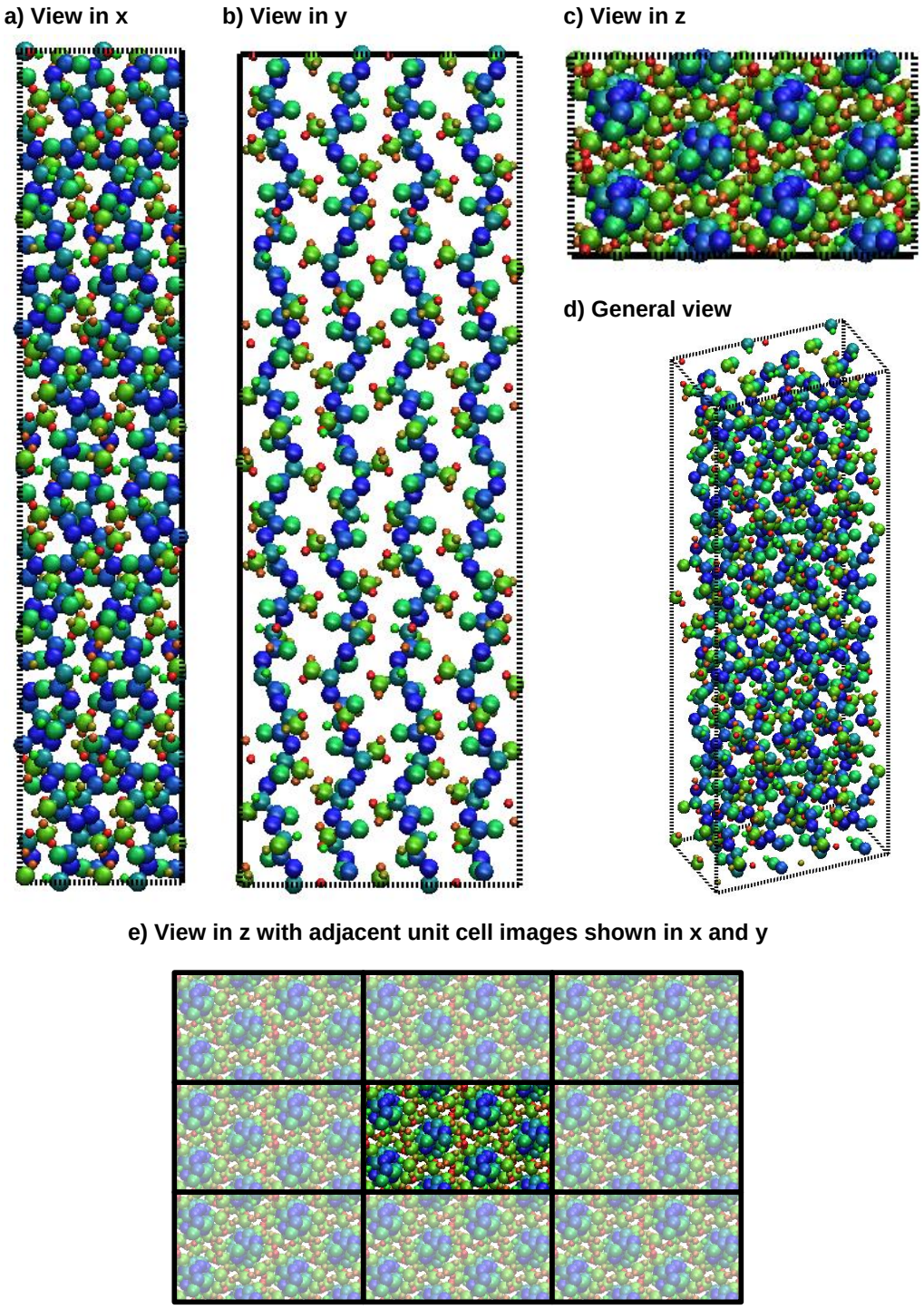

Fig. 9.1 The atomic unit cell structure for crystalline poly(lactide) contains 1440 atoms in 8 chain sections oriented in the z direction. The unit cell is shown viewed from the x direction (a), y direction (b), z direction (c), a general view (d) and from the z direction with periodic images of the central unit cell shown in x and y direction (e).

During the development of the PLAFF2 force field, McAliley created amorphous polymer structures which were supplied as supplementary information with the thesis [85]. The crystalline structure of Sasaki and Asakura [56] discussed above was also produced and supplied by McAliley. The amorphous unit cell is shown in Fig. 9.2 (a). It contains 3 amorphous chains, each consisting of 500 poly repeat units, and is in the form of a cube of side lengths 5.6098 nm. The chains have a molecular weight of 36000 g mol^{-1} which is a realistic initial molecular weight for a biodegradable polymer used in medical applications. Fig. 9.2 (b) shows 500 atoms from a single polymer chain and demonstrates how the polymer chains may pass out of one boundary and effectively re-enter through the opposite boundary. The schematic of a polymer chain in Fig. 9.2 (c) shows how a polymer chain passes through several periodic unit cells images. Every atom in the schematic polymer chain is either contained within the central unit cell or is a periodic image of an atom in the central unit cell. The atomic coordinates in the amorphous structure were relaxed by McAliley during MD simulations in order to minimise interatomic potential energy. While each AFEM simulation of the 1440 atom crystalline structure took less than 5 minutes on a personal computer, each amorphous simulation for 13500 atoms took approximately 3 hours when utilising 16 processors of a supercomputer.

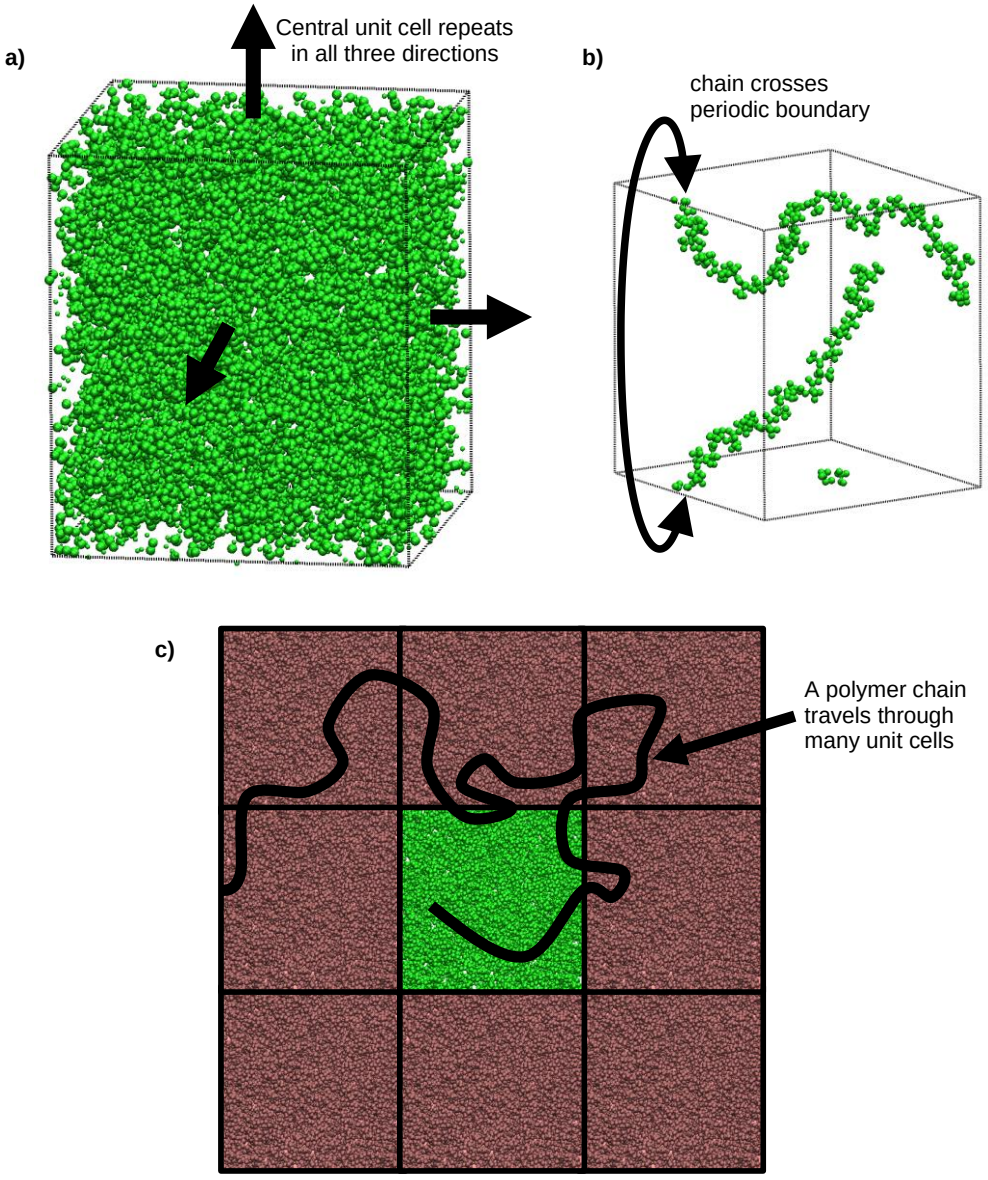

Fig. 9.2 The atomic unit cell structure for amorphous poly(lactide) contains 13500 atoms in 3 polymer chains. The unit cell is shown with a) all atoms, b) 500 atoms from a single polymer chain and c) all atoms when viewed in the z direction with the central unit cell (green) surrounded by the adjacent unit cell images in x and y (red).A polymer chain is shown schematically passing through several of the unit cells.

9.3 AFEM calculation of Young's modulus

The amorphous and crystalline structures described in the previous section are analysed in AFEM simulations to find values of Young's modulus. Fig. 9.3 shows the AFEM results for the crystalline structure when a strain is applied in the direction of the polymer chains. An atom on the left hand side of the structure and near the middle (x = 0.129 nm, y = 1.17 nm, z = 2.757 nm) is fixed in position during the simulations so the unit cell strains up and down away from the middle of the structure in the figure.

Poisson's ratio can be seen by the translation of the right-most polymer chain in the figure away from the edge of the periodic unit cell; the structure contracts in the horizontal directions when a vertical strain is applied. The structure was also strained in the x and y directions to determine the mechanical properties normal to the direction of the polymer chains.

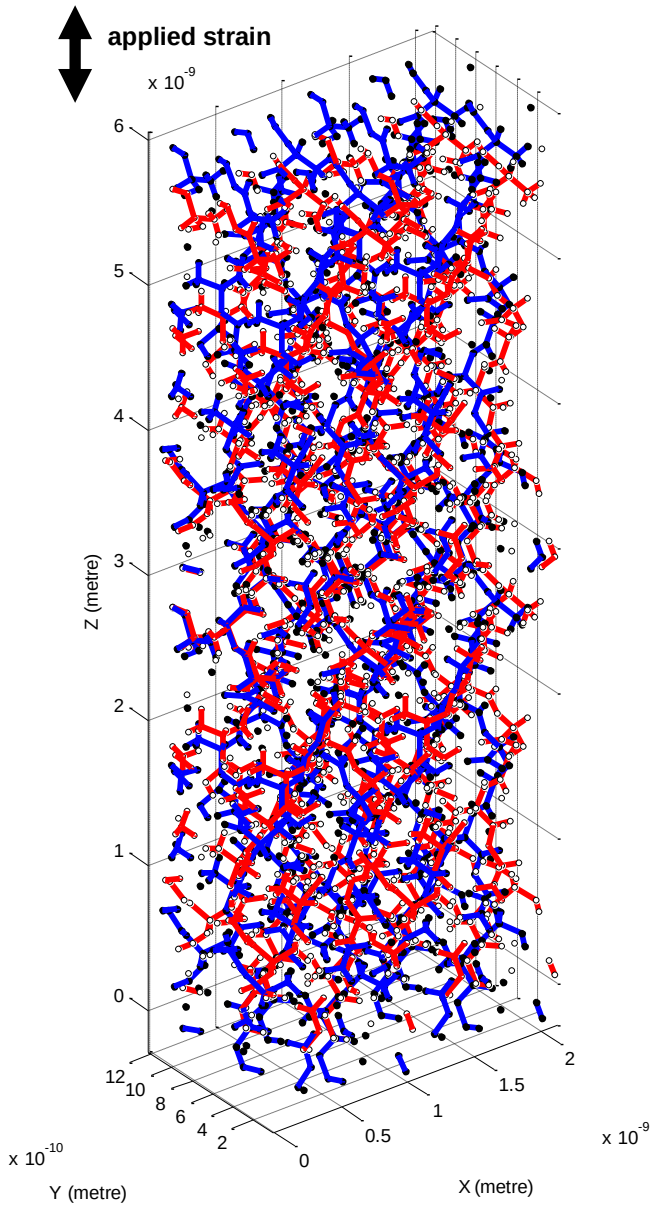

Fig. 9.3 AFEM results for the crystalline structure. The covalent bonds are shown for the unstrained (red bonds with hollow atoms) and strained (blue bonds with solid atoms) structures.

The values of Young's modulus and Poisson's ratio are given in Table 9.1 and Table 9.2. Young's modulus is greater in the z direction than in the x or y direction, which is to be expected since in the z direction the polymer chain covalent bonds must deform to allow the polymer chain to elongate. In the x and y directions, the polymer chains are

connected by weaker nonbonded interactions which could accommodate all of the strain if the covalent bonds were infinitely stiff. The Poisson's ratio values v_{zx} and v_{zy}, which indicate the z strains that result from applied x and y strains, are smaller than the other values as a result of the crystal being stiff in the direction of chains. The values of Poisson's ratio are reasonable since all values are below 0.5 which indicates that the material is compressible.

Table 9.1 also details the distribution of interatomic potential energy increases amongst the different AFEM element types, which is referred to as strain energy. The percentages of total strain energy attributed to each element type are shown. Nonbond elements contain the majority of strain energy. This supports the general understanding that strain in polymers is accommodated by deformation of weaker intermolecular bonding rather than of stiff covalent bonds. The strain energy fraction contained in nonbonds is much lower when the strain is applied in the z direction than in x and y. This is because for an applied strain in the z direction, it is not possible for the main chain elements to avoid strain since the chains are physically elongated in the z direction. The values of Young's modulus found in the AFEM simulations are high compared to values that may be expected experimentally. The high value of Young's modulus in AFEM simulations may be attributed to the fact that the AFEM simulations are static and therefore represent Young's modulus at a temperature of 0 Kelvin. Nakafuku and Takehisa [65] measured Young's modulus of poly(L-lactide) experimentally and found Young's modulus to almost double as the testing temperature of the sample decreased from 20°C to 10°C even though both temperatures are well below the glass transition temperature. Also, Ding et al. [62] conducted molecular dynamics simulations on polyethylene at various temperatures from near 0 Kelvin to well above the glass transition temperature. Their results indicate that the value of Young's modulus at 0 Kelvin may be approximately 5-8 times greater than the value near to but below the glass transition temperature. Highly crystalline (>50%) rods of poly(lactide) with aligned polymer chains may have Young's modulus values in the region of 6-8GPa [58, 107, 108]. If a single crystal had a Young's modulus of 3x this value, at 0K the Young's modulus in the direction of the polymer chains may be expected to be between 90GPa (5x3x6GPa) and 192GPa (8x3x8GPa). The value calculated in Table 9.1 of 128GPa is reasonable. It is possible to include thermal energy in the AFEM method in order to conduct simulations at non-zero temperatures but the method would then be non-linear and the computational benefits over MD would be lost.

The author of this thesis is aware of two atomic studies regarding the theoretical calculation of Young's modulus for crystalline poly(lactide). Montes de Oca and Ward [82] used the COMPASS force field within the molecular dynamics package Materials Studio while Lin et al. [84] used the ab initio method. The theoretical compliance matrix of crystalline poly(lactide) elastic properties was provided in both studies therefore the values of Young's modulus for uniaxial tension in the z direction can be calculated as

$$E_z = \frac{1}{s_{33}} \qquad 9.1$$

where s_{33} (GPa^{-1}) is the third diagonal term of the compliance matrix. According to Eq. 9.1, the simulations of Montes de Oca and Ward [82] and Lin et al. [84] find values of Young's modulus in the z direction of 36.0 GPa and 14.1 GPa respectively. The small values of Poisson's ratio found by Montes de Oca and Ward [82] of v_{zx} = 0.07 and v_{zy} = 0.08 support the small values found in the AFEM simulations.

For the AFEM simulations of the amorphous phase, the values of Young's modulus, Poisson's ratio and strain energy distribution are given in Table 9.3. The value of 0.255 for Poisson's ratio is reasonable for a glassy polymer. The value of Young's modulus is higher than typical experimental values (e.g. 0.5-5GPa) which may be due to the fact that the simulations are effectively conducted at 0 Kelvin. In comparison to the crystalline results, amorphous Young's modulus is lower than the crystalline Young's modulus. This result supports the validity of the AFEM simulations because it is to be expected that Young's modulus would be higher in a crystalline phase than in an amorphous phase. As with the crystalline structure, the distribution of strain energy is plausible because the nonbonded interactions contain the majority of strain energy in the AFEM results.

The discrepancies between the values of Young's modulus found by a) AFEM, b) Montes de Oca and Ward [82], c) Lin et al. [84] and d) experimentally, by may be due to factors such as different crystal structures and force fields being used in the simulations and the different assumptions/simplifications associated with each method. For the AFEM simulations, the main assumptions/simplifications are that the structure is fully relaxed, that elements with a negative stiffness are considered to represent broken nonbonds and therefore not included, and that the testing temperature is effectively 0 Kelvin. The primary purpose of the AFEM technique presented in this

thesis is to simulate the effect of chain scission on Young's modulus in the amorphous phase. Typically in experimental publications, the value of Young's modulus is normalised by the initial value so the absolute value is not of critical importance. It is more important that the AFEM simulations capture the main atomic trends expected in polymer deformation. The distributions of strain energy found in Table 9.1 and Table 9.3 support the ability of the AFEM technique to represent a polymer correctly because nonbonds are accommodating the majority of strain as expected for polymers. Also, the values of Poisson's ratio are believable.

Applied strain direction	x	y	z
Young's modulus (GPa)	50.363	53.575	128.220
Strain energy in bond-stretch elements	0.5%	1.1%	1.9%
Strain energy in bond-angle elements	1.5%	1.6%	5.9%
Strain energy in bond-dihedral elements	0.9%	0.8%	2.5%
Strain energy in nonbonds elements	97.1%	96.5%	89.7%

Table 9.1 Young's modulus and strain energy distribution in the crystalline structure for an applied displacement in the x, y and z directions.

v_{xy}	0.298
v_{xz}	0.281
v_{yx}	0.280
v_{yz}	0.328
v_{zx}	0.110
v_{zy}	0.138

Table 9.2 Poisson's ratio for the crystalline polymer structure.

Young's modulus (GPa)	37.1
Strain energy in bond-stretch elements	1.9%
Strain energy in bond-angle elements	4.2%
Strain energy in bond-dihedral elements	2.0%
Strain energy in nonbonds elements	91.9%
Poisson's ratio	0.255

Table 9.3 AFEM results for Young's modulus, Poisson's ratio and strain energy distribution in the amorphous unit cell.

9.4 Atomic force transfer through the unit cell

One of the benefits of the static AFEM simulations over alternative dynamic methods is that the results can be analysed with ease. It is useful to analyse the manner in which force is transferred through the structure. In this section, the manner in which force is transferred through atoms in the structure is analysed, for both crystalline and amorphous phases, in order to gain an atomic understanding of how the polymer structure resists deformation.

9.4.1 The method of calculating interatomic force transfer

For an atomic structure subject to tensile strain, the unit cell images on opposite sides of the central unit cell apply opposite forces to the central unit cell in order to elongate it. These forces are transferred through AFEM elements in the structure from one side to the other. Fig. 9.4 (a) shows how equal and opposite forces applied to atoms 1 and 3 in the figure must transfer through the two elements and through the central atom. The labelled forces in the figure are the forces that must be applied to the atoms (by other AFEM elements or external forces) in order to deform the elements being considered. The force that is transferred through an element can be calculated based on the stiffness of the element and the atomic displacement. For 3D simulations, the component of the force that is in the direction of applied stress is of interest. Since an atom may be utilised in several elements, the force that transfers through the atom is calculated as the sum of the force contributions from all the elements in which the considered atom is contained. The bond-angle and bond-dihedral elements contain more than two atoms, and the force that is transferred through the element changes at different positions within the element. In order to determine the force transferred through a particular atom, consider an imaginary cut through the structure immediately next to the atom in question as shown with respect to atom 1 in Fig. 9.4 (b) for a bond-angle element connecting three atoms. The force that is transferred through the element at the location of the imaginary cut plane in the figure is calculated as the sum of forces (applied to the element by other elements) for all atoms that are in the positive direction of applied strain (atoms 2 and 3 in the figure). Consider the case when the forces applied to atoms 2 and 3 are equal and opposite: there is no force transferred along the element in the section between atoms 1 and 2 and therefore the element does not contribute to the total force transferred through atom 1.

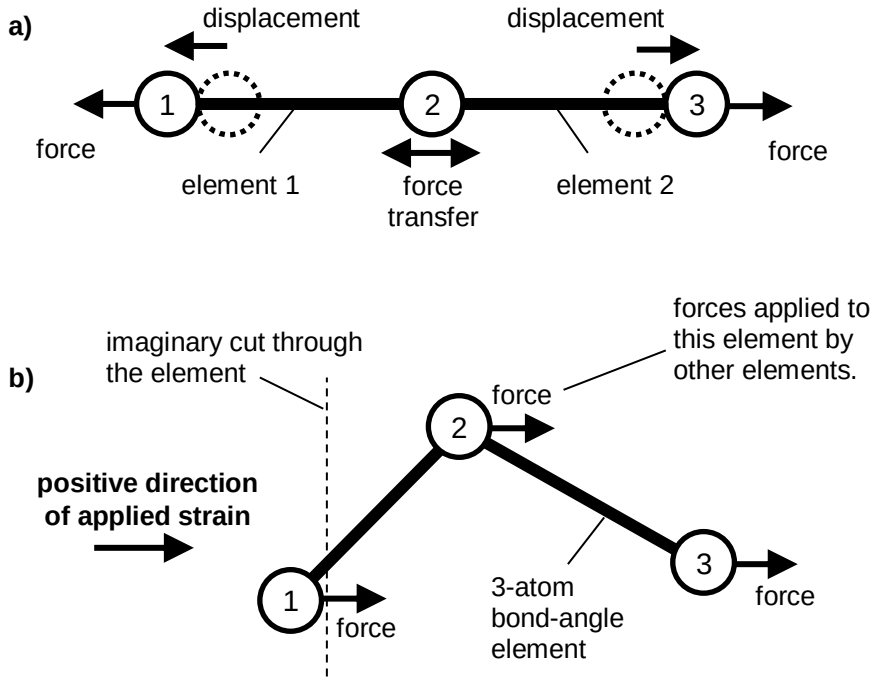

Fig. 9.4 a) A simple transfer of force through two bond-stretch elements and b) the force transferred to atom 1 by a bond-angle element between three atoms can be considered using an imaginary cut through the element.

9.4.2 Interatomic force transfer in the crystalline unit cell

The AFEM structure subject to 10% strain in the direction of the crystal chains in shown in Fig. 9.5 in which the colour indicates the normalised force that is transferred through each atom. The whole crystalline unit cell is shown viewed from the z direction, and a single chain is shown in isolation viewed from the y direction. There is a greater force sustained by the atoms in the polymer backbone and the carbonyl oxygen atom than in the hydrogen and methyl side group atoms. Therefore a greater force is required to increase the distance between backbone atoms than to increase the distance between methyl groups. This may be due to the higher charges of the main backbone and carbonyl oxygen atoms resulting in stronger nonbonded interactions. Also, these atoms are closer to the central axis of the helical chain structure. This means that on average the nonbonds are more likely to be aligned in the direction of applied strain. The isolated chain side view in the figure demonstrates how the methyl side groups have fewer atoms directly above/below them in the direction of applied stress, and hence fewer strain-aligned nonbonds. The carbonyl carbon atoms on the main polymer backbone sustain the most force, which can be explained by the fact that they have the highest charge of all atoms and therefore the strongest nonbonded interactions. Also, they are the closest atom to the centre of the helix so have the most strain-aligned

nonbonds. The overall result is analogous to a macroscale composite material in which stiff rods sustain high force in a weaker matrix. The stiff rods are effectively the main chain covalent bond elements combined with the strongest strain-aligned nonbond elements, while the matrix is the general complex of a large number of nonbonds oriented in all directions and between all atoms.

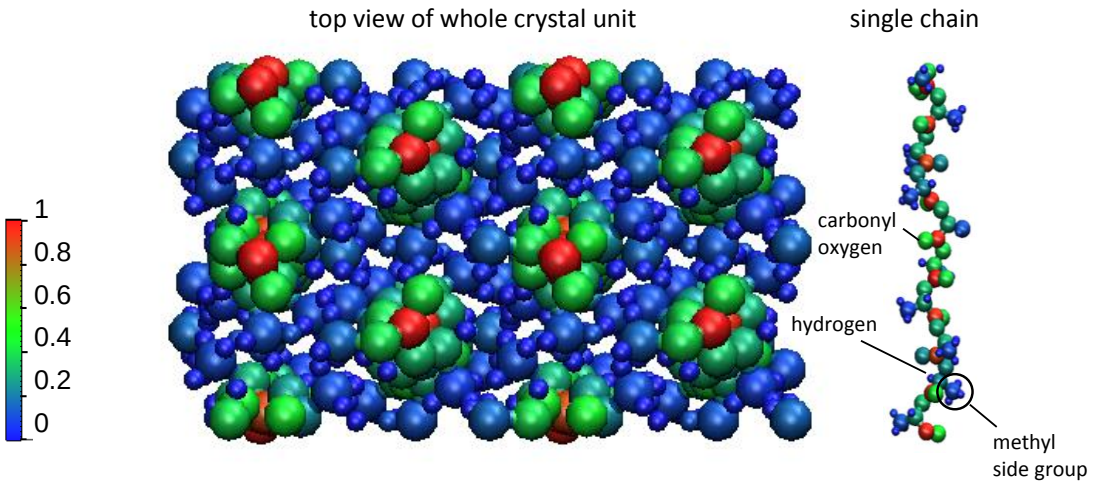

Fig. 9.5 The crystal unit cell with strain applied in the z direction is shown viewed in the z direction (in the direction of the polymer chains) and a single polymer chain is shown in isolation viewed in the y direction. Atom colours indicate the normalised force that is transferred through each atom as a result of the applied strain.

When the crystalline structure is strained in the y direction, normal to the direction of the polymer chains, pathways of high force transfer still exist as highlighted in Fig. 9.6 (a). For strain normal to the direction of the polymer chains, the high force is transferred along pathways where the distance between side-group atoms of adjacent chains is small, and where the stiff covalent bond between the main chain and the methyl side group is aligned in the direction of stress. The analogy to stiff rods in a weak matrix can again be used, at an even smaller length-scale, in understanding these results. Fig. 9.6 (b) shows how the covalent bond between the main chain and methyl group carbon atoms can be considered as a stiff rod in a matrix of weaker (or less strain-aligned) covalent bonds and weak intermolecular nonbonds.

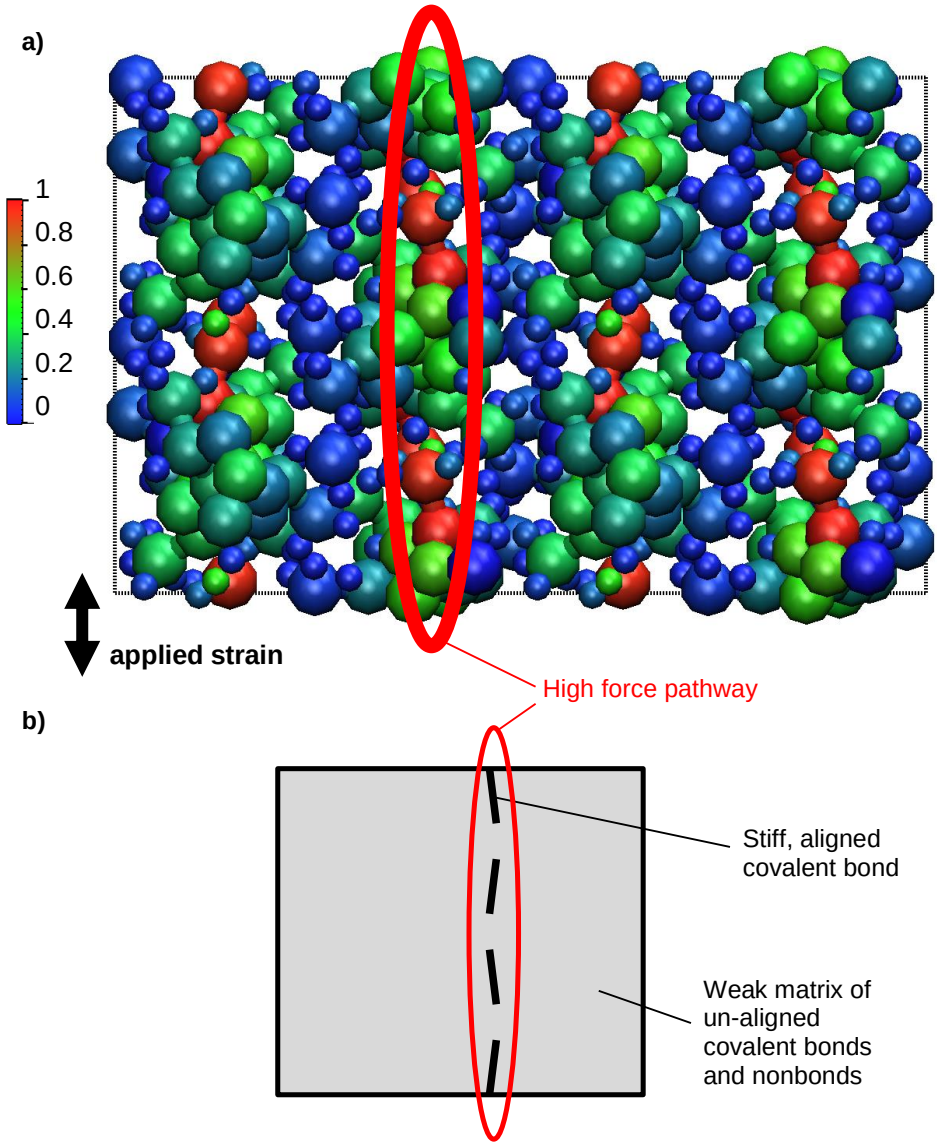

Fig. 9.6 In a) the crystal unit cell with strain applied in the y direction is shown viewed in the z direction. High interatomic forces exist in pathways across the structure when the carbon-carbon bond between the methyl group and the main chain is aligned in the direction of applied strain. In b) stiff, strain-aligned covalent bonds are shown schematically as rigid rods in a weak matrix of nonbonds and covalent bonds that are not aligned in the direction of stress.

9.4.3 Interatomic force transfer in the amorphous unit cell

For the amorphous polymer structure, a similar trend can be seen in that there are high force pathways but the pathways exist over a longer and less regular distance. Fig. 9.7 shows the results for a strained amorphous unit cell in which atoms are only displayed if they transfer an interatomic force of at least 40% of the maximum force transferred by any atom. There are vertically aligned groups of atoms which demonstrate a continuous high force transfer over a long polymer chain section. These regions of high

force transfer occur because the polymer chain sections oriented in the direction of applied stress. In the highly regular crystalline structure, high force pathways were dictated by the orientation of individual covalent bonds whereas in the irregular amorphous structure it is the orientation of long sections of polymer chains that dictate the high force pathways. These findings are supported by the great increases in stiffness that can be created by alignment of the polymer chains in the amorphous phase during drawing of polymer material into rods or fibres, often referred to as self-reinforcement. An amorphous polymer could be considered as a weak matrix (of nonbonds) in which randomly oriented stiff rod particles exist (polymer chain sections). Only those stiff rod particles that are oriented in the direction of stress contribute to increase the overall stiffness.

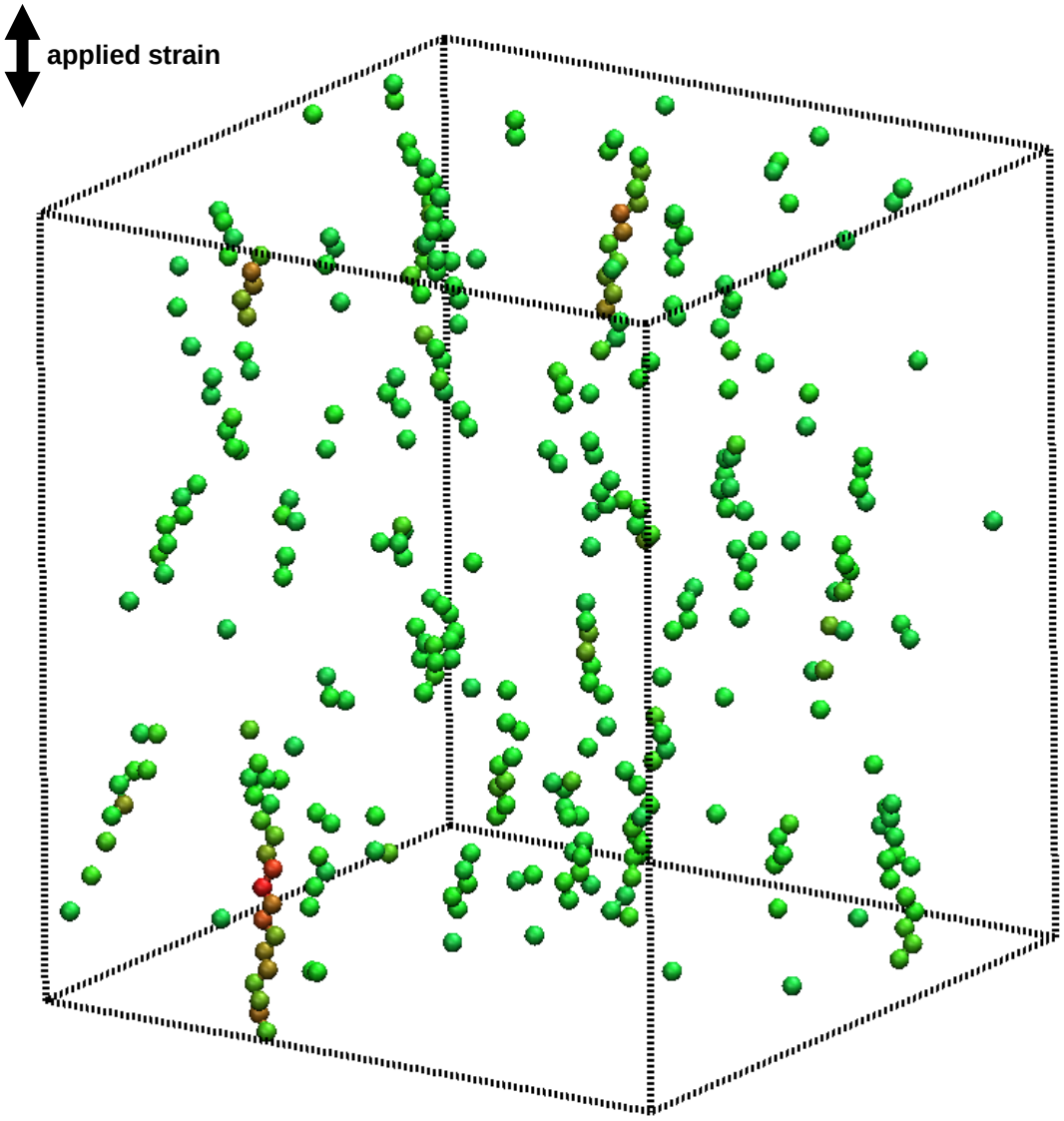

Fig. 9.7 High stress pathways in an amorphous AFEM simulation exist in long sections of polymer chains where the chains are most oriented in the direction of stress.

Fig. 9.8 shows the AFEM results for the distribution of forces that are transferred through the polymer repeat units for the whole amorphous polymer. Polymer repeat units are considered instead of individual atoms in order to reduce noise and because Fig. 9.7 demonstrates that the force transfer in an amorphous polymer is affected by the orientation or long sections of polymer chain rather than individual atoms or bonds. The polymer repeat unit force is calculated as the maximum interatomic force transferred by any of the nine atoms in the polymer repeat unit. In the figure, the polymer unit forces are normalised by the maximum force sustained by any atom in any polymer repeat unit. The probability distribution is greatly skewed towards weaker forces which indicates that the majority of polymer units do not sustain a high force. This agrees with Fig. 9.7 because only a small fraction of polymer units are contained within polymer chain sections that are oriented in the direction of applied strain over a considerable distance.

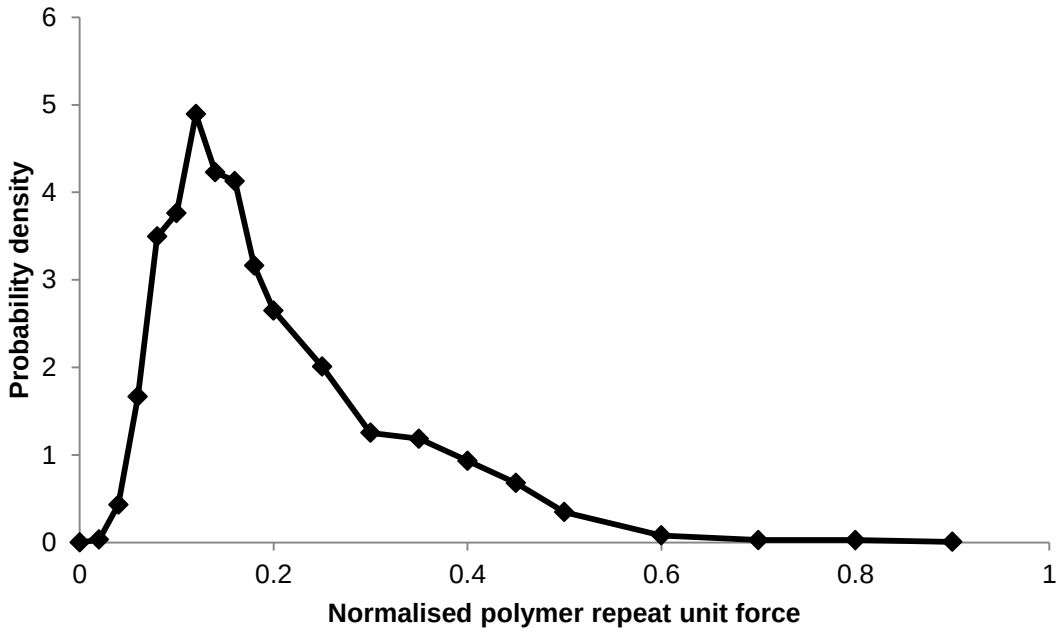

Fig. 9.8 The distribution of forces transferred through polymer units are shown as a probability density function.

9.5 Variation to the AFEM setup and parameters

To further understand the AFEM results and to test the sensitivity of the results to factors such as nonbond cut-off distance, the AFEM simulation setup is modified in this section to determine how the modifications affect the calculations of Young's modulus and the transfer of force through the structure. Factors that are considered along with nonbond cut-off distance are the effect of covalent bonds and the strength of nonbonds. Fig. 9.9 shows the AFEM simulation results for Young's modulus in the x and z directions for nonbond cut-off distances ranging from 0.3 to 1.5 nm. Results are also shown in the figure for simulations that only include nonbond elements, in which all AFEM elements related to covalent bonds (bond-stretch, bond-angle and bond-dihedral elements) are excluded. Increasing the nonbond cut-off distance causes the Young's modulus value to increase as is expected. The number of nonbonds in the simulations increases to the power 3 with cut-off distance. Therefore even though the stiffness of the nonbond elements reduce significantly with distance, the long range nonbonds contribute considerably to the overall Young's modulus value. For the AFEM simulations in the x direction (triangles in the figure), the Young's modulus value of the crystalline polymer approaches zero as the nonbond cut-off approaches 0.3 nm because the number of nonbonds between the polymer chains approaches zero. This is true regardless of whether covalent bond elements are included or not. In the z direction however, the value of Young's modulus does not approach zero if covalent bond elements are included (solid squares in the figure) because the main backbone of the polymer resists deformation along its length even without any nonbonds. When covalent bond elements are not included (hollow squares in the figure), the Young's modulus does approach zero as the nonbond cut-off distance reduces even for Young's modulus is the direction of the chains. This is because, in the PLAFF2 force field, nonbonds are not included between atoms that are linked by less than three covalent bonds. Short nonbonds cannot exist within a single chain for this reason. And short nonbonds do not exist between polymer chains due to the separation between chains. When main covalent bond elements are excluded from the simulations, there is a relatively small reduction in Young's modulus in the direction normal to the polymer chain direction. This is because the weak nonbonded interactions can accommodate the strain without the need to elongate covalent bonds, similar to the lower rule of mixtures composite theory in which small volume fractions of stiff rods do not greatly affect to the overall value of Young's modulus because strain can easily be accommodated by the weak matrix in between. The continuous increase in Young's modulus indicates that the long range nonbonds play an important role in the overall

Young's modulus. There is not a critical dependence on the short range nonbonds which indicates the results are not sensitive to small variations in the initial atomic coordinates. A nonbond cut-off distance of 0.95 nm is used in all simulations in this study, except those that specifically investigate the role of nonbond cut-off distance, because that value is often employed for molecular dynamics simulations.

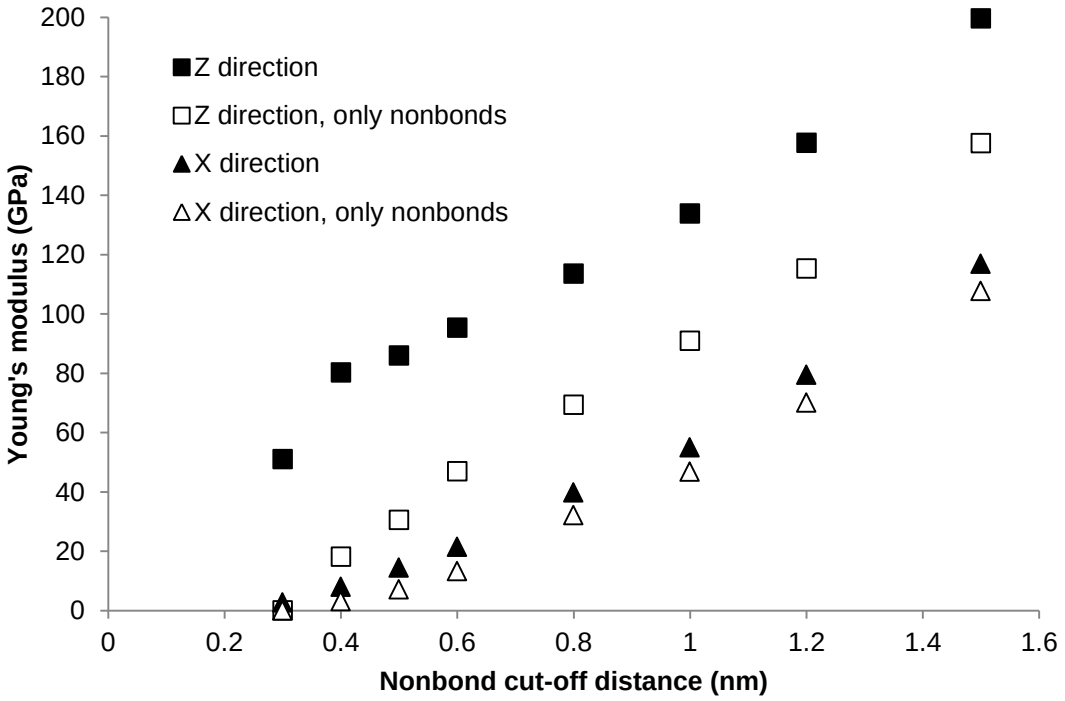

Fig. 9.9 Young's modulus of the crystalline poly(lactide) structure for different nonbond cut-off distances in the x (triangle) and z (square) directions, which are normal to and in the direction of applied strain, respectively. Results are shown for regular simulations with all AFEM elements (solid) and for simulations with no covalent bond AFEM elements (hollow).

For the amorphous polymer structure, Table 9.4 shows the results for Young's modulus when a) the nonbonds are reduced in stiffness to one hundredth of the regular value, b) the main chain covalent bond elements are excluded from simulations, and c) the nonbond cut-off distance is reduced from 0.95 nm to 0.5 nm. As can be seen by the 98.3% drop in Young's modulus associated with the 99% reduction in nonbond stiffness, the value of Young's is dominated by the contribution from nonbond elements. There is a contribution from covalent bond elements since the reduction in Young's modulus is less than the reduction in nonbond stiffness. Also the simulation with no covalent bond elements demonstrates a reduction in Young's modulus of 27%. For the crystalline simulations in Fig. 9.9 with a 1 nm nonbond cut-off distance, removing covalent bond elements resulted in a Young's modulus reduction of 15% and 32% in

the x and z directions respectively. The 27% reduction found for the amorphous simulation is in between the crystalline reductions (for Young's modulus parallel and normal to the chains) because in an amorphous structure some chains are oriented in the direction of applied strain and some are not.

AFEM setup	Young's modulus
Regular nonbonds	37.1
Hundredth stiffness nonbonds	0.615
Only nonbonds (no main chain)	27.0
5A max length nonbonds	9.92

Table 9.4 The AFEM simulation setup is varied to identify the effect on the results for Young's modulus in the amorphous polymer unit cell.

The transfer of force through the polymer structure is also affected by the AFEM simulation setup. Fig. 9.10 shows the pathways of greatest force transfer through the structure for a nonbond cut-off distance of 0.5 nm. Only atoms that transfer a force at least 40% of the maximum for all atoms are shown. By comparison to Fig. 9.7, in which the nonbond cut-off distance is 0.95 nm, it can be seen that for a shorter nonbond cut-off the high force is transferred along the polymer chains for a greater distance. This can be explained by two factors: 1) the force contained in stiff covalent bond elements accounts for a greater proportion of the total force when there are fewer nonbond elements. Therefore if the strain-aligned chain sections are considered to be stiff rods in a matrix of nonbonds, the rods effectively become stiffer relative to the matrix; and 2) there are fewer nonbond elements to distribute the force from the strain-aligned polymer chain to the surrounding polymer. Since the transfer of force is more localised for shorter nonbonds, it may be the case that high forces pass from a strain-aligned section on one polymer chain directly to a strain-aligned section of a different polymer chain through just a few nonbonds rather than being distributed to many surrounding polymer chains.

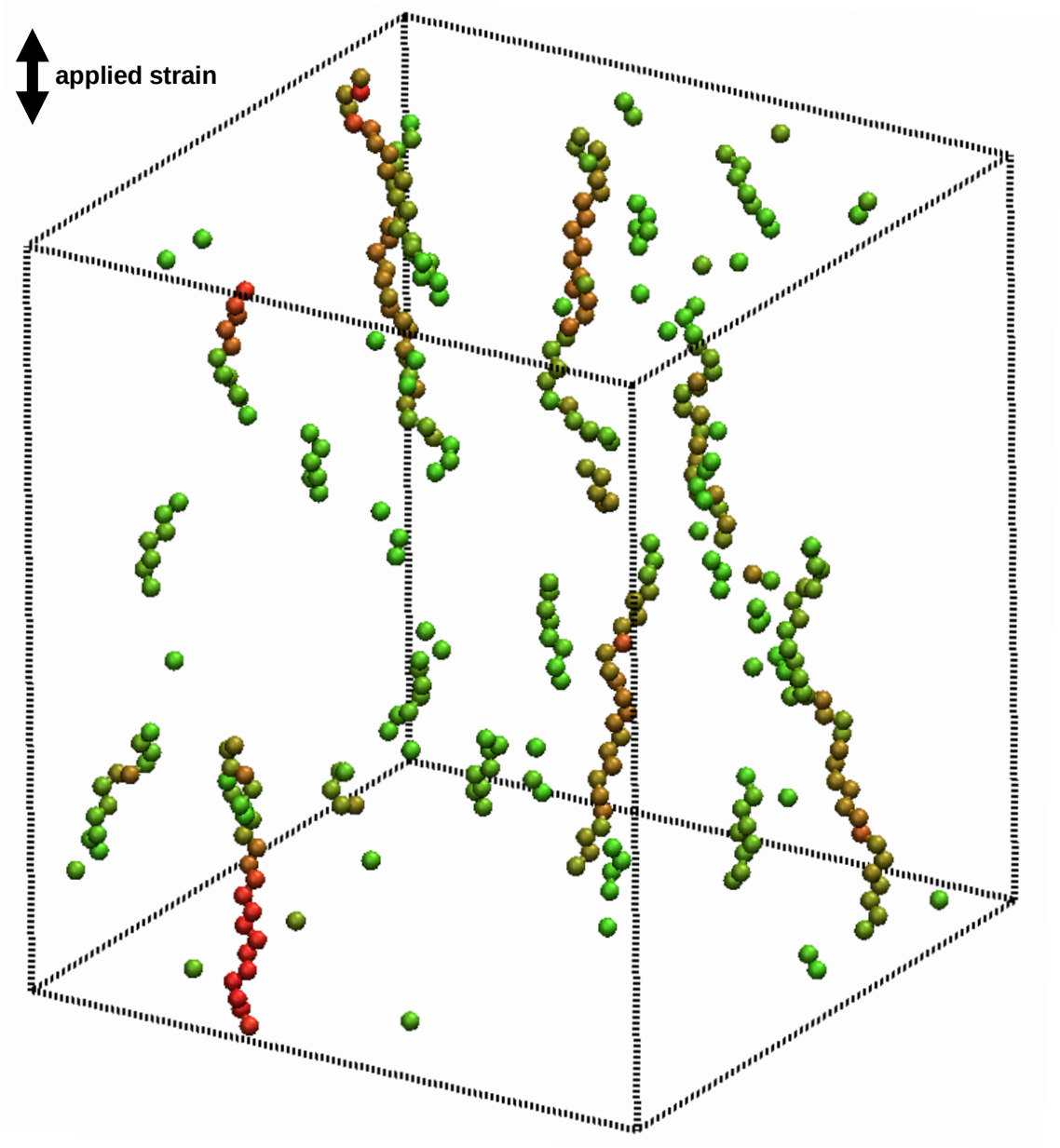

Fig. 9.10 The high stress pathways in amorphous AFEM simulations exist in longer sections of polymer chains when the nonbond cut-off distance is reduced from 0.95 nm in Fig. 9.7 to 0.5 nm for the simulation presented in this figure.

The analysis in this section regarding the variation of the AFEM setup finds that nonbonds are the main factor affecting force transfer and Young's modulus. Although the covalent bonds on the main polymer chain dictate where the highest forces exist in a strained structure, the majority of the force is contained within the nonbond elements. Polymers are typically drawn schematically with no indication of nonbonds as exemplified in Fig. 9.11 (a). This may be a misleading representation when used to explain mechanical properties. Although the main chain covalent bonds are important

for mechanical properties, the nonbonds are much more important. Therefore it may be most appropriate to show nonbonds schematically when discussing Young's modulus in terms of the polymer chains. Fig. 9.11 (b) shows an alternative polymer representation in which nonbonds are shown as a matrix that contains stiff polymer chain sections. The stiff polymer chain sections may be considered to be sections of polymer chains which are relatively straight and therefore stiffer than the more irregular sections. For an un-oriented amorphous polymer, the stiff polymer chain sections are positioned in any orientation and only those in the direction of applied strain will contribute significantly to increases in Young's modulus, as suggested by the findings in Fig. 9.7 and the fact that the crystalline Young's modulus is much greater in the direction of polymer chains than normal to them. Fig. 9.11 (c) shows a schematic of a self-reinforced polymer. Since the amorphous chains are oriented in the direction of stress, the stiff polymer chain sections are oriented in that direction too. Also, since the polymer chains are straighter, the stiff polymer chain sections may be longer than in the un-oriented polymer chains. The nonbond matrix may be considered to be less affected or unaffected by the orientation.

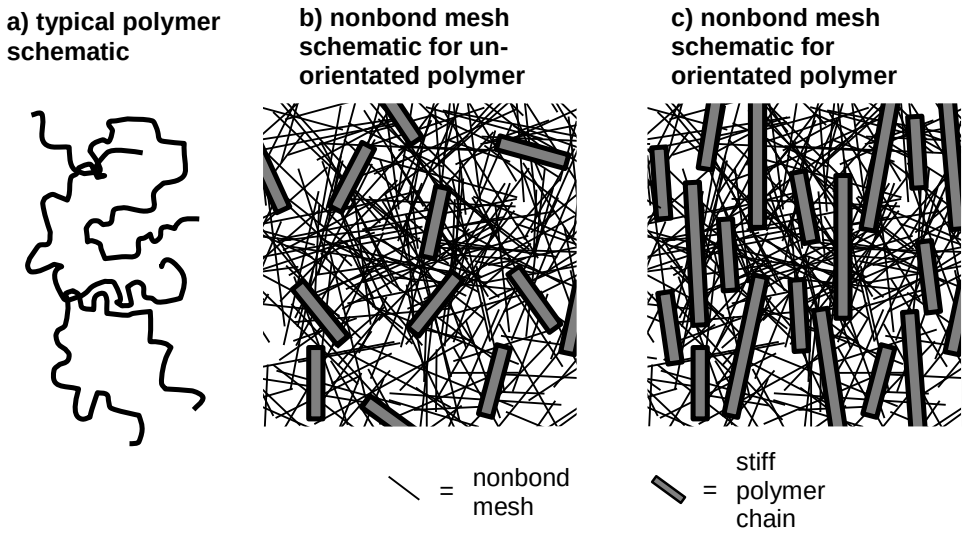

Fig. 9.11 Polymers are typically drawn similar to the schematic shown in (a). The schematics shown in (b) may be a more accurate schematic in which the complex of thin lines represents a matrix of nonbonded interactions in which stiff sections of polymer chains act a stiff rod particles. If the polymer chains are aligned to form a self-reinforced polymer, the stiff rod particles become aligned as shown in (c).

9.6 Atomic simulations for polymer chain scission

During degradation the value of Young's modulus decreases as a result of polymer chain scission and a reduction in molecular weight. The AFEM simulations can be used to simulate the degradation of Young's modulus and help understand the trends that are found experimentally. In order to represent one random chain scission, a polymer unit is selected at random and all AFEM elements that consider any atom in the chosen polymer unit are excluded from the simulations. For the purpose of analysing the effect of chain scission on the Young's modulus, chain scissions are applied cumulatively to the amorphous structure. Young's modulus is calculated at various molecular weights. In addition to the effect of chain scission on overall Young's modulus, the effects of chain scission are investigated in terms of the interatomic force that is transferred through the structure in order to reveal new insights into the degradation of Young's modulus. Chain scission of the crystalline phase in semi-crystalline poly(lactide) is not expected to play an important role in degradation since the crystalline phase degrades slowly compared to the amorphous phase. Therefore a relationship between Young's modulus and molecular weight is only studied for the amorphous phase. However, the crystal phase does still degrade and its regular structure makes the analysis of the effects of individual chain scissions much simpler than in the amorphous phase. AFEM simulations for chain scission are therefore performed on both the crystalline and amorphous unit cells when considering the effect of individual chain scissions on the interatomic force transfer.

9.6.1 The effect of chain scission on Young's modulus

Fig. 9.12 (a) shows the relationship between normalised Young's modulus and molecular weight that is found in the AFEM simulations for the amorphous polymer unit cell. The values of Young's modulus calculated are normalised by the values found at 8950 g mol^{-1}. The results for a regular AFEM setup are indicated by the solid line and demonstrate a reduction in Young's modulus only after the molecular weight has considerably reduced. This trend is in agreement with the findings of the literature review for experimental data in Fig. 2.15. In the review of experimental data, Young's modulus is lost at a higher molecular weight than in the AFEM simulations in Fig. 9.12 (a), which can be attributed to the fact that AFEM simulations are effectively at a temperature of 0 Kelvin. This is one of the drawbacks of the AFEM method but dynamic simulations at a finite temperature are too computationally demanding to be used to generate the data in this study. To further the understanding of Young's modulus degradation, the variations to the AFEM setup that were discussed in Section

0 are also considered here. Those variations are to reduce the stiffness of nonbonds by 99% and to reduce the nonbond cut-off distance to 0.5 nm. The scissions are applied to the same polymer repeat units in all three test setups. In both of the modified setups, the Young's modulus degradation occurs earlier, with respect to molecular weight degradation, than for the regular AFEM setup. This can be explained by the fact that both variations result in an increased contribution to overall Young's modulus from the covalent bond elements of the main polymer chains. When the polymer chains have a more important contribution, the scissions applied to these chains have a greater impact on Young's modulus. The general trend for all three simulation setups is quite similar, even though the setups differ considerably. This indicates that the general trend is not sensitive to small details such as the nonbond cut-off distance, the precise atomic coordinates, and the values of parameters in the force field.

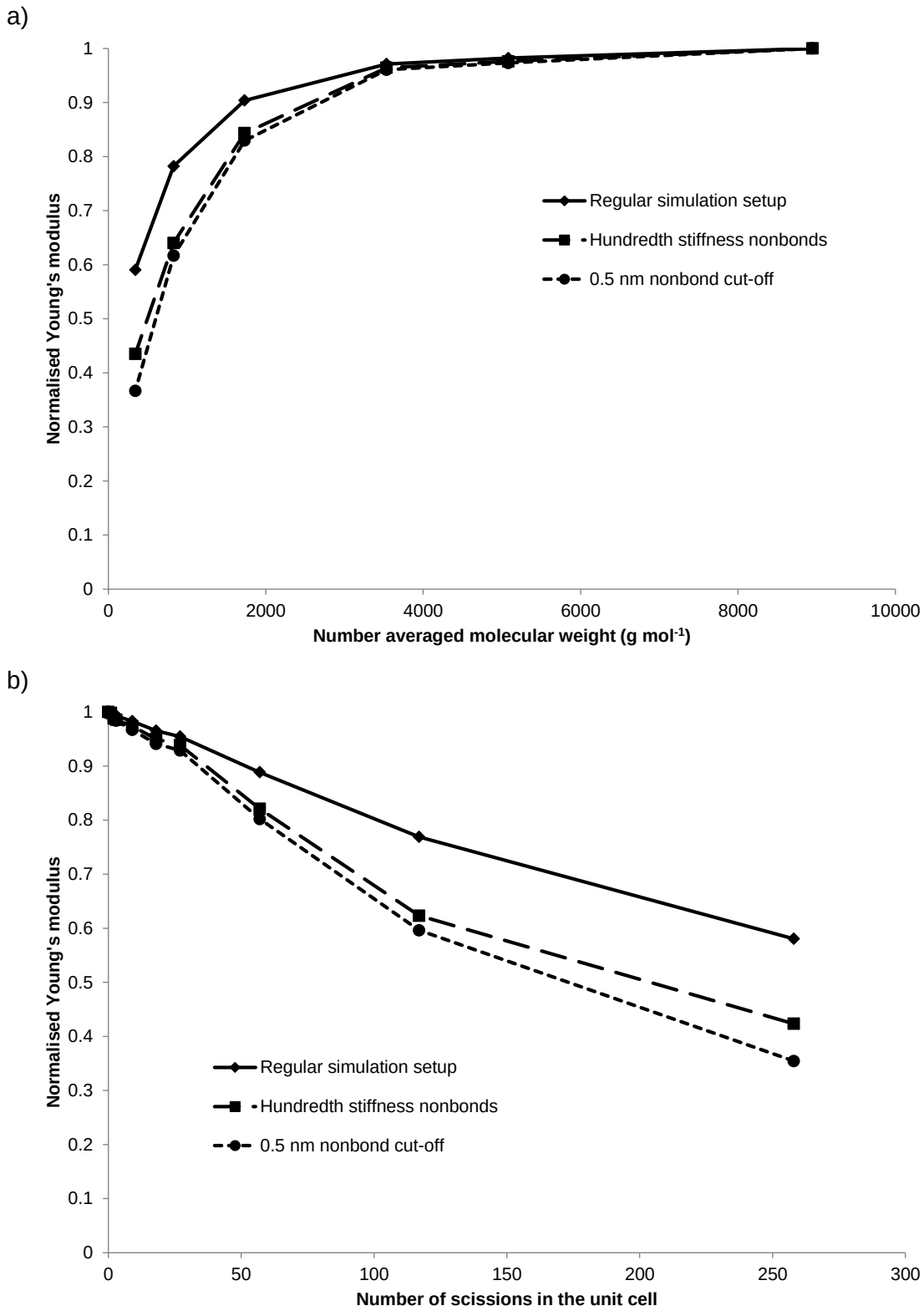

Fig. 9.12 AFEM simulations are used to find a relationship for normalised Young's modulus versus a) number averaged molecular weight and b) the number of chain scissions in the amorphous polymer unit cell. Simulations are conducted with a regular AFEM setup, with 99% reduced stiffness nonbonds, and with a reduced nonbond cut-off of 0.5 nm.

Fig. 9.12 (b) shows the relationship between normalised Young's modulus and the number of chains scissions applied to the amorphous polymer unit cell. It can be seen to be almost linear for all three AFEM setups. This can explain why Young's modulus drops more suddenly at lower molecular weights. Consider the chain scission of a polymer structure containing 10 initial polymer chains. Table 9.5 indicates the number of scissions that are required to reduce normalised molecular weight by various amounts. To reduce the normalised molecular weight by ≈0.1 takes just 1 scission initially. After scissions have been applied such that normalised molecular weight is 0.2 however, 50 scissions are required in order to reduce the normalised molecular weight by 0.1. In a degraded polymer with lower molecular weight, many more scissions are required to further reduce molecular weight. Therefore, for a linear relationship between Young's modulus and the number of scissions, as identified in Fig. 9.12 (b), the reduction of Young's modulus accelerates greatly as molecular weight reduces.

number of chains	number of scission	normalised M_n
10	0	1.000
11	1	0.909
12	2	0.833
15	5	0.667
20	10	0.500
30	20	0.333
40	30	0.250
50	40	0.200
100	90	0.100
200	190	0.050

Table 9.5 Demonstration of how the number of scissions must increase acceleratedly as normalised molecular weight reduces in order to further reduce normalised molecular weight.

9.6.2 The effect of chain scission on interatomic force transfer through the unit cell

The transfer of force through the polymer structure is analysed in Section 9.4, where high force pathways are identified along the stiffest regions of the polymer. In this section, the effect of individual chain scissions on the interatomic transfer of force through the polymer is analysed for the crystalline and amorphous phases.

Crystalline phase simulations

Fig. 9.13 shows the AFEM results for the crystalline structure subject to an applied strain in the z direction when one scission has been applied to a polymer chain. The value of applied strain is adjusted in order to ensure the same force is applied to the unit cell as was applied in the simulation without a scission. The atom colours in the figure indicate the change in force transferred through each atom versus the simulation without a scission and the scale bar is normalised by the maximum change in force for any atom. Since the covalent bonds of the scissioned polymer unit no longer exist in the model, that chain requires less force to elongate. The sections of the chain above and below the scission can separate from one another with a lower force than for the chains that were not subject to a scissions. As a result, the forces transferred through the atoms in the scissioned polymer chain decrease as highlighted in the figure. Since the same force is applied to the overall structure in comparison to the simulation without a scission, the reduction of force in one chain leads to an increase in force in the surrounding chains. The decrease in force is mostly constrained to the single chain in which the scission was applied. If there were no nonbonds, the chain with a scission would be free to separate at the point of the scission without any strain in the covalent bonds of the chain sections above/below the scission. However, the nonbonds that link the different polymer chains must effectively be sheared when the chains move relative to one another. The inter-chain nonbonds gradually transfer the force from the chains without scission to the chain with a scission. Therefore the magnitude of reduction of interatomic force transfer in the scissioned chain decreases with distance from the scission. The schematic shown to the right in Fig. 9.13 shows how the results are similar to stress distribution around a hole in a plate. There is stress concentration to either side of the hole, normal to applied strain, as the stress field flows around the hole. There is also a region of reduced stress to either side of the hole in the direction of applied stress.

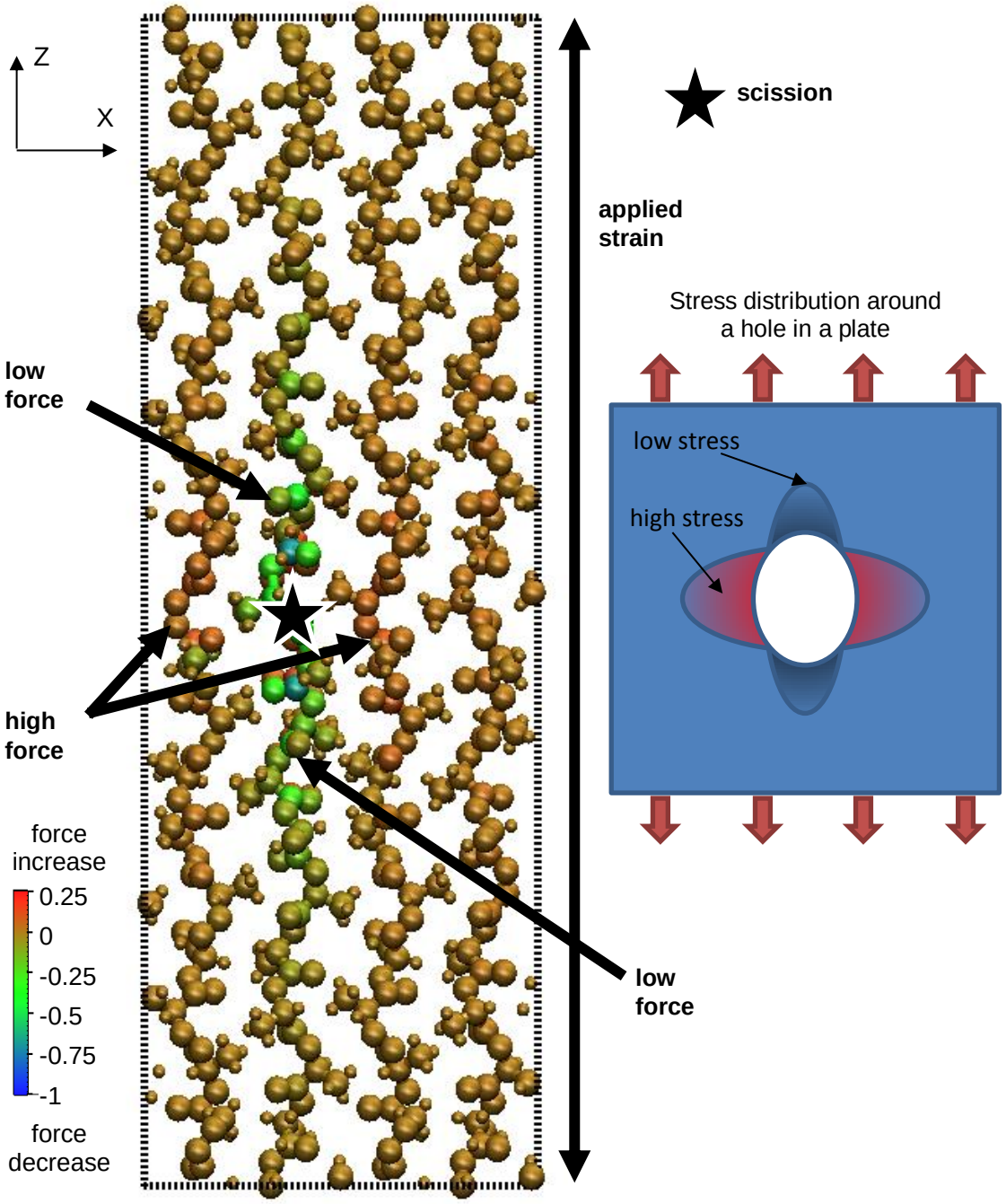

Fig. 9.13 A scission is applied to one of the chains as indicated by the star. The force transferred through the structure from top to bottom deviates around the scission so there is a reduction in force transferred through atoms above/below the scission and an increase for atoms to either side. The colour of the atoms indicates the change in normalised force that is transferred through them. The scission is similar to a hole in a plate often considered in macroscale stress distribution.

Fig. 9.14 shows the simulation results for the same scission and in the same format as in Fig. 9.13 but for an applied stress in the x direction. There is a decrease in the interatomic force transferred through atoms in the regions to the right and left of the scission in the figure. For the simulation in which strain is applied in the direction of the chains in Fig. 9.13, significant reductions in force are constrained to the single scissioned chain. Rather than strain the stiff covalent bonds of the chain above/below the scission, the two halves of the chain separated. For the simulation in Fig. 9.14 however, when strain is applied normal to the chain direction, the force is being transferred through the polymer by nonbonds between the chains to a much greater extent, as discussed in relation to Table 9.1. Since the nonbonds are much more distributed, in terms of length and orientation, compared to covalent bonds the reduction in atomic force transfer is dispersed in the directions normal to applied strain over a shorter distance. As with the simulations for strain applied in the direction of the polymer chains, there is an increase in force transferred through the atoms adjacent to the scission, normal to the direction of applied strain, which is similar to stress concentration around a hole in a plate.

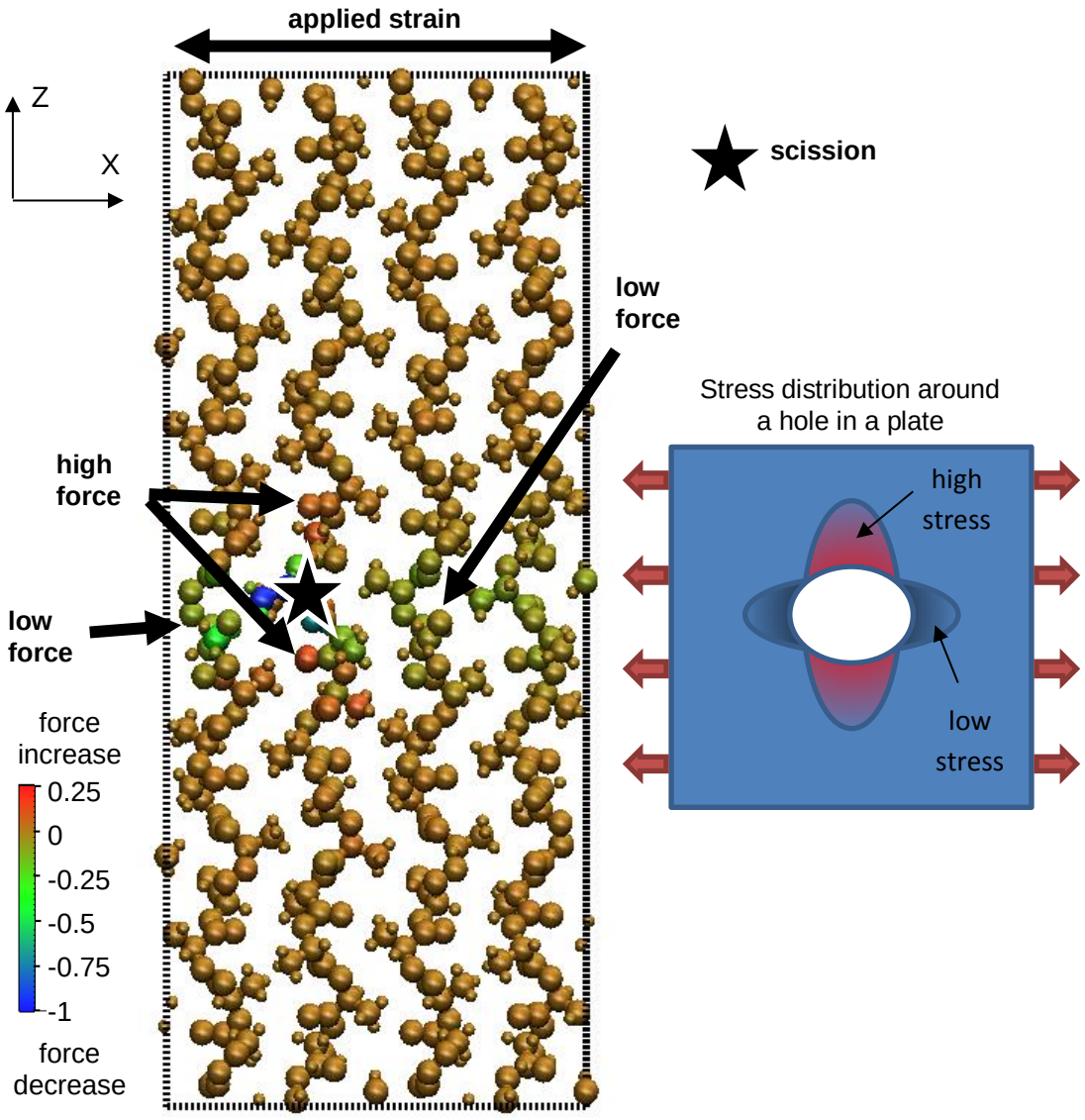

Fig. 9.14 The simulation demonstrated in Fig. 9.13 is repeated for applied strain in the x direction rather than the z. There is a reduction in interatomic force transferred through atoms to either side the scission and an increase for atoms above/below, similar to stress distribution around a hole in a plate.

Fig. 9.15 shows the results for simulations in which 10 polymer chain scissions are applied to random polymer repeat units in the crystalline unit cell. Three results are shown in the figure for applied strain in a) the x direction, b) the y direction, and c) the z direction. The scissions are applied to the same polymer units in all three simulations but are only indicated in Fig. 9.15 (a) in order to improve clarity. The atomic colours indicate changes to the interatomic force transferred through each atom as a result of the scissions. The colour scale bar is normalised by the maximum change in force for any atom in each of the three simulations. The result for the simulation in which strain is applied in the x direction shows that there is a region of increased force transfer as

highlighted in Fig. 9.15 (a). The force is higher in that region due to the lack of polymer scissions there. In effect, the force that transfers through the polymer concentrates away from the scissions because they result in a less stiff polymer. The same trend can be seen in the same region of polymer when strained in the y direction in Fig. 9.15 (b). There is a significant increase in force transferred through atoms in the highlighted region and a reduction in force transfer through atoms in the top half of the structure.

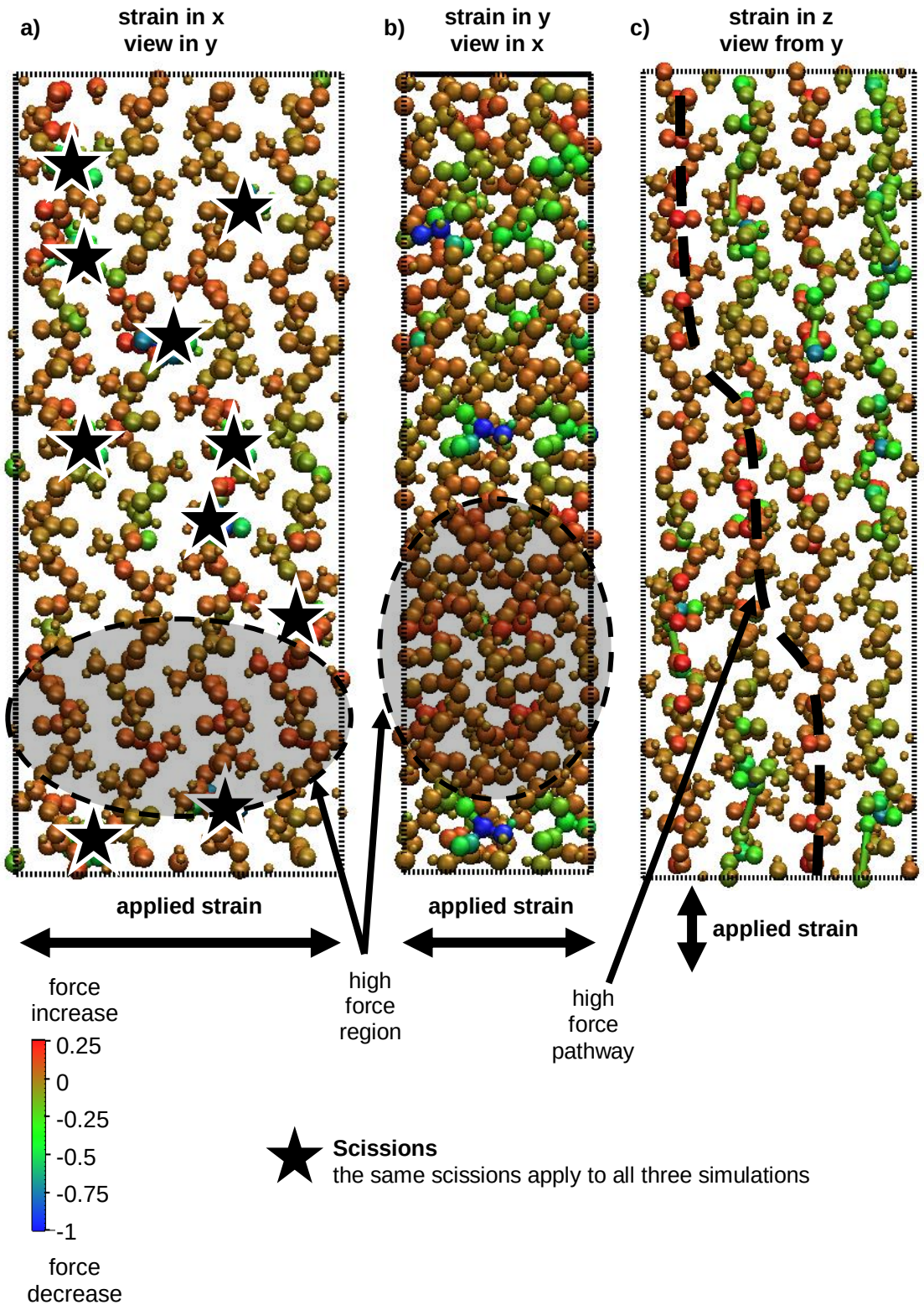

Fig. 9.15 The crystalline unit cell is strained in a) the x direction, b) the y direction and c) the z direction after 10 scissions have been applied. The scissions shown in a) also apply to simulations b) and c). The colour of the atoms indicates the change in the normalised interatomic force that is transferred through them as a result of the applied scissions. The force transferred through the structure increases in regions where there are fewer chain scissions.

In the result shown in Fig. 9.15 (c) for applied strain in the z direction, it can be seen that each scission causes a reduction in interatomic force transferred through the polymer for a considerable distance above and below the scission. The interatomic forces transferred through polymer chains that surround a scissioned polymer chain increase as a result of the chain scission. If these surrounding polymer chains are subject to chain scission further along their length, then the force must be transferred from the polymer chain to the neighbouring chains before the scission by inter-chain nonbonds. As the force transfers through the polymer, it deviates around the chain scissions and follows pathways of the stiffest polymer chain sections (without chain scission) as indicated by the dashed line in Fig. 9.15 (c).

Amorphous phase simulations

As with the crystalline structure, scissions are applied to the amorphous unit cell in order to determine their effect on the transfer of interatomic force through the polymer. It was demonstrated in Fig. 9.7 that sections of polymer chains which are aligned in the direction of stress are stiffer relative to the rest of the polymer and therefore transfer a high force through the polymer. When the polymer chain changes direction, so that it is no longer aligned in the direction of applied strain, the high force that was transferred along the chain is distributed through nonbond elements to several of the surrounding polymer chains. As scissions are applied to the polymer, the sections of stiff strain-aligned polymer chains may undergo chain scission. Fig. 9.16 shows views in the y direction of the original amorphous polymer unit cell in (with no scissions) in (a) along with the unit cell in which 258 random polymer chain scissions are applied (b). In both cases, atoms are only displayed if they transfer a force of at least 50% of the maximum force transferred for any atom in the structure. The plots effectively highlight atoms in the polymer chain sections which provide the greatest stiffness contribution to the polymer. In the figure, the structure that contains scissions demonstrates a greater distribution of the high force atoms. This is because shorter strain-aligned chains do not constrain deformation of the polymer over such a longer distance and therefore do not require such a high force (relative to the average force) as long sections of strain-aligned polymer. The results are similar to the difference between fibre-reinforced and particle-reinforced composites. Long fibres sustain a much greater force than particles and have a greater effect on Young's modulus. As scissions occur, new high force polymer chain sections develop when scissions weaken the original stiff regions of polymer chains.

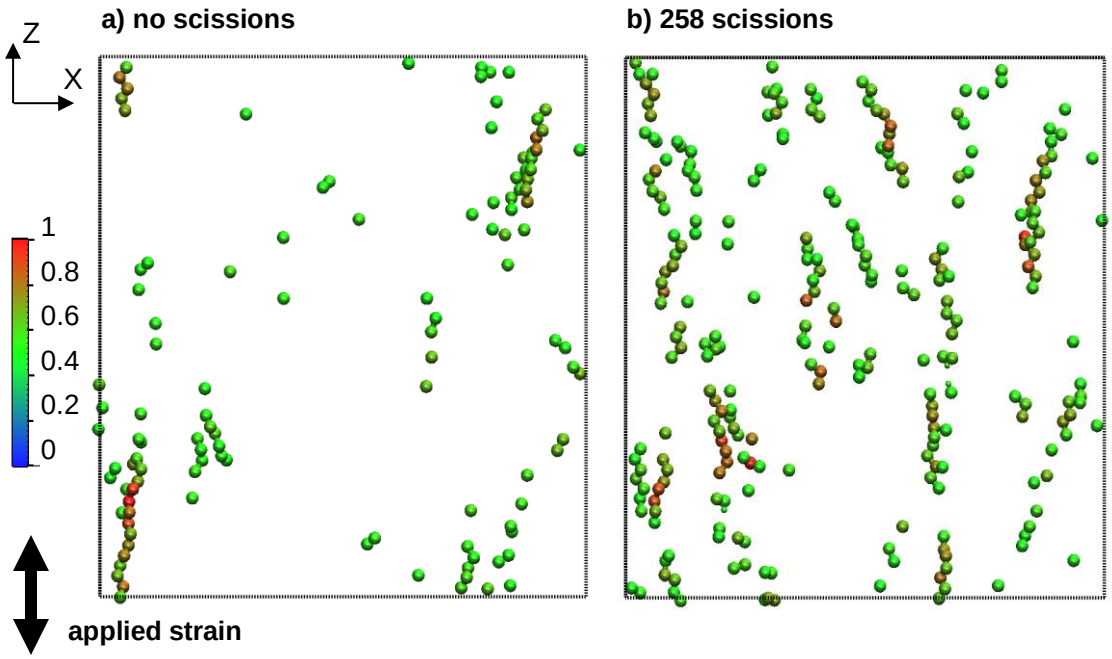

Fig. 9.16 Atoms in the amorphous unit cell are only shown if they transfer a force of at least 50% of the maximum force transferred by any atom in each of the simulations with a) zero scissions and b) 258 scissions in the unit cell. The chain scissions cause the highest forces to be more distributed throughout the polymer. The colour indicates the normalised force transferred by each atom.

In addition to understanding the effects of a large number of random chain scissions, the AFEM simulations allow the local atomic effects of individual scissions to be analysed. Fig. 9.19 shows the amorphous unit cell after one chain scission has been applied. Atoms are only shown if the interatomic force that they transfer in the direction of applied strain reduces by a threshold value in the simulation with the chain scission versus the simulation without the chain scission. The threshold is chosen to be a reduction in transferred force of at least 5% of the average force transferred for all atoms. A region of polymer near to the scission is highlighted in the figure that sustains less force as a result of the scission. This region therefore demonstrates a reduced contribution to overall Young's modulus. The reduction in interatomic force transferred by the atoms is dependent on the position of the atoms relative to the scission rather than on whether atoms exist in the scissioned chain. This is because the majority of interatomic force is transferred by nonbonds through the polymer rather than directly along polymer chains. The AFEM simulations do not consider the reconfiguration of the polymer as a result of chain scission, but it is reasonable to expect the end of chain ends to be more free to move than polymer units in the middle of a chain. This extra freedom means that polymer chain ends and the local surrounding polymer have a

lower effective Young's modulus than a region of polymer without a chain end. Each scission may instantiate a volume of less stiff polymer.

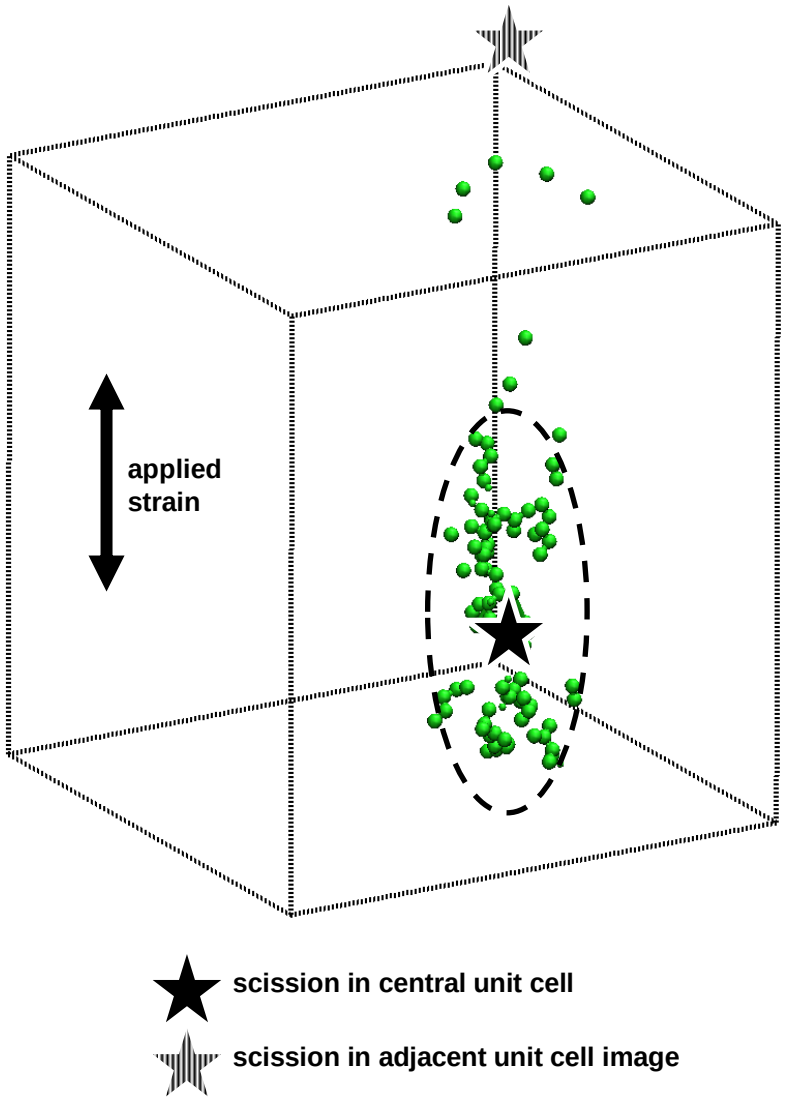

Fig. 9.17 The AFEM simulation result for a single scission in the amrophous unit cell. Atoms are only shown that demonstrate a threshold reduction in the interatomic force they transfer as a result of the chain scission. There is a localised reduction in stiffness near the applied chain scission.

Fig. 9.18 shows schematically how high stress may deviate around less stiff regions of polymer that may exist around polymer chain scissions. This understanding may indicate how polymer chain scissions affect the mechanical properties; rather than considering mechanical properties in terms of average molecular weight, it may be more appropriate to consider the concentration of chain scissions. Each chain scission may be considered to cause damage to the polymer. The Effective Cavity Theory

utilises this understanding in the next chapter of this thesis to form a model for overall polymer Young's modulus based on the existence of effective cavities around chain scissions.

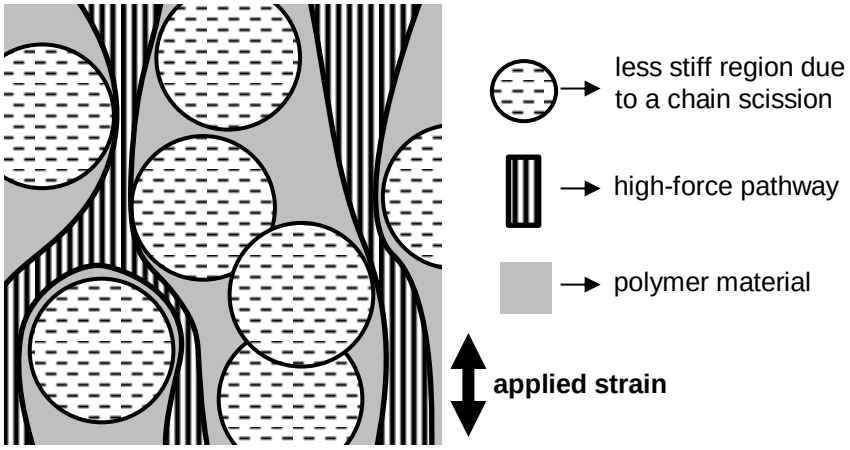

Fig. 9.18 Schematic of how high interatomic forces are transferred through regions of the polymer that do not contain scissions. The volumes of polymer surround a scission may be less stiff and therefore strain under lower interatomic forces.

The distribution of interatomic force transferred by each polymer unit in the amorphous polymer was shown earlier in Fig. 9.8. The scission applied in Fig. 9.17 is to a polymer repeat unit which sustained 0.16 of the maximum interatomic force sustained by any polymer unit. According to Fig. 9.8, this value is reasonably typical for the polymer. Fig. 9.19 (a) shows an alternative presentation of Fig. 9.17, viewed in the x direction. Fig. 9.19 (b) shows the same view but for a different scission which is applied to a polymer unit that sustains a higher interatomic force of 0.51 of the maximum for all polymer units. In both plots, the same threshold reduction in force transferred through each atom as a result of the scission is used as in Fig. 9.17 (5% of the average force transferred through any atom before a scission is applied). There are volumes of polymer with reduced force above and below the scissions. For the scission of the polymer unit that has a higher interatomic force transfer, many more atoms are shown in the figure because the scission effectively occurs in a stiffer region of the polymer. The scission therefore causes a greater reduction in polymer stiffness. A strain-aligned chain is highlighted that demonstrates a reduction in force transfer over a considerable portion of its length. As discussed in relation to Fig. 9.7, chains that are aligned in the direction of strain effectively act as stiff rods in a matrix of amorphous polymer chains and nonbonds. This chain is therefore partly responsible for the high force associated

with the scissioned polymer unit before the scission is applied. After the scission, the strain in the highlighted chain can reduce because the high local strain at the site of the scission accommodates a greater fraction of the overall strain in a direct line between the top and bottom faces of the unit cell.

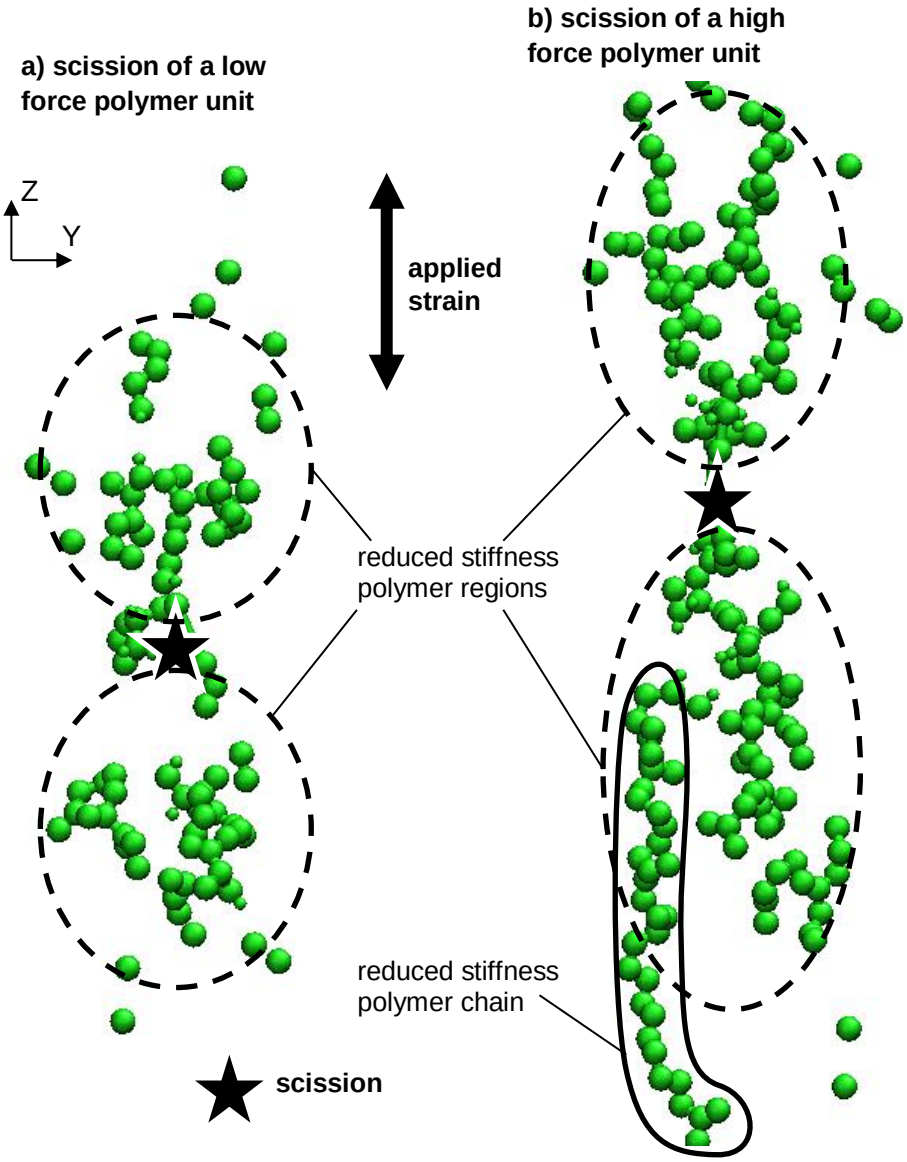

Fig. 9.19 The result from Fig. 9.17 is shown when viewed in the x direction in (a) along with the similar results for an alternative scission in (b). Only atoms that demonstrate a threshold reduction in interatomic force transfer after the scission are shown. The scission shown in (b) is applied to a polymer unit that transfers a higher force through the polymer than the polymer unit scissioned in (a). More atoms are shown in (b) because the region of polymer in which stiffness is reduced is greater. The transferred force is reduced over a considerable length of a single polymer chain as a result of the scission in (b).

The effect of chain scission depends upon which polymer unit is subject to the chain scission. Fig. 9.20 shows the effect of individual chain scissions on Young's modulus for the scission of ten different polymer units. The term polymer repeat unit force refers to the maximum interatomic force transferred through any atom in the polymer unit as defined in relation to Fig. 9.8. For the ten scissioned polymer units, the polymer repeat unit force before scission varies from 8% to 51% of the maximum interatomic force transferred for any repeat unit in the polymer. There is a general trend that polymer units through which a higher force transfers cause a greater reduction in Young's modulus when subject to chain scission than polymer units which initially transfer a lower force. This agrees with the finding in Fig. 9.19 that a greater volume of weaker polymer is created when a scission occurs in a stiffer region of the polymer. In semi-crystalline polymer theory, the tie chains in the amorphous volumes between crystalline lamellae are expected to contribute greatly to overall mechanical properties. They sustain a greater force than average amorphous polymer chains. The simulations in this study may indicate that even in a fully amorphous polymer, chains may exist that are oriented in the direction of stress and therefore sustain a higher force than average. The scission of these chains is likely to be more important in terms of the degradation of mechanical properties than the scission of chains that are not aligned in the direction of applied strain.

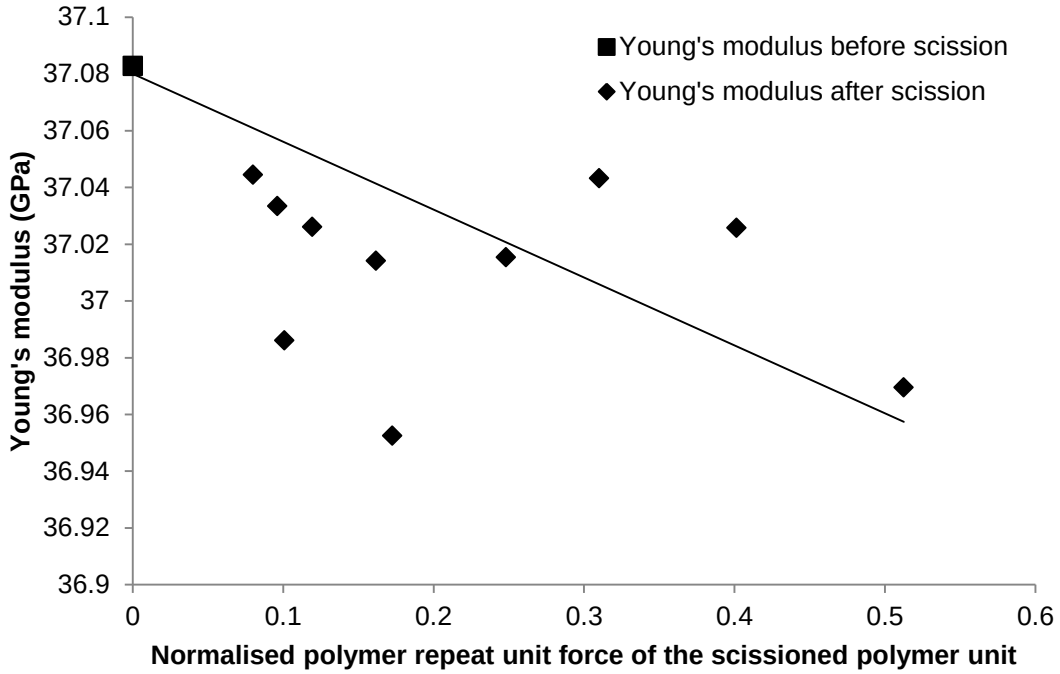

Fig. 9.20 Ten scissions are individually applied to the polymer. The value of Young's modulus is shown versus the force transferred by the scissioned polymer unit.

9.7 Conclusions

The atomic finite element method (AFEM), which was presented in the previous chapter of this thesis, was used to analyse the mechanical properties of both crystalline and amorphous poly(lactide) polymers. The strain energy in the strained structures was found to be contained mostly in nonbond elements between atoms that are not covalently bonded and between polymer chains. This finding supports the ability of the AFEM simulations because it is generally believed that strain is accommodated in between the polymer chains rather than in stiff covalent bonds. The values of Poisson's ratio were similar to the values expected experimentally. The Young's modulus values derived in the AFEM simulations were found to be higher than experimental values, which was attributed to the fact that AFEM simulations effectively consider mechanical properties at 0 Kelvin. The interatomic force that transfers between atoms in a strained polymer structure was analysed. In the highly regular crystalline phase, it was found that individual covalent bonds that are aligned in the direction of applied strain sustain the greatest force. In the amorphous phase, the forces are controlled by the atomic configuration over a much larger distance; the greatest forces were found in sections of polymer chains that were oriented in the direction of applied strain. It was proposed that the polymer chains and covalent bonds may act as rigid rods in a weaker matrix of long-range, unoriented or less oriented nonbonds, which model Coulomb and van der Waals interactions. The AFEM setup was varied by changing the stiffness and range of nonbonds in order to understand the contribution of each of the potential energy functions in the molecular dynamics force field. It was found that the nonbonds provide the bulk of a polymer's resistance to deformation, which is supported by the general understanding that Young's modulus, for polymers below the glass transition temperature, is controlled by nonbonded interactions between polymer chains.

Polymer chain scissions were implemented in order to simulate degradation. Up to 258 scissions were applied to the amorphous polymer structure in order to model an overall trend for Young's modulus versus molecular weight in a degrading poly(lactide); this trend was found to be similar to a trend identified in the review of experimental data in the literature in Chapter 2. The effect of individual chain scissions was also studied. It was found that chain scissions may instantiate a volume of reduced-stiffness polymer. Also, the interatomic force transfers through a polymer along pathways that deviate around polymer chain scissions. These understandings are used in the next chapter in a model for the degradation of Young's modulus by hydrolytic chain scission.

Chapter 10: An Effective Cavity Theory for change in Young's modulus due to polymer chain scission

In this chapter, the Effective Cavity Theory is presented to model the degradation of Young's modulus in biodegradable polymers. The theory is developed based on the AFEM analysis in Chapters 8 and 9 of this thesis. It is proposed that effective cavities may be considered to exist around polymer chain scissions, which do not sustain mechanical load. The Effective Cavity Theory model is validated using experimental data for Young's modulus degradation from the literature. Finally, the Effective Cavity Theory model is incorporated into the mathematical model, discussed in chapters 5, 6 and 7 of this thesis, to extend the modelling capabilities to include Young's modulus. This chapter is included in a publication draft [106].

10.1 Introduction

As discussed in the literature review in Chapter 2, the Young's modulus of a biodegradable polymer is related to many factors, of which molecular weight and crystallinity are particularly important. During degradation, crystallinity generally increases while molecular weight decreases. The increase in crystallinity causes Young's modulus to increase [57] while molecular weight reduction results in a Young's modulus decrease. Theoretical models help improve understanding of how mechanical properties degrade and can be used to simulate degradation in order to design the optimum device. Existing theoretical models are reviewed in Chapter 2. The author of this thesis is only aware of one mathematical model [61] that relates Young's modulus to the degradation of molecular weight in bioresorbable polymers and is based on a theoretical understanding of how mechanical properties change during degradation. That study considered polymers above their glass transition temperature. However, many biodegradable polymers are used below their glass transition temperature, in which case there is no current theoretical model that can be used to describe the degradation of Young's modulus. To address the lack of theoretical models for Young's modulus during degradation of biodegradable polymers below their glass transition temperature, the Effective Cavity Theory is presented in this chapter, which models the degradation of Young's modulus based on both crystallinity and molecular weight data. The effect of polymer chain scission on Young's modulus is analysed using the atomic finite element method (AFEM) simulations, which were presented and demonstrated in

the previous two chapters of this thesis. AFEM simulations are used for poly(lactide) polymer structures to analyse the atomistic mechanical response to polymer chain scission. It was found in the previous chapter of this thesis that chain scission may be considered to create effective cavities in the polymer. In this chapter, a model is presented, which considers how the effective cavities affect overall Young's modulus. The commercial finite element analysis package COMSOL Multiphysics 4.3b (license 7074366) is used to develop the model. The shape of the effective cavities is derived from AFEM simulations for chain scission. Experimental data for mechanical properties are used to test the Effective Cavity Theory. Also in this chapter, the Effective Cavity Theory is integrated into a simple mathematical model for the degradation of molecular weight and crystallinity.

10.2 AFEM simulations for effective cavities due to chain scission

The atomic finite element model (AFEM) model has been described in detail in Chapter 8 of this thesis. Briefly, in AFEM the interatomic potentials developed for molecular dynamics studies are represented by finite elements between atoms. The molecular dynamics force field PLAFF2 is used, which was developed specifically for poly(lactide) [85]. The atomic structure used in this thesis is the amorphous unit cell for poly(lactide) that was considered in Chapter 9; the structure was supplied with McAliley's thesis [85] regarding the PLAFF2 force field. Scissions are applied in the AFEM simulations by removing one polymer repeat unit from the structure. Analysis of interatomic force transfer through the atoms of the polymer, referred to as the atomic force transfer, enables the local atomic effect of chain scission to be studied. The method of calculating atomic force transfer was described in detail in the previous chapter of this thesis. Briefly, the force transferred through an atom is calculated as the force that is applied to the atom, in the direction of applied strain, by all atoms above it in the positive direction of strain. It is useful to consider an imaginary cut plane immediately above the atom in question. The force transferred through the atom is calculated as the force that is transferred through all AFEM elements which are connected to the atom when they pass through this imaginary cut plane.

The previous chapter in this thesis found that when a polymer chain is scissioned, the force that transfers through a strained polymer deviates around a volume of polymer near the scission. Fig. 10.1 (a) shows the overall polymer structure used in AFEM simulations and Fig. 10.1 (b) only shows atoms which exhibit a threshold reduction in the force that they transfer, as a result of one chain scission. The volume occupied by

the displayed atoms is effectively a volume of less stiff polymer. In the Effective Cavity Theory model, this volume is represented by an effective cavity near the chain scission. The threshold reduction value for atomic force transfer is chosen to be 2.5% of the average force transferred through all atoms. This value enables a suitable number of atoms to be displayed in order to facilitate clear visual analysis of the likely shape of effective cavities.

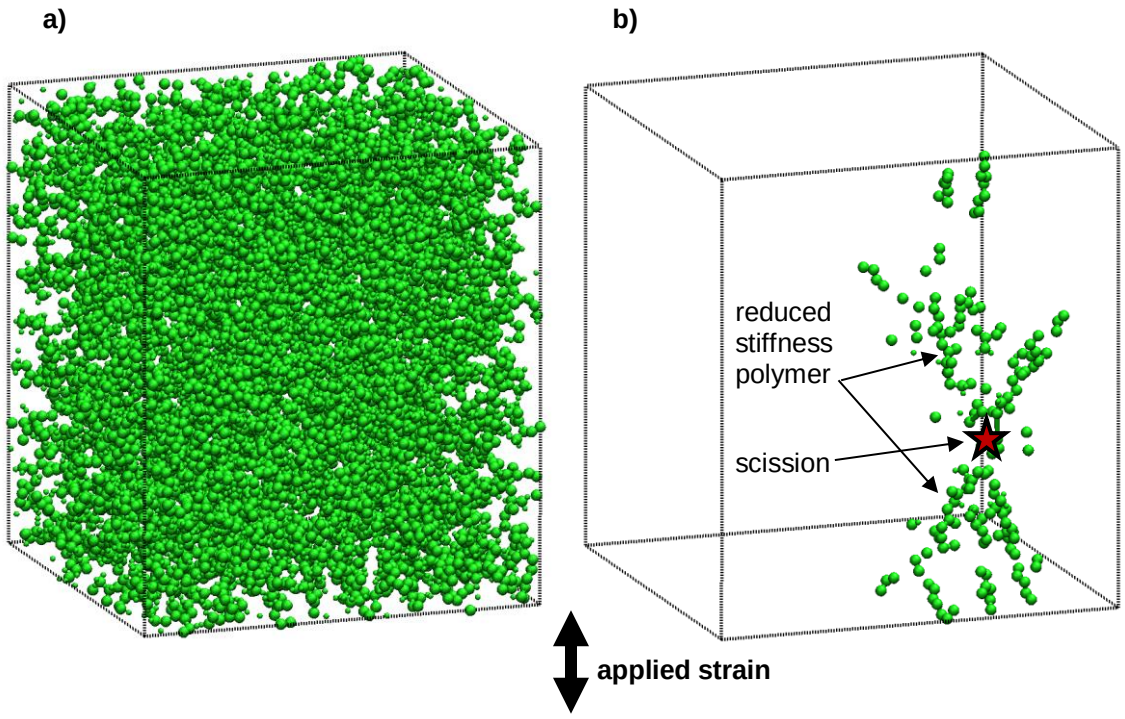

Fig. 10.1 The polymer unit cell is shown a) in its entirety and b) with atoms only displayed if they demonstrate a threshold reduction (as a result of the chain scission) in the force that they transfer through the polymer.

In order to identify the shape of the effective cavity, ten scissions are individually applied to random polymer units in the amorphous polymer structure used in AFEM simulations. Fig. 10.2 shows the AFEM results for the ten individual scissions, viewed normal to the direction of applied strain, utilising the same threshold value as in Fig. 10.1. The schematic in the figure demonstrates that flat-tipped cones may be used to approximate the volumes of reduced stiffness polymer that result from chain scission. For each scission, effective cavities may be considered to exist in the shape of flat-tipped cones oriented tip-to-tip. Pairs of flat-tipped cones are overlaid onto each of the simulation results in the figure to demonstrate that such a shape is a suitable approximation of the reduced stiffness polymer near each chain scission. The orientation of the flat-tipped cones depends on the direction of applied strain. If the direction of applied strain changes, so too does the position of effective cavities that

result from chain scission. Based on Fig. 10.2, a flat-tipped cone shape is used to represent the shape of effective cavities when developing the Effective Cavity Theory model to relate Young's modulus to chain scission. There is some variation between the shapes of the cones in Fig. 10.2. The shape can be characterised (i) by the ratio of the top radius to the base radius, and (ii) by the ratio of the cone height to the base radius. The base radius, top radius and cone height are all labelled in Fig. 10.2. For the ten cone shapes given in Fig. 10.2, the ratio of the top radius to the base radius varies from approximately 0.25 to 0.5 and the ratio of the cone height to the base radius varies from approximately 1 to 1.25. In order to account for the variation in cone dimensions, in the Effective Cavity Theory presented in this chapter, the ratio of the top radius to the base radius is varied from 0 to 0.667 and ratio of the cone height to the base radius is varied from 1 to 2.

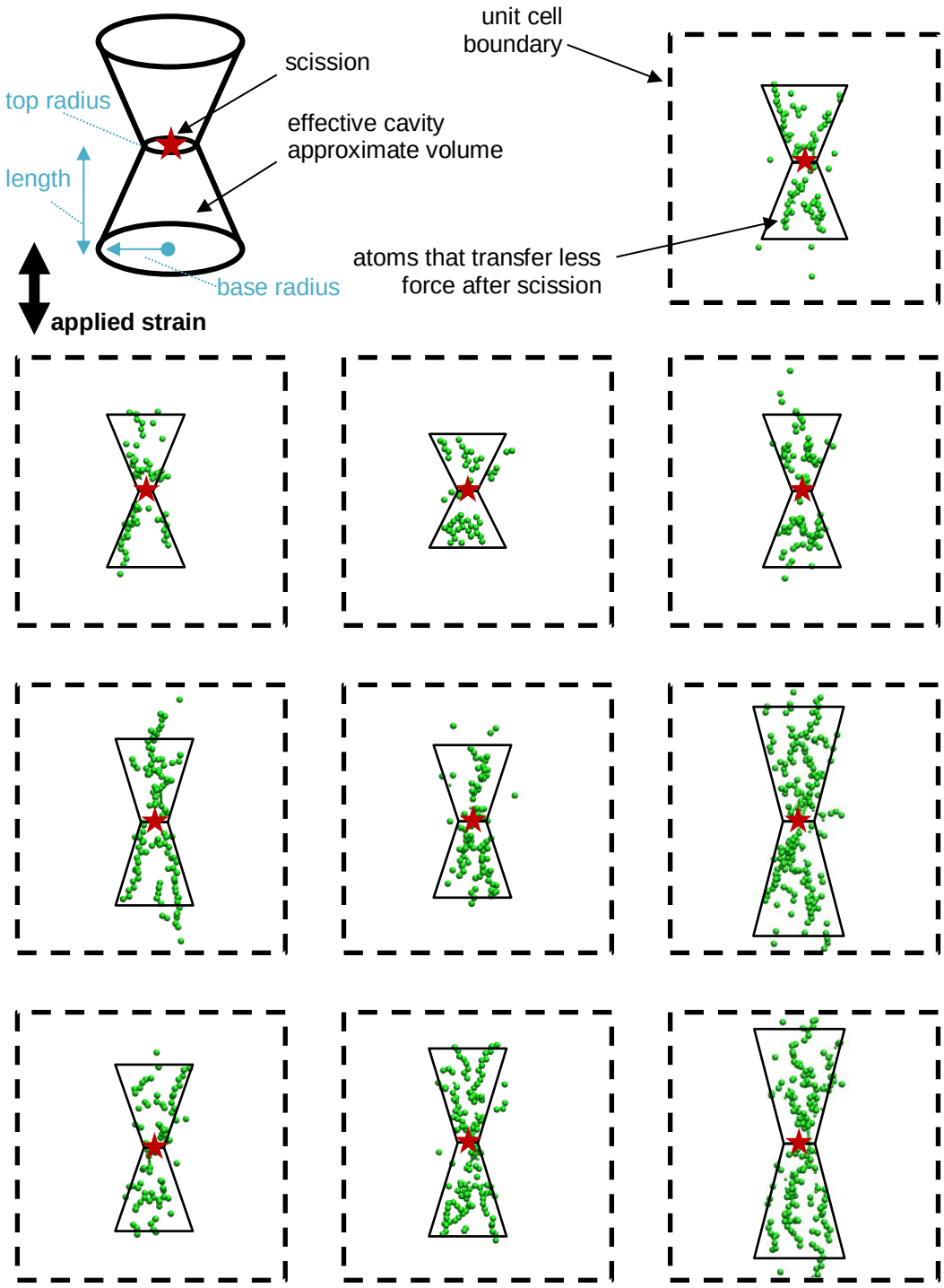

Fig. 10.2 Ten scissions are individually applied to the amorphous polymer. Atoms are only displayed if they demonstrate a threshold reduction in the force that they transfer through the polymer as a result of the chain scission. A volume of less stiff polymer may exist around each scission, which takes the shape of two flat-tipped cones oriented tip-to-tip in the direction of applied strain. This shape is chosen for the model of the Effective Cavity Theory presented in this thesis.

10.3 Effective Cavity Theory for change in Young's modulus due to chain scissions

The Effective Cavity Theory model for the degradation of Young's modulus in biodegradable polymers combines models for the effect of both chain scission and crystallinity on Young's modulus. In the model for chain scission, effective cavities in the shape of flat-tipped cones are considered to result from each chain scission. As the concentration of chain scissions increases in a polymer during degradation, the volume fraction of effective cavities increases. The model for chain scission effective cavities relates the volume fraction of effective cavities to Young's modulus. As crystallinity increases, Young's modulus increases because the crystallites have greater stiffness than amorphous polymer. Crystallites are generally considered to be cuboidal in shape, and hence the model for crystallinity considers a cubic crystal particle in a cubic matrix of amorphous polymer. To develop the models, the finite element analysis package COMSOL Multiphysics 4.3 is used.

10.3.1 Effect of chain scission on Young's modulus

To develop the model for effective cavities associated with chain scission, one quarter of a flat tipped cone is modelled as a void in a cubic matrix, which represents amorphous polymer. The FEA model including the mesh is shown in Fig. 10.3. The height and large radius of the cone are set to be 1nm. The small radius of the cone is set to be 0.333nm. These values are adjusted and discussed later in this section to investigate the effect of cone shape on the effective cavity theory. For the simulation shown in the figure, the overall cubic cell has side lengths of 1.5nm. Symmetry is assumed across the left, front and bottom faces of the cube in Fig. 10.3, which represents a cube eight times the volume containing two flat-tipped cone voids oriented tip-to-tip. Strain is applied to the top face of the cube in Fig. 10.3, while the back and right faces are free to displace in order to accommodate Poisson's effect but remain planar. The bottom face is restrained in the z direction. These boundary conditions represent the case that the larger cube, containing eight reflections of the cube shown in Fig. 10.3, is a unit cell that repeats to infinity in all directions. During the FEA simulations that develop the Effective Cavity Theory, the size of the flat-tipped cone effective cavity is kept constant while the overall cubic cell size reduces. A smaller cubic cell represents a reduced separation between chain scissions in the polymer and therefore more scissions per unit volume and a more degraded polymer.

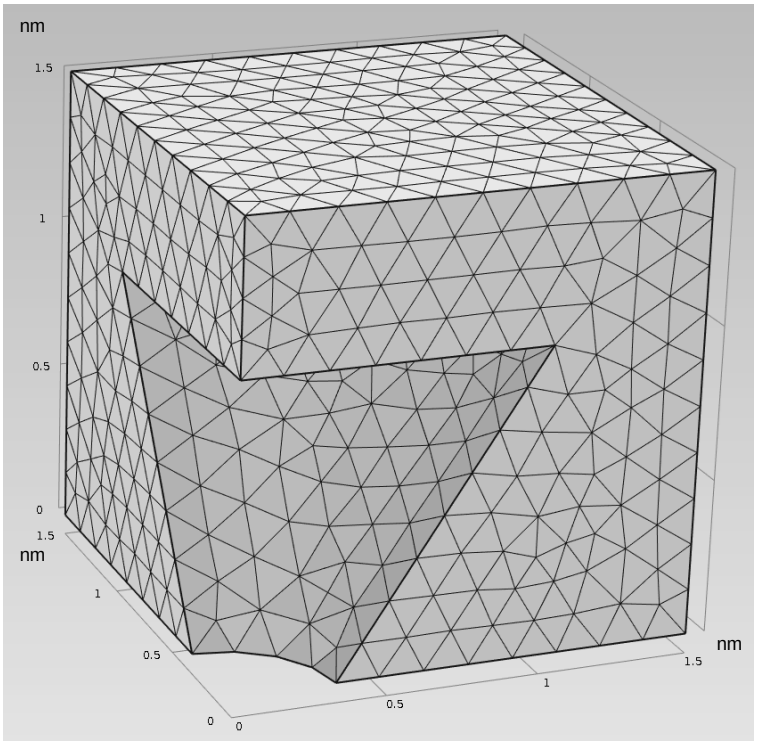

Fig. 10.3 The flat-tipped cone FEA model used to determine the model for a flat-tipped cone effective cavity in cubic matrix. The finite element mesh is indicated.

Young's modulus for the cubic matrix is arbitrarily set to 1 GPa. A void is used for the cavity volume as opposed to a reduced Young's modulus since the actual modulus value cannot be predicted from the atomic simulations; to include a non-zero modulus would result in another variable in the model that would effectively be arbitrarily set. Twelve simulations are conducted in total, in which the side length of the cube varies from the same height as the flat-tipped cone to twenty times longer. Further refinement of the mesh has little impact on the results. Young's modulus is calculated by finding the average stress that is applied to the top face of the cube in order to achieve 10% strain through static linear analysis. The results for normalised Young's modulus versus the volume fraction of effective cavities for all twelve simulations are given in Fig. 10.4. The values of Young's modulus found in the simulations are normalised by the initial value for a full cube without any effective cavity. A line of best fit indicates the relationship of

$$\overline{E} = e^{-2.483 Xec} \qquad 10.1$$

in which $\overline{E}$ is normalised Young's modulus (no units) and X_{ec} is the volume fraction of the effective cavity in the polymer matrix (no units). The final data point in Fig. 10.4 is

not included when fitting the line of best fit in order to determine Eq. 10.1 because the relationship between normalised Young's modulus and pore volume fraction begins to deviate from the curve for lower effective cavity volume fractions. This is due to high interaction between the effective cavity and the cell boundaries at such a high volume fraction. The final data point used in the fitting considers a Young's modulus reduction of ≈50%. Therefore, the use of the model for Young's modulus reductions greater than 50% should be considered with caution.

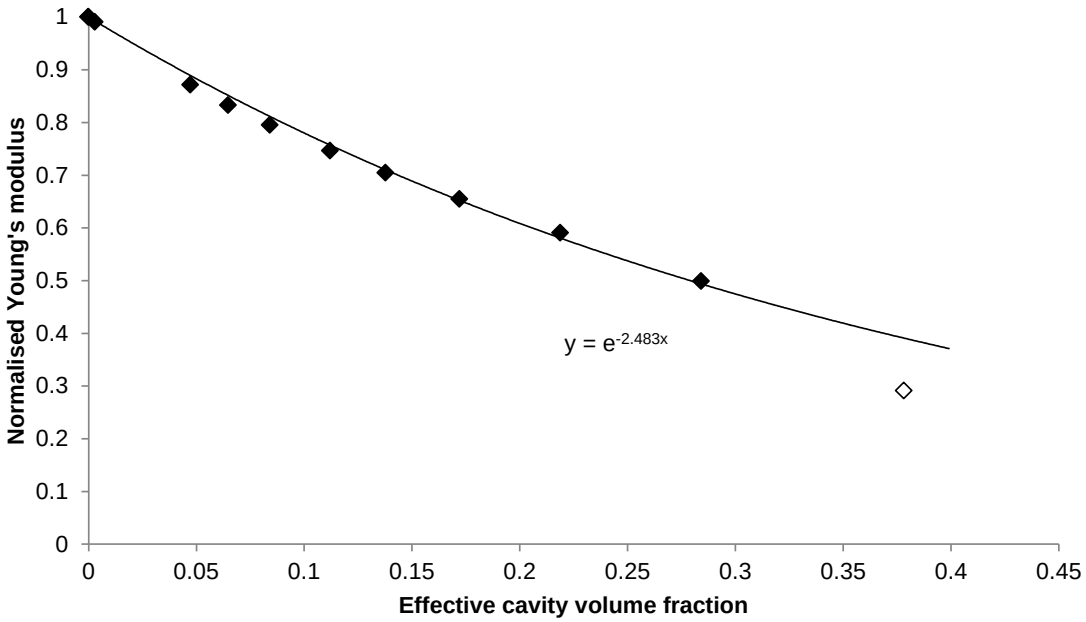

Fig. 10.4 Normalised Young's modulus versus effective cavity volume fraction for 12 simulations of a flat-tipped cone effective cavity in a cubic polymer matrix. An exponential line of best fitting to the first 11 data points (solid filled diamonds) is shown.

The cone shapes in Fig. 10.2 show some variation. The value of the exponent in Eq. 10.1 is dependent on the cone dimensions. In order to test the effect of cone dimensions on the relationship found in Eq. 10.1, the simulations discussed above are repeated for a range of cone dimensions. The fitting shown in Fig. 10.4 is repeated for each simulation setup. Table 10.1 gives the cone dimensions and the corresponding value of the exponent for Eq. 10.1. When fitting the Effective Cavity Theory to experimental data in Section 10.4, error margins indicate the range of Effective Cavity Theory results that the range of exponents in Table 10.1 gives. For the cone with a height of 2nm, the unit cell is adjusted to be twice as tall as it is wide to maintain proportionality.

Cone height (nm)	Cone large radius (nm)	Cone small radius (nm)	Eq. 10.1 exponent value
1	1	0	-3.439
1	1	0.333	-2.483
1	1	0.667	-1.845
2	1	0.333	-2.041

Table 10.1 Table of cone dimensions used in the simulations and the respective exponents for Eq.10.1.

10.3.2 Effect of crystallinity on Young's modulus

A similar approach is used to develop the model for crystallinity as was used for chain scissions in the previous section. The setup of the model is the same except the flat-tipped cone shaped void is replaced by a cube of material that represents a crystallite particle in an amorphous polymer matrix. Fig. 10.5 shows the model for a crystal with side lengths equal to 50% of the overall cube side length including the FEA mesh. As with the chain scission model, symmetry boundary conditions are applied to the left, front and bottom faces to represent an overall cube of eight times the volume of the one shown, which contains a single centrally located crystal particle. The bottom face is restrained in the z direction and the top face is displaced by 10% of the overall side-length. Poisson's contraction is permitted but the boundaries are constrained to be planar. For the amorphous matrix, Young's modulus is 37.1 GPa and Poisson's ratio is 0.255, which are the values found in the atomic simulations for amorphous poly(lactide) in the previous chapter of this thesis. For the crystal particle, Young's modulus is 77.4 GPa, which is the mean of the x, y and z values for crystalline poly(lactide) Young's modulus that is found in the atomic simulations in the previous chapter. Although the values for Young's modulus are higher than expected experimentally, which is discussed in the previous chapter, they are used because no experimental values for crystalline Young's modulus are available. In the simulations here, the absolute values do not affect the results; it is the ratio of crystalline:amorphous Young's moduli that is important. The ratio of 2.1 used here is reasonable. And this ratio is varied later in this section to ensure the results are not critically sensitive to it. The shape and isentropic properties of crystals are not well understood so it the model in this thesis is simplified to be isotropic and cube shaped. Poisson's ratio of the crystal particle is 0.239, which is the mean of the six Poisson's ratio values, v_{xy}, v_{xz}, v_{yx}, v_{yz}, v_{zx}, v_{zy}, found in the previous chapter.

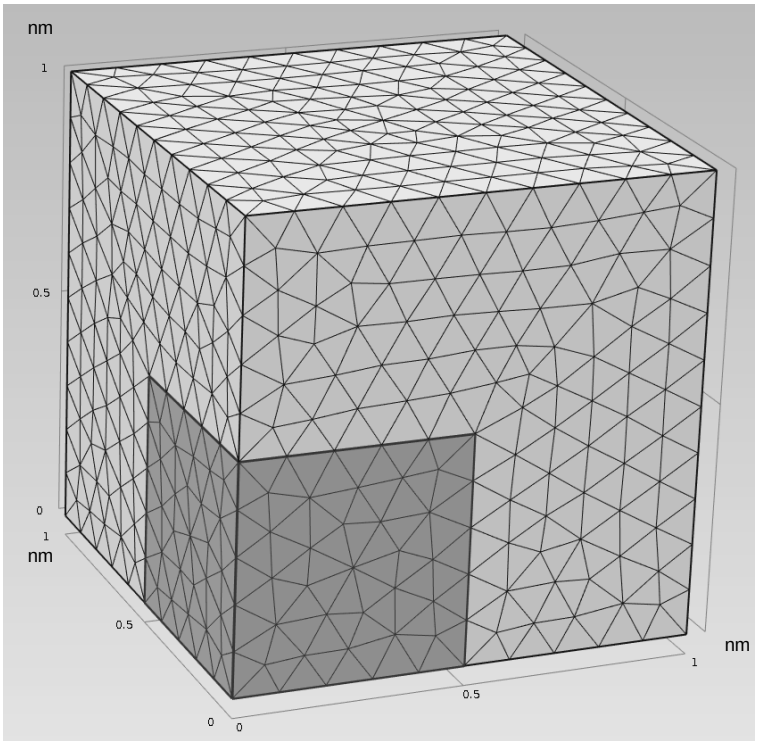

Fig. 10.5 The crystal cube within a cube FEA model used to determine the model for a crystal particle in an amorphous polymer matrix. The finite element mesh is indicated.

In the FEA simulations used to develop the model for crystallinity, the crystallite particle size remains constant while the size of the cubic cell amorphous matrix varies. As the overall cube size reduces relative to the crystal particle size, the cubic cell represents a polymer in which the crystallites are closer together and occupy a greater volume fraction. Therefore crystallinity is greater. Simulations were completed for 10 different ratios of particle side length to overall cube side length, varying from 0 to 0.9. The results for normalised Young's modulus versus crystal volume fraction are shown in Fig. 10.6. The exponential line of best fit indicates that normalised Young's modulus is related to crystal volume fraction X_c (no units) by

$$\overline{E} = e^{0.754Xc} . \qquad 10.2$$

The value of the exponent in Eq. 10.2 depends on the ratio between Young's modulus of the crystal particle and amorphous matrix. It also depends of the ratio between the values of Poisson's ratio. To determine the effects that the choices of Young's modulus and Poisson's ratio have on the exponent, a range of values for Young's modulus and Poisson's ratio are investigated here. In the above results, the isotropic crystal particle material properties are taken as the mean of the x, y and z uniaxial isentropic material

properties found in the atomic simulations of the previous chapter. Two additional simulations are conducted here, which represent upper and lower bounds. The material properties used are given in Table 10.2. For the upper bound, the crystal particle Young's modulus is taken as the maximum of the x, y and z Young's modulus and the Poisson's ratio is taken as the maximum of all six Poisson's ratio terms, found in the previous chapter for crystalline poly(lactide). This represents a crystal particle with high stiffness oriented in the direction of applied strain. For the lower bound, the crystal particle is given the minimum of all Young's modulus and Poisson's ratio values found in the atomic analysis, which represents a crystal particle with low stiffness oriented in the direction of applied strain. The fitting shown in Fig. 10.6 is repeated for the upper and lower bound setups to find the updated exponent values for Eq. 10.2. These are given in Table 10.2 and are used in Section 10.4, when fitting the Effective Cavity Theory to experimental data, in order to indicate error margins.

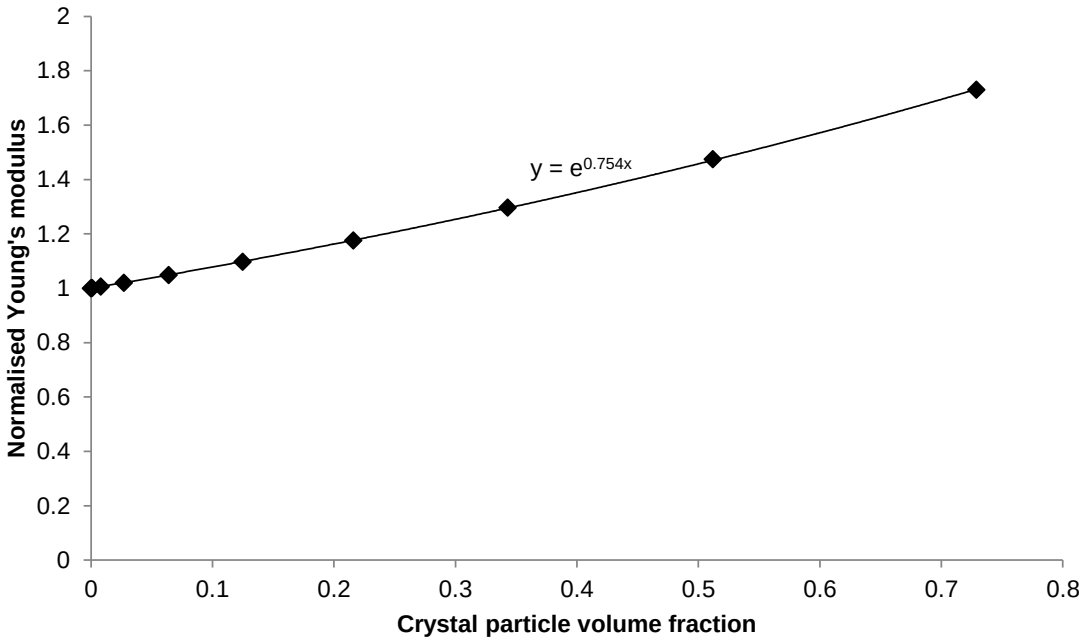

Fig. 10.6 Normalised Young's modulus versus crystal particle volume fraction for 10 simulations of a crystal particle in a cubic amorphous matrix. An exponential line of best fitting is shown.

Crystal properties	Young's modulus (GPa)		Poisson's ratio		Eq. 10.2 exponent value
	Matrix	Crystal	Matrix	Crystal	
Mean x, y, z	37.1	77.4	0.255	0.239	0.754
Lower bound	37.1	128	0.255	0.328	1.246
Upper bound	37.1	50.4	0.255	0.110	0.326

Table 10.2 Table of crystal material properties used in the simulations and the respective exponents for Eq. 10.2.

10.3.3 Young's modulus of semi-crystalline polymers

The model for chain scission and the model for crystallinity are combined to form the Effective Cavity Theory model, which considers both factors. Fig. 10.7 shows how effective cavities are assumed to incorporate both crystal particles and the amorphous polymer matrix. It is out of scope in this work to consider interaction between crystallites and effective cavities. Since the size of crystallites is not known, the model was also successfully fitted to experimental data utilising an assumption of large crystallites such that the voids occupy the amorphous phase only. Future studies may extend the model to consider the interaction between crystallites and effective cavities.

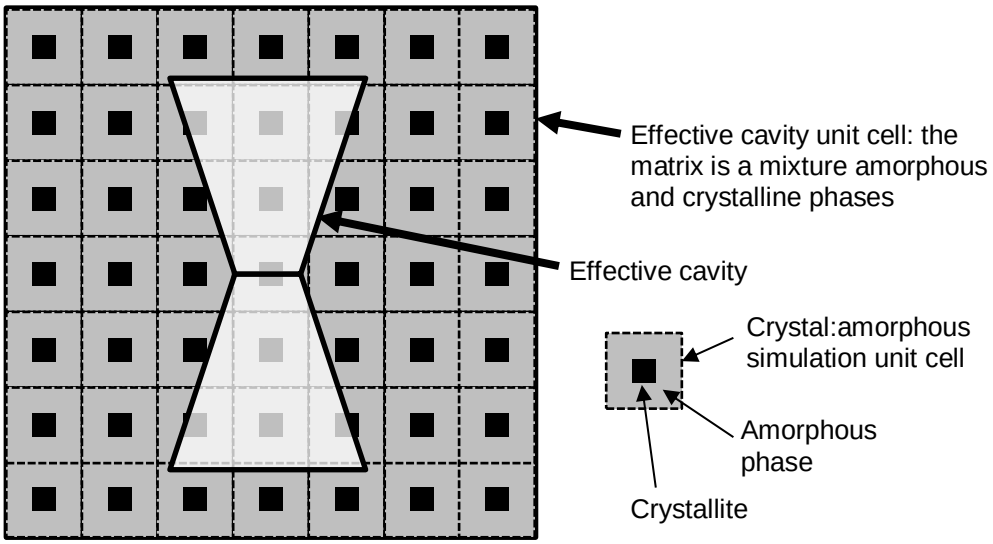

Fig. 10.7 Effective cavities are considered to occupy a volume of combined crystal and amorphous phases.

According to Eq. 10.2, the Young's modulus of the combined crystal particles and amorphous matrix phases, E_c (GPa), is empirically assumed to follow the relationship

$$E_c = E_\infty e^{0.754Xc} \quad 10.3$$

in which the Young's modulus of a fully amorphous polymer with no effective cavities or crystallinity, E_∞ (GPa), is calculated from initial experimental measurements for Young's modulus, number average molecular weight and crystallinity. E_c is used as the Young's modulus of the matrix phase in which the effective cavities occur. Therefore for the Effective Cavity Theory, Eq. 10.1 is used to model the overall polymer Young's modulus, E_p (GPa), according to

$$E_p = E_c e^{-2.483Xec} . \quad 10.4$$

Effective cavities are assumed to occur at the sites of initial chain ends as well as the polymer chain ends that result from chain scission to reflect the theory that the effective cavities are associated with chain ends. At any time during degradation the molar number of chains per unit volume, N_{chain} (mol m^{-3}), can be calculated from molecular weight according to

$$N_{chain} = \frac{\rho_p}{M_n} \quad 10.5$$

in which ρ_p (g m^{-3}) is the density of the polymer and M_n (g mol^{-1}) is the number averaged molecular weight. The concentration of chain ends, C_{end} (mol m^{-3}), is

$$C_{end} = 2N_{chain} \quad 10.6$$

And the volume fraction of effective cavities X_{ec} (no units) is therefore given by

$$X_{ec} = C_{end}V_{ec} \quad 10.7$$

in which V_{ec} (m^3 mol^{-1}) is the molar volume of each effective cavity.

10.4 Fitting of the Effective Cavity Theory with experimental data

In order to demonstrate the Effective Cavity Theory in Eqs. 10.3 - 10.7, a fitting of the model to experimental data for the degradation of Young's modulus is completed for five sets of experimental data [5, 6, 8, 11]. These sets of data are chosen because they concern poly(lactide) and have regular measurements for crystallinity, molecular weight and Young's modulus. The only variable that is adjusted in the experimental data fittings is the effective cavity volume V_{ec}. The value of X_c is measured experimentally in all cases. The density, ρ_p, is taken to be 1.25 x10^6 g m^{-3}. The values of N_{chain} and C_{end} are derived from measured M_n, and therefore allow the value of initial X_{ec} to be calculated in Eq. 10.7 based on the set value of V_{ec}. The value of E_∞ is derived from Eq. 10.3 by substitution of the initial measured Young's modulus into Eq. 10.4 as E_p, along with the measured and derived values of X_c and X_{ec}. The experimental setup and initial measurements are given for the five datasets in Table 10.3, where PBS indicates phosphate buffer solution.

Data Set [reference]	A [6]	B [5]	C [58]	D [58]	E [11]
Initial M_n (g mol^{-1})	159000	584000	153000	152000	42000
Initial X_c	0.448	0.540	0.480	0	0.570
Initial Young's modulus (GPa)	0.668	0.100	6.86	5.58	1.43
Sample type	0.8 mm plate	0.050 mm film	2 mm rod	3 mm rod	0.033 mm film
Polymer type	PLLA	PLLA	PLLA	PLLA	PLLA
Degradation medium	37°C PBS pH7.4	37°C PBS pH7.4	38°C PBS pH7.4	38°C PBS pH7.4	37°C PBS pH7.4

Table 10.3 Experimental setups and initial measurements for the five sets of data that are used in the Effective Cavity Theory fitting.

Fig. 10.8 shows the experimental measurements for the degradation of molecular weight and crystallinity in the five experiments. In Fig. 10.8 (c) and (d), crystallinity was not measured at week 12 so the values used for the Effective Cavity Theory fitting are taken as the average of the measurements at weeks 8 and 16 and these values are shown in the figure. Fig. 10.9 shows the experimental data for Young's modulus along with the Effective Cavity Theory results. The Effective Cavity Theory fitting gives discrete data points because Eqs. 10.4 - 10.7 are used at each experimental measurement time. A molar volume of 9.41 x10^{-3} m^3 mol^{-1} is used for effective cavity

volume V_{ec} for all five data sets in Fig. 10.9. It is justifiable to use several effective cavity volumes, since the samples may have different polymer chain configuration due to the different experimental setups. However, the value is not adjusted between fittings in order to reduce the number of parameters that can be varied to achieve the best fitting. The fittings can be improved if the value of V_{ec} is allowed to vary. The error bars indicate the minimum and maximum Young's moduli found by the Effective Cavity Theory for all combinations of exponents given in Table 10.1 and Table 10.2 being used in Eq. 10.4 and Eq. 10.3, respectively. The Effective Cavity Theory gives a very good fitting to the experimental data.

The fittings in Fig. 10.9 (c) and (d) consider experimental data for extruded rods, which have more aligned polymer chains than the amorphous polymer films. Therefore the effective cavity theory may slightly underestimate the reduction in Young's modulus for these data sets because it was found in the previous chapter that chain scissions have more of an effect on Young's modulus reduction when applied to chains that are aligned in the direction of applied strain. The model is able to consider Young's modulus increase due to crystallinity as demonstrated in the first two data points in Fig. 10.9 (c) and the first few weeks in Fig. 10.9 (d). The Effective Cavity Theory correctly reproduces the slightly erratic nature of Young's modulus reduction and increase in the first 5 data points in Fig. 10.9 (a). The trend can be linked to the molecular weight experimental measurements, which fluctuate in a similar manner to Young's modulus. The Effective Cavity Theory is intended for Young's modulus reductions up to 50% as discussed in relation to Fig. 10.4. Therefore, for the later stages in each of the fittings, the results should be considered with caution. However, the data fittings quite accurately model Young's modulus reduction to zero. For the chosen effective cavity volume, the experimental data considered in Fig. 10.9 (e) has a very high initial volume fraction of effective cavities (56%) compared to the other four studies (4-15%) because it has a much lower initial molecular weight. Although the Effective Cavity Theory is not intended for the data in Fig. 10.9 (e), it can be seen to achieve quite a good fitting, using the same volume of effective cavity.

The simple model presented in Eqs. 10.3 - 10.7 for the Effective Cavity Theory is based on the model for an isolated flat-tipped cone void and does not consider overlap of the effective cavities. If effective cavity overlap was considered in the Effective Cavity Theory, following a theory such as crystal overlap based on Avrami Theory in Chapters 5 - 7 in this thesis, the rate of Young's modulus reduction would reduce as it

approached zero. Such a trend may result in a better fit towards the end of degradation for the experimental data sets in Fig. 10.9 (c) and (d). The value of V_{ec} used in the Effective Cavity Theory model represents a cone height of 2.74 nm for the effective cavities. In the AFEM analysis of the previous chapter, the chain scissions affect a smaller volume than that used in the fitting here. This can be explained by the findings of that chapter that the AFEM analysis underestimates the effect of chain scission, most likely because it represents polymer properties at 0 Kelvin.

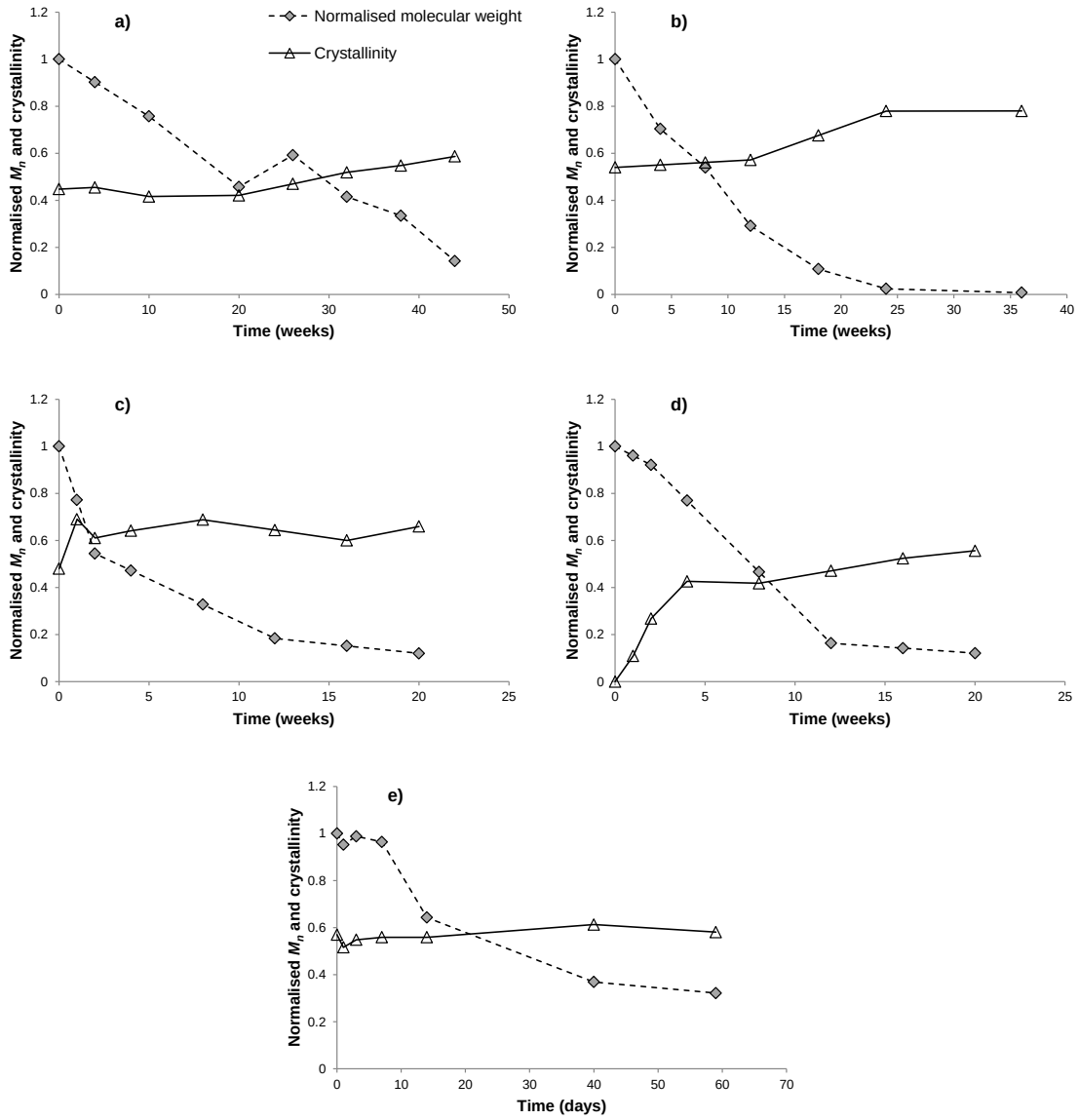

Fig. 10.8 Experimental data for crystallinity and molecular weight for five degradation studies: a) [6], b) [5], c) and d) [58] and e) [11].

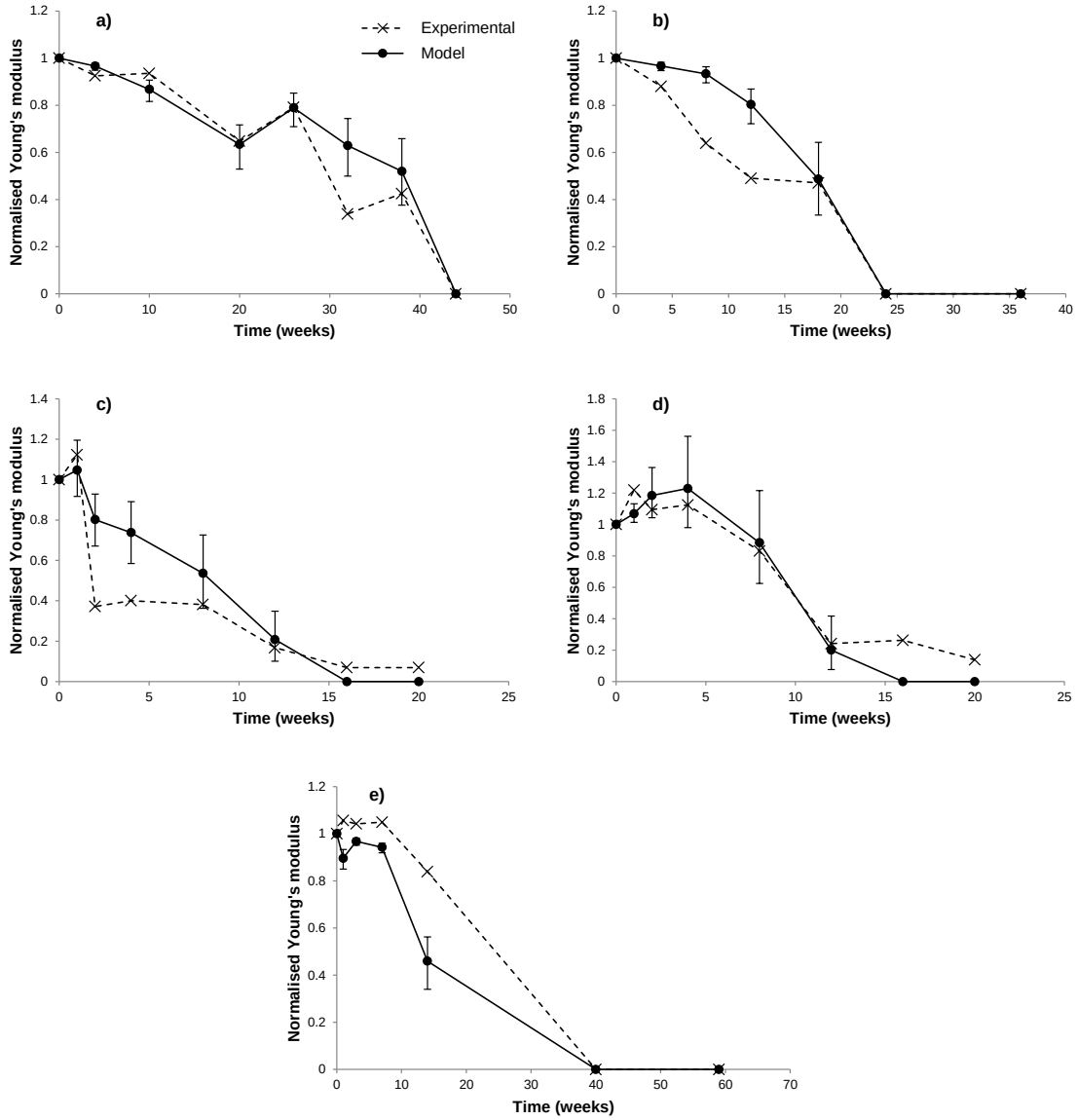

Fig. 10.9 Experimental data and the Effective Cavity Theory model for Young's modulus in five degradation studies: a) [6], b) [5], c) and d) [58] and e) [11].

10.5 A full mathematical model to simulate degradation of mechanical properties

The mathematical model presented in Chapter 5 is combined with the Effective Cavity Theory to fully model the degradation of molecular weight, crystallinity and Young's modulus. Initial experimental measurements of polymer properties such as molecular weight and degree of crystallinity are input to the model. The rates of chain scission and crystallisation are calculated to simulate overall changes to number-average molecular weight and degree of crystallinity during degradation according to Eqs. 5.1 – 5.6 in Chapter 5. This simulated data enables the Effective Cavity Theory to model Young's modulus, as described in Eqs. 10.4 - 10.7. The experimental data from Fig. 10.8 (d) and Fig. 10.9 (d) is used to demonstrate the implementation of the Effective Cavity Theory into the mathematical model for degradation by chain scission. Fig. 10.10 shows the fitting of the model to experimental data for molecular weight, crystallinity and Young's modulus. The experimental setup is given in Table 10.3 and model parameters used in the fitting are given in Table 10.4.

The effective cavity volume V_{ec} is set to be 9.41 x10^{-3} m^3 mol^{-1}, as in the fitting in the previous section. The value of E_∞ is derived from initial experimental measurements as described in the opening paragraph of Section 10.4. In the early stages of the fitting, crystallinity increase causes Young's modulus to increase to a greater extent than the effective cavities of chain scission cause it to reduce. Once crystallinity begins to plateau at about 5 weeks however, the change in Young's modulus is controlled by the effective cavities of chain scission and it begins to reduce. The model is proposed for Young's modulus reductions up to 50% so the model results past this point (indicated by the dashed line in the figure) are only included for reference.

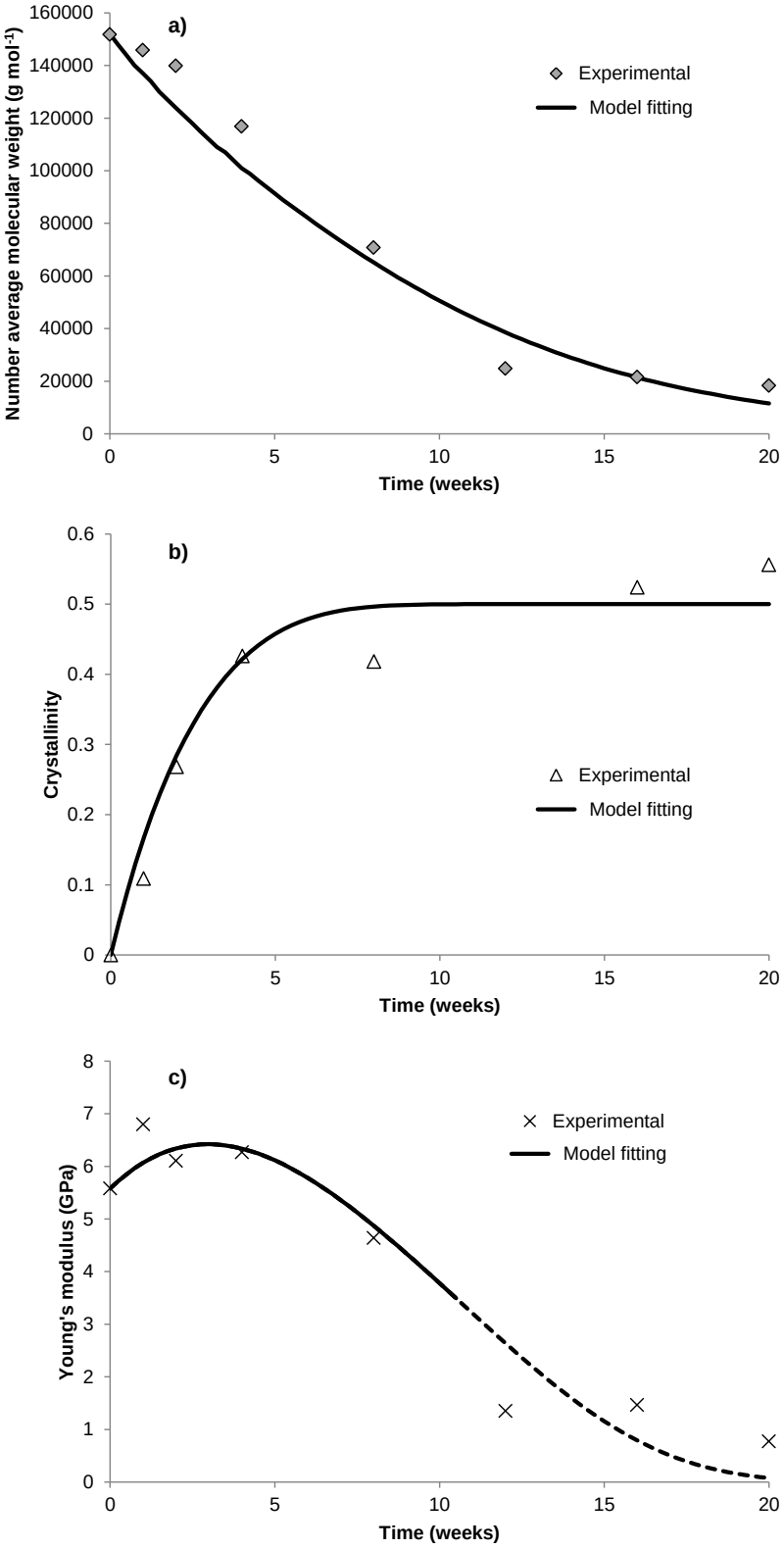

Fig. 10.10 The mathematical model fitting to a) molecular weight and b) crystallinity. The Effective Cavity Theory fitting to Young's modulus is shown in c). Discrete data points indicate experimental data [58] while the solid lines indicate the model fittings. The Effective Cavity Theory is proposed for Young's modulus reductions <50% although the results are included beyond this for reference (dashed line).

Model constant	C_{e0} (mol m^{-3})	k_1 (week^{-1})	k_2 ([mol^{-1}m^3]$^{0.5}$week^{-1})	p_x (no units)	V_c (nm^3)	M_0 (g mol^{-1})	m (no units)
Value	17300	5.0 x10^{-5}	6.0 x10^{-4}	0.18	4.19 x10^3	72	4
Model constant	X_{max} (no units)	ω (mol m^{-3})	V_{ec} (m^3 mol^{-1})	N_{chain0} (mol m^{-3})	ρ_p (g m^{-3})	α (no units)	β (no units)
Value	0.5	= C_{e0}	9.41 x10^{-3}	8.21	1.25 x10^6	28	*2*
Model variable	R_s, R_{ol} (mol m^{-3})	X_c, X_{ext} (no units)	Ce (mol m^{-3})	N_{chain} (mol m^{-3})			
Initial value	zero	zero	= C_{e0}	= $N_{chains0}$			

Table 10.4 Model parameters used in the fitting of the mathematical model and Effective Cavity Theory.

The diffusion of oligomers is not considered in the simple model here although it has been included in previous studies by Pan and his co-workers [48-50] and in Chapters 8 and 9 of this thesis. The volumes of polymer from which oligomers can readily diffuse out of the polymer, near the surface for example, demonstrate a reduced rate of degradation since the concentration of oligomers is reduced and therefore so too is the rate of autocatalytic chain scission. The Effective Cavity Theory model can be implemented into a mathematical model for chain scission that includes small chain diffusion. The Young's modulus can be modelled throughout a biodegradable medical device such as a biodegradable screw during the course of degradation. Such analysis could identify variation of Young's modulus degradation between the central shaft of a screw compared to screw teeth and allow for optimisation of the mechanical design.

10.6 Conclusions

Atomic finite element simulations (AFEM) were conducted to analyse the effect of chain scission on Young's modulus. The AFEM technique was presented in Chapter 8. In Chapter 9, it was found that effective cavities may exist as a result of chain scission in biodegradable polymer. In this chapter, the theory of effective cavities was used to present a model for Young's modulus degradation in biodegradable polymers. The shape of effective cavities was identified from a number of simulations for individual chain scissions. Finite element analysis simulations were conducted to find a relationship between the volume fraction of effective cavities and Young's modulus. Since crystallinity is known to affect Young's modulus, finite element analysis simulations were also conducted to find a relationship between the volume fraction of crystallites and Young's modulus. The Effective Cavity Theory was presented, which combines both models for Young's modulus during degradation, based on crystallinity and on chain scission. The Effective Cavity Theory model was fitted to experimental data for Young's modulus in five sets of data in the literature. A good fit was achieved when the same model parameter values were used for all five data sets; the only inputs to the model that varied were the experimentally measured values of molecular weight, crystallinity and initial Young's modulus. The Effective Cavity Theory was also combined with the mathematical model for biodegradable polymer degradation that was presented in Chapter 5 of this thesis. The combined model was demonstrated to be able to fit experimental data for molecular weight, crystallinity and Young's modulus.

Chapter 11: Discussion

The following objectives were originally targeted in this thesis:

1. Simplify the existing models for biodegradable polymer degradation.
2. Further the understanding of how the following factors affect degradation:
    a. Autocatalysis
    b. Random and end scission
    c. Initial molecular weight
    d. Residual monomer
3. Improve the understanding of how and why Young's modulus reduces during degradation.
4. Extend the existing mathematical degradation models to include the degradation of Young's modulus for glassy polymers.

These points are discussed here with reference to the overall field of medical biodegradable polymers.

11.1 Simplify the existing models

It is important to simplify numerical models for polymer degradation where possible to make them (i) more accessible to people with limited modelling experience, (ii) easier to configure to a specific polymer, and (iii) less computationally demanding. The simplified mathematical model presented in this thesis for molecular weight and crystallinity in degrading polymers contains fewer parameters than the original model on which it was based. It also has reduced computational demands due to the removal of integrational terms. The simplification was achieved by considering new crystallites, which nucleate as a result of chain scission, to grow at a much faster rate than chain scission. The simplification may introduce a risk of the model slightly overestimating crystallinity in the early stages of degradation, but this problem has not arisen when fitting to a considerable amount of experimental data in the work related to this thesis. Having fewer parameters in the model directly translates to fewer experiments being required to determine their values. The effort required to write a program to implement the model is also reduced by the removal of integrational terms. This makes the model usable by academic researchers with limited modelling experience, to the extent that it can be implemented in an Excel worksheet.

A major aim of research into modelling degradation is to increase clinical relevance by developing models that are able to optimise patient-specific medical devices. To achieve this aim, models must have predictive capacity. This capacity is currently limited by the fact that many degradation factors (i) are not fully understood and (ii) cannot be fully incorporated into the model without it becoming too complicated for clinical use. The first point is considered in the next section of this discussion. This thesis takes a step towards the second point by simplifying the crystallinity aspect of the model, which generates greater scope for additional degradation factors to be considered without over-complicating the model. It is important that all future aspects of degradation are modelled in the simplest manner appropriate, since a large number of factors will ultimately need to be considered in a fully predictive model.

11.2 Further the understanding of factors that affect degradation and modelling Young's modulus degradation

The simplified model was extended in Chapters 6 and 7 to enable analysis of several degradation factors that have been identified in experimental studies as important but are not fully understood. The model identified relationships between the degradation of biodegradable polymers and the following factors: noncatalytic hydrolysis, autocatalytic hydrolysis, end scission, random scission, residual monomer after processing, and initial molecular weight. These relationships can be used without any modelling experience to analyse experimental degradation results instantly and determine the most likely hydrolysis mechanisms controlling the degradation. Although these relationships improve the current understanding of degradation, their true value lies in offering support to future experimental studies: this support is achieved by enabling more thorough analysis of experimental results when modelling is not undertaken. The relationships may also be of value to industry in guiding the design of a polymer for a desired degradation trend. For example, if end scission is found to be the dominant mechanism and it is desired for the polymer to maintain mass over a longer period of time, the initial molecular weight may be increased to reduce the initial number of chain ends and therefore reduce the rate of end scission. Although the general relationships may increase researchers' abilities to analyse experimental data, fitting the model to the data facilitates the most comprehensive analysis. Therefore, the mathematical framework of the model is also of value to academic research. The analysis of a large number of data sets found that auto-catalysis almost always occurs and typically there is a combination of both random and end scission mechanisms. Again, this knowledge is of most value for the effective understanding of experimental results.

Presently, surgeons are unlikely to use the model since the in-hospital design of patient-specific biodegradable polymer devices is not widespread. However, as on-site manufacturing methods such as 3D printing become more popular, degradation models become more valuable. The models in this thesis can be implemented in finite element analysis simulations to design devices with geometries tailored for optimal degradation trends including mass loss and Young's modulus. For clinical applications, mechanical properties degradation may be the most important characteristic of biodegradable devices. Therefore, the extension of the model in this thesis to include Young's modulus degradation is of great interest. However, the predictive capability of the model, based purely on initial polymer information, must be increased for widespread clinical use. To achieve this, experimental studies should continue to investigate factors that affect degradation and models must be developed that can effectively reproduce the trends associated with these factors. Residual monomer is of great importance and should be further investigated. It is not always measured in experimental studies but has recently been shown to impact the degradation rate by an order of magnitude [18]. The model presented in this thesis also predicts such extensive effects of residual monomer. Another important factor that needs further understanding is the influence of polymer microstructure on degradation. This thesis modelled the degradation of polymers with various crystallinities and found that amorphous polymer within spherulites degrades at a much faster rate than amorphous polymer outside spherulites. Other aspects of polymer microstructure that should be considered in the future include polymer chain alignment and crystallite size and orientation. The analysis in this thesis has focussed on the polymer material; once this is better understood the effect of the degradation environment must also be considered since the type and temperature of degradation media is known to affect degradation, as is *in vitro* versus *in vivo* degradation.

11.3 Improve the understanding of Young's modulus degradation

A large number of experimental studies in the literature have analysed the degradation trends of Young's modulus. However, there is limited atomic-scale analysis due to the computational demands of modelling at such small length scales. The atomic finite element method presented here enables new atomic-scale analysis of the effects of polymer chain scission on Young's modulus. By adapting the non-linear interatomic potential energy equations from molecular dynamics into a format suitable for static linear analysis the computation demands are greatly reduced. However, the

simulations are limited to zero Kelvin, and hence do not capture all aspects of polymer chain interaction. They enable the first steps to be taken towards more complete atomic understanding. As computational power increases it may eventually be feasible to conduct dynamic simulations at finite temperatures. These simulations would be able to analyse polymer chain interaction in more detail and also consider other mechanical properties of interest including strength and elongation-at-break; the atomic finite element method is valid for small deformations only so cannot consider such properties.

A key finding of the atomic simulations is that volumes of polymer adjacent to a polymer chain scission are subject to a reduced force as a result of the scission. This understanding was used to develop the Young's modulus degradation model, in which effective cavities are considered to exist adjacent to each scission. The Young's modulus degradation model is incorporated into the molecular weight degradation model and fittings to experimental data had a high level of accuracy. A limitation of the zero Kelvin simulations is that the size and stiffness of the cavities cannot be directly predicted; in this thesis they are considered to have zero modulus as a simplification and the size is adjusted during the fitting of the model to experimental data. Dynamic analysis would be more predictive and may enable Young's modulus degradation to be simulated without the need to adjust the cavity size through fitting to experimental data. The model is not currently targeted at the latter stage of degradation when Young's modulus approaches zero. To target this stage the interaction between several cavities and between cavities and crystallites should be considered.

A previous study presented a model for Young's modulus degradation in polymers above their glass transition temperature [61], but the model presented in this thesis is the first to be developed that is applicable to polymers used below their glass transition temperature, including poly(lactide). For designers of medical fixation devices, the model can be programmed into commercial FEA packages and used to design a fixation device that supports a healing bone effectively throughout the healing process. The model for Young's modulus degradation is dependent on molecular weight degradation and crystallinity. Therefore, its clinical relevance depends on a comprehensive understanding of these factors. This thesis is focussed on the medical application of polymer degradation modelling. However, the models may be applicable to alternative applications such as UV degradation or non-polymer materials. In addition, by relating polymer degradation to biocompatibility, bone growth or cell adhesion, these factors could also be modelled.

Chapter 12: Major conclusions and future work

12.1 Major conclusions

This thesis presented new mathematical models for the degradation of biodegradable polymers and conducted atomic simulations in order to model the degradation of mechanical properties. A review of experimental degradation studies in the literature was conducted in order to further the understanding of mechanical properties degradation and to identify a relationship between molecular weight degradation and Young's modulus degradation.

The mathematical models that were presented were based on previous models from the group at the University of Leicester; they were either simplified, to make them more accessible to non-experts, or extended, in order to enable the analysis of individual hydrolysis mechanisms. The models were used to further the understanding of several factors in degradation. It was found that the amorphous polymer phase that is trapped inside spherulites degrades at a faster rate than the amorphous polymer outside spherulites. Simple qualitative trends in the degradation of molecular weight and mass loss were found to relate to the underlying hydrolysis mechanisms. These trends are that: (i) a deceleration of molecular weight reduction versus time indicates random scission whereas a lack of the deceleration indicates end scission; (ii) autocatalytic hydrolysis is indicated by a nonlinear relationship between ($1/M_n$) and time; (iii) mass loss while the polymer is still medium to high molecular weight indicates end scission; and (iv) a linear increase in mass loss with time indicates noncatalytic end scission.

The degradation trends in 31 experimental publications were analysed. It was found that a combination of random and end scission is expected to occur and that autocatalytic hydrolysis occurs more frequently in experiments than noncatalytic hydrolysis. It was found that molecular weight degradation is caused by random scission, whereas mass loss is caused by end scission.

The model was also used to analyse the effects of initial molecular weight and residual monomer. For the most common combination of hydrolysis mechanisms identified in the analysis of 31 experimental data sets, a combination of autocatalytic random scission and autocatalytic end scission, it was found that initial molecular weight did not typically affect the rate of normalised molecular weight degradation, although the rate

of chain cleavage was affected. The time taken for significant mass loss increased as initial molecular weight increased. For autocatalytic hydrolysis, an inverse square root law was found to relate molecular weight degradation to the residual monomer content. The model was able to fit experimental data [18], in which various different residual monomer contents were measured.

An atomic finite element method was presented for static linear analysis of poly(lactide). The simulation technique implemented existing molecular dynamics input files in order to model atomic coordinates and interactions. Three types of finite elements were presented to represent the potential energy functions in the molecular dynamics force field PLAFF2. The finite elements contained six, nine or twelve degrees of freedom, for linear, angular or dihedral atomic interactions, respectively. Simulations were conducted to calculate the strain energy in a deformed polymer structure in order to determine Young's modulus. Both crystalline and amorphous poly(lactide) polymer structures were analysed. Nonbonded interactions, between atoms that are not covalently bonded, were found to contain the greatest value of strain energy in the strained structures.

The effect of chain scission on the Young's modulus of poly(lactide) was analysed using the atomic simulations. The trend was found to be similar to that found in the literature review of experimental data. The transfer of force between atoms, in a strained polymer, was also investigated. In the regular crystalline phase, individual covalent bonds that were aligned in the direction of applied strain were found to sustain the greatest force, while in the amorphous phase, the forces were controlled by the atomic configuration over a much larger distance. Sections of polymer chains that were oriented in the direction of applied strain were found to sustain the greatest force. It was suggested that stiffer regions of polymer may act as rigid sections in a weaker matrix of long-range unoriented atomic interactions.

Individual chain scissions were found to instantiate regions of less-stiff polymer. A model for Young's modulus degradation was presented, called the Effective Cavity Theory, in which each chain scission is considered to create an effective cavity. Finite element analysis simulations were conducted to identify the effect of effective cavities on the overall Young's modulus. Similarly, the effect of crystallites on overall Young's modulus was also modelled. The Effective Cavity Theory model was presented to

relate overall Young's modulus degradation to the volume fraction of effective cavities and crystallites.

Experimental data from the literature was used to demonstrate the ability of the Effective Cavity Theory model. A good fitting was achieved to several experimental data sets. The Effective Cavity Theory was combined with one of the mathematical models presented in this thesis, in order to capture the overall degradation process, including molecular weight, crystallinity and Young's modulus.

12.2 Further work

Much progress has been made in recent years to model the degradation of bioresorbable polymers in terms of molecular weight, mass loss, crystallinity and mechanical properties. As discussed in the previous chapter of this thesis, these models will ultimately be used to tailor the design of medical devices, for example to support bone-fractures in the optimal manner during the entire healing process. It is currently necessary to determine the model parameters from experimental data before the models can be used. They are predictive to some degree but not all of the factors that affect degradation are currently understood so a single set of model parameters cannot be used for a wide range of experimental conditions. In this thesis, steps are taken to further understand the impact of some factors and it was recommended in the previous chapter that further research is needed to better understand the effect of residual monomer, polymer microstructure and the degradation medium.

One aspect of biodegradable polymers which is not yet modelled, and is of great interest to the scientific community, is the interaction between living tissue and the biodegradable polymer. There is some understanding about this interaction, including the theories that: (i) inflammation may result from the local acidic environment around a degrading polymer device [34-38], which occurs when significant amounts of monomer are released from a biodegradable device; (ii) the L-lactide isomer may be more biocompatible that the D-lactide isomer, because L-lactide is the naturally occurring isomer; and (iii) cell adhesion depends on several factors, including the hydrophobicity and hydrophilicity [109], roughness [110], charge [111] and surface energy [112]. These factors can be controlled to improve cell affinity [113]. Mathematical models for biocompatibility can help to further the current understanding of how living tissue and a

degrading polymer interact. This may lead to more successful and more widespread use of medical fixation devices manufactured from biodegradable polymers.

The mathematical model presented in this thesis is able to model the concentration of acidic chain ends and can be extended consider the production of individual L-lactide and D-lactide monomers that are produced during the degradation of poly(L-lactide) and poly(D-lactide) copolymers. Therefore the model is well suited to form the foundation of future models that simulate biocompatibility during degradation. Such models may consider the diffusion of monomers through a polymer device and model the transport of monomers away from the fixation device through living tissue. A simple model which relates pH to biocompatibility could then be integrated in order to form an overall model which considers degradation, monomer transport and biocompatibility.

In addition to biocompatibility, cell adhesion could be modelled. This is particularly important for biodegradable polymer scaffolds that are used in tissue engineering and regenerative medicine applications. The degradation products that are produced simultaneously with tissue growth, and erosion of the polymer surface, may affect cell adhesion. Future models may implement theories for cell adhesion into the mathematical model for degradation. The ability of the model to fit experimental data for cell growth can then be used to validate and improve the theories, and may ultimately be able to predict the rates of cell growth. Such models would enable biodegradable polymer scaffolds for tissue engineering to be designed to optimise cell growth, based on factors that the models consider.

References

[1] Lyu S, Schley J, Loy B, Lind D, Hobot C, Sparer R, et al. Kinetics and Time-Temperature Equivalence of Polymer Degradation. Biomacromolecules 2007;8:2301-10.

[2] Tsuji H. Autocatalytic hydrolysis of amorphous-made polylactides: effects of L-lactide content, tacticity, and enantiomeric polymer blending. Polymer 2002;43:1789-96.

[3] Schliecker G, Schmidt C, Fuchs S, Kissel T. Characterization and in vitro degradation of poly(2,3-(1,4-diethyl tartrate)-co-2,3-isopropyliden tartrate). Journal of Controlled Release 2004;98:11-23.

[4] Tan HY, Widjaja E, Boey F, Loo SCJ. Spectroscopy techniques for analyzing the hydrolysis of PLGA and PLLA. Journal of Biomedical Materials Research Part B: Applied Biomaterials 2009;91B:433-40.

[5] Tsuji H, Mizuno A, Ikada Y. Properties and morphology of poly(L-lactide). III. Effects of initial crystallinity on long-term in vitro hydrolysis of high molecular weight poly(L-lactide) film in phosphate-buffered solution. Journal of Applied Polymer Science 2000;77:1452-64.

[6] Weir N, Buchanan F, Orr J, Dickson G. Degradation of poly-L-lactide. Part 1: in vitro and in vivo physiological temperature degradation. Proceedings of the Institution of Mechanical Engineers, Part H: Journal of Engineering in Medicine 2004;218:307-19.

[7] Weir N, Buchanan F, Orr J, Farrar D, Dickson G. Degradation of poly-L-lactide. Part 2: increased temperature accelerated degradation. Proceedings of the Institution of Mechanical Engineers, Part H: Journal of Engineering in Medicine 2004;218:321-30.

[8] Migliaresi C, Fambri L, Cohn D. A study on the in vitro degradation of poly(lactic acid). Journal of Biomaterials Science, Polymer Edition 1994;5:591-606.

[9] Tsuji H. In vitro hydrolysis of blends from enantiomeric poly(lactide)s. Part 1. Well-stereo-complexed blend and non-blended films. Polymer 2000;41:3621-30.

[10] Tsuji H. In vitro hydrolysis of blends from enantiomeric poly(lactide)s. Part 4: well-homo-crystallized blend and nonblended films. Biomaterials 2003;24:537-47.

[11] Lam KH, Nieuwenhuis P, Molenaar I, Esselbrugge H, Feijen J, Dijkstra PJ, et al. Biodegradation of porous versus non-porous poly(L-lactic acid) films. Journal of Materials Science: Materials in Medicine 1994;5:181-9.

[12] Tsuji H, Del Carpio CA. In Vitro Hydrolysis of Blends from Enantiomeric Poly(lactide)s. 3. Homocrystallized and Amorphous Blend Films. Biomacromolecules 2002;4:7-11.

[13] Schliecker G, Schmidt C, Fuchs S, Wombacher R, Kissel T. Hydrolytic degradation of poly(lactide-co-glycolide) films: effect of oligomers on degradation rate and crystallinity. International Journal of Pharmaceutics 2003;266:39-49.

[14] Li S, McCarthy S. Further investigations on the hydrolytic degradation of poly (DL-lactide). Biomaterials 1999;20:35-44.

[15] Li SM, Garreau H, Vert M. Structure-property relationships in the case of the degradation of massive poly(α-hydroxy acids) in aqueous media. Journal of Materials Science: Materials in Medicine 1990;1:198-206.

[16] Cai Q, Shi G, Bei J, Wang S. Enzymatic degradation behavior and mechanism of Poly(lactide-co-glycolide) foams by trypsin. Biomaterials 2003;24:629-38.

[17] Tsuji H, Ikada Y. Properties and morphology of poly(L-lactide) 4. Effects of structural parameters on long-term hydrolysis of poly(L-lactide) in phosphate-buffered solution. Polymer Degradation and Stability 2000;67:179-89.

[18] Paakinaho K, Heino H, Väisänen J, Törmälä P, Kellomäki M. Effects of lactide monomer on the hydrolytic degradation of poly(lactide-co-glycolide) 85L/15G. Journal of the Mechanical Behavior of Biomedical Materials 2011;4:1283-90.

[19] Niemelä T. Effect of β-tricalcium phosphate addition on the in vitro degradation of self-reinforced poly-l,d-lactide. Polymer Degradation and Stability 2005;89:492-500.

[20] Niiranen H, Pyhältö T, Rokkanen P, Kellomäki M, Törmälä P. In vitro and in vivo behavior of self-reinforced bioabsorbable polymer and self-reinforced bioabsorbable polymer/bioactive glass composites. Journal of Biomedical Materials Research Part A 2004;69A:699-708.

[21] Vieira AC, Vieira JC, Ferra JM, Magalhães FD, Guedes RM, Marques AT. Mechanical study of PLA–PCL fibers during in vitro degradation. Journal of the Mechanical Behavior of Biomedical Materials 2011;4:451-60.

[22] Grizzi I, Garreau H, Li S, Vert M. Hydrolytic degradation of devices based on poly(dl-lactic acid) size-dependence. Biomaterials 1995;16:305-11.

[23] Hyon SH, Jamshidi K, Ikada Y. Effects of residual monomer on the degradation of DL-lactide polymer. Polymer International 1998;46:196-202.

[24] Dunne M, Corrigan OI, Ramtoola Z. Influence of particle size and dissolution conditions on the degradation properties of polylactide-co-glycolide particles. Biomaterials 2000;21:1659-68.

[25] Beslikas T, Gigis I, Goulios V, Christoforides J, Papageorgiou GZ, Bikiaris DN. Crystallization Study and Comparative in Vitro-in Vivo Hydrolysis of PLA Reinforcement Ligament. International journal of molecular sciences 2011;12:6597-618.

[26] Batycky RP, Hanes J, Langer R, Edwards DA. A theoretical model of erosion and macromolecular drug release from biodegrading microspheres. Journal of Pharmaceutical Sciences 1997;86:1464-77.

[27] Antheunis H, van der Meer J-C, de Geus M, Kingma W, Koning CE. Improved Mathematical Model for the Hydrolytic Degradation of Aliphatic Polyesters. Macromolecules 2009;42:2462-71.

[28] Antheunis H, van der Meer J-C, de Geus M, Heise A, Koning CE. Autocatalytic Equation Describing the Change in Molecular Weight during Hydrolytic Degradation of Aliphatic Polyesters. Biomacromolecules 2010;11:1118-24.

[29] Raman C, Berkland C, Kim K, Pack DW. Modeling small-molecule release from PLG microspheres: effects of polymer degradation and nonuniform drug distribution. Journal of Controlled Release 2005;103:149-58.

[30] Pitt CG, Gratzl MM, Kimmel GL, Surles J, Sohindler A. Aliphatic polyesters II. The degradation of poly (DL-lactide), poly (ε-caprolactone), and their copolymers in vivo. Biomaterials 1981;2:215-20.

[31] Pistner H, Bendi DR, Mühling J, Reuther JF. Poly (l-lactide): a long-term degradation study in vivo: Part III. Analytical characterization. Biomaterials 1993;14:291-8.

[32] Grimston SK, Willows ND, Hanley DA. Mechanical loading regime and its relationship to bone mineral density in children. Medicine and science in sports and exercise 1993;25:1203-10.

[33] Bubanj S, Obradović B. Mechanical force and bones density. Facta universitatis-series: Physical Education and Sport 2002;1:37-50.

[34] Ambrose CG, Clanton TO. Bioabsorbable Implants: Review of Clinical Experience in Orthopedic Surgery. Annals of Biomedical Engineering 2004;32:171-7.

[35] Pietrzak WS, Sarver DR, Verstynen ML. Bioabsorbable polymer science for the practicing surgeon. Journal of Craniofacial Surgery 1997;8:87-91.

[36] Peltoniemi H. Biocompatibility and fixation properties of absorbable miniplates and screws in growing calvarium. An experimental study in sheep[theses], University of Helsinki, Finland 2000.

[37] Böstman O, Pihlajamäki H. Clinical biocompatibility of biodegradable orthopaedic implants for internal fixation: a review. Biomaterials 2000;21:2615-21.

[38] Suganuma J, Alexander H. Biological response of intramedullary bone to poly-L-lactic acid. Journal of Applied Biomaterials 1993;4:13-27.

[39] Wiggins JS, Hassan MK, Mauritz KA, Storey RF. Hydrolytic degradation of poly(d,l-lactide) as a function of end group: Carboxylic acid vs. hydroxyl. Polymer 2006;47:1960-9.

[40] Siparsky GL, Voorhees KJ, Miao F. Hydrolysis of polylactic acid (PLA) and polycaprolactone (PCL) in aqueous acetonitrile solutions: Autocatalysis. Journal of Environmental Polymer Degradation 1998;6:31-41.

[41] Li SM, Garreau H, Vert M. Structure-property relationships in the case of the degradation of massive aliphatic poly-(α-hydroxy acids) in aqueous media. Journal of Materials Science: Materials in Medicine 1990;1:123-30.

[42] Li SM, Garreau H, Vert M. Structure-property relationships in the case of the degradation of massive poly(α-hydroxy acids) in aqueous media. Journal of Materials Science: Materials in Medicine 1990;1:131-9.

[43] Vey E, Roger C, Meehan L, Booth J, Claybourn M, Miller AF, et al. Degradation mechanism of poly(lactic-co-glycolic) acid block copolymer cast films in phosphate buffer solution. Polymer Degradation and Stability 2008;93:1869-76.

[44] Schliecker G, Schmidt C, Fuchs S, Kissel T. Characterization of a homologous series of d,l-lactic acid oligomers; a mechanistic study on the degradation kinetics in vitro. Biomaterials 2003;24:3835-44.

[45] de Jong SJ, Arias ER, Rijkers DTS, van Nostrum CF, Kettenes-van den Bosch JJ, Hennink WE. New insights into the hydrolytic degradation of poly(lactic acid): participation of the alcohol terminus. Polymer 2001;42:2795-802.

[46] Shih C. Chain-end scission in acid catalyzed hydrolysis of poly (D,L-lactide) in solution. Journal of Controlled Release 1995;34:9-15.

[47] Gleadall A, Pan J, Atkinson H. A simplified theory of crystallisation induced by polymer chain scissions for biodegradable polyesters. Polymer Degradation and Stability 2012;97:1616-20.

[48] Han X, Pan J. A model for simultaneous crystallisation and biodegradation of biodegradable polymers. Biomaterials 2009;30:423-30.

[49] Han X, Pan J, Buchanan F, Weir N, Farrar D. Analysis of degradation data of poly(l-lactide-co-l,d-lactide) and poly(l-lactide) obtained at elevated and physiological temperatures using mathematical models. Acta Biomaterialia 2010;6:3882-9.

[50] Wang Y, Pan J, Han X, Sinka C, Ding L. A phenomenological model for the degradation of biodegradable polymers. Biomaterials 2008;29:3393-401.

[51] Hiroyuki T. Structure and properties of crystalline polymers. Polymer 1984;25:147-64.

[52] Zong X-H, Wang Z-G, Hsiao BS, Chu B, Zhou JJ, Jamiolkowski DD, et al. Structure and morphology changes in absorbable poly(glycolide) and poly(glycolide-co-lactide) during in vitro degradation. Macromolecules 1999;32:8107-14.

[53] Kobayashi J, Asahi T, Ichiki M, Oikawa A, Suzuki H, Watanabe T, et al. Structural and optical properties of poly lactic acids. Journal of Applied Physics 1995;77:2957-73.

[54] Hoogsteen W, Postema AR, Pennings AJ, Ten Brinke G, Zugenmaier P. Crystal structure, conformation and morphology of solution-spun poly(L-lactide) fibers. Macromolecules 1990;23:634-42.

[55] Alemán C, Lotz B, Puiggali J. Crystal Structure of the α-Form of Poly(l-lactide). Macromolecules 2001;34:4795-801.

[56] Sasaki S, Asakura T. Helix Distortion and Crystal Structure of the α-Form of Poly(l-lactide). Macromolecules 2003;36:8385-90.

[57] Tsuji H, Ikada Y. Properties and morphologies of poly(L-lactide): 1. Annealing condition effects on properties and morphologies of poly(L-lactide). Polymer 1995;36:2709-16.

[58] Duek EAR, Zavaglia CAC, Belangero WD. In vitro study of poly(lactic acid) pin degradation. Polymer 1999;40:6465-73.

[59] Pitt CG, Zhong-wei G. Modification of the rates of chain cleavage of poly(ϵ-caprolactone) and related polyesters in the solid state. Journal of Controlled Release 1987;4:283-92.

[60] Han X, Pan J. Polymer chain scission, oligomer production and diffusion: A two-scale model for degradation of bioresorbable polyesters. Acta Biomaterialia 2011;7:538-47.

[61] Wang Y, Han X, Pan J, Sinka C. An entropy spring model for the Young's modulus change of biodegradable polymers during biodegradation. Journal of the Mechanical Behavior of Biomedical Materials 2010;3:14-21.

[62] Ding L, Davidchack R, Pan J. A molecular dynamics study of Young's modulus change of semi-crystalline polymers during degradation by chain scissions. Journal of the Mechanical Behavior of Biomedical Materials 2011;5:224-30.

[63] Gleadall A. Mechanical properties of biodegradable polymers. in: Pan, J. Modelling degradation of bioresorbable polymeric medical devices. Woodhead Publishing; 2015.

[64] Ward IM, Hadley DW. An Introduction to the Mechanical Properties of Solid Polymers. Chichester, New York: Wiley-Blackwell; 1993.

[65] Nakafuku C, Takehisa S-y. Glass transition and mechanical properties of PLLA and PDLLA-PGA copolymer blends. Journal of Applied Polymer Science 2004;93:2164-73.

[66] Saha SK, Tsuji H. Effects of molecular weight and small amounts of d-lactide units on hydrolytic degradation of poly(l-lactic acid)s. Polymer Degradation and Stability 2006;91:1665-73.

[67] Tsuji H, Suzuyoshi K. Environmental degradation of biodegradable polyesters 1. Poly([var epsilon]-caprolactone), poly[(R)-3-hydroxybutyrate], and poly(L-lactide) films in controlled static seawater. Polymer Degradation and Stability 2002;75:347-55.

[68] Tsuji H, Muramatsu H. Blends of aliphatic polyesters: V non-enzymatic and enzymatic hydrolysis of blends from hydrophobic poly(l-lactide) and hydrophilic poly(vinyl alcohol). Polymer Degradation and Stability 2001;71:403-13.

[69] Saha SK, Tsuji H. Effects of rapid crystallization on hydrolytic degradation and mechanical properties of poly(l-lactide-co-ε-caprolactone). Reactive and Functional Polymers 2006;66:1362-72.

[70] Yuan X, Mak AFT, Yao K. In vitro degradation of poly(L- lactic acid) fibers in phosphate buffered saline. Journal of Applied Polymer Science 2002;85:936-43.

[71] Tsuji H, Suzuyoshi K. Environmental degradation of biodegradable polyesters 2. Poly([var epsilon]-caprolactone), poly[(R)-3-hydroxybutyrate], and poly(L-lactide) films in natural dynamic seawater. Polymer Degradation and Stability 2002;75:357-65.

[72] Karjalainen T, Hiljanen-Vainio M, Malin M, Seppälä J. Biodegradable lactone copolymers. III. Mechanical properties of ε-caprolactone and lactide copolymers after hydrolysis in vitro. Journal of Applied Polymer Science 1996;59:1299-304.

[73] Tsuji H, Ikada Y. Blends of aliphatic polyesters. II. Hydrolysis of solution-cast blends from poly(L-lactide) and poly(E-caprolactone) in phosphate-buffered solution. Journal of Applied Polymer Science 1998;67:405-15.

[74] Flory PJ. Principles of Polymer Chemistry. Ithaca, NY: Cornell University Press; 1955.

[75] Deng M, Zhou J, Chen G, Burkley D, Xu Y, Jamiolkowski D, et al. Effect of load and temperature on in vitro degradation of poly(glycolide-co-l-lactide) multifilament braids. Biomaterials 2005;26:4327-36.

[76] Liu B, Huang Y, Jiang H, Qu S, Hwang KC. The atomic-scale finite element method. Computer Methods in Applied Mechanics and Engineering 2004;193:1849-64.

[77] Liu B, Jiang H, Huang Y, Qu S, Yu MF, Hwang KC. Atomic-scale finite element method in multiscale computation with applications to carbon nanotubes. Physical Review B 2005;72:035435.

[78] Wang Y, Sun C, Sun X, Hinkley J, Odegard GM, Gates TS. 2-D nano-scale finite element analysis of a polymer field. Composites Science and Technology 2003;63:1581-90.

[79] Wang Y, Zhang C, Zhou E, Sun C, Hinkley J, Gates TS, et al. Atomistic finite elements applicable to solid polymers. Computational Materials Science 2006;36:292-302.

[80] Blomqvist J, Mannfors B, Pietilä LO. Amorphous cell studies of polyglycolic, poly(-lactic), poly(,-lactic) and poly(glycolic/-lactic) acids. Polymer 2002;43:4571-83.

[81] Blomqvist J, Mannfors B, Pietilä LO. Studies on aliphatic polyesters. Part II. Ab initio, density functional and force field studies of model molecules with two carboxyl groups. Journal of Molecular Structure: THEOCHEM 2000;531:359-74.

[82] Montes de Oca H, Ward IM. Structure and mechanical properties of poly(L-lactic acid) crystals and fibers. Journal of Polymer Science Part B: Polymer Physics 2007;45:892-902.

[83] Montes de Oca H, Ward IM. Structure and mechanical properties of PGA crystals and fibres. Polymer 2006;47:7070-7.

[84] Lin T, Liu X-Y, He C. Ab Initio Elasticity of Poly(lactic acid) Crystals. The Journal of Physical Chemistry B 2010;114:3133-9.

[85] McAliley JH. Development of improved torsional potentials in classical force field descriptions of poly (lactic acid). United States: Clemson University; 2009.

[86] McAliley JH, Bruce DA. Development of force field parameters for molecular simulation of polylactide. Journal of chemical theory and computation 2011;7:3756-67.

[87] Ellä V, Nikkola L, Kellomäki M. Process-induced monomer on a medical-grade polymer and its effect on short-term hydrolytic degradation. Journal of Applied Polymer Science 2011;119:2996-3003.

[88] Huttunen M. Analysis of the factors affecting the inherent viscosity of oriented polylactides during hydrolytic degradation. Journal of Materials Science: Materials in Medicine 2013:1-14.

[89] Park TG. Degradation of poly(d,l-lactic acid) microspheres: effect of molecular weight. Journal of Controlled Release 1994;30:161-73.

[90] Gleadall A, Pan J. Computer Simulation of Polymer Chain Scission in Biodegradable Polymers. Journal of Biotechnology & Biomaterials 2013;3.

[91] Buchanan FJ. Degradation rate of bioresorbable materials: Prediction and evaluation. Cambridge, England/Boca Raton [FL]: Woodhead Publishing/CRC Press; 2008.

[92] Höglund A, Hakkarainen M, Albertsson A-C. Migration and Hydrolysis of Hydrophobic Polylactide Plasticizer. Biomacromolecules 2009;11:277-83.

[93] Avrami M. Kinetics of phase change. I General theory. The Journal of Chemical Physics 1939;7:1103-12.

[94] Avrami M. Kinetics of phase change. II Transformation-time relations for random distribution of nuclei. The Journal of Chemical Physics 1940;8:212-24.

[95] Avrami M. Granulation, phase change, and microstructure kinetics of phase change. III. The Journal of Chemical Physics 1941;9:177-84.

[96] Buchanan F. Degradation rate of bioresorbable materials : prediction and evaluation. Cambridge, England; Boca Raton [Fla.]: Woodhead Pub. ; CRC Press; 2008.

[97] Gleadall A, Pan J, Kruft M-A, Kellomäki M. Degradation mechanisms of bioresorbable polyesters. Part 1. Effects of random scission, end scission and autocatalysis. Acta Biomaterialia 2014;10:2223-32.

[98] Yoon J-S, Jung H-W, Kim M-N, Park E-S. Diffusion coefficient and equilibrium solubility of water molecules in biodegradable polymers. Journal of Applied Polymer Science 2000;77:1716-22.

[99] Gleadall A, Pan J, Kruft M-A, Kellomäki M. Degradation mechanisms of bioresorbable polyesters. Part 2. Effects of initial molecular weight and residual monomer. Acta Biomaterialia 2014;10:2233-40.

[100] Witschi C, Doelker E. Influence of the microencapsulation method and peptide loading on poly(lactic acid) and poly(lactic-co-glycolic acid) degradation during in vitro testing. Journal of Controlled Release 1998;51:327-41.

[101] Paakinaho K, Ellä V, Syrjälä S, Kellomäki M. Melt spinning of poly(l/d)lactide 96/4: Effects of molecular weight and melt processing on hydrolytic degradation. Polymer Degradation and Stability 2009;94:438-42.

[102] Gleadall A, Pan J, Ding L, Kruft M-A, Curco D. An atomic finite element model for biodegradable polymers. Part 1. Theory and validation. Submitted for publication.

[103] D. van der Spoel EL, B. Hess, A. R. van Buuren, E. Apol, P. J. Meulenhoff, D. P. Tieleman, A. L. T. M. Sijbers, K. A. Feenstra, R. van Drunen, H. J. C. Berendsen. Gromacs User Manual version 4.5.4. www.gromacs.org; 2010.

[104] PumMa > Theory > Potentials [online] Available at: http://cbio.bmt.tue.nl/pumma/index.php/Theory/Potentials [Accessed: 10 Feb 2014]. 2014.

[105] Smith IM, Griffiths DV. Programming the finite element method. 4 ed: Wiley. com; 2005.

[106] Gleadall A, Pan J, Kruft M-A. An atomic finite element model for biodegradable polymers. Part 2. A model for change in Young's modulus due to polymer chain scission. Submitted for publication.

[107] Nuutinen JP, Clerc C, Reinikainen R, Tormala P. Mechanical properties and in vitro degradation of bioabsorbable self-expanding braided stents. Journal of biomaterials science Polymer edition 2003;14:255-66.

[108] Pihlajamaki H, Bostman O, Hirvensalo E, Tormala P, Rokkanen P. Absorbable pins of self-reinforced poly-L-lactic acid for fixation of fractures and osteotomies. The Journal of bone and joint surgery British volume 1992;74:853-7.

[109] Webb K, Hlady V, Tresco PA. Relative importance of surface wettability and charged functional groups on NIH 3T3 fibroblast attachment, spreading, and cytoskeletal organization. Journal of Biomedical Materials Research 1998;41:422-30.

[110] Chehroudi B, Gould TRL, Brunette DM. Titanium-coated micromachined grooves of different dimensions affect epithelial and connective-tissue cells differently in vivo. Journal of Biomedical Materials Research 1990;24:1203-19.

[111] van Wachem PB, Hogt AH, Beugeling T, Feijen J, Bantjes A, Detmers JP, et al. Adhesion of cultured human endothelial cells onto methacrylate polymers with varying surface wettability and charge. Biomaterials 1987;8:323-8.

[112] Daw R, Candan S, Beck AJ, Devlin AJ, Brook IM, MacNeil S, et al. Plasma copolymer surfaces of acrylic acid/1,7 octadiene: Surface characterisation and the attachment of ROS 17/2.8 osteoblast-like cells. Biomaterials 1998;19:1717-25.

[113] Yang J, Wan Y, Tu C, Cai Q, Bei J, Wang S. Enhancing the cell affinity of macroporous poly(L-lactide) cell scaffold by a convenient surface modification method. Polymer International 2003;52:1892-9.